A CLIMATE PERSPECTIVE ON PALEOELEVATION AND EROSION PROCESSES IN THE ANDES

by

Mairi Louise Jeffery

A dissertation submitted in partial fulfillment
of the requirements for the degree of
Doctor of Philosophy
(Earth and Environmental Sciences)
in the University of Michigan
2013

Doctoral Committee:

Associate Professor Christopher J. Poulsen, Co-Chair
Visiting Associate Professor Todd A. Ehlers, Co-Chair
Assistant Professor Nathan D. Sheldon
Associate Professor Allison L. Steiner

ACKNOWLEDGEMENTS

I would like to thank my co-chairs and advisors Chris Poulsen and Todd Ehlers for their guidance and support. I am grateful that they both allowed me to pursue my own interests and offered sound scientific and professional advice throughout the dissertation processes. My research has benefitted greatly from having a broad perspective on the scientific problems addressed.

Brian Yanites is a co-author on two of the chapters in this dissertation (Chapters 3 and 4). I have really enjoyed our discussions over the last few years and have greatly appreciated his insight into the problems we have been working on. His knowledge of geomorphic processes and understanding of model behavior has been invaluable.

My two other committee members, Allison Steiner and Nathan Sheldon have been very supportive throughout the dissertation process. Their thoughts and comments have helped greatly to direct and focus the research. I also enjoyed taking a class with Allison that was both technically useful and increased my enthusiasm for and understanding of climate modeling.

The combined Surface Processes / Paleoclimate research group is a dynamic and interesting group to be a part of. Daniel Horton, Nadja Insel, Jing Zhou, Stephanie Olen, Allison Yanites, Rich Fiorella, Clay Tabor, Ran Feng and Dan Lowry - you have all been a pleasure to work with over the last few years. Thank you also to the other members of my cohort for scientific discussions, support and friendship, especially Rohit Warrier, Laura Waters, Laura Sherman, Jen Cotton and Meghan Wagner.

Thank you also, to all those who have made Ann Arbor a great place to live. I don't know what I'll do on Thursday evenings without everyone at netball,

especially Dalia, Denise, Ruth, Isabel, Jenny and Elspeth. Past and present residents of 293 and 407, you're all amazing. Stephanie, thank you for helping me keep everything in perspective.

Finally, thank you to my family who have supported and encouraged me throughout my education.

TABLE OF CONTENTS

LIST OF FIGURES

LIST OF TABLES

LIST OF APPENDICES

ABSTRACT

The topographic and climatic histories of the central Andes are closely coupled. As a result, geological evidence for the nature of past surface environments is commonly a record of both topographic and climatic changes. In order to understand tectonic, climate, and erosion mechanisms, the relative roles of climate and tectonics in changing surface environments must be resolved. This dissertation explores controls on late Cenozoic climate change in the Andes, and the response of surface processes to those changes. The knowledge gained is used (1) to evaluate end-member models of Andean plateau surface uplift, and (2) to determine whether climate is a strong control on erosional efficiency in the central Andes.

To explore the factors controlling South American climate during the late Cenozoic uplift of the central Andes, several paleoclimate scenarios were simulated by a global climate model with isotope tracking capabilities. The simulations are used to determine the relative importance of local and global factors on regional climate and precipitation $\delta^{18}O$. Results indicate that Andean topography is the strongest control on central Andean precipitation patterns and precipitation $\delta^{18}O$. As Andean plateau elevation increased, convective precipitation was triggered on the eastern flanks and precipitation $\delta^{18}O$ in the central Andes dropped by 4-8 ‰. Precipitation $\delta^{18}O$ was also modified by global cooling (up to 8 ‰) and during late Miocene seaway incursions into the western Amazon basin (1-8 ‰).

The response of surface processes to climate change as a result of Andean uplift is then quantified using a 1D river incision model embedded in a Monte Carlo search. The results indicate that increasing precipitation rates with increasing Andean elevation influenced the rate and timing of river incision on the Andean flanks. Quantitative analysis of the influence of climate on paleoelevation proxies

indicates that a steady uplift since ~40 Ma is the simplest surface uplift model compatible with existing paleoelevation proxy records.

To constrain the influence of climate on Andean surface processes further, a new analysis of satellite-based precipitation observations is presented and compared with topographic metrics in the central Andes. The dataset is used to identify which climate characteristics determine erosional efficiency at the orogen scale. Mean annual precipitation correlates strongly with mean hillslope gradients where an increase in mean annual precipitation causes an increase in vegetation cover. Where vegetation cover is fixed, mean precipitation intensity and mean interval duration are the dominant precipitation variables. Identification of the importance of vegetation to surface processes at the orogeny scale highlights a need for further research to constrain the role of vegetation changes in topographic development during mountain belt growth.

CHAPTER 1

INTRODUCTION

1.1 CLIMATE-TECTONIC INTERACTIONS IN THE ANDES

The Andes Mountains span a wide range of climatic zones from tropical through arid. The mountainous topography overprints latitudinal climate gradients by disrupting low-level circulation, which enhances orographic precipitation on the windward flanks and generates rain shadows on the leeward flanks [*Campetella and Vera*, 2002; *Lenters and Cook*, 1995]. These large-scale climate patterns affect topography at a range of spatial scales through erosional processes. For example, glacial processes limit maximum elevations, while fluvial processes modify cross-range asymmetry, orogen width and hypsometry [*D.R. Montgomery et al.*, 2001]. By removing material, erosional processes have the potential to change the stress state in orogens and thereby modify the rate and style of deformation [*Koons*, 1990; *Willett*, 1999; *Willett et al.*, 1993]. Potential consequences of locally enhanced erosion rates include increased uplift rates, retreat of the deformation front, increased sediment flux to sedimentary basins, and a reduction in relief [*Whipple*, 2009]. However, identifying coupled relationships between climate and tectonics in natural settings has proved challenging [*Whipple*, 2009].

As the second largest plateau on Earth and with large climatic gradients, the central Andes are an ideal location to explore climate-tectonic interactions. Multiple thermochronometry datasets, coupled with balanced cross-sections, [*Barnes et al.*, 2006; *Barnes et al.*, 2008; *McQuarrie et al.*, 2008a] indicate a north-south gradient in

late Cenozoic (~20 Ma to Present) exhumation rates that reflects modern precipitation patterns on the eastern central Andean flanks [*Horton*, 1999; *Masek et al.*, 1994; *McQuarrie et al.*, 2008b]. Modern precipitation rates are also coupled to the large-scale topography [*Bookhagen and Strecker*, 2008; *Masek et al.*, 1994]. However, correlations between erosion rates and precipitation patterns are not observed on shorter timescales [10^2 – 10^4 years *Insel et al.*, 2010b; *Safran et al.*, 2005]. Furthermore, it is not appropriate to compare past changes in erosion with modern precipitation patterns, because of the dependence of precipitation on the topography itself. It is more useful to consider the coupled evolution of both topography and climate throughout the development of the mountain belt [*Bookhagen and Strecker*, 2012a; *Norton and Schlunegger*, 2011].

Constraints on simultaneous topographic and climatic development are therefore required to establish the nature and magnitude of climate-tectonic interactions. A key challenge to overcome is that topographic and climatic changes can leave similar traces in the geological record. For example, an increase in erosion rates may be caused by either an increase in climatic erosional efficiency, or by an increase in local uplift rates. In this dissertation, the role of climate in modifying surface processes and paleoenvironments is quantified to enable better understanding of the roles of climate and tectonics in shaping Andean topography.

1.2 ANDEAN PALEOELEVATION

The past elevation of the central Andean plateau has been the focus of several recent studies. Past plateau elevations can help to constrain the mechanism and style of plateau deformation. Furthermore, a complete understanding of the nature and cause of past environmental changes in South America, and the development of tectonic-climate interactions, requires a good constraint on the topographic development of the Andes.

1.2.1 Existing paleoelevation constraints

Attempts to constrain Andean paleoelevation over the last decade led to the formation of two end-member models [*Barnes and Ehlers*, 2009]. In the first end-member scenario, central Andean surface uplift has occurred steadily over the last

~40 Ma. This scenario is consistent with constraints on the deformation, exhumation, magmatic, and sedimentology histories of the plateau and with geophysical constraints on present day lithospheric structure. In the second model, surface uplift rates were punctuated by a rapid surface uplift event of ~2.5 km, equivalent to around half of modern Andean elevations, during the late Miocene, 10-6 Ma. This second model is based on observations of a shift in the stable isotopic composition of Miocene soil carbonates on the Altiplano [*Garzione et al.*, 2006; *C N Garzione et al.*, 2008a; *Ghosh et al.*, 2006], and is further supported by the occurrence of a contemporaneous fluvial incision pulse on the Andean flanks [*Garzione and Hoke*, 2006; *Hoke et al.*, 2007; *Schildgen et al.*, 2007]. The timing and rate of surface uplift has significant implications for the mechanism driving the uplift and geologic models of plateau development. A slower, steadier uplift is compatible with uplift as a result of continuous deformation of a thickened, weak lithosphere [*Barnes and Ehlers*, 2009; *T A Ehlers and Poulsen*, 2009]. Rapid and recent uplift is more compatible with surface uplift caused by removal of dense lithosphere in a single event [*Garzione et al.*, 2006; *Molnar and Garzione*, 2007; *Tao and O'Connell*, 1992].

Barnes and Ehlers [2009] concluded in favor of the first, steady, uplift model and argued that the evidence supporting a late Miocene uplift event could also be explained by a change in climate, triggered by a steadily uplifting mountain belt [*T A Ehlers and Poulsen*, 2009; *Insel et al.*, 2010a]. The stable isotope composition of soil carbonates can be used as a proxy for past elevations because the isotopic composition reflects elevation dependent environmental conditions at the time of formation: local evaporation rate, soil temperature, and the isotopic composition of local meteoric water [*Quade et al.*, 1989; *Quade et al.*, 2007]. Original interpretations of Andean soil carbonate isotope records were based on modern precipitation isotope lapse rates. However, isotope lapse rates are dependent on regional climate properties, including moisture pathways and rainout amounts, which changed with topographic growth. Andean topography deflects moisture from the Amazon basin southwards, and triggers convective precipitation on the eastern Central Andean flanks [*Insel et al.*, 2010a; *Poulsen et al.*, 2010]. In studies that complement this

dissertation, the dependence of precipitation $\delta^{18}O$ on Andean topography was quantified using global and regional climate models with isotope tracking capabilities [*Insel et al.*, 2012; *Poulsen et al.*, 2010].

1.2.2 Mountain building in a changing global climate

However, Andean uplift did not occur in an isolated system, but in a changing global climate. Since the beginning of Andean uplift (60–40 Ma), global temperatures dropped by ~10°C [*Lear et al.*, 2000] and polar ice sheets developed [*Ehrmann and Mackensen*, 1992; *Zachos et al.*, 1992] as atmospheric CO_2 concentrations decreased [*Pagani et al.*, 2005; *Pearson and Palmer*, 2000]. Moreover, additional regional changes have occurred in South America. The western Amazonian basin was inundated by a wetland or inland seaway during the Miocene [*Frailey et al.*, 1988; *Rasanen et al.*, 1995]. The extent to which these additional factors affected Andean climate and the stable isotope composition of precipitation is unknown. If the effects are comparable in magnitude to the impacts of changing Andean elevation, then they must also be considered in paleoaltimetry and paeloenvironmental studies. In Chapter 2 of this dissertation [see also: *Jeffery et al.*, 2012], a global climate model with isotope tracking capabilities is run with modified boundary conditions to quantify the impacts of external factors on South American climate during the Cenozoic. The results are compared with existing South American stable isotope records in order to quantify uncertainties in paleoenvironment and paleoelevation that arise due to the different controlling factors explored.

1.2.3 River incision

The second line of evidence that supports a rapid surface uplift event during the late Miocene is indications of rapid river incision on both flanks of the Andes. River profile analysis and erosion rate measurements from the central Andes indicate that a large pulse of incision began around 10 million years ago [*Barke and Lamb*, 2006; *Hoke et al.*, 2007; *Schildgen et al.*, 2007; *Schildgen et al.*, 2009b]. River incision is an indicator of surface uplift because a change in relative base level steepens channels and drives river incision with the same magnitude as the base level change. Stratigraphic and thermochronometric techniques can be used to

estimate the timing and magnitude of incision, and therefore the timing and magnitude of surface uplift. However, river incision rates depend not only on channel steepness, but also on channel discharge. A change in precipitation magnitude that accompanies surface uplift may confound interpretations of surface uplift from geologic evidence of river incision. As discussed above, increasing Andean elevation triggered convective precipitation on the eastern flanks, which through increasing river discharge may have enhanced incision amounts resulting in an overestimation of surface uplift magnitudes [*Barnes and Ehlers*, 2009]. If the contribution of precipitation change to river incision magnitudes was high enough, the river incision observations may be reconciled with the slow and steady end member model of surface uplift. In Chapter 3 of this dissertation [see also: *Jeffery et al.*, in press], the role of increasing discharge rates in the topographic evolution of an Andean river is quantified using a 1D river profile evolution model embedded in a Monte Carlo search. In the river model, precipitation inputs are linked to the elevation of the headwaters using results from existing climate model simulations in which Andean topography was modified for lower elevations [*Insel et al.*, 2010a]. The use of climate model results in this way is a novel approach to explore the response of surface processes to coupled climate and tectonics processes and enables the quantification of the relative importance of the two factors. In combination with Chapter 2, the results of this study enable a quantitative evaluation of Barnes and Ehlers [2009] assertion that Andean paleoelevation proxies can be reconciled with a steady surface uplift model when climatic factors are accounted for.

1.3 EROSIONAL EFFICIENCY AND TOPOGRAPHY

Improved constraints on the timing of surface uplift and coupled changes in regional climate enable further exploration of the interactions between climate and tectonics at the topographic interface. To date, Andean topography and exhumation has been compared with mean annual precipitation rates as a measure of erosional efficiency [e.g. *Masek et al.*, 1994; *McQuarrie et al.*, 2008b; *D.R. Montgomery et al.*, 2001]. However, many erosion processes are non-linear and only occur when

driving forces exceed a critical threshold. Erosional efficiency, and the potential for climate to drive tectonic feedbacks, may therefore be better characterized by the distribution of individual events, rather than mean climate states such as mean annual precipitation. Quantifying the magnitude of precipitation events in tectonically active regions, such as the Andes, was challenging until the recent development of satellite based precipitation observations. In Chapter 4, a new precipitation dataset, including event scale characteristics, is derived from TRMM satellite observations. The new dataset is then compared with topographic metrics to determine how best to characterize precipitation in the Andes with respect to erosion processes. The results will help to determine which climate characteristics are relevant to long-term climate-tectonic development.

1.4 HYPOTHESES ADDRESSED

Two main hypotheses are addressed in this dissertation: (1) Central Andean proxy records that indicate a rapid surface uplift event in the late Miocene are compatible with a steady surface uplift rate when climate change is accounted for, and (2) Precipitation intensity is a dominant control on landscape morphology and erosional efficiency in the Central Andes.

The first hypothesis is addressed in two ways. First, in chapter 2, global climate model simulations with modified boundary conditions show that the stable isotope composition of South American precipitation was influenced by multiple factors, including Andean elevation, CO_2, and the presence of an inland seaway during the Cenozoic. The results are compared with existing $\delta^{18}O_{prec}$ proxy records to determine which factors can explain the magnitude, direction and timing of changes recorded in the proxy records. Furthermore, we quantify uncertainties in paleoaltimetry due to these climate factors and show that $\delta^{18}O_{prec}$ proxy records do not require a rapid late Miocene surface uplift event. Second, a numerical model is designed to simulate the evolution of a river profile under coupled changes in topography and climate. The river model is run under a wide range of boundary conditions to assess the extent to which climate change can modify the timing and

magnitude of river incision on the flanks of a plateau. Simulation results indicate that the available constraints on river incision timing and magnitude are compatible with either surface uplift end-member model.

The second hypothesis is addressed using modern day observations of precipitation intensity and landscape characteristics; specifically mean hillslope gradients (Chapter 4). The extent to which spatial variability in precipitation intensity can explain patterns in mean hillslope gradient is quantified by correlation and multiple linear regression analyses. We find that vegetation is an important factor in mediating climate-landscape interactions at the orogen scale.

In addressing the above hypotheses we demonstrate the value of considering both the multi-faceted nature of climate and the multiple factors that control regional climate patterns. These studies are an advance on previous work that considers simplified patterns of mean annual precipitation as a sufficient means of characterizing climate in active mountain belts. We develop an improved framework for understanding climate-tectonic interactions by (1) Identifying the relevant, or dominant, factors influencing precipitation on million year timescales, and (2) identifying the characteristics of precipitation that determine climatic erosional efficiency

1.5 REFERENCES

Barke, R., and S. Lamb (2006), Late Cenozoic uplift of the Eastern Cordillera, Bolivian Andes, *Earth and Planetary Science Letters*, *249*(3-4), 350-367, 10.1016/j.epsl.2006.07.012

Barnes, J. B., and T. A. Ehlers (2009), End member models for Andean Plateau uplift, *Earth-Science Reviews*, *97*(1-4), 105-132, 10.1016/j.earscirev.2009.08.003

Barnes, J. B., T. A. Ehlers, N. McQuarrie, P. B. O'Sullivan, and J. D. Pelletier (2006), Eocene to recent variations in erosion across the central Andean fold-thrust belt, northern Bolivia: Implications for plateau evolution, *Earth and Planetary Science Letters*, *248*(1-2), 118-133, 10.1016/j.epsl.2006.05.018

Barnes, J. B., T. A. Ehlers, N. McQuarrie, P. B. O'Sullivan, and S. Tawackoli (2008), Thermochronometer record of central Andean plateau growth, Bolivia (19.5 degrees S), *Tectonics*, *27*(3), 10.1029/2007tc002174

Bookhagen, B., and M. R. Strecker (2008), Orographic barriers, high-resolution TRMM rainfall, and relief variations along the eastern Andes, *Geophysical Research Letters*, *35*(6), 6, 10.1029/2007gl032011

Bookhagen, B., and M. R. Strecker (2012), Spatiotemporal trends in erosion rates across a pronounced rainfall gradient: Examples from the southern Central Andes, *Earth and Planetary Science Letters*, *327*, 97 - 110, 10.1016/j.epsl.2012.02.005

Campetella, C. M., and C. S. Vera (2002), The influence of the Andes mountains on the South American low-level, *Geophysical Research Letters*, *29*(17), 10.1029/2002gl015451

Ehlers, T. A., and C. J. Poulsen (2009), Influence of Andean uplift on climate and paleoaltimetry estimates, *Earth and Planetary Science Letters*, *281*(3-4), 238-248, 10.1016/j.epsl.2009.02.026

Ehrmann, W. U., and A. Mackensen (1992), Sedimentological evidence for the formation of an East Antarctic ice-sheet in Eocene Oligocene time, *Palaeogeography Palaeoclimatology Palaeoecology*, *93*(1-2), 85-112

Frailey, C. D., E. L. Lavina, A. Rancy, and J. P. de Souza Filho (1988), A proposed Pleistocene/Holocene lake in the Amazon basin and its significance to Amazonian geology and biogeography, *Acta Amazonica*, *18*, 119-143

Garzione, C. N., and G. D. Hoke (2006), Paleoelevation and geomorphic constraints on the late miocene rise of the andes: Geodynamic implications for the growth of orogenic plateaus, *Geochimica Et Cosmochimica Acta*, *70*(18), A195-A195, 10.1016/j.gca.2006.06.393

Garzione, C. N., P. Molnar, J. C. Libarkin, and B. J. MacFadden (2006), Rapid late Miocene rise of the Bolivian Altiplano: Evidence for removal of mantle

lithosphere, *Earth and Planetary Science Letters*, *241*(3-4), 543-556, 10.1016/j.epsl.2005.11.026

Garzione, C. N., G. D. Hoke, J. C. Libarkin, S. Withers, B. MacFadden, J. Eiler, P. Ghosh, and A. Mulch (2008), Rise of the Andes, *Science*, *320*(5881), 1304-1307, 10.1126/science.1148615

Ghosh, P., C. N. Garzione, and J. M. Eiler (2006), Rapid uplift of the Altiplano revealed through C-13-O-18 bonds in paleosol carbonates, *Science*, *311*(5760), 511-515, 10.1126/science.1119365

Hoke, G. D., B. L. Isacks, T. E. Jordan, N. Blanco, A. J. Tomlinson, and J. Ramezani (2007), Geomorphic evidence for post-10 Ma uplift of the western flank of the central Andes 18 degrees 30'-22 degrees S, *Tectonics*, *26*(5), 10.1029/2006tc002082

Horton, B. K. (1999), Erosional control on the geometry and kinematics of thrust belt development in the central Andes, *Tectonics*, *18*(6), 1292-1304, 10.1029/1999TC900051

Insel, N., C. J. Poulsen, and T. A. Ehlers (2010a), Influence of the Andes Mountains on South American moisture transport, convection, and precipitation, *Climate Dynamics*, *35*(7-8), 1477-1492, 10.1007/s00382-009-0637-1

Insel, N., C. J. Poulsen, T. A. Ehlers, and C. Sturm (2012), Response of meteoric $\delta^{18}O$ to surface uplift - Implications for Cenozoic Andean Plateau growth, *Earth and Planetary Science Letters*, *317 - 318*, 262-272, 10.1016/j.epsl.2011.11.039

Insel, N., T. A. Ehlers, M. Schaller, J. B. Barnes, S. Tawackoli, and C. J. Poulsen (2010b), Spatial and temporal variability in denudation across the Bolivian Andes from multiple geochronometers, *Geomorphology*, *122*(1-2), 65-77, 10.1016/j.geomorph.2010.05.014

Jeffery, M. L., C. J. Poulsen, and T. A. Ehlers (2012), Impacts of Cenozoic global cooling, surface uplift, and an inland seaway on South American paleoclimate and precipitation $\delta^{18}O$, *Geological Society of America Bulletin*, *124*(3-4), 335-351, 10.1130/B30467.1

Jeffery, M. L., T. A. Ehlers, B. J. Yanites, and C. J. Poulsen (in press), Quantifying the role of paleoclimate and Andean plateau uplift on river incision, *Journal of Geophysical Research - Earth Surface*

Koons, P. O. (1990), The two‐sided orogen: Collision and erosion from the sand box to the Southern Alps, New Zealand. , *Geology*, *18*(8), 679‐682, 10.1130/0091-7613(1990)018<0679:TSOCAE>2.3.CO;2

Lear, C. H., H. Elderfield, and P. A. Wilson (2000), Cenozoic deep-sea temperatures and global ice volumes from Mg/Ca in benthic foraminiferal calcite, *Science*, *287*(5451), 269-272

Lenters, J. D., and K. H. Cook (1995), Simulation and diagnosis of the regional summertime precipitation climatology of South America, *Journal of Climate*, *8*(12), 2988-3005

Masek, J. G., B. L. Isacks, T. L. Gubbels, and E. J. Fielding (1994), Erosion and tectonics at the margins of continental plateaus, *Journal of Geophysical Research*, *99*(B7), 13941-13956, 10.1029/94JB00461

McQuarrie, N., J. B. Barnes, and T. A. Ehlers (2008a), Geometric, kinematic, and erosional history of the central Andean Plateau, Bolivia (15-17 degrees S), *Tectonics*, *27*(3), 10.1029/2006tc002054

McQuarrie, N., T. A. Ehlers, J. B. Barnes, and B. Meade (2008b), Temporal variation in climate and tectonic coupling in the central Andes, *Geology*, *36*(12), 999-1002, 10.1130/g25124a.1

Molnar, P., and C. N. Garzione (2007), Bounds on the viscosity coefficient of continental lithosphere from removal of mantle lithosphere beneath the Altiplano and Eastern Cordillera, *Tectonics*, *26*(2), 10.1029/2006tc001964

Montgomery, D. R., G. Balco, and S. D. Willett (2001), Climate, tectonics, and the morphology of the Andes, *Geology*, *29*(7), 579-582, 10.1130/0091-7613(2001)029<0579:CTATMO>2.0.CO;2

Norton, K., and F. Schlunegger (2011), Migrating deformation in the central Andes from enhanced orographic rainfall, *Nature Communications*, *2*(484), 10.1038/ncomms1590

Pagani, M., J. C. Zachos, K. H. Freeman, B. Tipple, and S. Bohaty (2005), Marked decline in atmospheric carbon dioxide concentrations during the Paleogene, *Science*, *309*(5734), 600-603, 10.1126/science.1110063

Pearson, P. N., and M. R. Palmer (2000), Atmospheric carbon dioxide concentrations over the past 60 million years, *Nature*, *406*(6797), 695-699

Poulsen, C. J., T. A. Ehlers, and N. Insel (2010), Onset of Convective Rainfall During Gradual Late Miocene Rise of the Central Andes, *Science*, *328*(5977), 490-493, 10.1126/science.1185078

Quade, J., T. E. Cerling, and J. R. Bowman (1989), Systematic variations in the carbon and oxygen isotopic composition of pedogenic carbonate along elevation transects in the southern Great Basin, United States, *Geological Society of America Bulletin*, *101*(4), 464-475, 10.1130/0016-7606(1989)101<0464:SVITCA>2.3.CO;2

Quade, J., C. N. Garzione, and J. Eiler (2007), Paleoelevation reconstruction using pedogenic carbonates, in *Paleoaltimetry: Geochemical and Thermodynamic Approaches*, edited, pp. 53-87.

Rasanen, M. E., A. M. Linna, J. C. R. Santos, and F. R. Negri (1995), Late Miocene tidal deposits in the Amazonian foreland basin, *Science*, *269*(5222), 386-390

Safran, E. B., P. R. Bierman, R. Aalto, T. Dunne, K. Whipple, and M. Caffee (2005), Erosion rates driven by channel network incision in the Bolivian Andes, *Earth Surface Processes and Landforms*, *30*(8), 1007-1024, 10.1002/esp.1259

Schildgen, T. F., K. V. Hodges, K. X. Whipple, P. W. Reiners, and M. S. Pringle (2007), Uplift of the western margin of the Andean plateau revealed from canyon incision history, southern Peru, *Geology*, *35*(6), 523-526, 10.1130/g23532a.1

Schildgen, T. F., T. A. Ehlers, D. M. Whipp, M. C. van Soest, K. X. Whipple, and K. V. Hodges (2009), Quantifying canyon incision and Andean Plateau surface uplift, southwest Peru: A thermochronometer and numerical modeling approach, *Journal of Geophysical Research-Earth Surface*, *114*, 10.1029/2009jf001305

Tao, W. C., and R. J. O'Connell (1992), Ablative Subduction: A two-sided Alternative to the Conventional Subduction Model, *Journal of Geophysical Research - Solid Earth and Planets*, *97*(B6), 8877-8904, 10.1029/91JB02422

Whipple, K. X. (2009), The influence of climate on the tectonic evolution of mountain belts, *Nature Geoscience*, *2*(2), 97-104, 10.1038/ngeo413

Willett, S. D. (1999), Orogeny and orography: The effects of erosion on the structure of mountain belts, *Journal of Geophysical Research-Solid Earth*, *104*(B12), 28957-28981, 10.1029/1999jb900248

Willett, S. D., C. Beaumont, and P. Fullsack (1993), Mechanical model for the tectonics of doubly vergent compressional orogens. , *Geology*, *21*, 371-374, 10.1130/0091-7613(1993)021<0371:MMFTTO>2.3.CO;2

Zachos, J. C., J. R. Breza, and S. W. Wise (1992), Early Oligocene ice-sheet expansion on Antarctica - stable isotope and sedimentological evidence from Kerguelen Plateau, southern Indian-Ocean, *Geology*, *20*(6), 569-573

CHAPTER 2

IMPACTS OF CENOZOIC GLOBAL COOLING, SURFACE UPLIFT AND AN INLAND SEAWAY ON SOUTH AMERICAN PALEOCLIMATE AND PRECIPITATION $\delta^{18}O$[1]

Abstract

Stable isotope records of precipitation $\delta^{18}O$ ($\delta^{18}O_{prec}$) have been used as paleoclimate and paleoelevation archives of orogens. However, interpretation of these records is limited by knowledge of how $\delta^{18}O_{prec}$ responds to changes in global and regional climate during mountain building events. In this study the influence of atmospheric CO_2 levels, the extent of the Antarctic Ice Sheet, changes in Andean surface elevation and the presence of the South American inland seaway on climate and $\delta^{18}O_{prec}$ in South America are quantified using the GENESIS v3 atmospheric general circulation model with isotope-tracking capabilities. Results are presented in the context of Cenozoic South American climate and $\delta^{18}O_{prec}$ changes. More specifically, we find: (1) Precipitation rates in the Andes are sensitive to Andean surface elevation, the seaway and, to a lesser extent, CO_2 levels. Increasing Andean elevations and the presence of a seaway both cause large increases in precipitation, but in different parts of the Andes. The growth of the Antarctic ice sheet is found to have a small influence on South American precipitation. (2) The stable isotopic

[1] Official Citation:
Jeffery, M. L., C. J. Poulsen, and T. A. Ehlers (2012), Impacts of Cenozoic global cooling, surface uplift, and an inland seaway on South American paleoclimate and precipitation $\delta^{18}O$, *Geological Society of America Bulletin*, *124*(3-4), 335-351. doi:10.1130/B30480.1

composition of precipitation is sensitive to all of the parameters investigated. An increase in $\delta^{18}O_{prec}$ of up to 8‰ is found in simulations with higher atmospheric CO_2. In agreement with previous studies, $\delta^{18}O_{prec}$ decreases with increasing Andean elevation by an amount greater than that predicted by the modern adiabatic lapse rate. Furthermore, the presence of an inland seaway causes a decrease in $\delta^{18}O_{prec}$ of 1-8 ‰ in the northern and central Andes. The amount of depletion is dependent on the isotopic composition of the seaway. Simulations without the Antarctic ice sheet result in $\delta^{18}O_{prec}$ that is 0-3 ‰ lower than the modern. Finally, time-specific simulations for the Miocene and Eocene show that $\delta^{18}O_{prec}$ has decreased during the Cenozoic and that local geographical gradients of $\delta^{18}O_{prec}$ have increased, particularly in regions of high modern elevation. We demonstrate that in addition to Andean uplift and associated climate change, CO_2 levels and an inland seaway are likely to have influenced $\delta^{18}O_{carb}$ records from South America. Consideration of these global and paleogeographic changes is necessary when interpreting paleoclimate or paleoelevation from stable isotope records of $\delta^{18}O_{prec}$.

2.1 INTRODUCTION

The Cenozoic was a time of major mountain building events and global cooling of ~10 °C [*Lear et al.*, 2000]. These events altered global atmospheric circulation patterns and led to polar glaciation [*Ehrmann and Mackensen*, 1992; *Zachos et al.*, 1992]. These large-scale changes should be recorded in stable isotope records from orogenic regions. However, unravelling these signals is difficult, partly because the isotopic responses to changing geologic boundary conditions are not well constrained. Isotope-tracking climate models can be used to determine the response of the stable isotopic composition of precipitation ($\delta^{18}O_{prec}$) to changes in boundary conditions. The advantage to such an approach is that the spatial response to individual factors (e.g. surface uplift, global cooling, or Antarctic glaciation) can be quantified.

Recent studies of the Andean Plateau have highlighted that terrestrial paleosol and lacustrine carbonate stable isotope ($\delta^{18}O_{carb}$) records from South America are sensitive to both the paleoelevation and paleoclimate history of the

orogen [*T A Ehlers and Poulsen*, 2009; *Poulsen et al.*, 2010]. These studies demonstrated how increasing Andean Plateau elevations and consequent climate change alter $\delta^{18}O_{prec}$. However, global or regional climate and environmental changes that occurred during the evolution of the Andes were not taken into account. Furthermore, episodic occurrences of a marine seaway or freshwater lake in the Andean foreland have modified the regional paleogeography during the Cenozoic [*Frailey et al.*, 1988; *Rasanen et al.*, 1995]. A better understanding of the impacts of these global and regional changes, as well as the impacts of changing Andean Plateau elevations, on $\delta^{18}O_{prec}$ in South America is needed in order to accurately interpret $\delta^{18}O_{carb}$ records from this region.

In this study, we complement previous work by using a global climate model with isotopic tracking capabilities to quantify the impacts of global climate and paleogeographic change on the isotopic composition of meteoric waters. We establish the relative importance of 1) atmospheric greenhouse gas (CO_2) composition, 2) the Antarctic ice sheet, 3) Andean elevation, and 4) the presence of a South American inland seaway on the climate and $\delta^{18}O_{prec}$ in South America. We use these results to show the paleoclimate and paleoelevation signals that may be observed in $\delta^{18}O_{carb}$ records of South America.

2.2 BACKGROUND

2.2.1 South American Paleogeography and Paleoclimate

The ~7000 km long Andean mountains (Fig. 2.1) formed primarily as a result of the subduction of the Nazca plate beneath the South American plate. The morphology of the Andes varies considerably along strike with narrow ranges to the north and south separated by the wide Altiplano plateau of the Central Andes [15 – 27 °S, Fig. 2.1; *Isacks*, 1988]. South America has been located in the lower latitudes for the last 40 Ma and has drifted northwards by ~2 degrees since 10 Ma [*Smith et al.*, 1981].

In the following we briefly summarize the evolution of this orogen from south to north. In the southern Patagonian Andes, accelerated cooling and

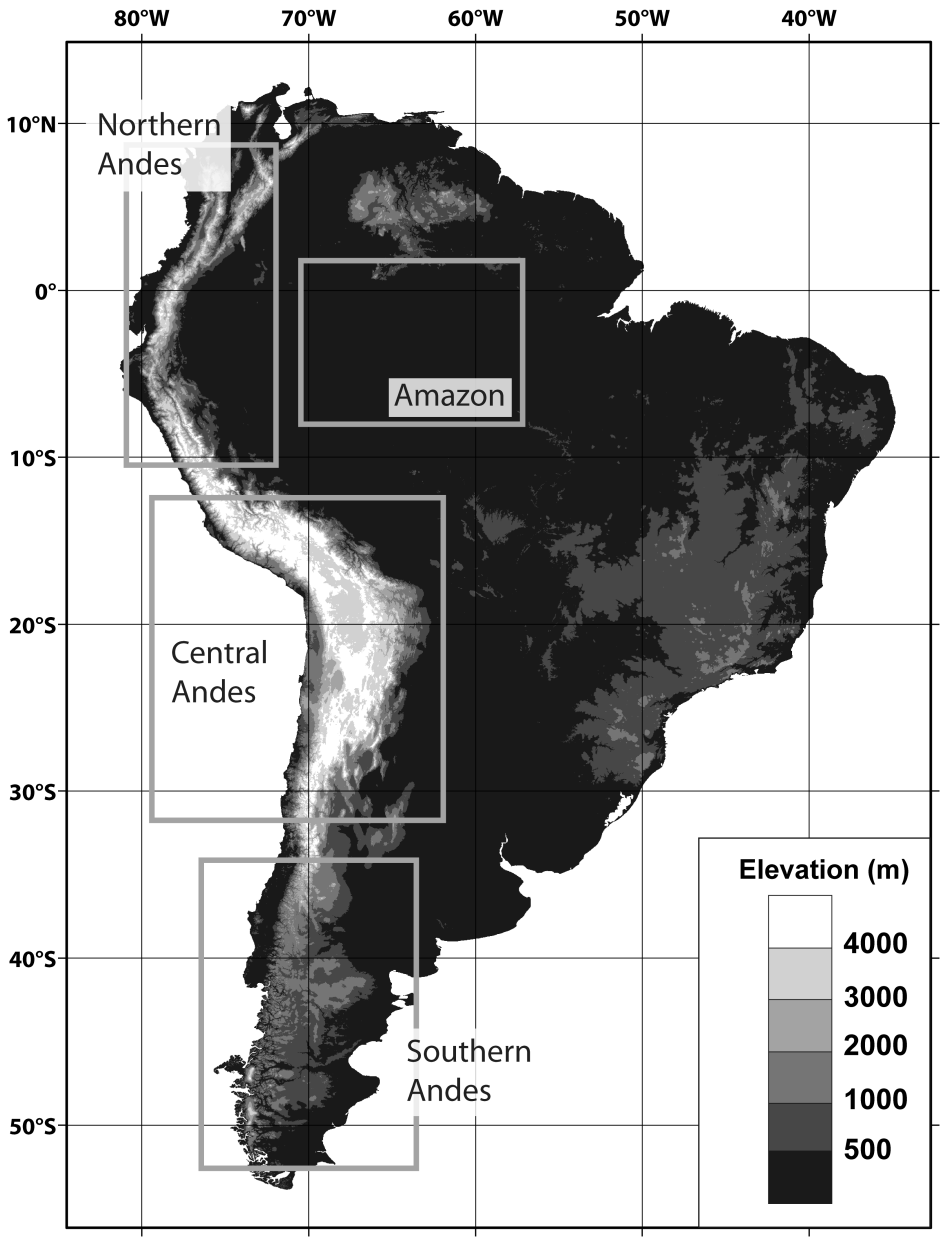

Figure 2.1 Modern South American topography.

Boxes delineate the regions discussed in the text.

denudation began ~30 Ma [*Thomson et al.*, 2001] and indicates the onset of significant deformation in this region. Deformation propagated eastward before slowing at 14 – 10 Ma following the subduction of the Chilean spreading ridge [*Blisniuk et al.*, 2006]. The Pampean segment of the Andes (27 – 33°S) is distinguished by a gap in modern volcanism over a region of flat slab subduction. Here, the main deformation phase in the principal Cordillera occurred between 20 and 8.6 Ma [*Ramos et al.*, 2002]. Again, deformation propagated eastward from the main Cordillera into the Sierra Pampeanas fold-and-thrust belt. In the central Andes, deformation began in the early Cenozoic [60-40 Ma, *DeCelles and Horton*, 2003; *McQuarrie et al.*, 2005] and accelerated around 25 Ma coincident with a change in the subduction geometry. The plateau formed mainly through crustal thickening and deformation that migrated eastward from the Altiplano-Puna Plateau into the foreland fold-and–thrust belt [*Barnes et al.*, 2008; *McQuarrie*, 2002]. Deformation in the Altiplano began 5-10 m.y. before the Puna region [*Allmendinger et al.*, 1997]. North of the Altiplano, the Andean range narrows and splits into three separate Cordilleras (north of 2 °N, Fig. 2.1). The northern Andes have a long history of deformation that is complicated by the subduction of the proto-Carribean plate in addition to the Nazca plate [*Gomez et al.*, 2005; *Taboada et al.*, 2000]. Earliest contractional deformation began in the late Cretaceous when accretion of an oceanic plateau initiated formation of the Western Cordillera and contemporaneous arc volcanism and crustal thickening began in the Central Cordillera. After plate re-organization at ~28-26 Ma, basin inversion in the foreland led to the uplift of the Eastern Cordillera in the late Oligocene and early Miocene [*Cooper et al.*, 1995; *Parra et al.*, 2010].

Central South America was episodically submerged under fresh or marine waters during the Neogene. Sedimentary evidence from the Andean foreland indicates the presence of a large lake [*Frailey et al.*, 1988] or an inland seaway during the Miocene [*Rasanen et al.*, 1995]. Miocene sedimentary deposits from Peruvian Amazonia are interpreted to have formed in a range of environments from fluvial [*Latrubesse et al.*, 2010] to marginal marine [*Gingras et al.*, 2002; *Rasanen et al.*, 1995]. Evidence for a marine influence includes diurnal cycles in rhythmic

bedding [*Hovikoski et al.*, 2005; *Hovikoski et al.*, 2007], mangrove pollen [*Hoorn*, 2006], marine palynmorphs [*Hoorn*, 2006], marine ichnofossils [*Gingras et al.*, 2002; *Wesselingh et al.*, 2002] and a high diversity of modern marine-derived fauna [*Lovejoy et al.*, 2006]. Others have interpreted the sedimentary structures as a fluvial system with avulsive rivers, megafans, swamps and lakes [*Latrubesse et al.*, 2010]. The conflicting evidence for continental and marine influences in the same formation can be reconciled by a scenario in which multiple incursions of brackish water occurred into an otherwise continental environment [*Hovikoski et al.*, 2010; *Hovikoski et al.*, 2007; *Wesselingh et al.*, 2006]. In a recent review [*Hoorn et al.*, 2010] describe the following three phases of seaway incursions in Amazonia; (1) ~24-16 Ma, Lacustrine conditions alternating with episodes of fluvial drainage and marginal marine influence, (2) ~16-11.3 Ma, Maximum extent of lacustrine conditions with a marginal marine influence, and (3) 11.3- ~7 Ma, Complex environment of deltaic, estuarine and fluvial environments. Probable causes of the incursions include tectonic loading of the foreland basin by the rising Andes and/or changes in eustatic sea level [*Hernandez et al.*, 2005].

These paleogeographic changes all occurred in the context of Cenozoic global climate change. Carbon dioxide levels and global temperatures have decreased throughout the Cenozoic. Carbon dioxide concentrations were around 900-1500 ppm in the middle to late Eocene [*Pagani et al.*, 2005; *Pearson et al.*, 2009] but have been relatively stable below ~500 ppm since the late Oligocene, ~25 Ma [*Demicco et al.*, 2003; *Royer*, 2006]. The Antarctic Ice Sheet (AIS) initially developed ~34 Ma [*Matthews and Poore*, 1980; *Miller et al.*, 1987; *Zachos et al.*, 1992] and fluctuated in size through the Oligocene and Miocene. The Eastern Antarctic Ice Sheet stabilized around 14 Ma and the modern ice sheet was established in the Plio-Pleistocene [*Siegert et al.*, 2008].

2.2.2 The isotopic composition of South American precipitation

The isotopic composition of meteoric water is primarily controlled by equilibrium isotopic fractionation during evaporation and precipitation [*Gat*, 1996]. It is energetically more favorable for molecules containing the lighter isotope (^{16}O)

to be in the gaseous phase. Therefore, precipitation is more enriched in ^{18}O than the vapor from which it formed and the remaining vapor becomes isotopically depleted. This fractionation is temperature dependent, with greater fractionation occurring at lower temperatures [*Dansgaard*, 1964].

In South America, $\delta^{18}O_{prec}$ decreases generally from north to south, particularly south of 45 °S, due to decreasing temperature with increasing latitude [*Rozanski et al.*, 1993]. $\delta^{18}O_{prec}$ is also more negative inland than at the coasts as a result of Rayleigh distillation, the progressive rainout of the heavier isotope. These continental effects are weaker in the Amazon region due to recycling through evapotranspiration of moisture with relatively high $\delta^{18}O_{prec}$ [*Salati et al.*, 1979]. A minimum in the $\delta^{18}O_{prec}$ pattern occurs in eastern Brazil (40-50 °W, 20 °S) due to high precipitation rates and long vapor transport distances over which Rayleigh distillation occurs.

Further modifications to the general latitudinal and continental pattern are caused by the presence of the Andean topography [*Aravena et al.*, 1999; *Gonfiantini et al.*, 2001; *Stern and Blisniuk*, 2002]. The lifting of air masses over high topography induces adiabatic cooling and condensation on the windward side resulting in more isotopically depleted precipitation at high elevation and on the leeward side of the mountain range [*Dansgaard*, 1964]. Elevation effects are particularly strong in the central Andes where the South American Low Level Jet brings moisture southwards and convective precipitation is induced on the eastern Andean flanks [*Insel et al.*, 2010a].

2.3 METHODS

2.3.1 Modeling approach

A suite of climate model simulations (table 2.1) is used to explore the response of South American climate and $\delta^{18}O_{prec}$ to a range of climate controls that have changed during the mid-late Cenozoic. The simulations were run using the global climate model GENESIS [*Thompson and Pollard*, 1995; 1997]. GENESIS is a multi-component Earth Systems model with an atmospheric model derived from NCAR's CCM1 coupled to land-surface, soil, snow, sea-ice and ocean components. In

our version of GENESIS, water isotopic transport and fractionation processes have been added to the atmospheric physics (Mathieu et al., 2002). The $^{18}O/^{16}O$ and D/H ratios are predicted in atmospheric vapor, liquid, and ice, and also in soil water reservoirs. Fractionation is modeled as a result of condensation and evaporation in the free atmosphere and from surface waters. Atmospheric isotopic ratios are transported using the same Lagrangian transport as for bulk vapor and clouds. We use a spectral resolution of T63 (~1.9° or ~210 km) for both the atmosphere and surface models. The atmospheric model has 18 vertical levels. Vegetation cover is prescribed based on Dorman and Sellers [1989] and is identical in each simulation. The ocean is represented by a mixed-layer slab model of 50 m depth. Oceanic heat transport is diffusive and zonally uniform. Atmospheric trace gas compositions are specified at pre-industrial levels, except for carbon dioxide as described below. The isotopic composition of the oceans and other large water bodies is prescribed from modern observational datasets [*Craig and Gordon*, 1965; *Epstein and Mayeda*, 1953; *Ferronsky and Brezgunov*, 1989; *GEOSECS*, 1987]. Orbital parameters are modern and constant in all experiments.

Each simulation was run for 55 years with isotope tracking enabled for the last 25 years. The results presented here were averaged over the final 20 years of each simulation. Twenty years is sufficient time to establish the mean climatic state because the use of a slab ocean does not enable the simulation of the ocean-atmosphere interactions that drive variability on annual and longer timescales in the modern climate. While this is a limitation of this study, the slab ocean model was chosen in order to maintain surface temperature equilibrium under increasing CO_2 levels. Furthermore, inter-annual variability is unlikely to be recorded in carbonate records of $\delta^{18}O_{prec}$ that form over comparatively long time periods of hundreds to thousands of years. Additionally, the changes in boundary conditions that we explore occur on timescales greater than that of carbonate formation.

2.3.2 Cenozoic boundary conditions

A series of simulations were completed that investigate the impact of 1) atmospheric CO_2 levels, 2) Andean elevation, 3) the South American Inland Seaway,

Table 2.1 Model experiments and boundary conditions

	Full Andes	**Half Andes**	**No Andes**
1× CO_2	Modern SW_{marine} $SW_{freshwater}$ NoIce NoIce_modOcean (App. 1)	Half Andes (App. 1) Half Andes, SW_{marine} (App. 1)	No Andes
2× CO_2	2×CO_2 (App. 1)	Middle Miocene 2×CO_2, Half Andes (App. 1)	
4× CO_2	4×CO_2		Eocene (NoIce, Ocean)

SW – Seaway; *marine* – marine isotopic composition (~1‰); *freshwater* – freshwater isotopic composition (-6‰); *NoIce* – topography and surface properties of the Antarctic ice sheet changed and ocean isotopic composition modified for an ice free world; NoIce_mod*Ocean* – Antarctic topography and surface properties changed but oceanic isotopic composition is modern; *NxCO₂* – CO_2 levels at N times pre-industrial level (280ppm); *App.* – Experiment results are shown in Appendix A.

and 4) the Antarctic ice sheet on $\delta^{18}O_{prec}$ in South America. Boundary conditions were specified to capture the range of conditions during the Cenozoic. The set of simulations (Table 1) consists of a base level, or control run, representing pre-industrial conditions and further simulations in which only one parameter is varied from the base level conditions. The exceptions to this are two time-specific simulations discussed at the end. CO_2 levels in the base level simulation are 1x, of pre-industrial levels (PIL) (280ppm). Additional simulations are run at 2x (560ppmv) and 4x (1120ppmv) PIL [*Pagani et al.*, 2005; *Pearson et al.*, 2009]. The influence of Andean surface uplift is examined with simulations at varying Andean elevations. Figure 2.2A shows the modern Andean topography represented in the Full Andes simulations. Two additional experiments were completed with modern Andean elevations reduced by 50% (Half Andes) and set to 250m (No Andes).

We have adapted a seaway reconstruction (Fig. 2.2A) modified from Hernandez et al. [2005] and Rasanen et al. [1995]. The reconstruction represents the maximum likely extent of the seaway. The isotopic composition of the seaway is not known, in part because it is not clear whether the seaway had a marine connection. To address this uncertainty, two experiments were conducted with

distinct isotopic compositions assigned to the seaway ($\delta^{18}O_{seaway}$). The first experiment representing a marine seaway has isotopic compositions similar to the modern Atlantic with zonal values ranging from 1‰ near the equator to 0‰ at 50 °S. The second experiment represents a freshwater seaway with an isotopic composition of -6‰, the value of the modern Amazon River. The 'marine' scenario could also represent a freshwater seaway that has undergone high rates of evaporation. These two simulations (SW_{marine} and $SW_{freshwater}$) encompass the range of potential influences a seaway could have on the $\delta^{18}O_{prec}$ in South America.

Changes in Antarctic ice volume influence $\delta^{18}O_{prec}$ by modifying the climate and by changing oceanic isotopic composition ($\delta^{18}O_{ocean}$). Our NoIce experiment simulates this using an ice-free isostatically rebounded Antarctic paleogeography. The $\delta^{18}O_{ocean}$ is prescribed by subtracting 1.2‰ from modern $\delta^{18}O_{ocean}$ values. The NoIce experiment tests the maximum impact of the AIS on $\delta^{18}O_{prec}$ for the Cenozoic because the AIS is completely removed. An additional experiment (NoIce_modOcean, table 2.1) explores the relative importance of climate and $\delta^{18}O_{ocean}$ changes to differences in $\delta^{18}O_{prec}$ in the absence of the AIS. In this experiment the AIS is removed but $\delta^{18}O_{ocean}$ is set to modern values. The Greenland Ice Sheet (GIS) was not modified in our experiments. Due to its distant location from South America, the topography and surface type of the GIS would have a very small effect on $\delta^{18}O_{prec}$ in South America compared to the other boundary conditions explored here.

In addition to sensitivity tests of the boundary conditions described above, two time-specific simulations were designed to represent the 1) Late Eocene (~40 Ma) and, 2) Middle Miocene (~15 Ma). The Eocene scenario has no AIS, an ice free world $\delta^{18}O_{ocean}$, 4x CO_2 (1120ppm) and No Andean elevation. The Miocene scenario has a modern AIS, modern $\delta^{18}O_{ocean}$, 2x CO_2 (560ppm) and Half Andean Elevation. All simulations and their boundary conditions are summarized in table 2.1.

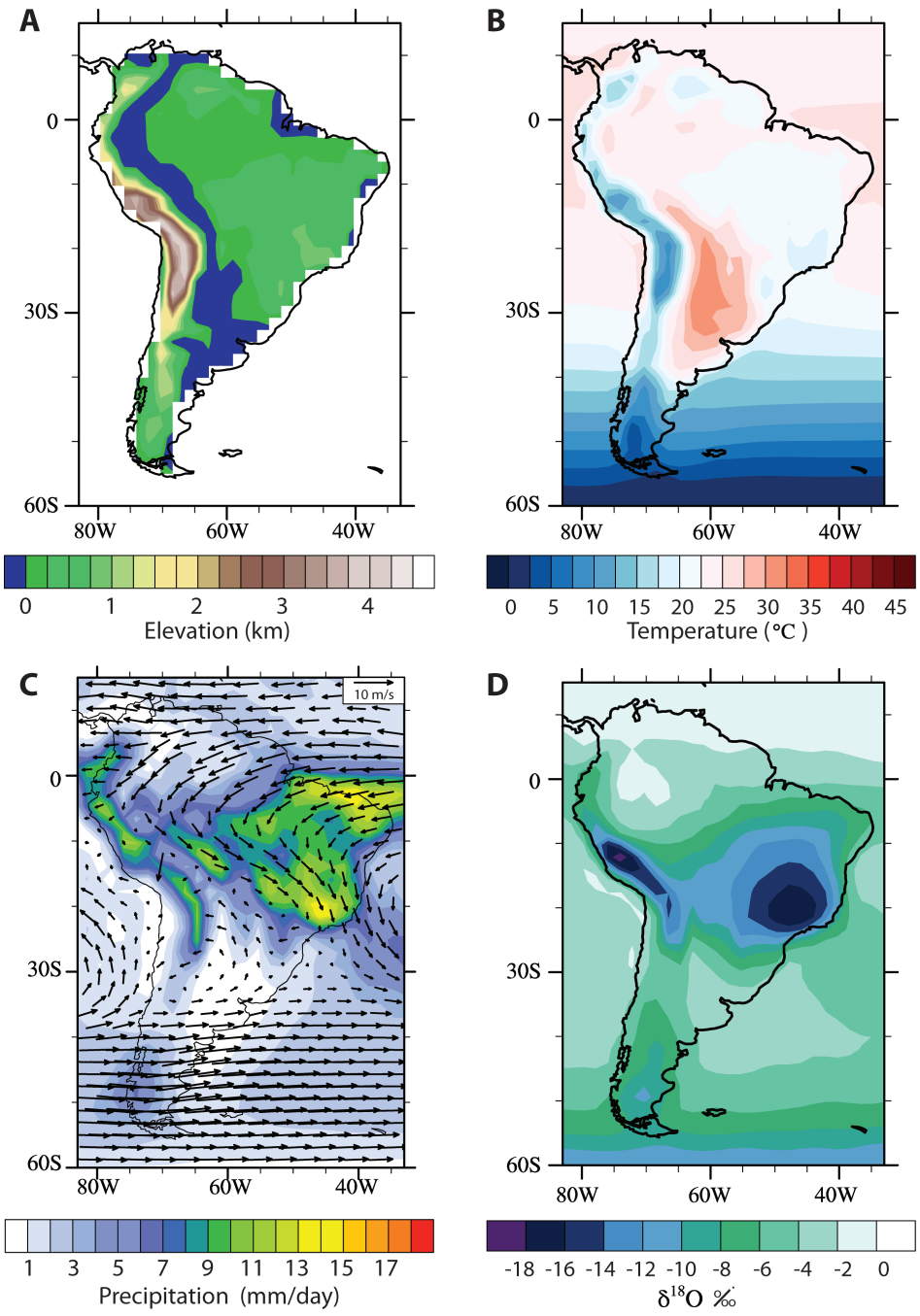

Figure 2.2 Model topography and austral summer climatologies for the modern simulation.

a) GENESIS modern South America topography. The location of the South American interior seaway is indicated by blue shading. The seaway is incorporated only in the $SW_{freshwater}$ and SW_{marine} simulations (see Table 1). b) Summer (DJF) average surface temperatures (°C). c) Summer (DJF) average precipitation (mm/day) and 800mb winds (m/s). Winds are not shown where surface elevation exceeds 2000m. d) Simulated amount-weighted summer $\delta^{18}O_{prec}$ (‰).

2.4 RESULTS

2.4.1 Modern (Control) Simulation

GENESIS has been used to realistically simulate both modern and past climates [e.g. *Sloan et al.*, 1996; *Thompson and Pollard*, 1995; *Zhou et al.*, 2008]. South American climate simulated in the control run compares well with modern data [Fig. 3, CMAP, CRU TS 2.0, NCEP 1, *Kalnay et al.*, 1996; *Pearson and Palmer*, 2000; *Xie and Arkin*, 1997]. For example, temperatures of ~25 °C in the Amazon and cooler temperatures (<10 °C) at high elevation and high latitudes (south of 40 °S) compare well with observational data (Figs. 2.3A – 2.3C). Predicted and observed precipitation patterns agree well, with high precipitation rates in the Amazon (3-6 mm/day) and northern and central Andes (up to 12 mm/day). GENESIS also captures low precipitation rates (<3 mm/day) at 30-40 °S (Figs. 2.3D-F). Discrepancies between the model and observations occur in Eastern Brazil, where the model overestimates precipitation rates by up to 4 mm/day. This is likely due to local sea surface temperatures being too high as a result of using the slab ocean model. Precipitation rates are also slightly too high on the eastern flanks of the Andes.

Modern $\delta^{18}O_{prec}$ patterns are well represented in the control simulation (Figs. 2.2D and 2.6A) when compared with currently available, and sparse, observational datasets [*(IAEA/WMO)*; *Mathieu et al.*, 2002; *Poulsen et al.*, 2010]. $\delta^{18}O_{prec}$ is high (> -6‰) over much of the Amazon basin and is low (< -10‰) in the central Andes, southeastern Brazil (40-50 °W, 20 °S) and in the southern Andes. Both the patterns and magnitude of $\delta^{18}O_{prec}$ are similar to those simulated in other climate models of a similar resolution [*Vuille et al.*, 2003] and higher resolution [*Sturm et al.*, 2007; *Vuille et al.*, 2003]. Any errors in climate simulation propagate into errors in $\delta^{18}O_{prec}$ simulation. As a result, GENESIS may under- or over-estimate the magnitude of $\delta^{18}O_{prec}$ where precipitation rates or temperatures are not well simulated. In eastern Brazil for example, simulated precipitation rates are too high which results in an underestimate of $\delta^{18}O_{prec}$. However, much of this paper focuses on the Andes where the model successfully simulates a decrease in $\delta^{18}O_{prec}$ from ~-6‰ at low elevations

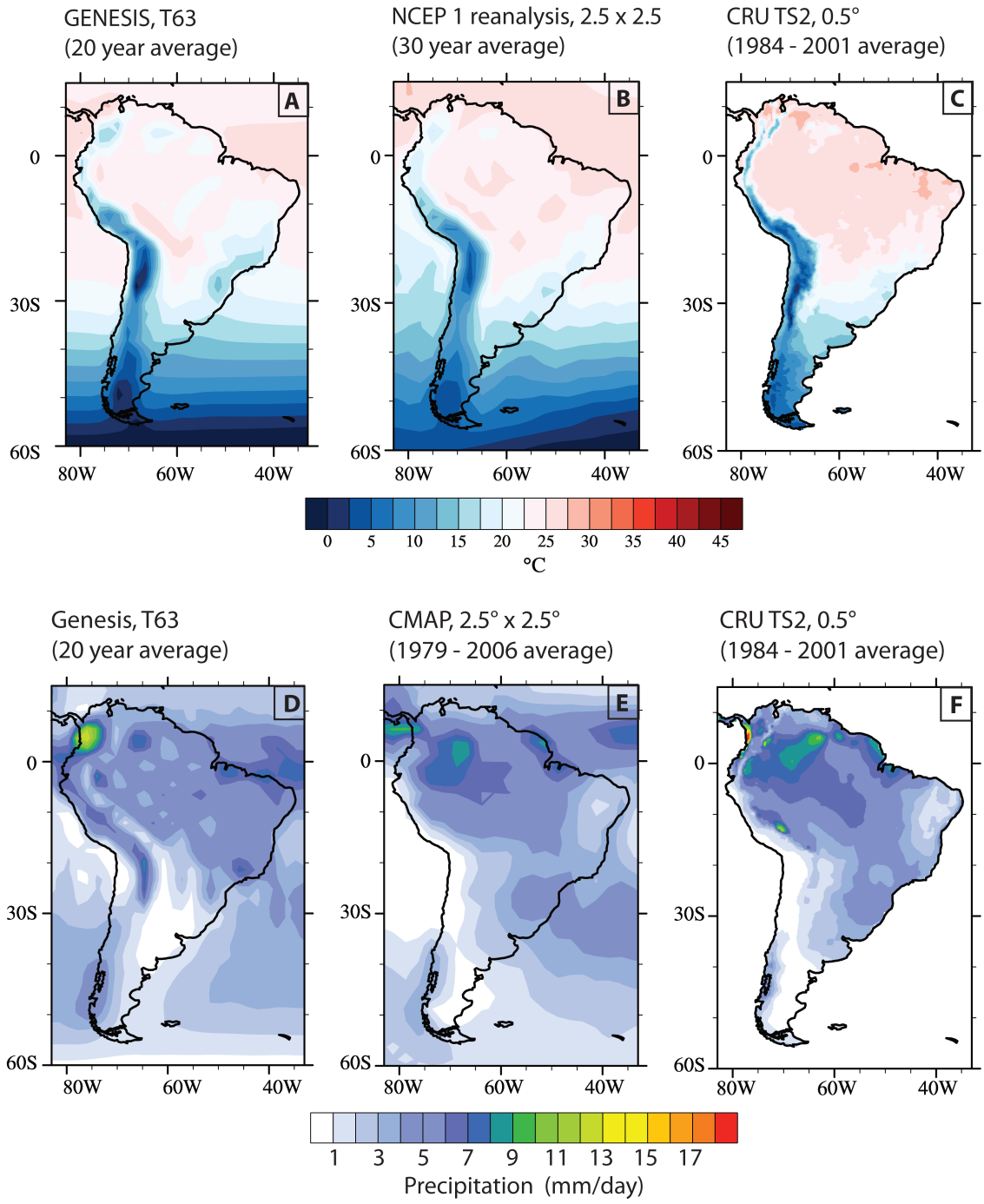

Figure 2.3 Model performance.

Simulated and observed mean annual temperature (°C) (a-c) and precipitation (mm/day) (d-e). a and d) GENESIS (this paper), b) NCEP 1 reanalysis product at 2.5° resolution, c and f) CRU TS2.0 at 0.5° resolution, and e) CMAP at 2.5° resolution.

to as low as <-16‰ on the eastern central Andean flanks (Fig. 2.6A), comparable to modern meteoric waters. Observed stream water and precipitation $\delta^{18}O$ decreases from ~-2 to -8‰ at low elevations to ~-11 to -18‰ at ~5km elevation [*Bershaw et al.*, 2010; *Gonfiantini et al.*, 2001]. At 33°S, river waters thought to reflect winter $\delta^{18}O_{prec}$ have values of -3 to -5‰ at low elevations, decreasing to ~-18‰ at 4km elevation [*Hoke et al.*, 2009]. In GENESIS winter $\delta^{18}O_{prec}$ ranges from -6‰ to -14‰ at the same latitude (Appendix Fig. A1.4M). Simulated $\delta^{18}O_{prec}$ is also comparable to observations from the Patagonian Andes [47-48 °S, *Stern and Blisniuk*, 2002]. At these two southerly locations, the most depleted values may not be well simulated because the model is too coarse to represent the full elevation where the range is narrow. We consider the model acceptable for the following experiments because it captures the important large-scale features of climate and $\delta^{18}O_{prec}$ in South America. We show our results in comparison to the control run in order to highlight the impact of particular changes in boundary conditions and to minimize the error in the results.

2.4.2 Sensitivity experiments

For each change in model parameters we present the changes in South American regional climate (Fig. 2.4) and $\delta^{18}O_{prec}$ (Fig. 2.5). The main results discussed here are 20-year austral summer (DJF) averages. Because austral summer is the wet season in the central Andes, it dominates the weighted mean annual average $\delta^{18}O_{prec}$ signal. The central Andes is also where many $\delta^{18}O_{prec}$ records and paleoaltimetry studies are focused. As DJF is not the dominant rainfall season in other parts of South America, we also show mean annual (Fig. 2.6) and austral winter (Appendix Figs. A1.2-A1.5) results.

2.4.2.1 CO_2 effects on $\delta^{18}O_{prec}$

The global mean annual temperature (MAT) is 12.6 °C, 15.4 °C and 19.1 °C in the control ($1xCO_2$), $2xCO_2$ and $4xCO_2$ simulations respectively. The temperature increase of ~2.8 °C between 1x and 2x CO_2 is consistent with other models and observational datasets [*Knutti et al.*, 2006; *Murphy et al.*, 2004]. Temperature increases are not spatially uniform (Fig. 2.4E), with temperatures increasing more

over land than the oceans. At $4xCO_2$, warming of 4-6 °C in the low-latitude ocean is accompanied by an increase of 8-10 °C in the center of the continent and an increase of 6-8 °C on the Central Andean plateau. At $4xCO_2$, precipitation decreases by up to 3-4 mm/day in the Central Andean foreland and increases by up to 6-8 mm/day on the northeast coast (Fig. 2.4A).

At higher CO_2 levels, $\delta^{18}O_{prec}$ increases across South America with the exception of the Amazon basin (Fig. 2.5A). The maximum change occurs in the central Andes where $\delta^{18}O_{prec}$ is -8‰ (Fig. 2.5A) at $4xCO_2$, 6-8‰ (Fig. 2.5F) less negative than the modern. In the southern Andes, $\delta^{18}O_{prec}$ is between -6 and -8‰ in the $4xCO_2$ simulation, 2-3‰ less negative than in the control simulation. Increases in $\delta^{18}O_{prec}$ can be attributed primarily to temperature controls (Fig. 2.4E) on the amount of kinetic fractionation and to a lesser degree to changes in precipitation (Fig. 2.4A), which alter the amount of rainout. At higher temperatures, isotopic fractionation during surface evaporation and cloud condensation is reduced. The specific humidity is also higher which, according to distillation principles, leads to less negative $\delta^{18}O_{vapor}$. For the same precipitation pattern, the $\delta^{18}O$ of water vapor is therefore less negative than the control simulation throughout the vapor transport path. In the Amazon region $\delta^{18}O_{prec}$ is -2 to -6‰, 1-3‰ more negative than in the control simulation. This decrease can be attributed to an increase in precipitation that enhances Rayleigh distillation. These effects of increased precipitation rates on $\delta^{18}O_{prec}$ are geographically restricted. As the prevailing winds (Fig. 2.2C) transport depleted moisture from the northeast coast of Brazil westwards across the Amazon basin and towards the central Andes, high temperatures and mixing with less depleted air masses counteract the depletion caused by high rainout rates over the Atlantic (Fig. 2.4A). At $2xCO_2$, the changes in precipitation, temperature and $\delta^{18}O_{prec}$ (Appendix Figs. A1.1A and A1.1F) relative to the control simulation are smaller in magnitude than at $4xCO_2$ but follow a similar pattern.

2.4.2.2 Andean Elevation effects on $\delta^{18}O_{prec}$

In agreement with other studies [*Campetella and Vera*, 2002; *T A Ehlers and Poulsen*, 2009; *Insel et al.*, 2010a; *Lenters and Cook*, 1995], the elevation of the Andes

is shown to exert a strong control on the regional climate. In the No Andes simulation, precipitation (Fig. 2.4B) decreases by 8 mm/day on the eastern flanks of the central Andes and increases in the western Amazon basin by 3-5 mm/day compared to the control simulation. Temperatures increase by 20-25 °C in the central Andes when the Andes are lowered but remain constant in regions where elevation is identical in both simulations (Fig. 2.4F).

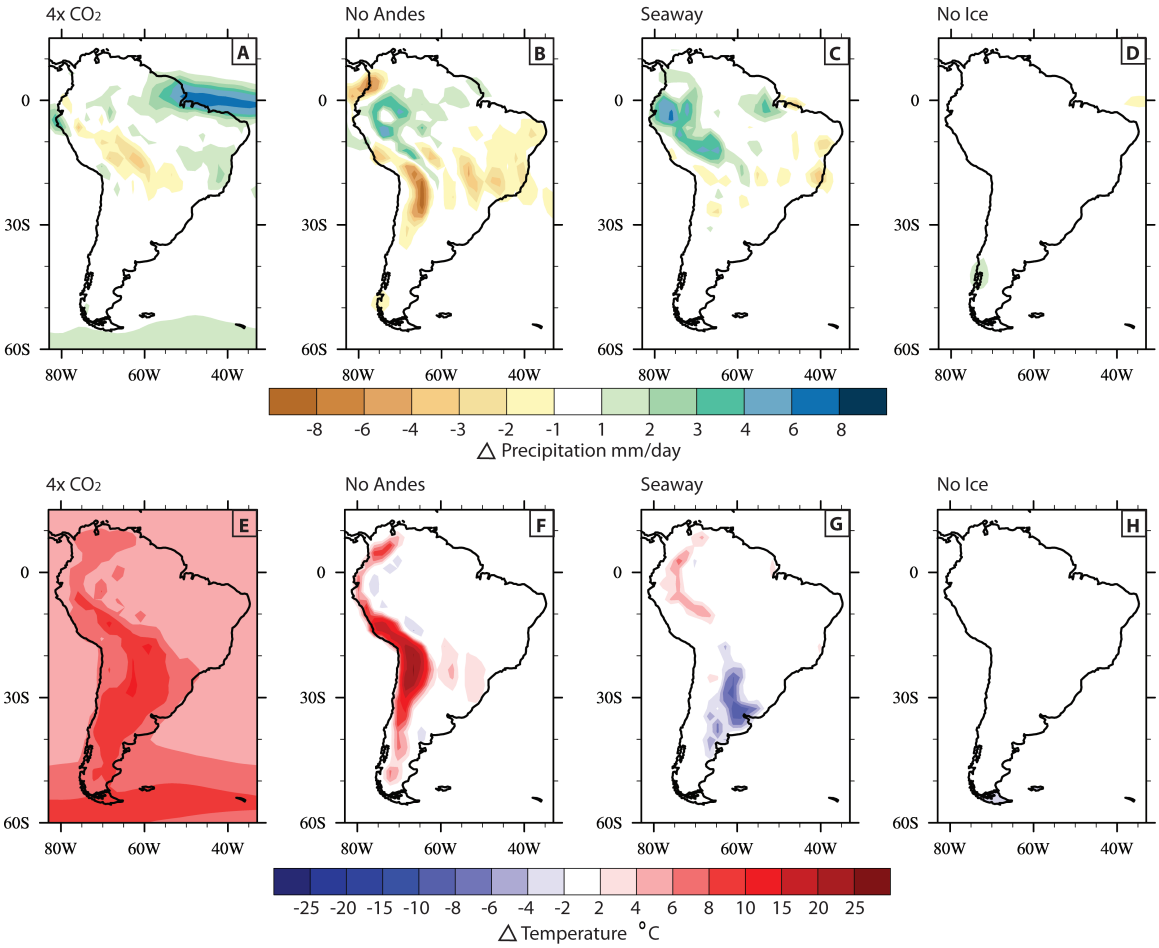

Figure 2.4. Austral summer climatology.

Simulated summer precipitation (mm/day) (a-d) and temperature (°C) (e-h) difference between simulation and control (simulation minus control, see Fig. 2b and 2c) for a and e) 4xCO2, b and f) No Andes, c and g) Seaway, d and h) No Ice. Note that the contour intervals change at 6 mm/day and 10°C in the precipitation and temperature plots respectively. Although isotopes are different in the freshwater and marine seaway runs, the climate is identical.

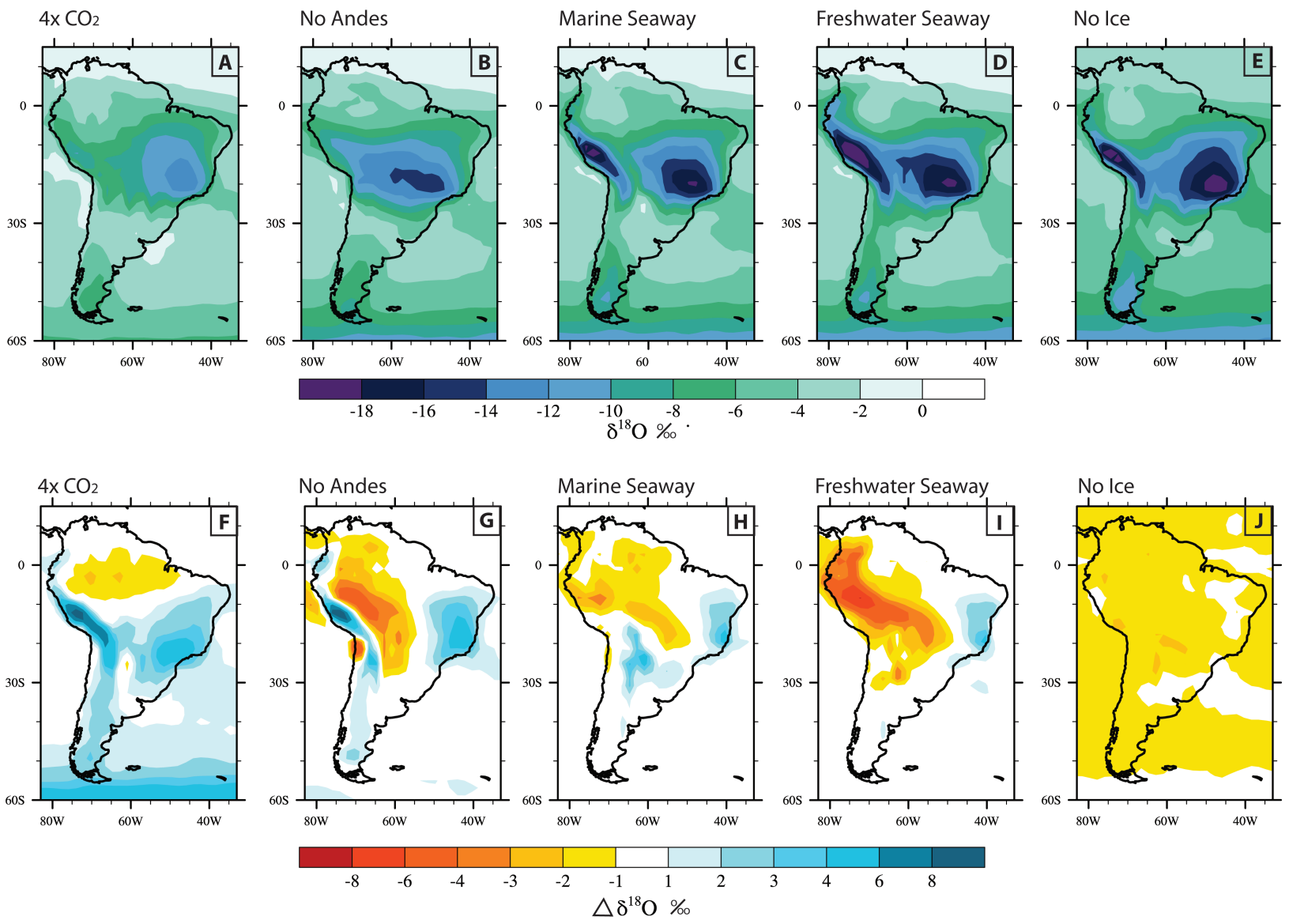
4x CO2
No Andes
Marine Seaway
Freshwater Seaway
No Ice
A
B
C
D
E
0
30S
60S
80W
60W
40W
60
-18
-16
-14
-12
-10
-8
-6
-4
-2
0
δ18O ‰
F
G
H
I
J
-8
-6
-4
-3
-2
-1
1
2
3
4
6
8
△δ18O ‰

Figure 2.5 Austral summer $\delta^{18}O_{prec}$.

(previous page) A-E) Simulated amount-weighted summer $\delta^{18}O_{prec}$ (‰) predicted by GENESIS with A) 4xCO_2, B) No Andes, c) $SW_{marine,}$ a seaway (see Fig. 2.2A) with a marine, Atlantic-like, isotopic composition, D) $SW_{freshwater}$, a seaway with freshwater (-6‰) composition and, E) No Ice, Ocean - no Antarctic Ice Sheet, ($\delta^{18}O_{ocean}$ = modern $\delta^{18}O_{ocean}$ - 1.2‰). F-J) Summer $\delta^{18}O_{prec}$ difference (simulation minus control) between the sensitivity simulation and the control run (Fig. 2.2D) for the simulations in (A-E). Note that the contour interval changes at 4‰.

Figure 2.6. Mean annual $\delta^{18}O_{prec}$.

(next page) A-F) Simulated amount-weighted mean annual $\delta^{18}O_{prec}$ (‰) predicted by GENESIS with A) modern conditions, B) 4xCO_2, C) No Andes, D) $SW_{marine,}$ a seaway (see Fig. 2.2A) with a marine, Atlantic-like, isotopic composition, E) $SW_{freshwater}$, a seaway with freshwater (-6‰) composition and, F) No Ice, Ocean - no Antarctic Ice Sheet, ($\delta^{18}O_{ocean}$ = modern $\delta^{18}O_{ocean}$ - 1.2‰). G-K) Mean annual $\delta^{18}O_{prec}$ difference (simulation minus control) between the sensitivity simulation and the control run (Fig. 2.6A) for the simulations in (B-F). Note that the contour interval changes at 4‰.

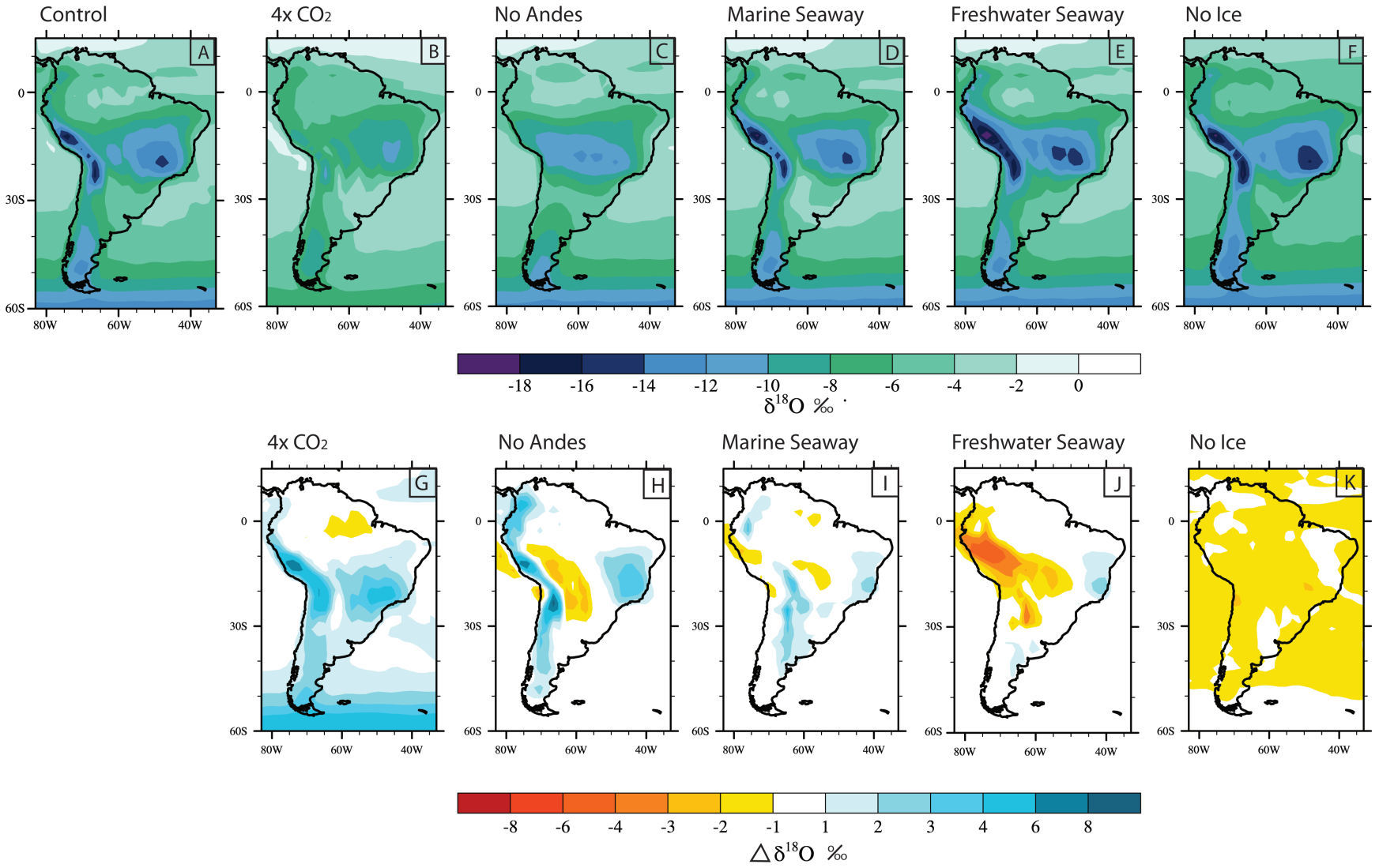
Control
4x CO2
No Andes
Marine Seaway
Freshwater Seaway
No Ice
A
B
C
D
E
F
0
30S
60S
80W
60W
40W
-18 -16 -14 -12 -10 -8 -6 -4 -2 0
δ18O ‰
4x CO2
No Andes
Marine Seaway
Freshwater Seaway
No Ice
G
H
I
J
K
-8 -6 -4 -3 -2 -1 1 2 3 4 6 8
△δ18O ‰

$\delta^{18}O_{prec}$ in the northern, central and southern Andes is 2-3‰, 4-8‰ and 2-3‰, less negative in the No Andes experiment than in the control simulation (Fig. 2.5G). The opposite signal is observed in the Amazon basin; $\delta^{18}O_{prec}$ is more negative by as much as 4-6‰ in the No Andes simulation (Fig. 2.5G). The Half Andes simulation shows a similar pattern of change as a result of elevation decrease but of a smaller magnitude (Appendix Figs. A1.1A and A1.1F).

In the Amazon basin the higher precipitation rates at lower Andean elevation result in more negative $\delta^{18}O_{prec}$. In the northern and central Andes, changes in adiabatic cooling, amount effects and moisture source all play a role in determining $\delta^{18}O_{prec}$. In the central Andes and north of the equator, an increase in precipitation (Fig. 2.4B) with increasing elevation enhances the decrease in $\delta^{18}O_{prec}$ expected from adiabatic cooling alone. In addition, as elevations increase, the Andes act as a barrier to zonal circulation and prevent moisture derived from the Pacific from penetrating inland resulting in greater influence from Atlantic sourced moisture [*Insel et al.*, 2010a]. In western South America, Pacific sourced water has a shorter travel distance and undergoes less Rayleigh distillation than Atlantic sourced water vapor, causing it to be less depleted. Switching from a Pacific to Atlantic moisture source therefore results in more negative $\delta^{18}O_{prec}$. In the southern Andes, where a slight increase in precipitation (1-2mm/day at 50 °S, Fig. 2.4B) accompanies uplift and there is no change in moisture source [*GEOSECS*, 1987], the increase in $\delta^{18}O_{prec}$ with increasing elevation is weaker than in the central Andes and dominated by adiabatic cooling effects.

2.4.2.3 Seaway effects on $\delta^{18}O_{prec}$

The seaway exerts a strong, local control on regional climate. We compare the areas affected by 1) the southern, Paranan (60 °W, 25-40 °S), and 2) northern, Amazonia (Brazil, Peru, Bolivia), regions of the seaway. In the Paranan region, evaporation and humidity increase but temperature decreases (Fig. 2.4G) and precipitation rates remain very low (Figs. 2.2C and 2.4C). In the Amazonia region, summer surface temperatures (Fig. 2.4G) are higher in the presence of a seaway. Higher relative and specific humidity over the seaway results in an increase in

precipitation downwind in the northern and central Andes of up to 4-6 mm/day (Fig. 2.4C).

The effects of the seaway and the resultant climatic changes on $\delta^{18}O_{prec}$ depend on the $\delta^{18}O_{seaway}$. Two experiments, SW_{marine} and $SW_{freshwater}$, have a $\delta^{18}O_{seaway}$ of ~-1‰ and -6‰ respectively. In the SW_{marine} experiment (Figs. 2.5C and 2.5H), the $\delta^{18}O_{prec}$ south of 25 °S (Paranan) is up to 4‰ less negative than the control simulation. North of 25 °S (Amazonia), $\delta^{18}O_{prec}$ is more negative than the control simulation by 2-4‰. Maximum depletion occurs in the northern Andes and the Amazon basin. In contrast, the $SW_{freshwater}$ experiment results in more negative $\delta^{18}O_{prec}$ throughout the continent (Figs. 2.5D and 2.5I). Maximum depletion occurs in the northern Andes where the lowest values are between -22 and -20‰, 6-8‰ more negative than the control simulation.

Source and amount effects are responsible for changes in $\delta^{18}O_{prec}$ in the presence of a seaway. In the Paranan region, where simulated average precipitation rates are <1 mm/day, the isotopic composition of the seaway dictates the direction of change in $\delta^{18}O_{prec}$. The $\delta^{18}O_{prec}$ will shift in the direction of the $\delta^{18}O_{seaway}$. For example, in the SW_{marine} case, $\delta^{18}O_{prec}$ becomes more negative. In the Amazonian region, the seaway drives an increase in precipitation and therefore rainout effects, lowering the $\delta^{18}O_{prec}$. The $\delta^{18}O_{seaway}$ determines the magnitude of $\delta^{18}O_{prec}$ depletion relative to the control. A more depleted seaway ($SW_{freshwater}$) causes a more negative $\delta^{18}O_{prec}$ (Figs. 2.5H and 2.5I). Temperature changes (Fig. 2.4G) may also alter the $\delta^{18}O_{prec}$ but are not the dominant control as the simulated temperature changes are expected to have the opposite effect on $\delta^{18}O_{prec}$ than those simulated.

2.4.2.4 Antarctic Ice Sheet effects on $\delta^{18}O_{prec}$

The removal of the ice sheet results in a global MAT rise of 0.9 °C from 12.6 °C to 13.5 °C. However, temperature increases predominantly occur south of 45 °S and are not observed in the summer average over South America (Fig. 2.4H). Precipitation rates change by 1-2 mm/day in a few isolated regions (e.g. 75 °W; 40 °S, Fig. 2.4D).

The physical removal of the ice sheet (NoIce_modOcean experiment) results in small regions that are 0-2‰ more negative than the control simulation (e.g. 0 °S, 65 °W; Figs. A1.1E and A1.1J). The addition of isotopically light meltwater to the oceans results in precipitation that is isotopically more depleted by a further ~1.2‰ (NoIce experiment, Fig. 2.5E). In the model, the change in $\delta^{18}O_{ocean}$ therefore causes a change in $\delta^{18}O_{prec}$ of the same magnitude and is the dominant mechanism by which Antarctic ice formation alters South American $\delta^{18}O_{prec}$. The maximum impact of the ice sheet on $\delta^{18}O_{prec}$ is ~2-3‰ but the impact is generally <2‰ (Fig. 2.5J).

2.4.3 Time-Specific Paleoclimate Scenarios

Interpretation of $\delta^{18}O_{prec}$ records requires quantifying the combined effects of more than one control. Here we explore two time scenarios: 1) the late Eocene (Figs. 2.7A – 2.7D), when Andean uplift began and, 2) the middle Miocene (Figs. 2.7E – 2.7H), preceding and during the formation of many of the central Andean $\delta^{18}O_{prec}$ records.

2.4.3.1 Late Eocene, ~40Ma

The late Eocene scenario includes a low-elevation Andes, $4xCO_2$, no AIS or interior seaway, and a $\delta^{18}O_{ocean}$ corrected for ice sheet volume. Maximum temperatures of >40 °C occur between 20 °S and 30 °S in the Eocene simulation, which is >10 °C warmer than the present day foreland and >30 °C warmer than the present-day (control simulation) high Andes at this latitude (Figs. 2.2B and 2.7D). Precipitation rates are reduced in the central and northern Andes as a result of the removal of an orographic barrier while elevated CO_2 and low Andean elevation lead to increased precipitation in the Amazon and equatorial Atlantic (Figs. 2.2C and 2.7C).

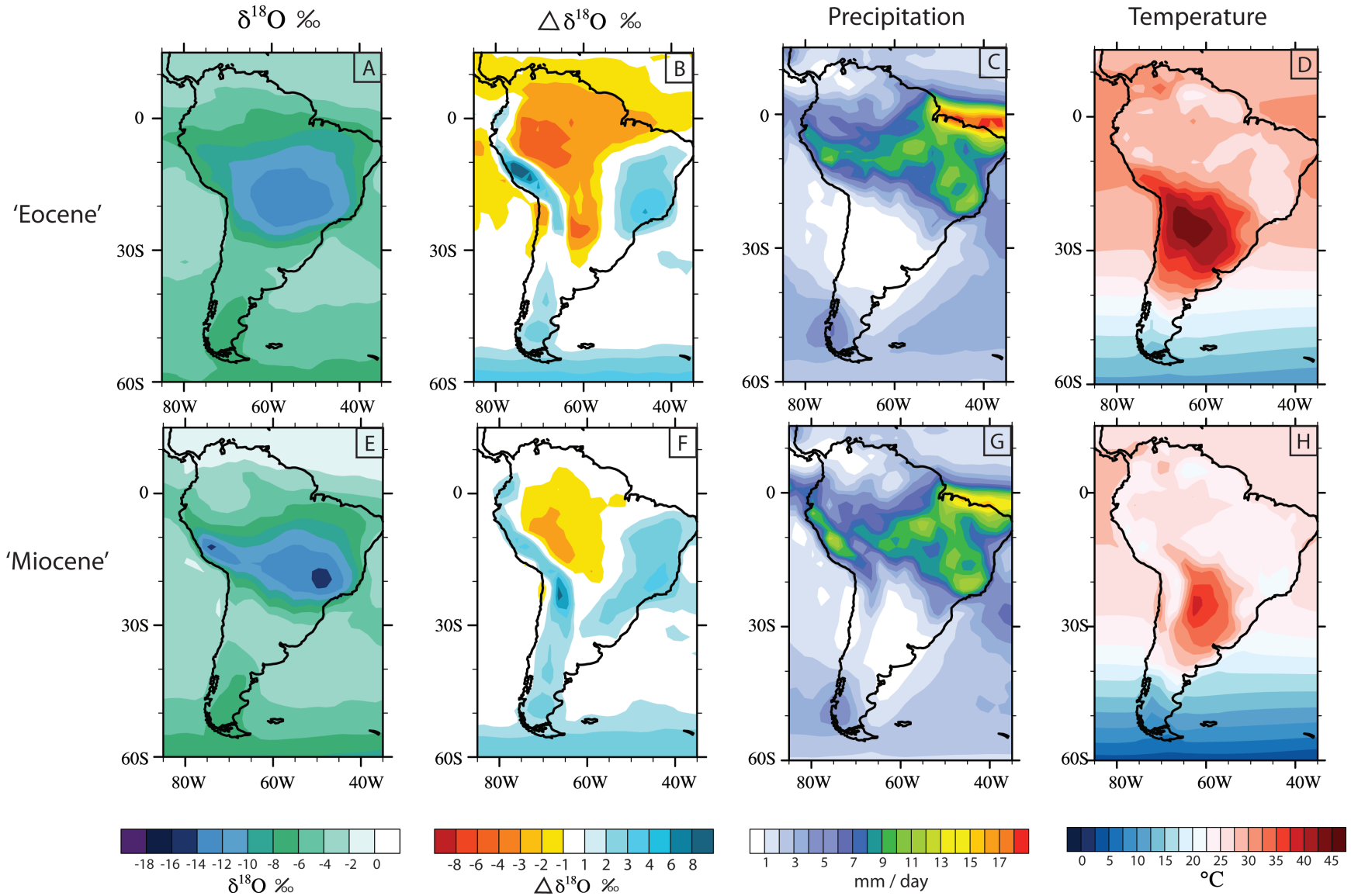
δ18O ‰
△δ18O ‰
Precipitation
Temperature
'Eocene'
'Miocene'
A
B
C
D
E
F
G
H
0
30S
60S
80W
60W
40W
-18 -16 -14 -12 -10 -8 -6 -4 -2 0
δ18O ‰
-8 -6 -4 -3 -2 -1 1 2 3 4 6 8
△δ18O ‰
1 3 5 7 9 11 13 15 17
mm / day
0 5 10 15 20 25 30 35 40 45
°C

Figure 2.7 Climatology and $\delta^{18}O_{prec}$ for Eocene and Miocene scenarios.

(previous page) Simulated austral summer amount-weighted $\delta^{18}O_{prec}$, difference in $\delta^{18}O_{prec}$, precipitation (mm/day), and temperature (°C) for the late Eocene (A-D) and middle Miocene (E-H) simulations. Difference in $\delta^{18}O_{prec}$ (B and F) is simulation minus control (Fig. 2D). The Eocene simulation has No Andean elevation, $4xCO_2$ and No Antarctic Ice Sheet ($\delta^{18}O_{ocean}$ = modern $\delta^{18}O_{ocean}$ - 1.2‰). The Miocene simulation has half Andean elevation, $2xCO_2$ and a modern ice sheet and $\delta^{18}O_{ocean}$. Neither simulation includes a seaway. Note that the contour level changes in $\Delta\delta^{18}O_{prec}$.

The middle Eocene $\delta^{18}O_{prec}$ pattern (Fig. 2.7A) is significantly different than the modern (Fig. 2.2D). A single strong $\delta^{18}O_{prec}$ minimum occurs in central South America, with a weaker minimum in the southern Andes. In the Eocene simulation, precipitation is isotopically less depleted by >8‰ along the Andean range and 6-8‰ in Eastern Brazil (Fig. 2.7B). Maximum differences between the Eocene and control simulation occur in the northern central Andes and western Amazon. The more negative $\delta^{18}O_{prec}$ in the Amazon is associated with greater upwind precipitation rates (Figs. 2.2C and 2.7C). Higher temperatures (Figs. 2.2B and 2.7D) and reduced rainfall rates (Figs. 2.2C and 2.7C) result in less negative $\delta^{18}O_{prec}$ values elsewhere and particularly on the eastern central Andean flanks.

2.4.3.2 Middle Miocene, ~15 Ma

The middle Miocene experiment is performed using half Andean elevation and $2xCO_2$ (table 2.1). Simulated middle Miocene temperatures in the Altiplano region are 20-25 °C and precipitation rates are 3-11 mm/day (Figs. 2.7G and 2.7H), 10-15 °C cooler on the Altiplano and 6 mm/day drier on the eastern flanks than the control simulation (Figs. 2.2B, 2.2C, 2.7G and 2.7H). In the Miocene simulation, $\delta^{18}O_{prec}$ is less negative everywhere in the Andes (by 2-8‰) and in Eastern Brazil than the control simulation but in the Amazon basin $\delta^{18}O_{prec}$ is more negative. The maximum decrease in $\delta^{18}O_{prec}$ occurs in the southern Altiplano (Fig. 2.7F).

2.4.3.3 Cenozoic $\delta^{18}O_{prec}$ patterns in South America

Combining the boundary conditions in these time-appropriate scenarios allows us to make estimations of past climate and $\delta^{18}O_{prec}$ patterns. Based on the modern, Miocene and Eocene simulations, we expect that $\delta^{18}O_{prec}$ had lower spatial

gradients and variability in the past (Figs. 2.2D, 2.7A and 2.7E). For example, the extreme low values in the central and southern Andes and in Eastern Brazil (45 °W, 20 °S) that are present in the control simulation are not as low in the Miocene scenario and are weak or not present in the Eocene scenario. The Miocene $\delta^{18}O_{prec}$ pattern is similar to modern but shifted toward less negative values with lower spatial gradients. At half the modern elevation, the Andes are still capable of modifying the regional climate and $\delta^{18}O_{prec}$. The Eocene $\delta^{18}O_{prec}$ pattern is simple with $\delta^{18}O_{prec}$ decreasing away from the coasts and towards higher latitudes.

In both scenarios, changes in temperature and precipitation patterns are consistent with the sensitivity experiments of the individual parameters. However, the total change in $\delta^{18}O_{prec}$ in the Eocene scenario (Fig. 2.7B) is less than that expected from sensitivity experiments in which only Andean elevation, CO_2 or $\delta^{18}O_{ocean}$ are changed (Figs. 2.5F, 2.5G and 2.5J). This discrepancy is mainly due to $\delta^{18}O_{prec}$ responding differently to increasing CO_2 in the absence of the Andes. A strengthening of the Chaco Low, a low pressure system in central South America, and changes in moisture source with increasing CO_2 result in precipitation that is isotopically more depleted at low Andean elevations despite an increase in temperature.

2.5 IMPACTS OF CENOZOIC GLOBAL CLIMATE AND REGIONAL GEOGRAPHY CHANGES ON SOUTH AMERICAN CLIMATE AND $\delta^{18}O_{prec}$ RECORDS

The simulations presented here show that global and regional climatic change can exert a significant influence on $\delta^{18}O_{prec.}$ Here we compare the simulation results with existing climate and stable isotope records.

2.5.1 Impact of global climate and regional geography changes on South American climate

The climate of South America is significantly altered by a rise in CO_2, a change in Andean elevation and the presence of an inland seaway (Figs. 2.4A-2.4C, 2.4E-2.4G) but less so by the presence or absence of the AIS (Figs. 2.4D and 2.4H). Although spatially variable, temperatures increase everywhere in response to an increase in CO_2, whereas only local temperature changes occur in response to

increasing Andean elevations and seaway incursions. An increase from no Andean elevation to full Andean elevation causes the greatest changes in surface temperature (up to 25 °C in the central Andes, Fig. 2.4F) but temperature changes under high (4x) CO_2 conditions are significant in comparison (10 °C, Fig. 2.4E). Predicted temperature changes in the presence of a seaway are mainly limited to the seaway and do not extend to high elevations (Fig. 2.4G). Given this, surface temperature records from multiple locations could help to distinguish between these factors. For example, a drop in temperature of 10 °C on the Andean plateau could represent an elevation increase of around half (~2000m), or a doubling of CO_2 and an elevation increase of one third. The former would not be accompanied by temperature changes in the foreland while the latter would show an increase in temperature of ~3 °C in the foreland. This example highlights how sampling strategies could not only quantify the paleoclimate, but also help delineate between different mechanisms of climate change.

The seaway, Andean elevation and, to a lesser extent, CO_2 levels are capable of causing large changes in the magnitude of precipitation rates in the northern Andes (Figs. 2.4A–2.4C). Precipitation rates in the central Andes are modified primarily by Andean elevation; an increase in elevation causes an increase in precipitation on the Eastern flanks. In the southern Andes, atmospheric CO_2 is the dominant control on precipitation, particularly in the winter months (Appendix Fig. A1.2), in addition to some changes in response to elevation increase. Precipitation rates in the Amazon region and Eastern Brazil depend on CO_2 levels, Andean elevation and the seaway.

2.5.2 Impact of global climate and regional geography changes on South American $\delta^{18}O_{carb}$ records

2.5.2.1 Existing South American stable isotope records

Simulation of $\delta^{18}O_{prec}$ can improve interpretations of $\delta^{18}O_{prec}$ records by showing the relative importance of different controls on $\delta^{18}O_{prec}$ for a given region. A brief summary of currently available records of Cenozoic South American $\delta^{18}O_{prec}$,

including data from soil carbonates, lacustrine carbonates and biogenic-apatite from fossil mammal teeth, is as follows (see also Fig. 2.8):

(i) In the northern Andes few carbonate stable isotope records exist because the climate is wet and not conducive for soil carbonate formation. An exception to this is a recent study by Giovanni et al. [2010b] who report lacustrine carbonate data from the Cordillera Blanca, Peru that were deposited <5.4 Ma (Fig. 2.8A). The $\delta^{18}O_{carb}$ sample values range from -13.2 to -17.8‰, indicating that $\delta^{18}O_{prec}$ was strongly depleted and suggesting that high elevations had been attained in this region by ~5 Ma.

(ii) Central Andean climate is more conducive to carbonate formation and data is available from the plateau and both flanks. Palustrine and pedogenic carbonates from the northern Altiplano (Fig. 2.8B) record a decrease in $\delta^{18}O_{carb}$ from between -6 and -8‰ at ~28 Ma to between -10 and -16‰ at ~6 Ma [*C Garzione et al.*, 2008; *Garzione et al.*, 2006]. The late Miocene part of this record indicates a 3-4‰ decrease in mean $\delta^{18}O_{mw}$ between 10 and 6 Ma [*Garzione et al.*, 2006], when converted from $\delta^{18}O_{carb}$ using paleotemperatures extracted from the same records using Δ_{47} clumped isotope paleothermometry [*Ghosh et al.*, 2006]. Fossil mammal teeth from the northern Altiplano show a decrease of ~10‰ in $\delta^{18}O_{mw}$ from ~26 Ma to 10-8 Ma [Fig. 2.8C, *Bershaw et al.*, 2010]. $\delta^{18}O_{carb}$ from the eastern Andean flanks record a decrease of ~5‰ between 12.4 and 8.5 Ma and then an increase of ~4‰ by 7.5 Ma [Fig. 2.8D, *Mulch et al.*, 2010]. This pattern was attributed to Andean uplift and the initiation of a wetter and more seasonal climate [*Mulch et al.*, 2010]. A second record from the eastern flanks, but at lower modern elevations, shows fluctuations of $\delta^{18}O_{carb}$ between -14 and -6‰, prior to 7 Ma [*Uba et al.*, 2009]. The less negative $\delta^{18}O_{carb}$ values are from facies that are interpreted as marine inland seaway deposits. Palustrine and lacustrine carbonates from the Atacama desert document a ~5‰ increase in $\delta^{18}O_{carb}$ between 12 and 6 Ma, which is attributed to

$\delta^{18}O$ records from South America from the last 30 million years

Records are from:
A: Giovanni et al., 2010
B: Garzione et al., 2006
Garzione et al., 2008
C: Bershaw et al., 2010
D: Mulch et al., 2010
E: Rech et al., 2010
F: Kleinert and Strecker, 2001
G: Latorre et al., 1997
H: Blisniuk et al., 2005

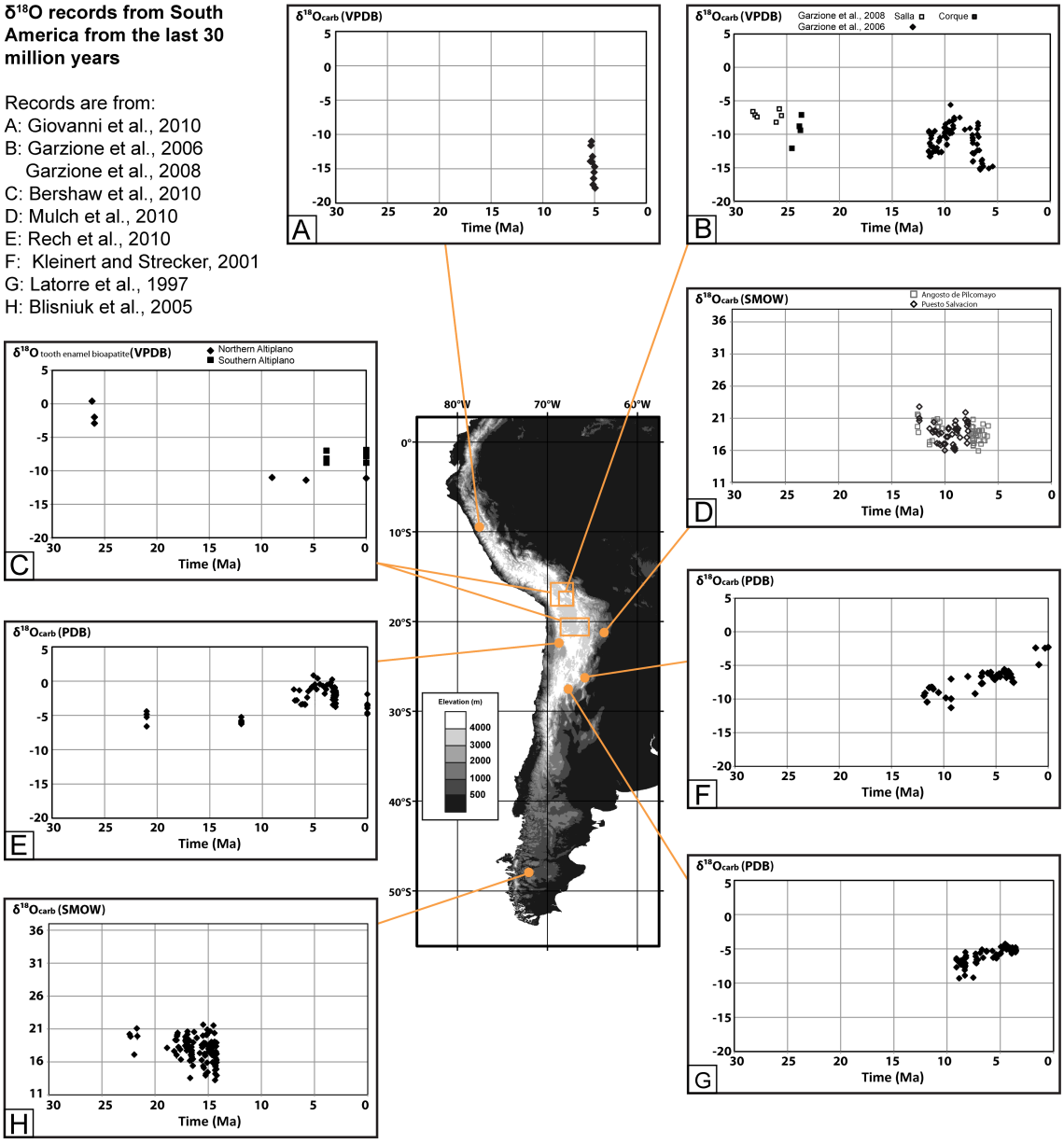

Figure 2.8 $\delta^{18}O$ records from South America (30 Ma – present).

(previous page) Records presented here are derived from soil or lake carbonates unless otherwise stated. Circles and boxes indicate the location of sample sites within South America. A) Giovanni et al. [2010a], B) Garzione et al. [2006] and Garzione et al. (2008) C) Bershaw et al. [2010] – $\delta^{18}O$ of carbonate component of bioapatite in fossil mammal tooth enamel, D) Mulch et al. [2010], E) Rech et al. [2010], F) Kleinert and Strecker [2001], G) Latorre et al. [1997], and H) Blisniuk et al. [2005]. In order to plot the data on the same plots, some of the data have been assigned ages based on the age constraints and sedimentation rate estimates given in the original papers (Blisniuk et al., 2005; Giovanni et al., 2010; Mulch et al., 2010; Rech et al., 2010). Where possible, constant sedimentation rates are assumed based on dated horizons within the observed stratigraphy. The record presented in Giovanni et al. (2005) has only one age constraint of 5.45 Ma at the base of the section. For ease of viewing we assume that the first sample is 5.45 Ma and consecutive measurements are at 0.05 m.yr. intervals. Datasets reported against different $\delta^{18}O$ standards have been plotted so that the y-axes correspond to approximately equivalent $\delta^{18}O_{carb}$ values.

increased aridity due to the creation of an orographic barrier when Andean heights are >2 km [Fig. 2.8E, *Rech et al.*, 2010]. To the south in Northwest Argentina, Kleinert and Strecker [2001] identify an increase in pedogenic $\delta^{18}O_{carb}$ from between -11 and -8‰, 12-9 Ma, to ~-6.5‰ by 7-3 Ma and a further increase to between -5.5 and -1.5‰ during the Plio-Pleistocene (Fig. 2.8F). The $\delta^{18}O_{carb}$ increase was attributed to increasing evaporation in a more seasonal and drier climate, despite expected depletion due to the development of a rain shadow. Nearby, Latorre et al. [1997] document an increase in $\delta^{18}O_{carb}$ of 4‰ between 9 and 3.5 Ma (Fig. 2.8G), which they suggested may be due to an increase in seasonality and evaporation, possibly on a global scale.

(iii) Finally, in the eastern foreland of the Patagonian Andes a decrease of 2‰ and an increase in variability is observed in pedogenic $\delta^{18}O_{carb}$ at ~16.5 Ma [Fig. 2.8H, *Blisniuk et al.*, 2005]. This change is attributed to rain shadow development that is slightly masked by increased evaporation, both of which are a consequence of Andean uplift.

2.5.2.2 Evaluation of $\delta^{18}O_{prec}$ records based on simulation results

This wealth of $\delta^{18}O_{prec}$ data records provides valuable constraints on the tectonic and climatic evolution of South America. However, the majority of these

records are currently interpreted in terms of local and regional scale processes and do not account for either global climate change or a seaway incursion. In some cases, local controls may dominate the signal; however, discounting regional change may lead to an over- or under-estimation of the magnitude of change in the dominant control.

The $\delta^{18}O$ composition of carbonates is dependent on the local evaporation rate and soil temperature during carbonate precipitation as well as the $\delta^{18}O$ composition of the local meteoric water ($\delta^{18}O_{mw}$). Increasing evaporation rates and decreasing soil temperatures drive increases in $\delta^{18}O_{carb}$ [*Kim and O'Neil*, 1997; *Quade et al.*, 1989]. Distinguishing these 3 different controls is complex but is possible with 1) additional constraints on temperature, 2) sedimentological evidence of increasing aridity / humidity as an indicator of changing evaporation rates and 3) prediction of $\delta^{18}O_{prec}$ based on climate models and known climatic constraints. Climate models enable us to estimate both changes in surface temperature and $\delta^{18}O_{prec}$ for a given change in boundary conditions. Predictions of both $\delta^{18}O_{prec}$ and temperature effects on carbonate formation can then be combined when examining $\delta^{18}O_{carb}$ records. Assuming that a decrease in surface temperature causes an increase in $\delta^{18}O_{carb}$ of ~0.12‰/°C [*Kim and O'Neil*, 1997], a temperature increase of ~10°C would increase $\delta^{18}O_{carb}$ by 1.2‰. As GENESIS simulates surface temperature and not temperature at the depth of carbonate formation these values are an approximation but help to determine the relative importance of temperature and $\delta^{18}O_{prec}$ changes. For many of the boundary conditions presented here, predicted temperature effects are small compared to changes in $\delta^{18}O_{prec}$. Exceptions to this are the climatic responses to increasing elevation and decreasing CO_2 at low elevations. On the Andean Plateau, increasing elevation from low to full Andean elevation results in a temperature increase of 20-25 °C and a decrease in $\delta^{18}O_{prec}$ of 3-6‰, leading to a net decrease of ~0–3.5‰ in $\delta^{18}O_{carb}$. Decreasing CO_2 from 4x to 1x PIL results in a temperature decrease of 6-8°C, a $\delta^{18}O_{prec}$ decrease of 4-6‰ and therefore a decrease in $\delta^{18}O_{carb}$ of ~3-5‰. The seaway and ice sheet do not affect surface temperatures (Figs. 2.4G and 2.4H).

The very negative ~5 Ma $\delta^{18}O_{carb}$ found in the northern Andes [Fig. 8A, Giovanni et al. 2010] has been attributed to high Andean elevations at that time. Our results show that the presence of a freshwater seaway could lower $\delta^{18}O_{prec}$ by >4‰ in this region. However, the seaway had retreated by ~7Ma [*Hoorn et al.*, 2010] and it is therefore unlikely that a seaway contributed to these low $\delta^{18}O_{carb}$ observations. Increasing Andean elevation from half to modern elevation leads to a simulated decrease in $\delta^{18}O_{prec}$ of only 2-3‰ in the northern Andes (Appendix Fig. A1.1F), which is less than the spread of values recorded over a short period of time. We suggest that this record is consistent with Andean elevations that were within ~2000m of the modern elevation by ~5Ma.

Andean Plateau $\delta^{18}O_{carb}$ records indicate a decrease of ~1-2‰ in $\delta^{18}O_{carb}$, and an increase in $\delta^{18}O_{carb}$ variability between 10 and 6 Ma [*Garzione et al.*, 2006]. Ehlers and Poulsen [2009] and Poulsen et al [2010] demonstrate that this record is consistent with increasing Andean uplift accompanied by a decrease in surface temperature and increases in convective precipitation on the Andean flanks. However, decreasing CO_2 could also have contributed to decreasing $\delta^{18}O_{carb,}$ reducing the amount of surface uplift required to produce the same $\delta^{18}O_{carb}$ signal. $\delta^{18}O_{prec}$ is lowered by >3‰ on the Altiplano when CO_2 decreases from 2x to 1x PIL (Appendix Fig. A1.1G). CO_2 levels have not exceeded 2x PIL since 10 Ma [*Demicco et al.*, 2003; *Pagani et al.*, 2005; *Pearson and Palmer*, 2000], but even a 1.5‰ CO_2-driven decrease in $\delta^{18}O_{prec}$ would result in under-estimates of paleoelevation by ~500 – 750m. Conversely, the presence of a freshwater seaway from 15 to 7 Ma, but not after ~7Ma, would mask an increase in elevation between 10 and 6 Ma.

The ~30 m.y. isotopic record of mammal teeth from the Altiplano indicates a decrease in $\delta^{18}O_{mw}$ of ~10‰ between 26 Ma and 10 Ma [*Bershaw et al.*, 2010]. Due to lack of data, it is impossible to determine whether the transition from 26 to 10 Ma was gradual or punctuated. Increasing elevation and decreasing CO_2 levels are capable of decreasing $\delta^{18}O_{mw}$. However, a decrease of 10‰ exceeds the isotopic response to any one control, or the combination of controls in the Miocene and Eocene scenarios. Possible reasons for this discrepancy include regional changes, e.g. ocean circulation, that are not accounted for in our experiments or higher

evaporation rates at 26 Ma. Another possibility is that a seaway lowered $\delta^{18}O_{prec}$ at ~10 Ma, contributing to the overall decrease from 26 to 10 Ma. This decrease in $\delta^{18}O_{mw}$ is consistent with the decrease in $\delta^{18}O_{carb}$ observed over a similar time period [Fig. 2.8B, *C Garzione et al.*, 2008], although the observed decrease in $\delta^{18}O_{carb}$ is smaller possibly due to changes in temperature or evaporation rates.

The late Miocene decreasing trends in $\delta^{18}O_{carb}$ on the Altiplano contrast with records from the western and eastern Andean flanks, which indicate increases of between 5 and 8‰ since ~11 Ma [Figs. 2.8E, 2.8F and 2.8G; *Kleinert and Strecker*, 2001; *Latorre et al.*, 1997; *Rech et al.*, 2010]. These $\delta^{18}O_{carb}$ increases are consistent with decreasing local surface temperatures, increasing evaporation rates, and changing seasonality. Changing seasonality could alter $\delta^{18}O_{carb}$ by changing the aridity and $\delta^{18}O_{prec}$ during the season of carbonate formation. This increase is also consistent with increasing Andean elevation. On the eastern flanks, our simulation results show that as Andean elevation increases, $\delta^{18}O_{prec}$ in the adjacent foreland increases. This is because as Andean plateau elevations increase, the strengthening South American Low Level Jet transports enriched water vapor further across the Amazon basin [*Poulsen et al.*, 2010]. Additionally, simulated evaporation rates on the eastern flanks increase with increasing elevation. However, precise identification of the locations of $\delta^{18}O_{carb}$ increase relative to $\delta^{18}O_{prec}$ increase would require simulations at a higher resolution than those presented here and this mechanism does not explain the contemporaneous increase in $\delta^{18}O_{carb}$ on the western flanks (Fig. 2.8E). Increasing ice sheet size may have contributed ~1‰ to increasing $\delta^{18}O_{prec}$ since 10 Ma. Retreat of the seaway occurred before ~7 Ma and is therefore unlikely to have contributed to increases in $\delta^{18}O_{carb}$ that extend throughout the last 10 Ma.

However, the seaway could have contributed to the negative $\delta^{18}O_{carb}$ excursion observed in the eastern Bolivian Andes by Mulch [2010, Fig. 2.8D] between 10 and 7 Ma. Although an Amazonia seaway was present from ~24-7 Ma, the extent of the seaway fluctuated through time [*Hovikoski et al.*, 2007; *Uba et al.*, 2009]. Constraining the timing, extent and isotopic composition of the seaway is a critical step in determining the influence of the seaway on $\delta^{18}O_{carb}$ records. Results

show that the seaway has the potential to drive a decrease in $\delta^{18}O_{carb}$ at this location but at this time it is not possible to determine how important the seaway was to these $\delta^{18}O_{carb}$ records. It is likely that the seaway did influence the $\delta^{18}O_{carb}$ records but it may have contributed to the observed variability rather than the long term trends.

When examining $\delta^{18}O_{carb}$ records from the southern Andes it is more appropriate to use the mean annual $\delta^{18}O_{prec}$ results because DJF is not the dominant rainfall season there. CO_2 exerts the strongest control on $\delta^{18}O_{prec}$ (Figs. 2.7F – 2.7J) and we suggest that the contribution of CO_2 to $\delta^{18}O_{carb}$ from this region (Fig. 2.8H) has previously been underestimated. For example, fluctuating CO_2 levels associated with the Middle Miocene Climatic Optimum [*Kurschner et al.*, 2008; *Retallack*, 2009; *Sheldon*, 2006] may have at least contributed to the high variability seen in the $\delta^{18}O_{carb}$ record, if not the longer term trends as well.

This review of the available South American $\delta^{18}O_{carb}$ records from South America indicates that Andean uplift likely played a dominant role in determining $\delta^{18}O_{prec}$ during the last 15 Ma. Uplift of the Andes alters $\delta^{18}O_{prec}$ both as a direct result of lower temperatures at higher elevation and also through modification of regional circulation patterns. However, CO_2 levels and an inland seaway also contributed to $\delta^{18}O_{prec}$. Discounting these latter effects could lead to misinterpretations of paleoelevation and paleoclimate. Key uncertainties in making more detailed predictions about observed $\delta^{18}O_{carb}$ records using simulation results include knowledge of CO_2 levels, timing of Andean uplift and the timing and isotopic composition of seaway incursions. Terrestrial temperature records and good spatial distribution of contemporaneous $\delta^{18}O_{carb}$ records are potential avenues by which to improve constraints on the relevant controls for a particular time period.

2.5.3 Implications for paleoaltimetry data interpretation

Stable isotope paleoaltimetry techniques use modern isotopic lapse rates to infer changes in elevation from records of $\delta^{18}O_{prec}$. Paleoelevation estimates from the Andes place an important constraint on plateau formation mechanisms [*Barnes and Ehlers*, 2009; *Garzione et al.*, 2006]. Our results show that changes in global and

regional climate can complicate the extraction of paleoelevation estimates from the $\delta^{18}O_{carb}$ record. Specifically, the model results show that an underestimate of paleoelevation would be made from carbonates that formed at elevated CO_2 levels and estimates that do not account for climatic change caused by Andean surface uplift. In contrast, $\delta^{18}O_{ocean}$ changes associated with lower ice volumes would lead to paleoelevation estimates that are too high. Impacts of the seaway on paleoaltimetry depend on the timing and composition of the seaway; if the seaway were present at the time of carbonate formation, paleoelevations would again be overestimated, possibly by as much as ~1000m. For example, a shift in $\delta^{18}O_{mw}$ of 4 ‰ would be interpreted as an elevation change of 1400 m based on a modern global average lapse rate of 2.8 ‰/km [*Poage and Chamberlain*, 2001]. We note however that this number is an approximation because lapse rates have been documented to be temporally and spatially variable [*Poulsen et al.*, 2010]. A local Andean lapse rate of 2.1 ‰/km [*Gonfiantini et al.*, 2001] would yield an estimated elevation change of 1900 m for a $\delta^{18}O_{mw}$ shift of 4‰, approximately half of the modern Andean Plateau elevation. At least half of such a 4‰ shift in $\delta^{18}O_{mw}$ could be driven by changing CO_2 levels or an inland seaway incursion. If this were the case, paleo-elevation estimates would be in error by ~700-1000m or more.

2.5.4 Caveats

Like all modeling studies, this study has limitations that should be considered in evaluating the results. In comparison to most paleoclimate studies, we have used a fairly high-resolution global climate model. Nonetheless, spectral truncation reduces the maximum elevation of high, narrow mountain ranges such as the Andes, which reduces the maximum orographic precipitation and raises minimum temperatures. As a result of using an older topographic dataset, the simulated topography in the southern Andes is slightly too low, which may reduce the magnitude of simulated change in $\delta^{18}O_{prec}$ when the Andes are lowered. However, due to the spectral truncation of narrow topography, a higher elevation in the initial dataset is unlikely to make a large difference. We confirm this by comparison with a similar study that uses a higher resolution regional model with

higher topography that gives similar results in the southern Andes [*Insel et al.*, 2012]. However, the general patterns of wet or dry and cold or warm regions are well represented in the model, as are the $\delta^{18}O_{prec}$ patterns. Our use of a slab ocean model prohibits the simulation of ocean surface currents and longitudinal variations in sea surface temperatures. The distribution of sea surface temperatures are known be important to modern South American climate. For example, the Humboldt current promotes hyperaridity in the Atacama desert [*Hartley*, 2003; *Houston and Hartley*, 2003] and ENSO governs interannnual variability [*Ropelewski and Halpert*, 1987]. A more realistic SST distribution improves the simulated modern climate using GENESIS and is likely to improve the simulated $\delta^{18}O_{prec}$ distribution as well. Future simulations incorporating an ocean circulation model will help to reduce this uncertainty. The vegetation in our simulations is prescribed as modern. Important climatic processes such as moisture recycling in the Amazon region depend on vegetation properties. Given the amount of climatic change simulated, it is likely that the vegetation patterns have also changed. Such vegetation changes are unlikely to have large direct impacts on $\delta^{18}O_{prec}$ but may influence the climate, and thus indirectly $\delta^{18}O_{prec}$. Finally, uncertainties in the paleoclimate record of the boundary conditions and their implementation in the model lead to uncertainties in the interpretation of $\delta^{18}O_{carb}$. In particular, improved knowledge of past atmospheric CO_2 levels and the nature and timing of the inland seaway would provide better constraints on potential causes of $\delta^{18}O_{carb}$ shifts.

2.6 CONCLUSIONS

Our results indicate that both global and regional factors have significantly modified the climate and $\delta^{18}O_{prec}$ of South America during the Cenozoic. Precipitation rates are modified by changes in elevation and higher precipitation rates are caused by the presence of the South American inland seaway in the mid to late Miocene.

$\delta^{18}O_{prec}$ is sensitive to Cenozoic climate and environmental change. In particular, $\delta^{18}O_{prec}$ is expected to have decreased over most of the continent through the Cenozoic, except in the Amazon basin, due to increasing Andean elevation and

decreasing atmospheric CO_2. This trend is partially counteracted by an increase in $\delta^{18}O_{ocean}$ as a consequence of ice sheet formation. An excursion toward more negative $\delta^{18}O_{prec}$ is predicted during the mid-late Miocene when an inland seaway was present. Uncertainty in the timing, extent and isotopic composition of the South American inland seaway limits our ability to predict the impact of the seaway on $\delta^{18}O_{carb}$ records. $\delta^{18}O_{prec}$ is more sensitive to changes in CO_2 at higher elevations [*Poulsen and Jeffery*, 2011]. Thus as Andean elevation has increased $\delta^{18}O_{prec}$ has become more sensitive to smaller changes in CO_2.

Existing stable isotope records of $\delta^{18}O_{prec}$ are consistent with predictions of changes in $\delta^{18}O_{prec}$ due to Andean uplift and associated climate change. However, these records are also consistent with Andean uplift accompanied by changing CO_2 levels and inland seaway incursions, as well as local changes in temperature and evaporation rates. We therefore suggest alternative explanations for existing records, quantify uncertainties in paleoelevation estimates, and show that it is necessary to consider all of these factors when interpreting Cenozoic records of $\delta^{18}O_{prec}$ in South America.

2.7 ACKNOWLEDGEMENTS

This work was funded by grants to C.J.P. and T.A.E. from NSF (EAR Awards 0738822 and 0907817) and the University of Michigan's Graham Environmental Sustainability Institute. M.L.J. was also supported by a University of Michigan, Rackham International Student Fellowship. *NCEP Reanalysis and CMAP Precipitation data provided by the NOAA/OAR/ESRL PSD, Boulder, Colorado, USA, from their Web site at http://www.esrl.noaa.gov/psd/.* This research benefited from discussions with Nadja Insel. We are grateful for comments by Page Chamberlain and an anonymous reviewer that helped to improve this manuscript.

2.8 REFERENCES

(IAEA/WMO), I. A. E. A.-W. M. O. Global network of isotopes in precipitation: The GNIP database, edited.

Allmendinger, R. W., T. E. Jordan, S. M. Kay, and B. L. Isacks (1997), The evolution of the Altiplano-Puna plateau of the Central Andes, *Annual Review of Earth and Planetary Sciences*, *25*, 139-174

Aravena, R., O. Suzuki, H. Pena, A. Pollastri, H. Fuenzalida, and A. Grilli (1999), Isotopic composition and origin of the precipitation in Northern Chile, *Applied Geochemistry*, *14*(4), 411-422

Barke, R., and S. Lamb (2006), Late Cenozoic uplift of the Eastern Cordillera, Bolivian Andes, *Earth and Planetary Science Letters*, *249*(3-4), 350-367.10.1016/j.epsl.2006.07.012

Barnes, J. B., and T. A. Ehlers (2009), End member models for Andean Plateau uplift, *Earth-Science Reviews*, *97*(1-4), 105-132.10.1016/j.earscirev.2009.08.003

Barnes, J. B., T. A. Ehlers, N. McQuarrie, P. B. O'Sullivan, and J. D. Pelletier (2006), Eocene to recent variations in erosion across the central Andean fold-thrust belt, northern Bolivia: Implications for plateau evolution, *Earth and Planetary Science Letters*, *248*(1-2), 118-133.10.1016/j.epsl.2006.05.018

Barnes, J. B., T. A. Ehlers, N. McQuarrie, P. B. O'Sullivan, and S. Tawackoli (2008), Thermochronometer record of central Andean plateau growth, Bolivia (19.5 degrees S), *Tectonics*, *27*(3).10.1029/2007tc002174

Bershaw, J., C. N. Garzione, P. Higgins, B. J. MacFadden, F. Anaya, and H. Alvarenga (2010), Spatial-temporal changes in Andean plateau climate and elevation from stable isotopes of mammal teeth, *Earth and Planetary Science Letters*, *289*(3-4), 530-538.10.1016/j.epsl.2009.11.047

Blisniuk, P. M., L. A. Stern, C. P. Chamberlain, B. Idleman, and P. K. Zeitler (2005), Climatic and ecologic changes during Miocene surface uplift in the Southern Patagonian Andes, *Earth and Planetary Science Letters*, *230*(1-2), 125-142.10.1016/j.epsl.2004.11.015

Blisniuk, P. M., L. A. Stern, C. P. Chamberlain, P. K. Zeitler, V. A. Ramos, E. R. Sobel, M. Haschke, M. R. Strecker, and F. Warkus (2006), Links between Mountain Uplift, Climate, and Surface Processes in the Southern Patagonian Andes, in *The Andes - Active Subduction Orogeny*, edited by O. Oncken, G. Chong, G. Franz, P. Giese, H.-J. Götze, V. A. Ramos, M. R. Strecker and P. Wigger, pp. 429 - 440, Springer.

Bookhagen, B., and M. R. Strecker (2008), Orographic barriers, high-resolution TRMM rainfall, and relief variations along the eastern Andes, *Geophysical Research Letters*, *35*(6), 6.10.1029/2007gl032011

Bookhagen, B., and M. R. Strecker (2012), Spatiotemporal trends in erosion rates across a pronounced rainfall gradient: Examples from the southern Central Andes, *Earth and Planetary Science Letters*, *327*, 97 - 110.10.1016/j.epsl.2012.02.005

Campetella, C. M., and C. S. Vera (2002), The influence of the Andes mountains on the South American low-level, *Geophysical Research Letters*, *29*(17).10.1029/2002gl015451

Cooper, M. A., et al. (1995), Basin development and tectonic history of the Llanos Basin, Eastern Cordillera, and middle Magdalena Valley, Colombia, edited, pp. 1421-1443, American Association of Petroleum Geologists, Tulsa, OK.

Craig, H., and L. I. Gordon (1965), Deuterium and oxygen 18 variations in the ocean and marine atmosphere, paper presented at Stable Isotopes ion Oceanography Studies and Paleotemperatures, Laboratorio di Geologia Nucleare, Pisa.

Dansgaard, W. (1964), Stable isotopes in precipitation, *Tellus*, *16*(4), 436-468

DeCelles, P. G., and B. K. Horton (2003), Early to middle Tertiary foreland basin development and the history of Andean crustal shortening in Bolivia, *Geological Society of America Bulletin*, *115*(1), 58-77

Demicco, R. V., T. K. Lowenstein, and L. A. Hardie (2003), Atmospheric pCO(2) since 60 Ma from records of seawater pH, calcium, and primary carbonate mineralogy, *Geology*, *31*(9), 793-796

Dorman, J. L., and P. J. Sellers (1989), A global climatology of albedo, roughness length and stomatal-resistance for atmsopheric general-circulation models as represented by the simple biosphere model (SIB), *Journal of Applied Meteorology*, *28*(9), 833-855

Ehlers, T. A., and C. J. Poulsen (2009), Influence of Andean uplift on climate and paleoaltimetry estimates, *Earth and Planetary Science Letters*, *281*(3-4), 238-248.10.1016/j.epsl.2009.02.026

Ehrmann, W. U., and A. Mackensen (1992), Sedimentological evidence for the formation of an East Antarctic ice-sheet in Eocene Oligocene time, *Palaeogeography Palaeoclimatology Palaeoecology*, *93*(1-2), 85-112

Epstein, S., and T. Mayeda (1953), Variation of ^{18}O content of waters from natural sources, *Geochimica Et Cosmochimica Acta*, *4*(5), 213-224

Ferronsky, V. I., and V. S. Brezgunov (1989), Stable isotopes and ocean dynamics, in *Handbook of Environmental Isotope Geochemistry*, edited by P. Fritz and J. Fontes, pp. 1-73, Elsevier Science, New York.

Frailey, C. D., E. L. Lavina, A. Rancy, and J. P. de Souza Filho (1988), A proposed Pleistocene/Holocene lake in the Amazon basin and its significance to Amazonian geology and biogeography, *Acta Amazonica*, *18*, 119-143

Garzione, C., G. D. Hoke, J. C. Libarkin, S. Withers, B. J. MacFadden, J. Eiler, P. Ghosh, and A. Mulch (2008), Rise of the Andes, *Science*, *320*(5881), 1304-1307. 10.1126/science.1148615

Garzione, C. N., and G. D. Hoke (2006), Paleoelevation and geomorphic constraints on the late miocene rise of the andes: Geodynamic implications for the growth of orogenic plateaus, *Geochimica Et Cosmochimica Acta*, *70*(18), A195-A195.10.1016/j.gca.2006.06.393

Garzione, C. N., P. Molnar, J. C. Libarkin, and B. J. MacFadden (2006), Rapid late Miocene rise of the Bolivian Altiplano: Evidence for removal of mantle lithosphere, *Earth and Planetary Science Letters*, *241*(3-4), 543-556.10.1016/j.epsl.2005.11.026

Garzione, C. N., G. D. Hoke, J. C. Libarkin, S. Withers, B. MacFadden, J. Eiler, P. Ghosh, and A. Mulch (2008), Rise of the Andes, *Science*, *320*(5881), 1304-1307.10.1126/science.1148615

Gat, J. R. (1996), Oxygen and hydrogen isotopes in the hydrologic cycle, *Annual Review of Earth and Planetary Sciences*, *24*, 225-262

GEOSECS, A., Pacific and Indian Ocean expeditions (1987), *Shore-based data and graphics*, National Science Foundation, Washington, D.C.

Ghosh, P., C. N. Garzione, and J. M. Eiler (2006), Rapid uplift of the Altiplano revealed through C-13-O-18 bonds in paleosol carbonates, *Science*, *311*(5760), 511-515.10.1126/science.1119365

Gingras, M. K., M. E. Rasanen, S. G. Pemberton, and L. P. Romero (2002), Ichnology and sedimentology reveal depositional characteristics of bay-margin parasequences in the Miocene Amazonian foreland basin, *Journal of Sedimentary Research*, *72*(6), 871-883

Giovanni, M. K., B. K. Horton, C. Garzione, B. McNulty, and M. Grove (2010a), Extensional basin evolution in the Cordillera Blanca, Peru: Stratigraphic and isotopic records of detachment faulting and orogenic collapse in the Andean hinterland, *Tectonics*, *29*.10.1029/2010TC002666

Giovanni, M. K., B. K. Horton, C. N. Garzione, B. McNulty, and M. Grove (2010b), Extensional basin evolution in the Cordillera Blanca, Peru: Stratigraphic and isotopic records of detachment faulting and orogenic collapse in the Andean hinterland, *Tectonics*, *29*.10.1029/2009TC002583

Gomez, E., T. E. Jordan, R. W. Allmendinger, and N. Cardozo (2005), Development of the Colombian foreland-basin system as a consequence of diachronous exhumation of the northern Andes, *Geological Society of America Bulletin*, *117*(9-10), 1272-1292.10.1130/b25456.1

Gonfiantini, R., M. A. Roche, J. C. Olivry, J. C. Fontes, and G. M. Zuppi (2001), The altitude effect on the isotopic composition of tropical rains, *Chemical Geology*, *181*(1-4), 147-167

Hartley, A. J. (2003), Andean uplift and climate change, *Journal of the Geological Society*, *160*, 7-10

Hernandez, R. M., T. E. Jordan, A. D. Farjat, L. Echavarria, B. D. Idleman, and J. H. Reynolds (2005), Age, distribution, tectonics, and eustatic controls of the Paranense and Caribbean marine transgressions in southern Bolivia and Argentina, *Journal of South American Earth Sciences*, *19*(4), 495-512.10.1016/j.jsames.2005.06.007

Hoke, G. D., B. L. Isacks, T. E. Jordan, N. Blanco, A. J. Tomlinson, and J. Ramezani (2007), Geomorphic evidence for post-10 Ma uplift of the western flank of the central Andes 18 degrees 30'-22 degrees S, *Tectonics*, *26*(5).10.1029/2006tc002082

Hoke, G. D., C. N. Garzione, D. C. Araneo, C. Latorre, M. R. Strecker, and K. J. Williams (2009), The stable isotope altimeter: Do Quaternary pedogenic carbonates predict modern elevations?, *Geology*, *37*(11), 1015-1018.10.1130/g30308a.1

Hoorn, C. (2006), Mangrove forests and marine incursions in neogene Amazonia (Lower Apaporis River, colombia), *Palaios*, *21*(2), 197-209.10.2110/palo.2005.p05-131

Hoorn, C., F. P. Wesselingh, J. Hovikoski, and J. Guerrero (2010), The development of the Amazonian mega-wetland (Miocene; Brazil, Colombia, Peru, Bolivia), in *Amazonia, Landscape and Species Evolution: A look into the Past*, edited by C. Hoorn and F. P. Wesselingh, pp. 123 - 142, Blackwell Publishing.

Horton, B. K. (1999), Erosional control on the geometry and kinematics of thrust belt development in the central Andes, *Tectonics*, *18*(6), 1292-1304.10.1029/1999TC900051

Houston, J., and A. J. Hartley (2003), The central andean west-slope rainshadow and its potential contribution to the origin of hyper-aridity in the Atacama desert, *Int. J. Climatol.*, *23*(12), 1453-1464.10.1002/joc.938

Hovikoski, J., F. P. Wesselingh, M. Rasanen, M. Gingras, and H. B. Vonhof (2010), Marine influence in Amazonia: evidence from the geological record, in *Amazonia, Landscape and Species Evolution: A Look into the Past*, edited by C. Hoorn and F. P. Wesselingh, pp. 143 - 161, Blackwell Publishing.

Hovikoski, J., M. Rasanen, M. Gingras, M. Roddaz, S. Brusset, W. Hermoza, and L. R. Pittman (2005), Miocene semidiurnal tidal rhythmites in Madre de dios, Peru, *Geology*, *33*(3), 177-180

Hovikoski, J., et al. (2007), The nature of Miocene Amazonian epicontinental embayment: High-frequency shifts of the low-gradient coastline, *Geological Society of America Bulletin*, *119*(11-12), 1506-1520

Insel, N., C. J. Poulsen, and T. A. Ehlers (2009), Influence of the Andes Mountains on South American moisture transport, convection and precipitation, *Climate Dynamics*.10.1007/s00382-009-0637-1

Insel, N., C. J. Poulsen, and T. A. Ehlers (2010a), Influence of the Andes Mountains on South American moisture transport, convection, and precipitation, *Climate Dynamics*, *35*(7-8), 1477-1492.10.1007/s00382-009-0637-1

Insel, N., C. J. Poulsen, T. A. Ehlers, and C. Sturm (2012), Response of meteoric $\delta^{18}O$ to surface uplift - Implications for Cenozoic Andean Plateau growth, *Earth and Planetary Science Letters*, *317 - 318*, 262-272.10.1016/j.epsl.2011.11.039

Insel, N., T. A. Ehlers, M. Schaller, J. B. Barnes, S. Tawackoli, and C. J. Poulsen (2010b), Spatial and temporal variability in denudation across the Bolivian Andes from multiple geochronometers, *Geomorphology*, *122*(1-2), 65-77.10.1016/j.geomorph.2010.05.014

Isacks, B. L. (1988), Uplift of the central Andean plateau and bending of the Bolivian orocline, *Journal of Geophysical Research-Solid Earth and Planets*, *93*(B4), 3211-3231

Jeffery, M. L., C. J. Poulsen, and T. A. Ehlers (2012), Impacts of Cenozoic global cooling, surface uplift, and an inland seaway on South American paleoclimate and precipitation $\delta^{18}O$, *Geological Society of America Bulletin*, *124*(3-4), 335-351.10.1130/B30467.1

Kalnay, E., et al. (1996), The NCEP/NCAR 40-year reanalysis project, *Bulletin of the American Meteorological Society*, *77*(3), 437-471

Kim, S. T., and J. R. Oneil (1997), Equilibrium and nonequilibrium oxygen isotope effects in synthetic carbonates, *Geochimica Et Cosmochimica Acta*, *61*(16), 3461-3475

Kleinert, K., and M. R. Strecker (2001), Climate change in response to orographic barrier uplift: Paleosol and stable isotope evidence from the late Neogene Santa Maria basin, northwestern Argentina, *Geological Society of America Bulletin*, *113*(6), 728-742

Knutti, R., G. A. Meehl, M. R. Allen, and D. A. Stainforth (2006), Constraining climate sensitivity from the seasonal cycle in surface temperature, *Journal of Climate*, *19*(17), 4224-4233

Koons, P. O. (1990), The two‐sided orogen: Collision and erosion from the sand box to the Southern Alps, New Zealand. , *Geology*, *18*(8), 679–682.10.1130/0091-7613(1990)018<0679:TSOCAE>2.3.CO;2

Kurschner, W. M., Z. Kvacek, and D. L. Dilcher (2008), The impact of Miocene atmospheric carbon dioxide fluctuations on climate and the evolution of terrestrial ecosystems, *Proceedings of the National Academy of Sciences of the United States of America*, *105*(2), 449-453.10.1073/pnas.0708588105

Latorre, C., J. Quade, and W. C. McIntosh (1997), The expansion of C-4 grasses and global change in the late Miocene: Stable isotope evidence from the Americas, *Earth and Planetary Science Letters*, *146*(1-2), 83-96

Latrubesse, E. M., M. Cozzuol, S. A. F. da Silva-Caminha, C. A. Rigsby, M. L. Absy, and C. Jaramillo (2010), The Late Miocene paleogeography of the Amazon Basin and the evolution of the Amazon River system, *Earth-Science Reviews*, *99*(3-4), 99-124.10.1016/j.earscirev.2010.02.005

Lear, C. H., H. Elderfield, and P. A. Wilson (2000), Cenozoic deep-sea temperatures and global ice volumes from Mg/Ca in benthic foraminiferal calcite, *Science*, *287*(5451), 269-272

Lenters, J. D., and K. H. Cook (1995), Simulation and diagnosis of the regional summertime precipitation climatology of South America, *Journal of Climate*, *8*(12), 2988-3005

Lovejoy, N. R., J. S. Albert, and W. G. R. Crampton (2006), Miocene marine incursions and marine/freshwater transitions: Evidence from Neotropical fishes, *Journal of South American Earth Sciences*, *21*(1-2), 5-13.10.1016/j.jsames.2005.07.009

Masek, J. G., B. L. Isacks, T. L. Gubbels, and E. J. Fielding (1994), Erosion and tectonics at the margins of continental plateaus, *Journal of Geophysical Research*, *99*(B7), 13941-13956.10.1029/94JB00461

Mathieu, R., D. Pollard, J. E. Cole, J. W. C. White, R. S. Webb, and S. L. Thompson (2002), Simulation of stable water isotope variations by the GENESIS GCM for modern conditions, *Journal of Geophysical Research-Atmospheres*, *107*(D4).4037, 10.1029/2001jd900255

Matthews, R. K., and R. Z. Poore (1980), Tertiary $\delta^{18}O$ record and glacio-eustatic sea-level fluctuations, *Geology*, *8*(10), 501-504

McQuarrie, N. (2002), The kinematic history of the central Andean fold-thrust belt, Bolivia: Implications for building a high plateau, *Geological Society of America Bulletin*, *114*(8), 950-963

McQuarrie, N., J. B. Barnes, and T. A. Ehlers (2008a), Geometric, kinematic, and erosional history of the central Andean Plateau, Bolivia (15-17 degrees S), *Tectonics*, *27*(3).10.1029/2006tc002054

McQuarrie, N., T. A. Ehlers, J. B. Barnes, and B. Meade (2008b), Temporal variation in climate and tectonic coupling in the central Andes, *Geology*, *36*(12), 999-1002.10.1130/g25124a.1

McQuarrie, N., B. K. Horton, G. Zandt, S. Beck, and P. G. DeCelles (2005), Lithospheric evolution of the Andean fold-thrust belt, Bolivia, and the origin of the central Andean plateau, *Tectonophysics*, *399*(1-4), 15-37.10.1016/j.tecto.2004.12.013

Miller, K. G., R. G. Fairbanks, and G. S. Mountain (1987), Tertiary oxygen isotope sythesis, sea-level history, and continental margin erosion, *Paleoceanography*, *2*, 1 - 19

Molnar, P., and C. N. Garzione (2007), Bounds on the viscosity coefficient of continental lithosphere from removal of mantle lithosphere beneath the Altiplano and Eastern Cordillera, *Tectonics*, *26*(2).10.1029/2006tc001964

Montgomery, D. R., G. Balco, and S. D. Willett (2001), Climate, tectonics, and the morphology of the Andes, *Geology*, *29*(7), 579-582.10.1130/0091-7613(2001)029<0579:CTATMO>2.0.CO;2

Mulch, A., C. E. Uba, M. R. Strecker, R. Schoenberg, and C. P. Chamberlain (2010), Late Miocene climate variability and surface elevation in the central Andes, *Earth and Planetary Science Letters*, *290*(1-2), 173-182.10.1016/j.epsl.2009.12.019

Murphy, J. M., D. M. H. Sexton, D. N. Barnett, G. S. Jones, M. J. Webb, and M. Collins (2004), Quantification of modelling uncertainties in a large ensemble of climate change simulations, *Nature*, *430*(7001), 768-772.10.1038/nature02771

Norton, K., and F. Schlunegger (2011), Migrating deformation in the central Andes from enhanced orographic rainfall, *Nature Communications*, *2*(484).10.1038/ncomms1590

Pagani, M., J. C. Zachos, K. H. Freeman, B. Tipple, and S. Bohaty (2005), Marked decline in atmospheric carbon dioxide concentrations during the Paleogene, *Science*, *309*(5734), 600-603.10.1126/science.1110063

Parra, M., A. Mora, C. Jaramillo, V. Torres, G. Zeilinger, and M. R. Strecker (2010), Tectonic controls on Cenozoic foreland basin development in the north-eastern Andes, Colombia, *Basin Research*, *22*(6), 874-903.10.1111/j.1365-2117.2009.00459.x

Pearson, P. N., and M. R. Palmer (2000), Atmospheric carbon dioxide concentrations over the past 60 million years, *Nature*, *406*(6797), 695-699

Pearson, P. N., G. L. Foster, and B. S. Wade (2009), Atmospheric carbon dioxide through the Eocene-Oligocene climate transition, *Nature*, *461*(7267), 1110-U1204.10.1038/nature08447

Poage, M. A., and C. P. Chamberlain (2001), Empirical relationships between elevation and the stable isotope composition of precipitation and surface waters: Considerations for studies of paleoelevation change, *American Journal of Science*, *301*(1), 1-15

Poulsen, C. J., T. A. Ehlers, and N. Insel (2010), Onset of Convective Rainfall During Gradual Late Miocene Rise of the Central Andes, *Science*, *328*(5977), 490-493.10.1126/science.1185078

Quade, J., T. E. Cerling, and J. R. Bowman (1989), Systematic variations in the carbon and oxygen isotopic composition of pedogenic carbonate along elevation transects in the southern Great Basin, United States, *Geological Society of America Bulletin*, *101*(4), 464-475.10.1130/0016-7606(1989)101<0464:SVITCA>2.3.CO;2

Quade, J., C. N. Garzione, and J. Eiler (2007), Paleoelevation reconstruction using pedogenic carbonates, in *Paleoaltimetry: Geochemical and Thermodynamic Approaches*, edited, pp. 53-87.

Ramos, V. A., E. O. Cristallini, and D. J. Perez (2002), The Pampean flat-slab of the Central Andes, *Journal of South American Earth Sciences*, *15*(1), 59-78

Rasanen, M. E., A. M. Linna, J. C. R. Santos, and F. R. Negri (1995), Late Miocene tidal deposits in the Amazonian foreland basin, *Science*, *269*(5222), 386-390

Rech, J. A., B. S. Currie, E. D. Shullenberger, S. P. Dunagan, T. E. Jordan, N. Blanco, A. J. Tomlinson, H. D. Rowe, and J. Houston (2010), Evidence for the development of the Andean rain shadow from a Neogene isotopic record in the Atacama Desert, Chile, *Earth and Planetary Science Letters*, *292*(3-4), 371-382.10.1016/j.epsl.2010.02.004

Retallack, G. J. (2009), Refining a pedogenic-carbonate CO2 paleobarometer to quantify a middle Miocene greenhouse spike, *Palaeogeography Palaeoclimatology Palaeoecology*, *281*(1-2), 57-65, 10.1016/j.palaeo.2009.07.011

Ropelewski, C. F., and M. S. Halpert (1987), Global and regional scale precipitation patterns associated with the El-Nino Southern Oscillation, *Mon. Weather Rev.*, *115*(8), 1606-1626

Royer, D. L. (2006), CO2-forced climate thresholds during the Phanerozoic, *Geochimica Et Cosmochimica Acta*, *70*(23), 5665-5675.10.1016/j.gca.2005.11.031

Rozanski, K., L. Araguds-Araguds, and R. Gonfiantini (1993), Isotopic patterns in modern global precipitation, edited by P. K. Swart, K. C. Lohmann, J. McKenzie and S. Savin, pp. 1-36, American Geophysical Union.

Safran, E. B., P. R. Bierman, R. Aalto, T. Dunne, K. Whipple, and M. Caffee (2005), Erosion rates driven by channel network incision in the Bolivian Andes, *Earth Surface Processes and Landforms*, *30*(8), 1007-1024.10.1002/esp.1259

Salati, E., D. O. Attilio, E. Matsui, and J. R. Gat (1979), Recycling of water in the Amazon Basin: An isotopic study, *Water Resources Research*, *15*(5), 1250 - 1258

Schildgen, T. F., K. V. Hodges, K. X. Whipple, P. W. Reiners, and M. S. Pringle (2007), Uplift of the western margin of the Andean plateau revealed from canyon incision history, southern Peru, *Geology*, *35*(6), 523-526.10.1130/g23532a.1

Schildgen, T. F., T. A. Ehlers, D. M. Whipp, M. C. van Soest, K. X. Whipple, and K. V. Hodges (2009), Quantifying canyon incision and Andean Plateau surface uplift, southwest Peru: A thermochronometer and numerical modeling approach, *Journal of Geophysical Research-Earth Surface*, *114*.10.1029/2009jf001305

Sheldon, N. D. (2006), Using paleosols of the Picture Gorge Basalt to reconstruct the middle Miocene climatic optimum, *Paleobios 26*(2), 27-36

Siegert, M. J., P. Barrett, R. Decont, R. Dunbar, C. O. Cofaigh, S. Passchier, and T. Naish (2008), Recent advances in understanding Antarctic climate evolution, *Antarctic Science*, *20*(4), 313-325.10.1017/s0954102008000941

Sloan, L. C., T. J. Crowley, and D. Pollard (1996), Modeling of middle pliocene climate with the NCAR GENESIS general circulation model, *Marine Micropaleontology*, *27*(1-4), 51-61

Smith, A. G., A. M. Hurley, and J. C. Briden (1981), *Phanerozoic paleocontinental world maps*, 107 pp., Cambridge University Press.

Stern, L. A., and P. M. Blisniuk (2002), Stable isotope composition of precipitation across the southern Patagonian Andes, *Journal of Geophysical Research-Atmospheres*, *107*(D23).4667, 10.1029/2002jd002509

Sturm, C., G. Hoffmann, and B. Langmann (2007), Simulation of the stable water isotopes in precipitation over South America: Comparing regional to global circulation models, *Journal of Climate*, *20*(15), 3730-3750

Taboada, A., L. A. Rivera, A. Fuenzalida, A. Cisternas, H. Philip, H. Bijwaard, J. Olaya, and C. Rivera (2000), Geodynamics of the northern Andes: Subductions and intracontinental deformation (Colombia), *Tectonics*, *19*(5), 787-813

Tao, W. C., and R. J. O'Connell (1992), Ablative Subduction: A two-sided Alternative to the Conventional Subduction Model, *Journal of Geophysical Research - Solid Earth and Planets*, *97*(B6), 8877-8904.10.1029/91JB02422

Thompson, S. L., and D. Pollard (1995), A global climate model (GENESIS) with a land-surface transfer scheme (LSX). 1. Present climate simulation, *Journal of Climate*, *8*(4), 732-761

Thompson, S. L., and D. Pollard (1997), Greenland and Antarctic mass balances for present and doubled atmospheric CO2 from the GENESIS version-2 global climate model, *Journal of Climate*, *10*(5), 871-900

Thomson, S., F. Hervé, and B. Stöckhert (2001), Mesozoic‐Cenozoic denudation history of the Patagonian Andes (southern Chile) and its correlation to different subduction processes, *Tectonics*, *20*(5), 693-711.10.1029/2001TC900013

Uba, C. E., C. A. Hasler, L. A. Buatois, A. K. Schmitt, and B. Plessen (2009), Isotopic, paleontologic, and ichnologic evidence for late Miocene pulses of marine incursions in the central Andes, *Geology*, *37*(9), 827-830.10.1130/g30014a.1

Vuille, M., R. S. Bradley, M. Werner, R. Healy, and F. Keimig (2003), Modeling delta O-18 in precipitation over the tropical Americas: 1. Interannual variability and climatic controls, *Journal of Geophysical Research-Atmospheres*, *108*(D6), 4174, 10.1029/2001jd002038

Wesselingh, F. P., R. J. G. Kaandorp, H. B. Vonhof, M. Rasanen, and W. Renema (2006), The nature of aquatic landscapes in the Miocene of western Amazonia: an integrated palaeontological and geochemical approach, *Scripta Geologica*(133), 363-393

Wesselingh, F. P., M. E. Rasanen, G. Irion, H. B. Vonhof, R. J. G. Kaandorp, W. Renema, L. Romero Pittman, and M. Gingras (2002), Lake Pebas: A palaeoecological reconstruction of a Miocene, long-lived lake complex in western Amazonia, *Cainozoic Research*, *1*, 35-81

Whipple, K. X. (2009), The influence of climate on the tectonic evolution of mountain belts, *Nature Geoscience*, *2*(2), 97-104.10.1038/ngeo413

Willett, S. D. (1999), Orogeny and orography: The effects of erosion on the structure of mountain belts, *Journal of Geophysical Research-Solid Earth*, *104*(B12), 28957-28981.10.1029/1999jb900248

Willett, S. D., C. Beaumont, and P. Fullsack (1993), Mechanical model for the tectonics of doubly vergent compressional orogens. , *Geology*, *21*, 371-374.10.1130/0091-7613(1993)021<0371:MMFTTO>2.3.CO;2

Xie, P. P., and P. A. Arkin (1997), Global precipitation: A 17-year monthly analysis based on gauge observations, satellite estimates, and numerical model outputs, *Bulletin of the American Meteorological Society*, *78*(11), 2539-2558

Zachos, J. C., J. R. Breza, and S. W. Wise (1992), Early Oligocene ice-sheet expansion on Antarctica - stable isotope and sedimentological evidence from Kerguelen Plateau, southern Indian-Ocean, *Geology*, *20*(6), 569-573

Zhou, J., C. J. Poulsen, D. Pollard, and T. S. White (2008), Simulation of modern and middle Cretaceous marine delta O-18 with an ocean-atmosphere general circulation model, *Paleoceanography*, *23*(3). Pa3223, 10.1029/2008pa001596

CHAPTER 3

QUANTIFYING THE ROLE OF PALEOCLIMATE AND ANDEAN PLATEAU UPLIFT ON RIVER INCISION[2]

Abstract

River incision over geologic time scales can be a valuable indicator of regional surface uplift. However, extracting the timing of surface uplift relative to the onset of incision is complicated by changes in precipitation commensurate with topographic development. Evidence of large-scale river incision on the flanks of the Andean plateau has been cited in support of a rapid and recent surface uplift event. Recent climate modeling studies demonstrate large magnitudes of regional climate change associated with surface uplift of the Andes, which may have influenced river incision processes. Here we present an analysis of mid-Miocene (16 Ma) to Present river incision of the southwest Peruvian Ocoña River. A Monte Carlo approach with $\sim 1.6 \times 10^5$ different simulations is used to explore the range of surface uplift and paleoclimate histories that are compatible with the modern river profile and geological constraints on the incision timing and magnitude. A range of channel properties, including channel width parameterization, erodibility coefficient, and erosion threshold, are considered. Results indicate that deep canyon incision on the plateau flanks may not be as diagnostic of rapid surface uplift as previously thought. More specifically, the evolution of the Ocoña River is consistent with local plateau elevations of 1-3 km at 16 Ma, and either a steady or punctuated uplift of 1.5 – 3.5

[2] Citation:
Jeffery, M. L., T. A. Ehlers, B. J. Yanites, and C. J. Poulsen (accepted) Quantifying the role of paleoclimate and Andean Plateau uplift on river incision, *Journal of Geophyscial Research – Earth Surface,* 2012JF002533

km since then. The range of acceptable uplift histories is sensitive to the magnitude and temporal evolution of precipitation. Similar paleoprecipitation changes are expected to have modified river profile evolution elsewhere in the Andes.

3.1 INTRODUCTION

Bedrock river profiles are sensitive to tectonics, climate, and the internal dynamics of rivers such as channel width variation or river capture [*Roe et al.*, 2003; *Whipple*, 2009]. Analysis of modern river profiles is a useful tool for quantifying interactions of these processes over million year time scales. For example, records of river incision have been used to infer shifts in climate, discrete uplift events, and large-scale changes in catchment geometry [e.g. *Attal et al.*, 2008; *Clark et al.*, 2004; *Crosby and Whipple*, 2006; *Duvall et al.*, 2004; *Kirby and Whipple*, 2001; *Snyder et al.*, 2000; *Whipple and Tucker*, 1999; *Whittaker et al.*, 2008; *Yanites et al.*, 2010]. Constraining the timing of surface uplift is an important but challenging goal in the study of orogen development. Geological constraints on the timing and magnitude of river incision can constrain surface uplift because a change in relative base level (e.g. surface uplift) can drive incision of a comparable depth. However, precipitation can also play a significant role in shaping the landscape by modifying river discharge and erosion [*Roe et al.*, 2003; *Whipple*, 2009; *Willett*, 1999]. The spatial distribution of precipitation modifies the shape of steady-state longitudinal river profiles [*Roe et al.*, 2002; *Wu et al.*, 2006], and increases in mean annual precipitation can drive river incision by decreasing the gradient of river profiles [*Wobus et al.*, 2010; *Zaprowski et al.*, 2005]. Regional climate can be strongly modified by mountain belt development and surface uplift [e.g., *Kutzbach et al.*, 1989; *Roe*, 2005]. Consequently, tectonics and climate are inter-dependent controls on the development of fluvial landscapes.

The surface uplift history of the central Andes is unresolved, with end-member models that include (1) a 'slow and steady' uplift of ~4 km since ~40 Ma, and (2) a 'punctuated' uplift with a rapid rise of ~2.5 km between 10 and 6 Ma [*Barnes and Ehlers*, 2009; *Ehlers and Poulsen*, 2009; *Garzione and Hoke*, 2006]. Deeply incised canyons on both flanks of the Central Andean Plateau have the

potential to help distinguish between these two models. Estimates of incision magnitudes have been derived from a variety of techniques including thermochronometry, paleosurface degradation, and analysis based on river profile knick-point migration [*Barke and Lamb*, 2006; *Barnes et al.*, 2006; *M Farias et al.*, 2008; *Garzione et al.*, 2006; *Gubbels et al.*, 1993; *Hartley et al.*, 2007; *Hoke et al.*, 2007; *Kennan et al.*, 1997; *Kober et al.*, 2006; *McQuarrie et al.*, 2008a; *McQuarrie et al.*, 2008b; *Schildgen et al.*, 2010; *Schildgen et al.*, 2007; *Schildgen et al.*, 2009a; *Schildgen et al.*, 2009b; *Schlunegger et al.*, 2006; *Simpson*, 2004; *Walcek and Hoke*, 2012]. Incision magnitudes range from 0.25–3 km and, in most cases, incision began in the late Miocene (10–5 Ma) suggesting a contemporaneous, regional scale driver such as surface uplift of the plateau. The largest incision estimates are for the Maran-Cotahuasi-Ocoña catchment (hereafter, Ocoña) in southwestern Peru (14–16° S, Fig. 1A) where thermochronometry and $^{40}Ar/^{39}Ar$ dated, valley filling, ignimbrite flows indicate >2.5 km incision since ~9 Ma [*Gunnell et al.*, 2010; *Schildgen et al.*, 2010; *Schildgen et al.*, 2007; *Schildgen et al.*, 2009b; *Thouret et al.*, 2007]. In many cases, a distinction between different plateau surface uplift models cannot be made based on incision timing and magnitudes because the observations can fit either model within error [*Barnes and Ehlers*, 2009]. Incision depths and rates in the Ocoña catchment require surface uplift of ~2.4 – 3 km since 14 Ma [*Schildgen et al.*, 2009a].

However, recently it has been suggested that the late Miocene incision was not driven by rapid surface uplift, but rather by an increase in precipitation rates [*Barnes and Ehlers*, 2009; *Ehlers and Poulsen*, 2009]. At plateau elevations greater than ~50% of the modern; Andean topography blocks westerly flow, convective precipitation is initiated on the eastern flanks, and a rain shadow develops on the western flanks [*Campetella and Vera*, 2002; *Ehlers and Poulsen*, 2009; *Insel et al.*, 2010; *Lenters and Cook*, 1995; *Poulsen et al.*, 2010]. Convective precipitation initiated on the eastern flanks of the Andes reaches the headwaters of the larger catchments on the western flanks. Previous studies have demonstrated that modern river profiles, catchment scale erosion rates and drainage basin morphology reflect spatial variations in modern precipitation rates [*Abbuehl et al.*, 2011; *Bookhagen*

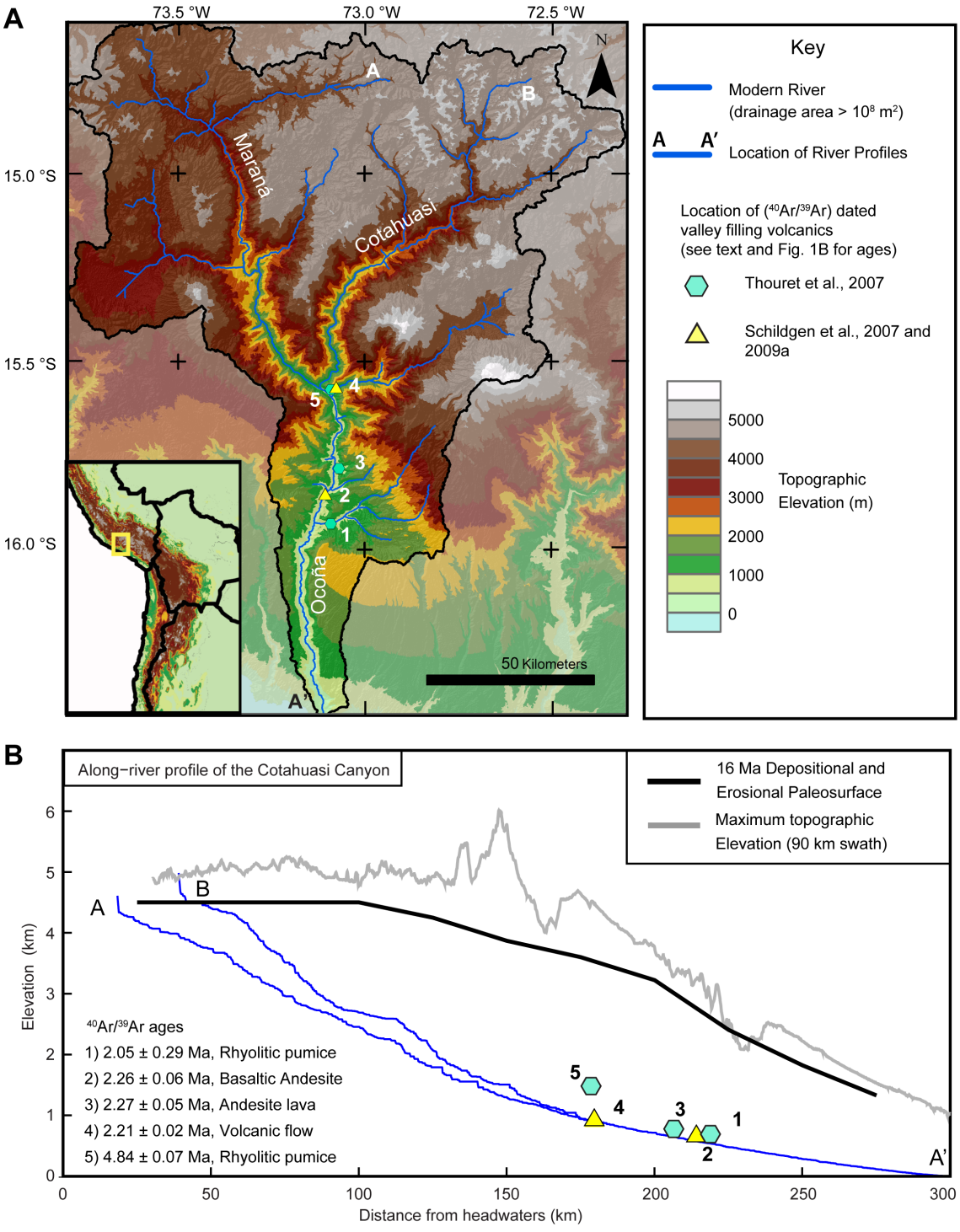
A
73.5 °W
73.0 °W
72.5 °W
15.0 °S
15.5 °S
16.0 °S
N
A
B
Marañá
Cotahuasi
Ocoña
A'
1
2
3
4
5
50 Kilometers
Key
Modern River
(drainage area > 10⁸ m²)
A A'
Location of River Profiles
Location of (⁴⁰Ar/³⁹Ar) dated
valley filling volcanics
(see text and Fig. 1B for ages)
Thouret et al., 2007
Schildgen et al., 2007 and
2009a
5000
4000
3000
2000
1000
0
Topographic
Elevation (m)
B
Along−river profile of the Cotahuasi Canyon
16 Ma Depositional and
Erosional Paleosurface
Maximum topographic
Elevation (90 km swath)
Elevation (km)
Distance from headwaters (km)
⁴⁰Ar/³⁹Ar ages
1) 2.05 ± 0.29 Ma, Rhyolitic pumice
2) 2.26 ± 0.06 Ma, Basaltic Andesite
3) 2.27 ± 0.05 Ma, Andesite lava
4) 2.21 ± 0.02 Ma, Volcanic flow
5) 4.84 ± 0.07 Ma, Rhyolitic pumice

Figure 3.1. Ocoña catchment and geological constraints on incision.
(previous page) A) Modern topography of the Ocoña catchment and its location on the western flanks of the northern Altiplano (inset). Locations of dated volcanic deposits that provide stratigraphic constraints on the timing of incision are indicated (yellow triangles, [Schildgen et al., 2007; *Schildgen et al., 2009a*] and blue hexagons [*Thouret et al., 2007*]. Locations of river profiles shown in Fig. 3.1B are indicated by A, A' and B. B) Longitudinal profiles. River profiles corresponding to the western (A) and eastern (B) branches of the river (blue). 90 km wide swath of maximum topography centered on the canyon mouth (gray). Modern elevation of the 16 Ma paleosurface (black, see text and supplementary material for details). Profiles were extracted from a filled 30 m ASTER GDEM.

and Strecker, 2012; *Garcia et al.*, 2011; *Schlunegger et al.*, 2011] suggesting that regional precipitation patterns exert a control on the modern fluvial landscape [*Strecker et al.*, 2009]. However, the influence of climate change in determining the timing and magnitude of river incision on million year timescales has not been quantified for this region. Furthermore, it is not clear whether increased precipitation could induce sufficient erosion to account for late Miocene river incision.

In this study, a one-dimensional (1D) river incision model is developed to simulate the incision history of the Ocoña canyon (Fig. 3.1A). A Monte Carlo search process is used to identify the range of surface uplift conditions that are consistent with geological observations and simulated changes in regional climate [*Ehlers and Poulsen*, 2009; *Insel et al.*, 2010]. The Monte Carlo search approach is also used to account for a range of different possible erosion mechanisms and river channel properties.

3.2 GEOLOGIC AND CLIMATIC SETTING

The Andes Mountains formed as the result of Nazca Plate subduction beneath the South American plate. Deformation in the central Andes began ~60–40 Ma [*DeCelles and Horton*, 2003; *McQuarrie et al.*, 2005], accelerated ~25 Ma, and has since migrated eastward from the Altiplano Plateau into the foreland fold-and-thrust belt [*Barnes et al.*, 2008; *McQuarrie*, 2002]. In southern Peru, crustal shortening of ~123 km has been recorded on the eastern flanks [*Gotberg et al.*, 2010]. In contrast, shortening rates on the western flanks are much lower, although high-angle reverse faults accommodated shortening prior to ~8 Ma [*M. Farias et al.*,

2005; *Muñoz and Charrier*, 1996; *Victor*, 2004], and there is geomorphic evidence for active deformation on smaller contractile structures that continues to the present [*Hall et al.*, 2012]. In the Ocoña catchment, late Cenozoic activity on the Iquipi fault accommodated left lateral motion prior to 25-15 Ma [*Roperch et al.*, 2006], and a later component of north side down motion (~100-200 m) [*Schildgen et al.*, 2009a]. Plateau relief on the western flank is therefore attributed to a crustal scale monocline [*Hall et al.*, 2012; *Isacks*, 1988; *Schildgen et al.*, 2009a; *Wörner et al.*, 2002]. A smooth topographic ramp links the active Western Cordillera to a ~1 km high escarpment at the Pacific Coast. This topographic ramp is dissected to depths of up to 3.5 km by the Ocoña Canyon (Fig. 3.1).

The Ocoña River cuts through Middle to Late Miocene ignimbrites, the Cenozoic Moquegua Formation, and Paleozoic-Mesozoic igneous and metamorphic basement in its deepest reaches. Deposition of the Lower Moquegua group occurred ~50–30 Ma [*Decou et al.*, 2011; *Roperch et al.*, 2006]. This formation consists of predominantly terrestrial red mudstones, siltstones and sandstones with intercalated conglomerates that were deposited in endorheic basins. Since ~30 Ma, a clastic wedge of alluvial, deltaic and debris flow deposits of the Upper Moquegua formed on the western Andean flanks with some late Oligocene marine deposits at the base [*Roperch et al.*, 2006]. Decou et al. [2011] report an increase in the energy of depositional environment and a transition from distal to more proximal sources though the Cenozoic. In the region of the Ocoña canyon, sedimentary deposition ceased ~16-14 Ma and was capped by one or more regionally extensive ignimbrites between 16.2 and 13.2 Ma [*Schildgen et al.*, 2007; *Schildgen et al.*, 2009a; *Thouret et al.*, 2007]. The base of this ignimbrite forms a regional paleosurface [Fig. 3.1B, *Schildgen et al.*, 2007; *Thouret et al.*, 2007] that we use to constrain the amount of incision since the cessation of deposition of the Upper Moquegua group.

Results from multiple thermochronometry studies combined with dates of valley filling ignimbrite and basaltic andesite lava flows provide estimates on the timing of canyon incision. Thermal modeling constrained by apatite and zircon (U-Th)/He data shows that canyon incision into the ~16 - 14 Ma paleosurface began 11–8 Ma and ended 5–2 Ma [*Schildgen et al.*, 2010; *Schildgen et al.*, 2007; *Schildgen*

et al., 2009b]. The modeled delay between paleosurface formation and the onset of deep incision is further supported by observations of ~9 Ma ignimbrite flows that fill up to ~600 m deep paleo-channels in the neighboring Caravelí valley [*Thouret et al.*, 2007]. Furthermore, dated volcanic deposits on the valley floor and walls provide constraints on the incision history (Fig. 3.1B). These deposits show that a minimum of 75 % of the incision had occurred by ~4 Ma near the confluence of the Maran and Cotahuasi rivers [Sample 5, Fig. 3.1, *Thouret et al.*, 2007] and 90–100 % of incision was complete by 2 Ma [Samples 1-4, Fig. 3.1, *Schildgen et al.*, 2007; *Schildgen et al.*, 2009b; *Thouret et al.*, 2007]. In contrast to the rapid (0.1–1 mm yr^{-1}) incision of the canyon, denudation rates of interfluve surfaces constrained by (U-Th)/He apatite cooling ages, cosmogenic exposure dating, and sediment budgets are as low as 0.001 mm yr^{-1} in northern Chile [*Kober et al.*, 2007], and up to ~0.05 mm yr^{-1} in the Ocoña region [*Schildgen et al.*, 2007].

On the western Andean flanks in southern Peru, modern mean annual precipitation rates increase from <0.1 m yr^{-1} at the coast to ~1 m yr^{-1} at the plateau margin [Fig. 3.2, *Bookhagen and Strecker*, 2008; *Houston and Hartley*, 2003; *Huffman et al.*, 2007]. Hyper-arid conditions at the coast have been attributed to: (1) the subtropical location; (2) blocking of moisture by the Andes; and (3) the cold Humboldt current that creates a temperature inversion along the coast and traps moisture below ~800 m [*Houston and Hartley*, 2003]. In the present climate, moisture that reaches the headwaters of the Ocoña catchment is predominantly the result of spillover of summertime convective precipitation from air masses that originate in the Amazon basin and cross the plateau [*Garreaud*, 1999; *Garreaud et al.*, 2003; *Houston and Hartley*, 2003]. Climate modeling studies have demonstrated that the amounts of convective precipitation increase with increasing Andean elevation [*Campetella and Vera*, 2002; *Ehlers and Poulsen*, 2009; *Insel et al.*, 2010; *Lenters and Cook*, 1995; *Poulsen et al.*, 2010]. The precipitation response to plateau elevation is spatially variable and displays a threshold behavior; convective precipitation increases when plateau elevations exceed ~70 % [*Poulsen et al.*, 2010]. Other than Andean uplift, significant drivers of regional climate change during the late Cenozoic include global cooling, Amazonian seaway incursions [*Frailey et al.*,

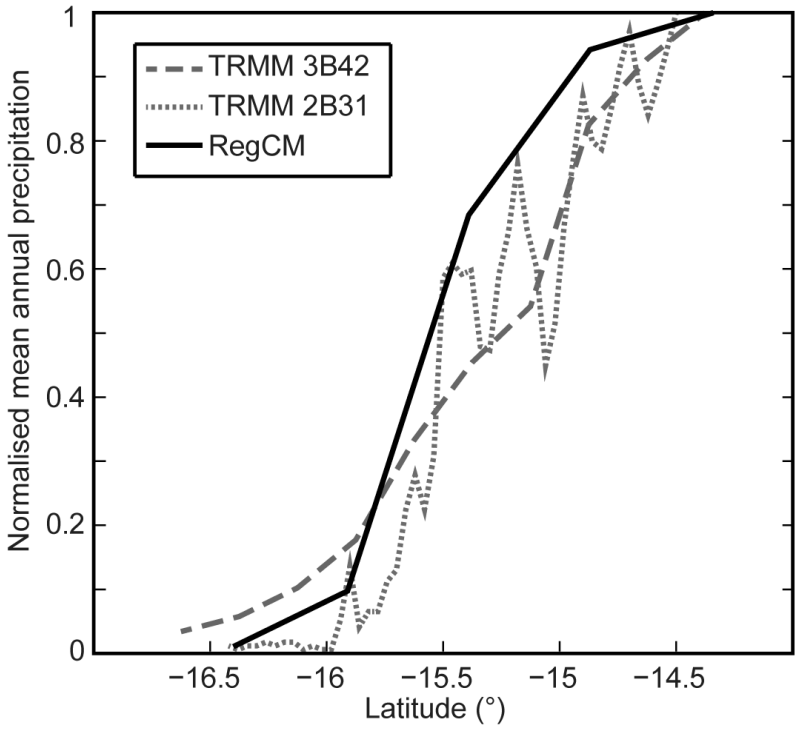

Figure 3.2. Modern precipitation rates

Normalized mean annual precipitation rates across the Ocoña canyon from two TRMM products [Bookhagen and Strecker, 2008; Huffman et al., 2007] and the RegCM model results used in this study. All datasets are normalized by the maximum value in the region to enable comparison of spatial distributions.

1988; *Rasanen et al.*, 1995], and onset of the Humboldt Current along the west coast of South America [*Houston and Hartley*, 2003]. Paleoclimate simulations indicate that global cooling through lowering of atmospheric CO_2, and Amazonian seaway incursions have had little effect on precipitation rates in southwestern Peru [*Jeffery et al.*, 2012]. This study therefore focuses on climate change in response to increased surface elevation and the resulting effect on fluvial discharge and erosion.

3.3 METHODS: SIMULATING RIVER PROFILE EVOLUTION WITH A MONTE CARLO SEARCH APPROACH

In this study, we identify the range of surface uplift conditions that are consistent with geologic and geomorphic observations and quantify the importance of precipitation to the river incision history. This range is determined by simulating the evolution of the Ocoña River profile using a 1D river profile evolution model. All

simulations are initiated at 16 Ma when a regionally extensive paleosurface formed (Fig. 3.1B and Fig. 3.3A) and run forward to the present day. Many of the parameters that describe river behavior are under-constrained for both the modern and past Ocoña River. To account for a range of all possible combinations of plausible incision parameters and boundary conditions, a Monte Carlo search method is used. This resulted in a total of 1.64×10^5 river profile evolution scenarios. Each simulated scenario is evaluated using the shape of the modern river profile (Fig. 3.1B) and geological constraints on the timing and evolution of incision. Results are presented in terms of surface uplift histories that fit these constraints. In this section, we describe the model set up in detail. First, the basic model equations are described and free parameters identified. Second, the initial and boundary conditions for the Ocoña catchment are outlined. Third, the geological constraints used to evaluate the

Table 3.1. Range of parameter values in Monte Carlo Search

Parameter	Symbol	Range of Values		Units
Erosion Law				
Erosivity Constant	k_b	$5x10^{-34}$; $7.5x10^{-34}$; $1x10^{-33}$; $2.5x10^{-33}$; $5x10^{-33}$; $7.5x10^{-33}$; $1x10^{-32}$; $2.5x10^{-32}$; $5x10^{-32}$; $7.5x10^{-32}$; $1x10^{-31}$; $5x10^{-31}$; $1x10^{-30}$		$m^{5/2}\ yr^2\ kg^{-3/2}$
Shear Stress Exponent	a	3/2		Dimensionless
Grain Size	D	0; 0.02; 0.05; 0.1; 0.2; 0.3; 0.5; 1.0		m
Channel Properties				
Channel width coefficient	k_w	0.001		$yr^{bw}\ m^{(3bw-1)}$
Channel width exponent	b_w	0.40; 0.45; 0.50; 0.55		Dimensionless
Drainage area exponent	h	1.5		Dimensionless
Drainage area coefficient	k_a	130		
Tectonics				
Initial Plateau Elevation	E_i	1000 – 3000;	500 m interval	m
Uplift Stage 1				
Fraction of total amount	U_a	0 – 0.9;	0.1 interval	Dimensionless
Fraction of total time	U_t	– 0.9;	0.1 interval	Dimensionless
3-stage uplift only				
Fraction of total amount	U_{a1} ; U_{a2}	0 – 0.8;	0.2 interval	Dimensionless
Fraction of total time	U_{t1} ; U_{t2}	0 – 0.9;	0.1 interval	Dimensionless

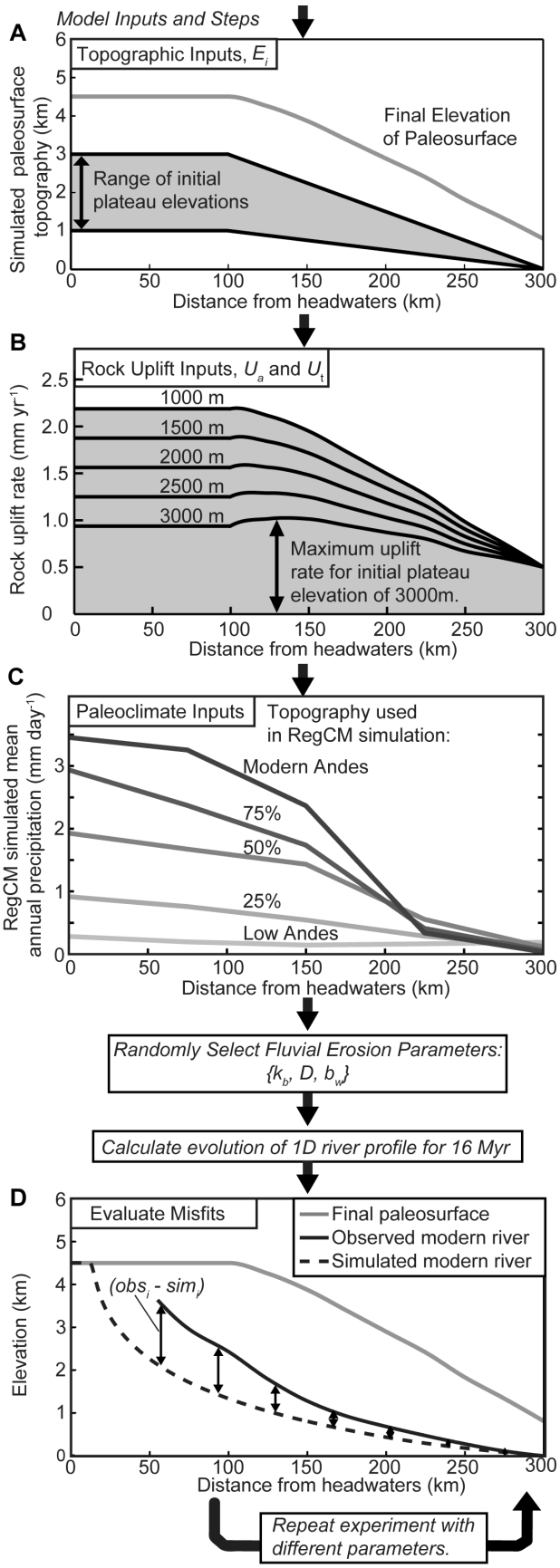
Model Inputs and Steps
A
Topographic Inputs, E_i
Final Elevation of Paleosurface
Range of initial plateau elevations
Simulated paleosurface topography (km)
Distance from headwaters (km)
B
Rock Uplift Inputs, U_a and U_t
1000 m
1500 m
2000 m
2500 m
3000 m
Maximum uplift rate for initial plateau elevation of 3000m.
Rock uplift rate (mm yr^{-1})
Distance from headwaters (km)
C
Paleoclimate Inputs
Topography used in RegCM simulation:
Modern Andes
75%
50%
25%
Low Andes
RegCM simulated mean annual precipitation (mm day^{-1})
Distance from headwaters (km)
Randomly Select Fluvial Erosion Parameters: {k_b, D, b_w}
Calculate evolution of 1D river profile for 16 Myr
D
Evaluate Misfits
Final paleosurface
Observed modern river
Simulated modern river
(obs_i - sim_i)
Elevation (km)
Distance from headwaters (km)
Repeat experiment with different parameters.

Figure 3.3. Monte Carlo Search: Model setup and evaluation.

(previous page) A) Initial and final paleosurface elevations. Initial plateau elevation is randomly selected from discrete 0.5 km intervals between 1.0 and 3.5 km. B) Range of rock uplift rates for each initial plateau elevation. Rock uplift occurs in two stages with rates that together raise the initial surface to the modern observed paleosurface elevation (Fig. 3.3A). Typical uplift rates are ~0.1–0.2 mm yr^{-1} C) Precipitation rates simulated by RegCM for plateau elevations at 100%, 75%, 50% and 25% of modern elevations and a 'Low Andes' scenario in which maximum elevation is 250 m [*Ehlers and Poulsen, 2009; Insel et al., 2010*]. In river incision simulations, precipitation rates are tied to plateau elevations and interpolated for elevations between those simulated by RegCM. Additional fluvial erosion parameters are selected at random from a range of discrete values (Table 3.1) and river profile erosion is simulated for 16 Myr. D) χ^2 misfit. The final river profile is compared with the modern river profile using a χ^2 misfit (Equation 5). Input parameters for all simulations that fit the modern river profile with a $\chi^2 \leq 10$ are stored, and the experiment repeated with new parameters

model output are defined. Finally, the model sensitivity to the assumptions used is evaluated.

3.3.1 Stream power based river incision model

The river incision model calculates the elevation profile of a river bed through time. River bed elevations are a function of relative rates of uplift (U) and incision. River incision is calculated following a commonly used, detachment limited, shear stress based erosion law [*Howard et al.*, 1994; *Seidl and Dietrich*, 1992; *Snyder et al.*, 2000; *Whipple and Tucker*, 1999]. Active incision occurs only when the basal shear stress exceeds a critical shear stress required to move sediment. River profile evolution is therefore described by the conditional equations,

$$\frac{dh}{dt} = U - k_b\left(\tau_b - \tau_c\right)^a \qquad \tau_b > \tau_c \qquad (3.1a)$$

$$\frac{dh}{dt} = U \qquad \tau_b \leq \tau_c \qquad (3.1b)$$

where dh/dt (m yr^{-1}) is the change in elevation of the river bed through time, U (m yr^{-1}) is the rock uplift rate, τ_b (Pa) is the basal shear stress, τ_c (Pa) is the critical

shear stress, a is a dimensionless constant dependent on the physical process of erosion, and k_b ($m^{(a+1)}\,yr^{(2a-1)}\,kg^{(-a)}$) is an erosivity constant that incorporates erosion process and bedrock lithology and strength. Theoretically determined values for a include $a = 1$ for erosion by plucking [*Howard and Kerby*, 1983; *Whipple et al.*, 2000]; $a = 5/2$ for a suspended-load abrasion based model [*Foley*, 1980; *Hancock et al.*, 1998; *Whipple et al.*, 2000]; $a = 7/2$ for cavitation erosion [*Whipple et al.*, 2000]; and $a = 3/2$ for a stream power based law, in which the rate of incision is proportional to the rate of energy dissipation per unit bed area [*Howard et al.*, 1994; *Seidl and Dietrich*, 1992; *Whipple and Tucker*, 1999]. A stream power erosion law ($a = 3/2$) is used in all experiments shown here. Sensitivity experiments verified that the range of uplift histories found does not depend on the choice of a (see section *3.5.3.3*). Empirically determined values of the dimensional erosion coefficient k_b vary over several orders of magnitude [*Stock and Montgomery*, 1999], and the units of k_b are dependent on the value of a. k_b is a free parameter in the Monte Carlo search (see Table 3.1 for range of values) because it exerts a strong control on the magnitude of incision rates and is dependent on multiple, under-constrained properties, such as bedrock erodibility.

The basal shear stress (τ_b), and therefore the potential for erosion, is dependent on channel flow properties according to:

$$\tau_b = \rho_w C_f^{\frac{1}{3}} g^{\frac{2}{3}} \left(\frac{Q}{W}\right)^{\frac{2}{3}} S^{\frac{2}{3}} \qquad (3.2)$$

where ρ_w (kg m^{-3}) is the density of water, C_f is the Darcy-Weisbach dimensionless friction factor, g (m yr^{-2}) is gravitational acceleration, Q (m^3 yr^{-1}) is channel discharge, W (m) is channel width, and S (m m^{-1}) is the local channel bed slope, which is an approximation for the channel surface slope [*Snyder et al.*, 2000; *Wolman and Miller*, 1960]. Values assigned to parameters ρ_w, C_f, and g are listed in Table 3.2. Channel slope is calculated by differencing the elevation of the local node with that of the downstream node.

Table 3.2 Constants used in 1D river profile model

Variable	Symbol	Value	Units
Darcy-Weisbach friction factor	C_f	0.03	dimensionless
Shield's stress	τ_c^*	0.045	dimensionless
Density contrast	$\Delta\rho$	1650	kg m^{-3}
Gravitational acceleration	g	9.81	m s^{-2}
Density of water	ρ_w	1000	kg m^{-3}

Parameterization of the discharge terms (Q and W) in equation 2 determines the shape of the steady-state river profile and the river response to changes in discharge. In this study, we explicitly account for non-uniform precipitation distributions within the catchment (see section 3.3.2) and the dependence of channel width on discharge [Montgomery and Gran, 2001; Yanites and Tucker, 2010]. Total discharge at a point on the profile is the integral of upstream drainage area and precipitation rates. Upstream drainage area, A (m^2), is prescribed following Hack's law [*Hack*, 1957]

$$A = k_a x^h \qquad (3.3)$$

where k_a ($m^{2\text{-}h}$) is a dimensional constant and h (dimensionless) is the reciprocal of the Hack exponent. Appropriate values of k_a = 130 and h = 1.5 were determined for the Ocoña catchment from a 30m ASTER GDEM [*METI and NASA*, 2001]. The relatively low value of h for this catchment [*Hack*, 1957; *Rigon et al.*, 1996] indicates the relatively large proportion of the catchment area that lies in the upper reaches, making this catchment particularly sensitive to climatic change in the headwater region. The distribution of precipitation within the catchment, and therefore along-stream discharge volume, is taken from climate simulation results as described in section 3.3.2. Channel width at node i is related to stream discharge according to:

$$w_i = k_w Q_i^{b_w} \qquad (3.4)$$

where k_w ($yr^{bw}m^{(3bw-1)}$) is a dimensional coefficient, and b_w is a dimensionless positive constant. Empirically determined values of b_w vary from ~0.4–0.6 [*Leopold and Maddock*, 1953; *Montgomery and Gran*, 2001; *Yanites and Tucker*, 2010]. In this study we hold k_w constant at 0.001 in all simulations because variation in this parameter is countered by variation of k_b and inclusion of k_w as a free parameter does not increase the range of plausible uplift histories. However, b_w is a free parameter in the Monte Carlo search (Table 3.1). Values that are both consistent with empirical observations, and that give reasonable channel widths, were selected to limit the range of search parameters.

The final river incision parameter that is a free parameter in the Monte Carlo search determines the critical shear stress (τ_c, equation 3.1). We assume that the critical shear stress is related to the shear stress required to lift sediment from the bed and expose bedrock [*Howard et al.*, 1994; *Lave and Avouac*, 2001; *Sklar and Dietrich*, 2004]. It is evaluated according to

$$\tau_c = \tau_c^* \Delta \rho g D \qquad (3.5)$$

where τ_c^* is a dimensionless critical shear stress (Shield's stress), $\Delta\rho$ (kg m^{-3}) is the density difference between the fluid and the sediment, g (m yr^{-2}) is gravitational acceleration and D (m) is the median grain size. In the model, critical shear stress values are determined from a range of grain sizes (D) between 0.02 and 1 m (D, Table 1), which is equivalent to critical shear stresses of 15–730 Pa when combined with appropriate values of τ_c^*, $\Delta\rho$ and g (Table 2). An option of a critical shear stress of zero, and consequently no erosion threshold, is also included in the Monte Carlo search experiments (Table 3.1).

The evolution of the river profile through time is evaluated by solving equations 3.1–3.5 using an explicit, finite difference, forward modeling approach. Equation 3.1a is approximated [*Tucker*, 2004] by

$$\frac{dh}{dt} = U - \left(k_b \tau_b{}^a - k_b \tau_c{}^a\right) \qquad \tau_b > \tau_c \qquad (3.6)$$

At each time step, the slope values, discharge and channel width are used to calculate the local shear stress for each node (equation 3.2). Node spacing is 500 m and the model time step is 1000 years. Topography is then updated based on equations 3.6 and 3.1b, except for the final node, which is held fixed at sea level. The evolution of the profile and the total amount of incision is tracked throughout the simulation.

3.3.2 Initial and boundary conditions for the Ocoña catchment

Initial and boundary conditions for the Ocoña catchment are defined as follows. The modern elevation of the 16 Ma paleosurface was extracted from a 30 m ASTER DEM [*METI and NASA*, 2001] and regional geologic maps [*INGEMMET*, 2004] by spline-fitting the modern elevation of the Huaylillas ignimbrite base following the method of Schildgen et al. [2007] (see supplementary material for details). Assuming negligible hillslope erosion, rock uplift has raised the original paleosurface from an initial, unknown elevation to its modern elevation over the last 16 Myr. The geometry of the paleosurface at the onset of the simulation is prescribed as a flat plateau and ramp to zero elevation at the coast (Fig. 3.3A). A ramp-and-flat geometry was chosen for the initial topography because it defines an uplift rate that is constant on the plateau, suggests some outward growth of the plateau, and decreases towards the coast. This pattern is consistent with the conclusion of Schildgen et al. [2009b] who describe the uplift pattern as a combination of monocline development and block uplift. For simplicity, our initial simulations combine these two deformation styles throughout the simulation. We explore scenarios in which monocline uplift switches to block-uplift during the late Miocene in Section 3.5.1. Alternative geometries for the initial shape of the paleosurface were explored including a river profile that has a concavity similar to the modern river. However, these geometries require an uplift rate that has a maximum ~200 km from the headwaters that is not compatible with regional tectonic development. The initial elevation of the plateau is treated as a free

parameter, E_i, in the Monte Carlo search (Table 3.1). Plateau elevations of less than 3.1 km at 16 Ma are unlikely because significant material had already been shed from the mountain front at this time [*Roperch et al.*, 2006], indicating the prior establishment of significant topography. Conversely, plateau elevations >3 km at 16 Ma are inconsistent with geologic evidence for at least 1.5 km of surface uplift since deposition of regional ignimbrites 16 – 14 Ma. Simulated initial plateau elevations considered are therefore limited to range between 1 and 3 km (Fig. 3.3A and Table 3.1), with simulations initiated at discrete 500 m intervals.

In our initial suite of simulations, rock uplift rates are defined to raise the initial surface up to the modern paleosurface elevation in two stages of different rates (Fig. 3.3B). In the model, the rock uplift rate is determined by two random numbers that describe the first uplift stage in terms of the amount of uplift (U_a) that occurs in, and the duration (U_t) of, the first uplift stage (Table 3.1). The spatial distribution of uplift rates is dependent on the shape of the prescribed initial topography and the magnitude of uplift rates depends on the initial plateau elevation (Fig. 3.3B). Rock uplift rates and surface uplift are considered to be equivalent because background erosion rates and flexural isostatic response are likely to be small compared to uplift amounts [*Lamb*, 2011; *Simpson*, 2004]. We explore more complex uplift histories, including 3-stage uplift and a component of block uplift, in section 3.5.1.

The discharge term *(Q/W,* equation 3.3*)* is commonly calculated based on the assumption that precipitation rates are uniform throughout the catchment and that each unit area therefore contributes the same volume to the total discharge. For this study we account for spatial and temporal variability in precipitation rates by using results from the regional climate model RegCM. Ehlers and Poulsen [2009] and Insel et al. [2010] performed several climate model simulations in which the Andean topography was modified for lower plateau elevations. South American climate was simulated at 5 different plateau elevations representing modern, 75%, 50%, 25% and low (250 m) Andean elevations. For this study, a north-south transect of mean annual precipitation rates was extracted across the Ocoña catchment from each of these simulations (Fig. 3.3C). At each point on the climate data transect, mean

annual precipitation rates were averaged across three longitudinal grid cells spanning the width of the catchment. RegCM is known to overestimate precipitation rates in this region, so absolute values were scaled to give precipitation rates of ~3.5 mm day^{-1} (~1.3 m yr^{-1}) in the headwaters (Fig. 3.3C) while maintaining the spatial gradient that compares well with observations (Fig. 3.2). In the river incision model, precipitation rates at each time step are interpolated to the appropriate elevation. Climate inputs are not a free parameter in the Monte Carlo search. The Monte Carlo search therefore includes seven free parameters (Table 3.1) that account for uncertainties in river incision parameterization (k_b, b_w, and D), initial conditions at 16 Ma (E_i), and surface uplift history (U_a and U_t).

3.3.3 Model evaluation criteria

For each simulation in the Monte Carlo search, model output is evaluated based on a comparison with the modern river profile, and the ability to replicate the timing of incision onset and completion (Fig. 3.3D). The success of the model in simulating the observed river profile is measured using the reduced χ^2 misfit function:

$$\chi^2 = \frac{1}{n - \upsilon - 1} \sum_{i}^{n} \left(\frac{sim_i - obs_i}{tolerance} \right)^2 \qquad (3.7)$$

where n is the number of nodes on the river profile (601 nodes, 500m spacing), ν is the number of free variables, sim_i is the simulated river elevation at node i, obs_i is the elevation of the smoothed, observed river profile at node i. The tolerance is 150 m, given by the estimated error on the filled and smoothed river profile extracted from a 30 m ASTER GDEM [*METI and NASA*, 2001]. In this study, the western, Maran, branch of the river (Fig. 3.1) is simulated because it is more deeply incised. Furthermore, the upper Cotahuasi (eastern) branch was filled by volcanics ~2 Ma which complicates model evaluation based on the modern river profile [*Thouret et al.*, 2007]. To ensure that previously glaciated regions were not included in the

analysis, the observed profile was truncated at ~50 km from the headwaters (Fig. 3.3). The χ^2 misfit is a measure of how well the model reproduces the shape and elevation of the modern river profile. The χ^2 misfit also measures the total amount of incision, because the total amount of incision is the difference between the elevation of the modern river profile and the modern elevation of the 16 Ma paleosurface, which is fixed for all simulations. Only simulations that yield a χ^2 misfit ≤ 2 (Fig. 3.4) are discussed in the results (section 3.4).

Acceptable river simulations must also obey two constraints on the timing of incision: (1) erosion into the paleosurface must be less than 600 m at 12 Ma along the full length of the profile, and (2) at least 90% of the total incision must have occurred by 2 Ma between 80 and 125 km from the river outlet. Hereafter, these two constraints are referred to as the 'incision onset constraint' and the 'incision completion constraint', respectively. Incision onset timing is constrained by modeling of thermochronometry data [*Schildgen et al.*, 2009b] and dated channel fill deposits [*Thouret et al.*, 2007]. Timing of incision completion is constrained by dated volcanic deposits close to, or at, the present day valley floor [Fig. 3.1, *Schildgen et al.*, 2007; *Schildgen et al.*, 2009b; *Thouret et al.*, 2007]. The model constraints were chosen as a combination of multiple available constraints with the goal of identifying simulations that display both an increase in incision rate during the first few million years of simulation, and a slowing to near completion by the end of the simulation. Due to the simplicity of the model, stricter constraints that more faithfully represent some of the geological observations, for example, less than 300 m incision by 8 Ma and 100 % complete incision by 2 Ma, result in the rejection of all simulated scenarios. In the following section we therefore demonstrate the different effects of climate and tectonics factors on profile evolution under relatively simple tectonic and incision conditions, and discuss more complicated uplift models in sections 3.5.1.2 and 3.5.1.3.

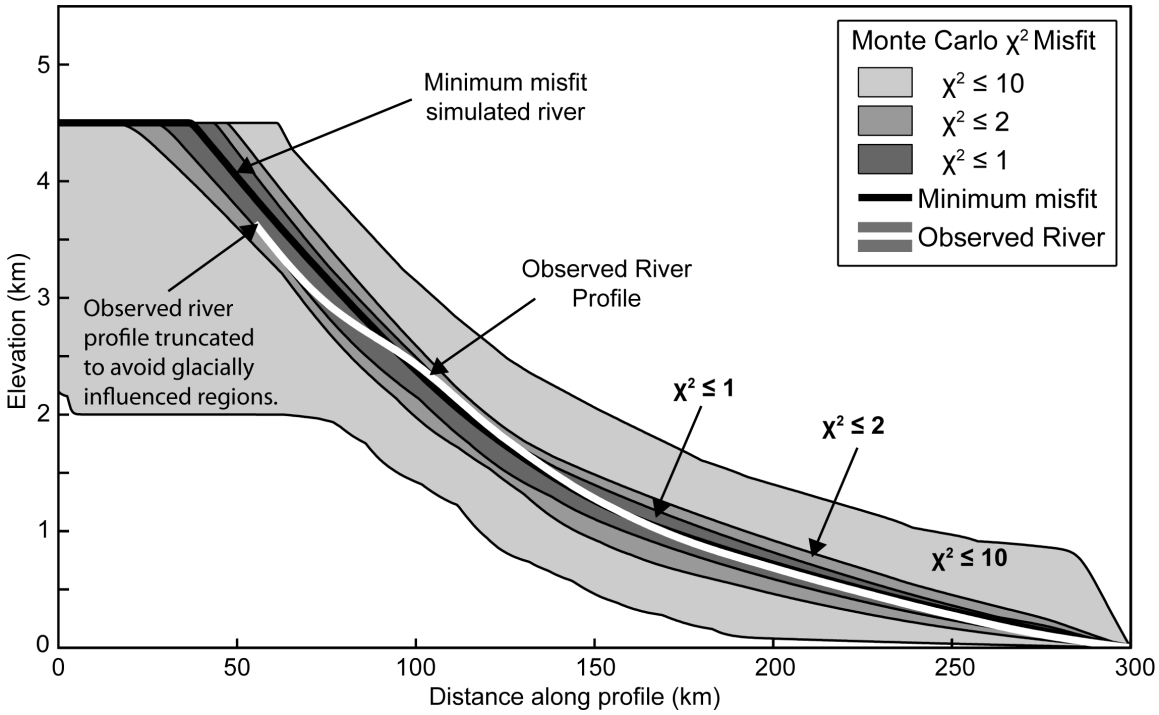

Figure 3.4. χ^2 misfit.

Range of simulated river profiles that match the modern river profile (white) within a specified χ^2 limit. The final river profile with the lowest χ^2 misfit found by the Monte Carlo search is shown in black. The modern river profile is truncated at ~50 km to remove the region influenced by glacial erosion and the χ^2 misfit is calculated only for the portion of river shown.

3.3.4 Model caveats

The model simulations presented here include simplifications and assumptions. Geological factors that are not explicitly accounted for in the model include drainage re-organization, lithological variations, volcanic valley infill, mass wasting, and glaciation. The model assumes that the river is governed by detachment-limited erosion that includes a threshold; variations in sediment flux are not accounted for. It is assumed that RegCM precipitation rates are representative of the long-term discharge and that all precipitation becomes surface runoff. Finally, surface uplift is prescribed to occur in two stages, which does not permit more complex uplift histories. In order to validate our results, we examine and quantify (see Sections 3.5.2 and 3.5.3) the impact of these factors on the results using additional Monte Carlo searches with slightly modified model formulation.

3.4 RESULTS

Monte Carlo searches were successful in finding a range of geologic and geomorphic parameters that fit the observational constraints defined in section 3.3.3. Experiment results are presented in the following way. First, the sensitivity of the model to climate and tectonics is demonstrated with example simulations using parameter values chosen from the suite of successful simulations. Second, results of the Monte Carlo search are presented in terms of plausible plateau uplift histories. Finally, the influence of erosion parameters on the model is examined. The fit of the Monte Carlo model to the data is presented in the following two ways: (1) a 'good-fit' simulation is defined here as one that obeys the geologic timing constraints, and fits the modern river profile with a χ^2 misfit ≤ 1 (equation 3.7). This criterion was chosen because it implies the model is fitting the observed modern river profile within one standard deviation of uncertainty in elevation. (2) An 'acceptable' simulation is defined as one that obeys the timing constraints and river profile elevation with a χ^2 misfit ≤ 2. This criterion means the model fits the modern river profile elevation at the two standard deviation level. Fits greater than this (e.g. χ^2 misfit ≤ 10, Fig. 3.4) are shown only for reference to illustrate model sensitivity to poor combinations of parameters.

3.4.1 Demonstration of model behavior

3.4.1.1 Baseline simulation

Results are shown for three individual simulations to illustrate the model setup and behavior with respect to different parameter choices. The first of these is the 'baseline simulation' (Fig. 3.5), which is an example of a single simulation (i.e. without a Monte Carlo search) that yields a good fit to observations. The baseline simulation was initiated with a plateau elevation of 2 km at 16 Ma. Surface uplift rates of ~0.24 mm yr^{-1} on the plateau were applied between 16 and 9.6 Ma (Fig. 3.5A). At 9.6 Ma, uplift rates on the plateau were reduced to ~0.11 mm yr^{-1} and remained at this rate until the end of the simulation (present day). Precipitation rates change with increasing plateau elevation according to RegCM climate model simulations (Fig. 3.3C). The river profile was recorded every 4 million years

throughout the simulation (Fig. 3.5B) and tracks the response of the river to both surface uplift and changing precipitation rates. The initial river profile at 16 Ma (Fig. 3.5B) is a flat ramp to the coast. Incision is initially strongest at the coast (300 km, Fig. 3.5B) and propagates inland through time with active incision dissecting the plateau margin after ~12 Ma. At the end of the simulation, the river is still actively incising. The most distal 50 km of the river profile attain steady-state by 8 Ma.

The timing and spatial distribution of incision is also recorded throughout the simulation. The total amount of incision is recorded in 2 million year intervals (Fig. 3.5C). Maximum total amounts of incision are greater than 2.5 km and occur in the middle reaches of the river (~150 km along the profile, Fig. 3.5C). In the baseline simulation, the amount of incision between 16 and 14 Ma is low (< 200 m). Through time, incision rates increase and the locus of maximum incision rate (denoted by the distance between two adjacent lines) propagates upstream. By 2 Ma, maximum incision rates are located at ~90 km along the profile and the most distal ~100 km are at, or near, topographic steady-state (Figs. 3.5B and 3.5C).

Figure 3.5C also demonstrates how the incision timing constraints are used to evaluate the model. If the total erosion at 12 Ma lies outside of the gray shaded area (600 m total incision), the simulation violates the incision onset constraint. Similarly, the total erosion since 2 Ma must lie within the red shaded box (10% of the total erosion), to obey the incision completion constraint. In this baseline simulation, the final river profile fits the modern observed river with a χ^2 misfit of 0.39 (Fig. 3.5D). In this example, all three evaluation criteria are met and the model is considered to represent a good-fit to the observations. In a Monte Carlo search, the input parameters would be stored and included in the range of good-fit results. If any of these three criteria were not met, then the experiment is discarded. For a given set of erosion parameters, the simulations are sensitive to the tectonic and climatic conditions. We demonstrate this sensitivity with two additional individual experiments. As with the previous simulation (Fig. 3.5), these experiments are individual simulations and a Monte-Carlo search is not used.

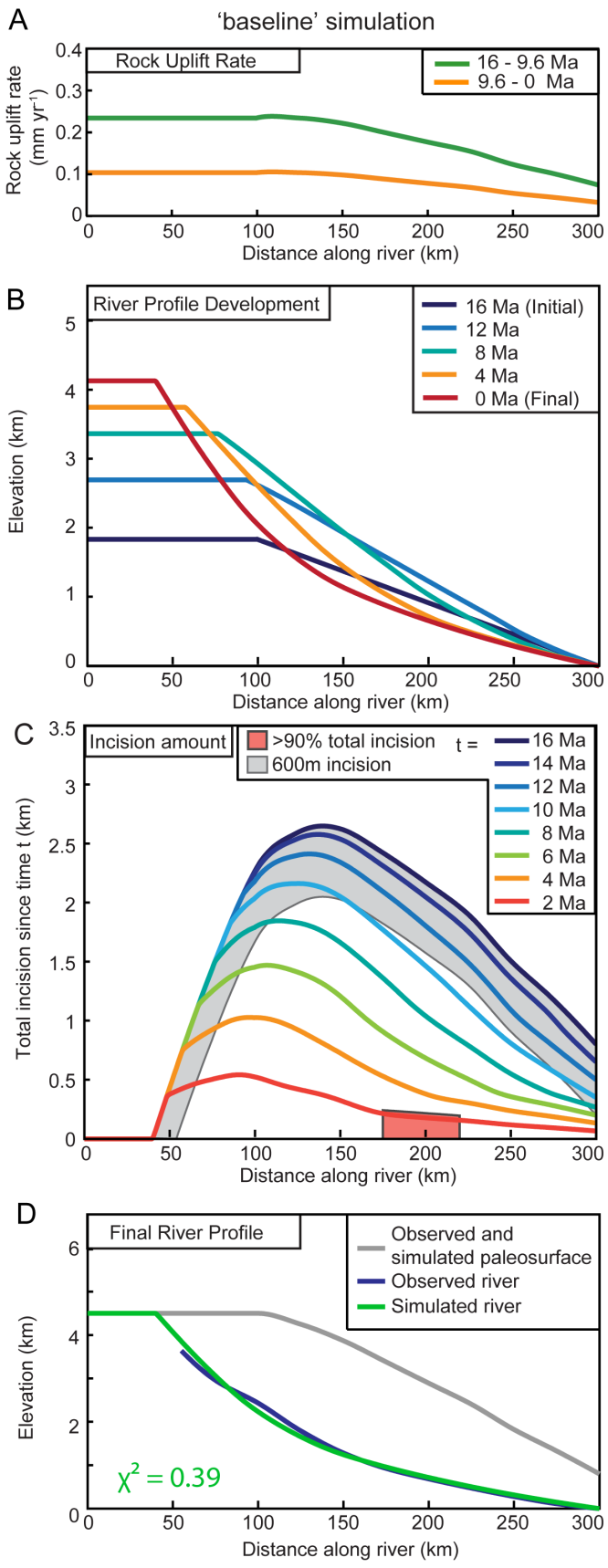
A
'baseline' simulation
Rock Uplift Rate
16 - 9.6 Ma
9.6 - 0 Ma
Rock uplift rate (mm yr⁻¹)
Distance along river (km)
B
River Profile Development
16 Ma (Initial)
12 Ma
8 Ma
4 Ma
0 Ma (Final)
Elevation (km)
Distance along river (km)
C
Incision amount
>90% total incision
600m incision
t =
16 Ma
14 Ma
12 Ma
10 Ma
8 Ma
6 Ma
4 Ma
2 Ma
Total incision since time t (km)
Distance along river (km)
D
Final River Profile
Observed and simulated paleosurface
Observed river
Simulated river
Elevation (km)
χ² = 0.39
Distance along river (km)

Figure 3.5. Example 'baseline' simulation.

(previous page) A) Rock uplift rates applied between 16 and 9.6 Ma (green), and 9.6 to 0 Ma (orange). B) River profile development at 4 Myr intervals during the simulation. C) Total incision since time t. Differences between consecutive time lines indicates the amount of erosion that occurred in that time interval. Incision onset constraint: maximum of 600 m incision before 12 Ma (gray shading). Incision completion constraint: at least 90% of incision must occur by 2 Ma (red shading). D) Simulated final river profile (green), observed modern profile (blue), and simulated and observed modern elevation of 16 Ma paleosurface (gray). The χ^2 misfit for this simulation is 0.87.

3.4.1.2 Tectonic sensitivity experiment

In the first of these, the 'tectonic sensitivity experiment', uplift rates are held steady at ~1.6 mm yr^{-1} throughout the simulation (Fig. 3.6). Uplift rates during the first 6.4 Myr of simulation are therefore lower than the baseline simulation, and uplift rates since 9.6 Ma are higher than the baseline simulation (Fig. 3.6A). Due to the lower initial uplift rates, the river gradient from the plateau margin to the coast is lower than the baseline simulation (Fig. 3.6B). Additionally, because plateau elevations are lower during the simulation, and precipitation rates increase with increasing elevation (Fig. 3.3C), the discharge is also lower than in the baseline simulation. Consequently, initial incision rates are lower and incision propagates upstream more slowly (Fig. 3.6B).

Slower incision rates throughout the simulation result in less total erosion than the baseline experiment (Fig. 3.6C). Total incision is less than 90 % between 80 and 125 km from the outlet by 2 Ma and the incision completion constraint is therefore broken. Furthermore, the total erosion throughout the simulation is too low (Fig. 3.6D) and the final river profile has a χ^2 misfit of 2.65. A steady uplift from 2 km at 16 Ma is therefore not compatible with the incision constraints under the specified erosion parameters because incision rates are initially too low due to the lower elevation, but the increase in uplift rate results in incision rates that are too high during the last 4 million years of simulation.

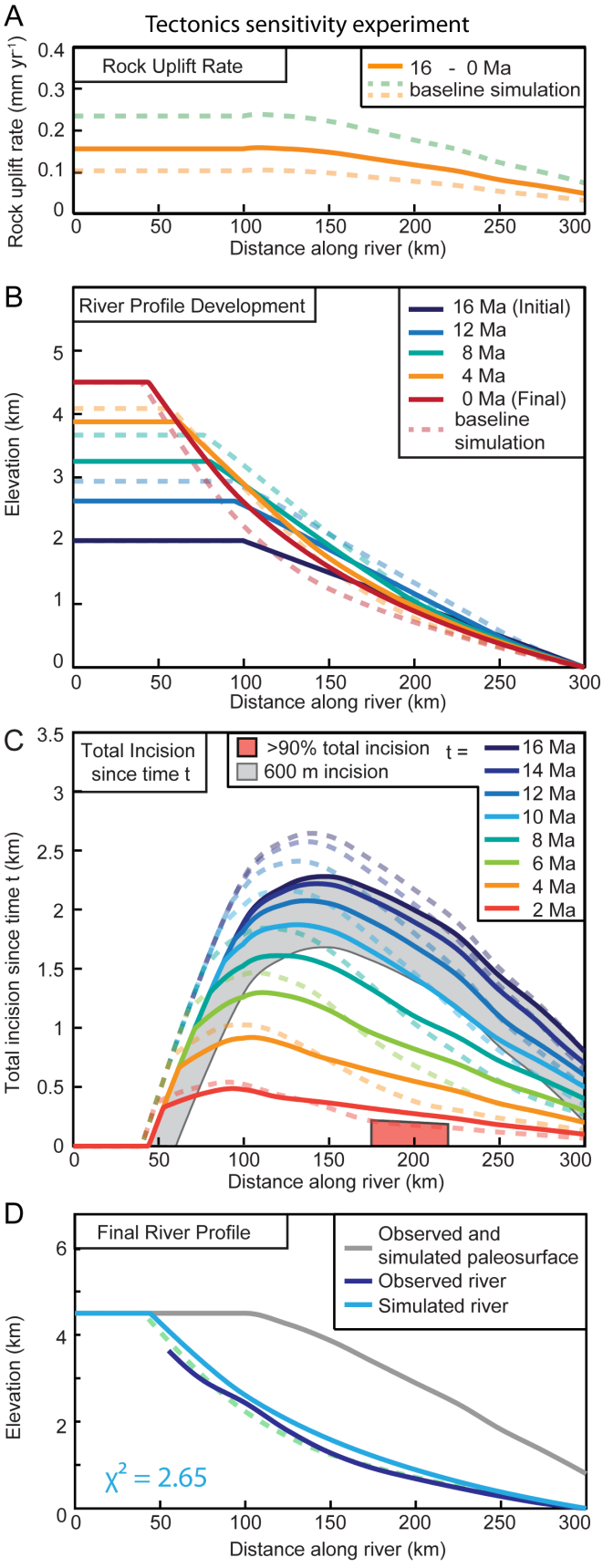
A
Tectonics sensitivity experiment
Rock Uplift Rate
16 - 0 Ma
baseline simulation
Rock uplift rate (mm yr⁻¹)
Distance along river (km)
B
River Profile Development
16 Ma (Initial)
12 Ma
8 Ma
4 Ma
0 Ma (Final)
baseline simulation
Elevation (km)
Distance along river (km)
C
Total Incision since time t
>90% total incision
600 m incision
t =
16 Ma
14 Ma
12 Ma
10 Ma
8 Ma
6 Ma
4 Ma
2 Ma
Total incision since time t (km)
Distance along river (km)
D
Final River Profile
Observed and simulated paleosurface
Observed river
Simulated river
Elevation (km)
χ² = 2.65
Distance along river (km)

Figure 3.6. Tectonics sensitivity experiment.

(previous page) This simulation is identical to the baseline experiment (Figure 3.5) except that the initial plateau elevation is 3 km, 1 km higher than the baseline experiment. For comparison, the results of the baseline experiment (Fig. 3.5) are shown as dashed lines and the following comments describe differences between the two experiments. A) Uplift rates are lower between 16 and 9.6 Ma, and higher between 9.6 and 0 Ma. B) The elevation of the river profile remains similar throughout the simulation as the paleosurface is uplifted around the canyon. C) Incision rates at the end of the simulation are higher, but 90% incision is not achieved by 2 Ma and the incision completion constraint is broken. D) The final river is not so deeply incised with a χ^2 misfit of 2.65. This simulation therefore does not yield a good fit to the observations.

3.4.1.3 Climate sensitivity experiment

In the final individual experiment we demonstrate the importance of the temporal variation of precipitation by holding precipitation rates constant through time. Precipitation rates are therefore not linked to plateau elevation, as is the case in the previous simulations (Figs. 3.5 and 3.6). The previous experiment (Fig. 3.6) showed how a combination of topographic and precipitation conditions controls the timing of the onset of rapid incision. By holding precipitation rates constant we demonstrate the importance of elevation dependent precipitation. For the simulation shown in Figure 3.7, all model parameters are identical to those in the baseline simulation (Fig. 3.5) except for precipitation rates, which are taken from the 100% Andean elevation case (Fig. 3.3C). Modern precipitation rates enable rapid incision at low (<3 km) plateau elevations. The lower reaches of the river quickly approach topographic steady-state (200–300 km along profile, Fig. 3.7B). Incision amounts between 16 and 12 Ma are high enough to break the incision onset constraint between 210 and 230 km along the river profile (Fig. 3.7C). A constant precipitation rate also results in greater total incision amounts (Fig. 3.7D) giving a final river profile χ^2 misfit of 2.06, lower than with the steady uplift rate, but higher than the baseline simulation (Fig. 3.7D).

Together, these three experiments demonstrate how different tectonic and climatic conditions can alter the river profile evolution for a specific set of erosion parameters. However, simulations with a different uplift rate or initial elevation may be compatible with geological constraints under a different set of erosion parameters (b_w, D, *and* k_b). Monte Carlo searches over a wide range of parameter

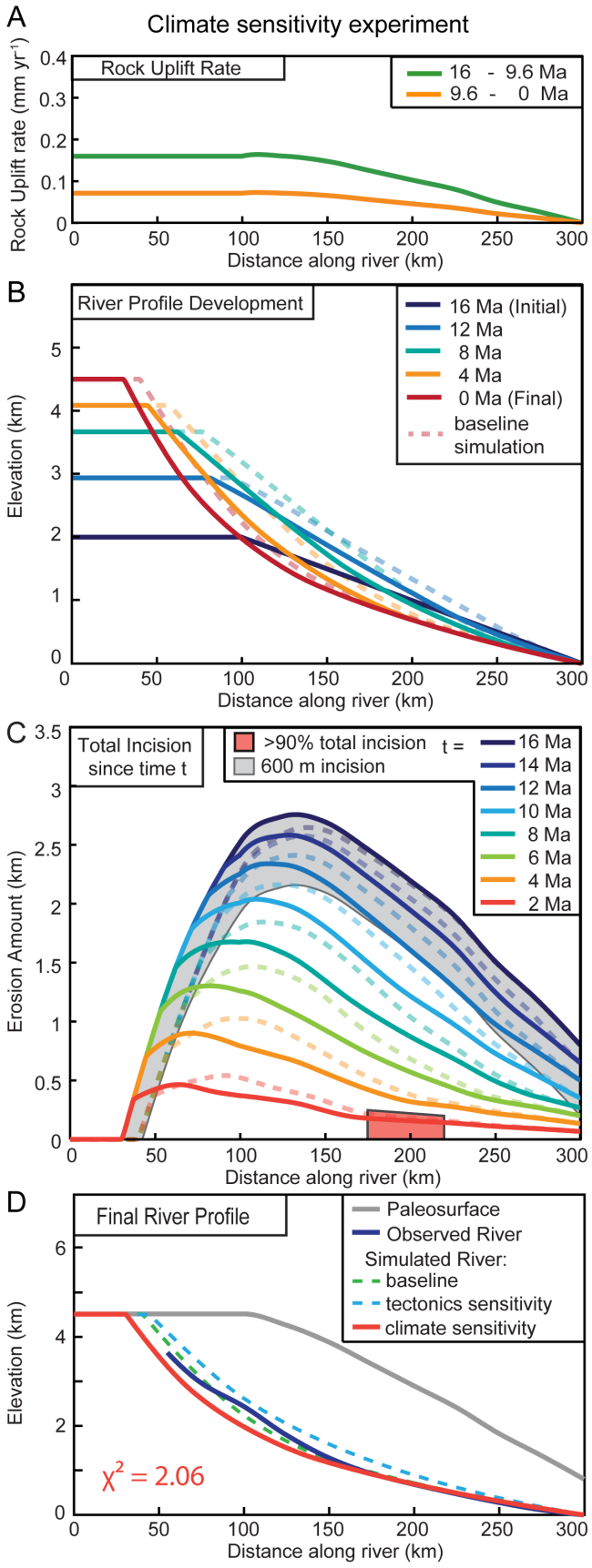
A
Climate sensitivity experiment
Rock Uplift Rate
16 - 9.6 Ma
9.6 - 0 Ma
Rock Uplift rate (mm yr-1)
Distance along river (km)
B
River Profile Development
16 Ma (Initial)
12 Ma
8 Ma
4 Ma
0 Ma (Final)
baseline simulation
Elevation (km)
Distance along river (km)
C
Total Incision since time t
>90% total incision
600 m incision
t =
16 Ma
14 Ma
12 Ma
10 Ma
8 Ma
6 Ma
4 Ma
2 Ma
Erosion Amount (km)
Distance along river (km)
D
Final River Profile
Paleosurface
Observed River
Simulated River:
baseline
tectonics sensitivity
climate sensitivity
χ2 = 2.06
Elevation (km)
Distance along river (km)

Figure 3.7. Climate sensitivity experiment.

(previous page) This simulation is identical to the baseline experiment (Fig. 3.5) except that the precipitation rate is held at rates corresponding to 100 % Andean elevation (see Fig. 3.3C) throughout the simulation. For comparison the results of the baseline experiment (Fig. 3.5) are shown as dashed lines and the following comments describe differences between the two experiments. A) Uplift rates for each stage are identical. B) River incision is more rapid at the onset of the simulation and the lower reaches attain topographic steady-state at an earlier time. C) Total incision by 12 Ma exceeds 600 m, breaking the incision onset constraint. D) The final river profile has a $\chi^2 = 2.06$. It is more deeply incised than the baseline and tectonics sensitivity experiments. This simulation does not yield a good fit to the constraints.

values are therefore needed to establish the full range of plausible uplift histories. The following sections present Monte-Carlo search results.

3.4.2 Monte Carlo results for Northern Altiplano surface uplift histories

A Monte Carlo search, performed as described in section 3.3 (see also Fig. 3.3), with 1.64×10^5 simulations identifies a wide range of uplift histories that produce acceptable or good-fit results. Figure 3.8A shows the range of plateau uplift histories that are compatible with geological constraints. Ranges of plateau uplift histories are shown for cumulatively applied constraints, to demonstrate how each of the good fit criteria (incision onset constraint, incision completion constraint, and river χ^2 misfit) determines the final set of results. Each shaded region encompasses several individual uplift histories that fit the specified constraints (Fig. 3.8B). Not all past elevation paths within the shaded region can necessarily produce a good fit result, rather all good fit results lie within the shaded region. Different regions indicate how each individual constraint determines the acceptable uplift history range. In these, and all following figures, 'plateau elevation' refers to the elevation of the undissected plateau (e.g. Fig. 3.7B).

Monte Carlo searches reproduce the modern river profile with a $\chi^2 < 2$ under a wide range of uplift histories and the χ^2 misfit alone does not define a meaningful uplift history range (region 1, Fig. 3.8A). This range includes uplift histories with initial elevations at 16 Ma between 1.5 and 3 km, those with close to modern elevations at 14 Ma, and those in which elevations remain below 2 km until 2 Ma.

The more extreme of these uplift scenarios are geologically unrealistic. Applying incision-timing constraints greatly reduces the range of acceptable uplift histories. Application of the incision onset constraint results in the rejection of uplift histories in which high (>3.5 km) plateau elevations are attained prior to 13 Ma (region 2, Fig. 3.8A).

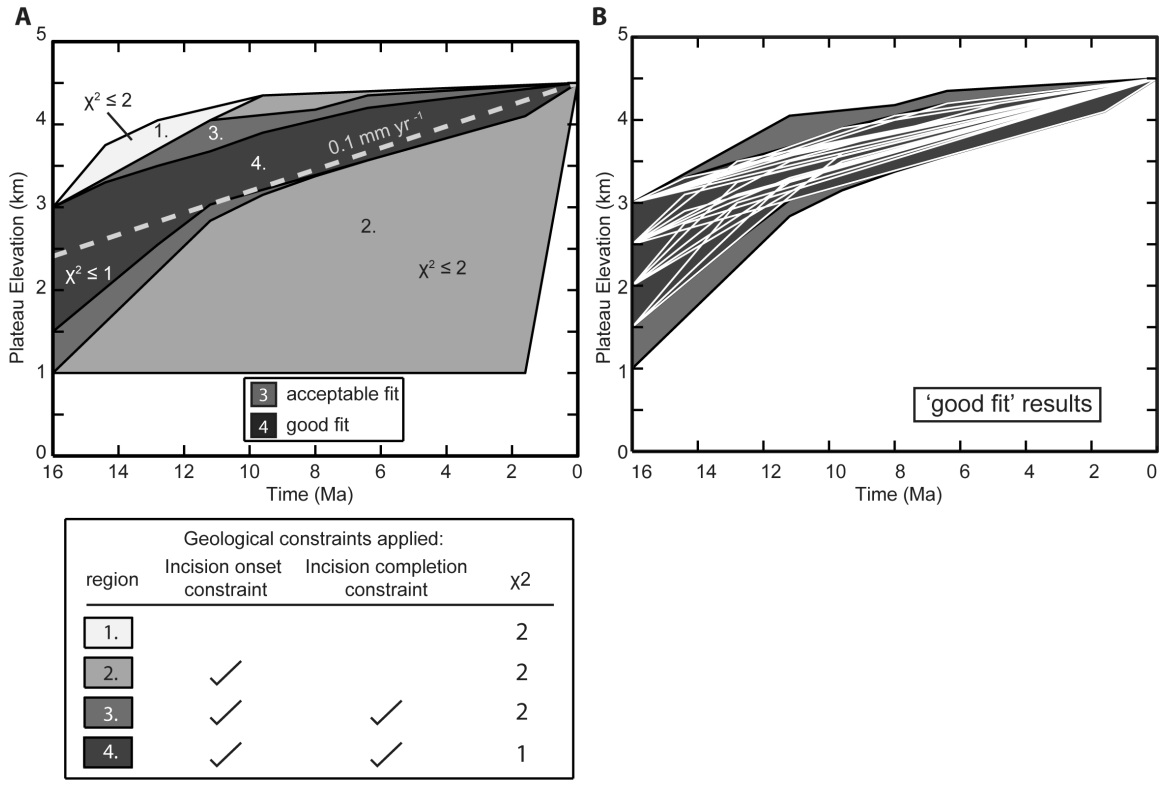

Figure 3.8. Past plateau elevations consistent with geological constraints.

A) Past plateau elevations that produce acceptable fits to the following, cumulatively applied, geological constraints in a Monte Carlo search: 1) River χ^2 misfit less than or equal to 2, 2) Incision onset constraint; Total incision at 12 Ma must be less than 600 m, 3) Incision completion constraint; Incision is at least 90 % complete by 2 Ma. 4) Simulations that fit both timing constraints with a river χ^2 misfit less than or equal to 1. An uplift rate of 0.1 mm yr^{-1} is shown for reference (dashed gray line). 'Acceptable' and 'good' fit results are shown as regions 3 and 4 respectively. B) Individual plateau uplift histories (white) that define region 4 of Fig. 3.8A.

Application of the incision completion constraint reduces the parameter space by rejecting scenarios in which low elevations persist throughout the simulation (region 3, Fig. 3.8A). The range of uplift histories is reduced still further when results are restricted to those that fit both geological constraints and have a river χ^2 misfit < 1 (region 4, Fig. 3.8A). Of the 1.64×10^5 scenarios tested, 114 produced an acceptable fit to the model constraints (region 3, Fig. 3.8A) and 52 produced a good fit to the model constraints (region 4, Fig. 3.8A and 3.8B).

In combination, the constraints require that plateau elevations were 1.5–3 km at 16 Ma, reached a minimum of ~3 km by 10 Ma, and ~3.5 km by 5 Ma. Plateau elevations close to the modern may have been attained as early as 6 Ma and as late as <1 Ma. Individual uplift paths (Fig. 3.8B) indicate that, with one exception, most good fit simulations have an uplift history that slows over time. The switch to a lower uplift rate occurs anywhere between 14 and 5 Ma. Only uplift rates that were close to, or less than, ~0.1 mm yr^{-1} over the last 6 Ma are compatible with the incision completion constraint.

3.4.3 River incision parameters

The Monte Carlo search not only identifies the range of uplift histories, but also the range of river erosion parameters that are capable of producing good fit results. The number of simulations that produced acceptable or good-fit results with each discrete value of parameters k_b, D, and b_w, and the initial elevation, E_i, are shown in Figure 3.9. Simple, individual simulations (not shown) demonstrate that the sensitivity of profile evolution to an individual erosion parameter is significant. However, many parameter values included in the search yield an acceptable fit when combined with an appropriate combination of other parameters. Search results demonstrate that the erosivity constant, k_b, is limited to between 1.25×10^{-33} and $50\text{x}10^{-33}$ $m^{5/2}yr^2kg^{-3/2}$ (Fig. 3.9A). The largest number of good-fit results were found for $k_b = 2.5\times10^{-33}$ $m^{5/2}yr^2kg^{-3/2}$.

The frequency plots do not indicate a strong preference for particular values of the other model parameters. The range of grain sizes that resulted in acceptable fit simulations is limited to those with a median grain size of less than 10 cm (D, Fig.

3.9B), corresponding to a critical shear stress of 73 Pa. No simulations with zero erosion threshold were successful at the $\chi^2 \leq 1$ level, which indicates the importance of including an erosion threshold in the model formulation and suggests that threshold processes were important in the evolution of the canyon. Only values of b_w between 0.4 and 0.5 produced good fit results (Figs. 3.9C and 3.9D), and only one simulation with b_w equal to 0.55 gave an acceptable fit to the results. Similarly, larger median grain sizes, and therefore a higher erosion threshold require more easily erodible substrate to produce a good fit to the constraints. Figure 8 emphasizes the benefits of using a Monte Carlo search approach to the investigation

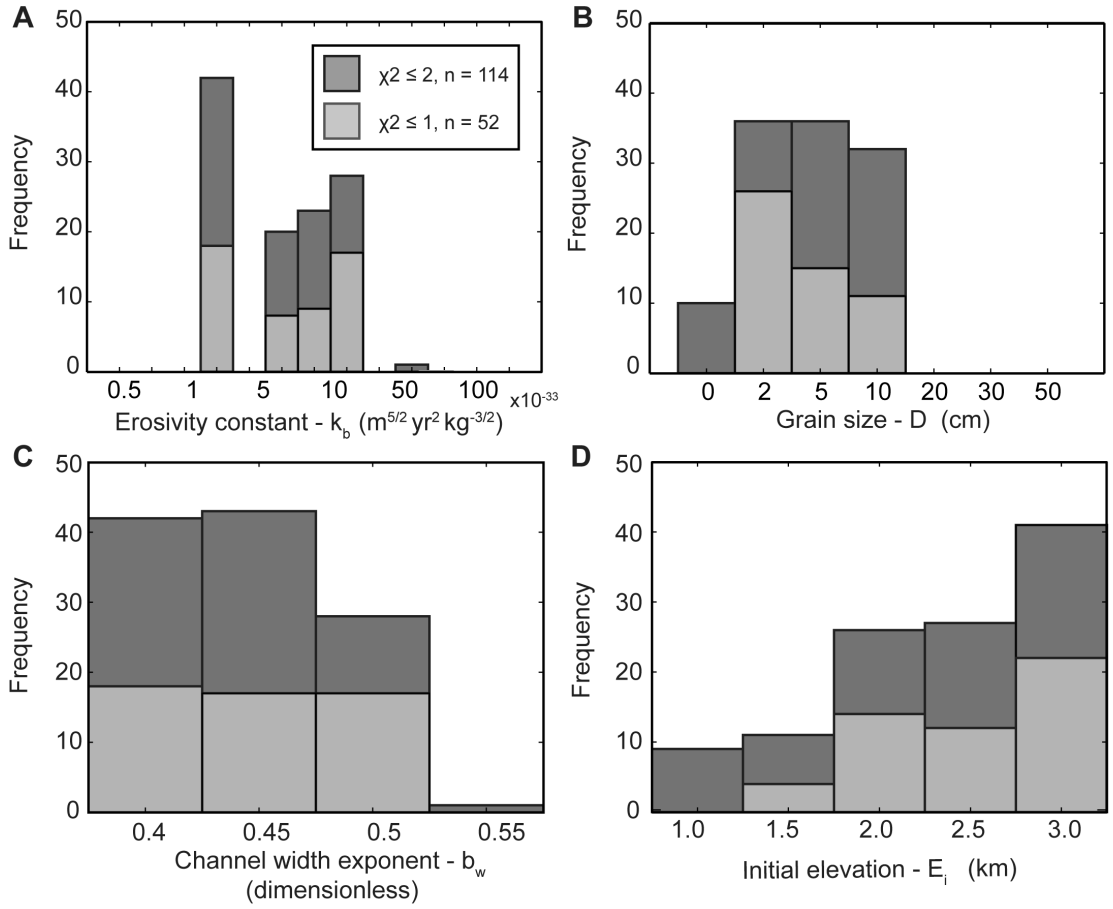

Figure 3.9. Frequency histograms of parameters that give good fit results.

Number of parameter combinations found that fit both timing constraints and the modern river profile with a $\chi^2 < 2$ (dark gray) and $\chi^2 < 1$ (light gray). A) Erosivity constant, k_b, ($m^{5/2}yr^2kg^{-3/2}$). B) Modal grain size, D (cm). C) Channel width exponent, b_w, (dimensionless) D) Initial elevation, E_i (km). See Table 3.1 and section 3.3 for further explanation of parameters.

of river incision development. The three river erosion parameters are under-constrained for the river of interest and assuming a single value for each parameter would have resulted in the omission of plausible uplift histories (Fig. 3.8).

3.5 DISCUSSION

3.5.1 Surface uplift of the Northern Altiplano

This study is motivated by the hypothesis that the influence of climate change on river incision could reconcile observations of high-magnitude river incision with a slow and steady end-member model of surface uplift [*Barnes and Ehlers*, 2009; *Ehlers and Poulsen*, 2009]. Our results show that a wide range of Northern Altiplano uplift histories are consistent with records of incision on the western flanks. Our results suggest that at 16 Ma, the Northern Altiplano was between 1 and 3 km elevation (Fig. 3.8), by 10 Ma elevations had reached 3–3.75 km, and by 5 Ma plateau elevations exceeded 3.5 km. Both the range of good-fit uplift histories (Fig. 3.8) and uplift paths from individual simulations indicate that uplift rates slowed through time. That is, most successful search results indicate uplift rates were slower in the second uplift stage than the first uplift stage. Timing of the transition between the two uplift stages varies considerably between 14 and 5 Ma and is independent of the initial plateau elevation.

Incision timing constraints play an important role in determining the good-fit uplift history range shown in Figure 3.8. The incision onset constraint determines the upper limit of plateau elevation through time and requires that plateau elevations were below 3.5 km until 13 Ma. In contrast, the incision completion constraint determines the lower limit of plateau elevation development. Volcanic deposits that are close to the modern day river elevation and dated at ~2 Ma were used to define the incision completion constraint (Fig. 3.1B). Simulations that have sufficiently low incision rates during the last 2 Ma to fit this constraint are those in which recent (<5 Ma) plateau uplift rates are low (< ~0.1 mm yr^{-1}) and the river profile is approaching topographic steady-state. The lack of knick-points is consistent with, though not conclusive evidence for, topographic steady state and low incision rates. Other processes, such as a reduction in precipitation, lithological

boundaries, drainage re-organization, or volcanic infill, can limit incision rates and may explain the small incision magnitudes since 2 Ma. If these processes are important, modern uplift rates may be higher than those found in the Monte Carlo process. It is unlikely that a lithological change caused a slowing of incision rates in the last 2–5 Ma because the river has incised through >1 km of Paleozoic to Mesozoic intrusive rocks. Volcanic valley fill may have slowed river incision by covering the valley base and by providing an additional source of sediment that would delay bedrock incision until the sediment was flushed out of the system.

3.5.2 Three-stage uplift scenario

Stable isotope based paleoelevation reconstructions from the Southern Altiplano that assume no change in climate from the modern suggest that a phase of rapid elevation increase of up to ~2 km occurred between 10 and 6 Ma [*Garzione and Hoke*, 2006; *Garzione et al.*, 2008; *Ghosh et al.*, 2006; *Quade et al.*, 2007]. By prescribing a two-phase uplift history, the model-setup presented in Figure 8 does not permit a pulse of rapid uplift during the late Miocene and therefore does not permit a fair comparative evaluation of the 'slow and steady' and 'punctuated' end-member models of surface uplift [*Barnes and Ehlers*, 2009]. We address this alternative uplift scenario with an additional Monte Carlo search in which uplift is permitted to occur in 3 stages (Fig. 3.10). In order to reduce the number of possible parameter combinations and to make the search viable, the discretization of parameter space is coarser than in the two stage uplift search. During each stage, uplift amounts (U_{a1} and U_{a2}) are discretized at 0, 0.2, 0.4, 0.6, and 0.8 times the total elevation increase (Table 3.1). To evaluate this we conducted an additional 1.6×10^6 Monte-Carlo simulations, of which 1013 produced an acceptable fit to the model constraints and 352 produced a good fit to the model constraints.

The initial elevation range found by the three-stage uplift search is greater than that found in the two-stage uplift search (1–3 km, Fig. 3.8 and Fig. 3.10). Furthermore, three-stage uplift permits a wider range of elevations throughout the remainder of the simulation duration. For three-stage uplift, good fit results indicate plateau surface elevations were between 2.75 km and 4 km at 10 Ma, and between

3.0 and 4.25 km at 5 Ma. Good-fit results include some that are consistent with the punctuated uplift end-member model. These simulations have uplift rates that are initially low (<0.15 mm yr^{-1}) followed by a pulse of high uplift rates. However, the timing of the uplift pulse is generally earlier than that found in proxy records. Simulated uplift pulses begin 14-11 Ma and last for 1.5-3 Myr, before decreasing for the final uplift stage. The Monte Carlo search also found good fit scenarios in which uplift rates are slowest during the second stage, and those in which uplift rates are close to steady throughout the simulation. The lower bound on acceptable past plateau elevation is lower for three-stage uplift than two-stage throughout the time period of simulation. The upper bound on the plateau elevation range is similar.

Uplift histories constrained by incision of the Ocoña canyon are consistent with either a 'slow and steady' or a 'punctuated' model of surface uplift. In reality, it is likely that the regional uplift history was more complex than any of the scenarios explored in this study, both in space and in time. For example, coastal morphology suggests renewed uplift of >100 m during the Quaternary [*Regard et al.*, 2010]. However, existing geological constraints do not require or enable the identification of these complexities. Because the Ocoña canyon is located at the northern margin of the Altiplano, the range of uplift histories presented here are most relevant to the northern Altiplano. However, climate change as a result of Andean uplift may also help to explain incision amounts and timing elsewhere on the Altiplano flanks. Climate driven incision may have been more substantial on the eastern flanks where the magnitude of precipitation change was greatest.

3.5.3 Block uplift scenario

Based on combined sedimentology and thermochronology observations, Schildgen et al., [2009a] suggest that uplift of the south Peruvian Forearc occurred in two phases with distinct styles. Within ~50 km of the coast, a regional bajada surface is capped by coarse river gravels that are thought to have graded to sea level at the time of abandonment. Intercalated ashes indicate that the bajada was active until ~5 Ma in the Vitor and Sihuas valleys, to the east of the Ocoña catchment. These valleys also contain large (~1 km) knick-points at 40-60 km from the modern

coastline that are likely related to abandonment of the bajada surface [*Schildgen et al.*, 2009a]. Similar gravels are present in the Ocoña catchment, but no major knick-point is present due to the relatively faster response time of the larger catchment. To account for both incision onset prior to ~8 Ma and active, shallow river channels near the coast at ~5 Ma, Schildgen et al., [2009a] propose a change in uplift style ~5 Ma. In this scenario, the Western Cordillera was initially uplifted relative to the piedmont by monoclinal folding during phase one, followed by a second phase of ~1 km of block uplift extending from the plateau to the coast.

The original Monte Carlo search presented does not include a stage of block uplift, and due to the model formation, incision of the piedmont begins early (<14 Ma) in all simulations. We therefore test the above scenario with a suite of simulations in which the uplift style is prescribed to change from monoclinal to block uplift during the simulation. During phase one (monoclinal uplift), two uplift

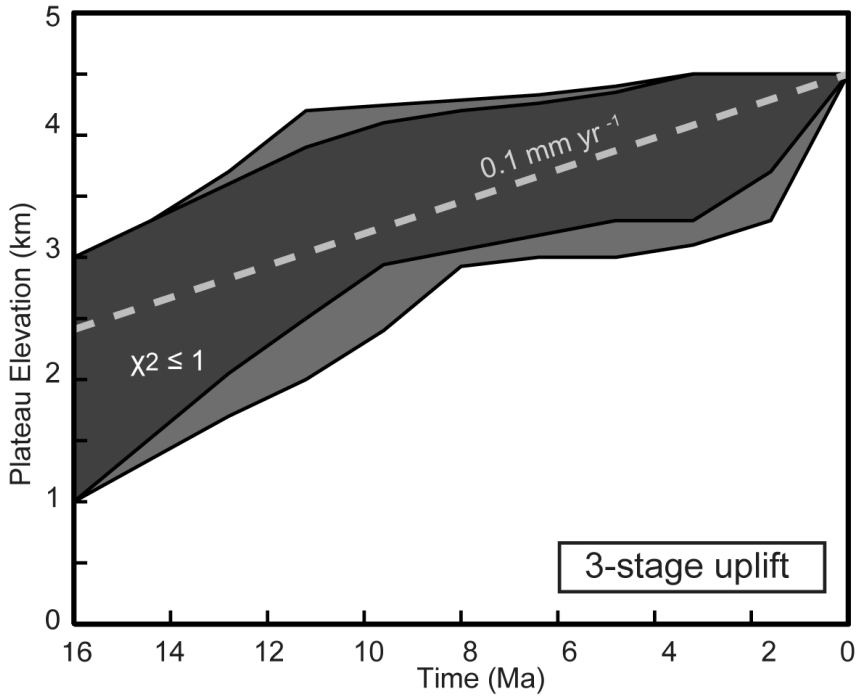

Figure 3.10. Three-stage uplift experiment.

Past plateau elevations that fit both timing constraints with a $\chi^2 \leq 1$ (light gray) and a $\chi^2 \leq 2$ (dark gray) for simulations in which uplift is permitted to occur in three stages. Dashed gray line is a visual guide and indicates a steady uplift rate of 0.1 mm yr^{-1}.

stages are permitted to raise the paleosurface from the initial elevation to a prescribed height below the modern paleosurface elevation. Phase two (block uplift) is permitted to begin between 9.6 and 3.2 Ma. The uplift amount during phase two is defined as the modern elevation of the paleosurface at the coast (800 m). All other parameter ranges are the same as in the original Monte Carlo search (Table 3.1, Fig. 3.8) and precipitation rates are prescribed to vary with plateau elevation (Fig. 3.3C). Simulations are evaluated in the same way as the previous Monte Carlo searches using the incision onset and completion constraints, and a χ^2 comparison with the model river profile. There are therefore two aspects of the uplift history that are explored using the 'block uplift' Monte Carlo search; 1) the rates of uplift during the two stages of the first monoclonal uplift phase, and 2) the timing of transition to block uplift.

Good fit results found in the block uplift search have initial elevations between 1 and 2 km at 16 Ma (Fig. 3.11A), which is lower than in the two and three-stage uplift searches. Many good fit simulations have uplift rates that are initially slow and start to increase between 10 and 8 Ma for the second stage of the monoclinal uplift phase (Fig. 3.11A). However, some good fit simulations have a steady uplift rate during the first phase. Transition to the block uplift phase occurs between 9.6 and 6.4 Ma, with later block uplift initiation (at 4.8 or 3.2 Ma) not yielding good fit results. Uplift rates are slower during the second uplift phase than the first. Based on the original constraints alone, these results indicate that the proposed block uplift scenario is equally successful as previous searches in fitting the incision observations. Importantly, this scenario identifies some scenarios with low plateau elevations (<2.5 km) that persist until at least 11 Ma, and a rapid uplift event between 11 and 6 Ma that are consistent with the punctuated uplift model.

However, simulations that are identified as 'successful' by the existing constraints produce river profiles that do not compare well with the modern river profile, despite low χ^2 values (Fig. 3.11B). The change in uplift style results in the generation of knick-points that are not fully transmitted through the catchment before the end of the simulations. In contrast, simulations that yield low χ^2 values in the two and three-stage uplift scenarios (Fig. 3.8 and Fig. 3.10) have final river

profiles that do not contain knick points and compare well with the modern river profile (Fig. 3.3). The block uplift search was therefore unable to find a set of parameters that could both propagate the knick-point upstream before the end of the simulation and fit the timing constraints. There are two possible explanations for this; 1) the block uplift hypothesis is not able to explain the observations, or 2) the current model formulation is too simple. In reality, for example, the plateau may have attained modern elevations before the present day, or the transition from monoclinal to block uplift may not have been so abrupt. Future research efforts could explore variations on the block uplift model presented here to identify uplift rates and patterns that incorporate a component of block uplift and produce a better fit to the modern river profile.

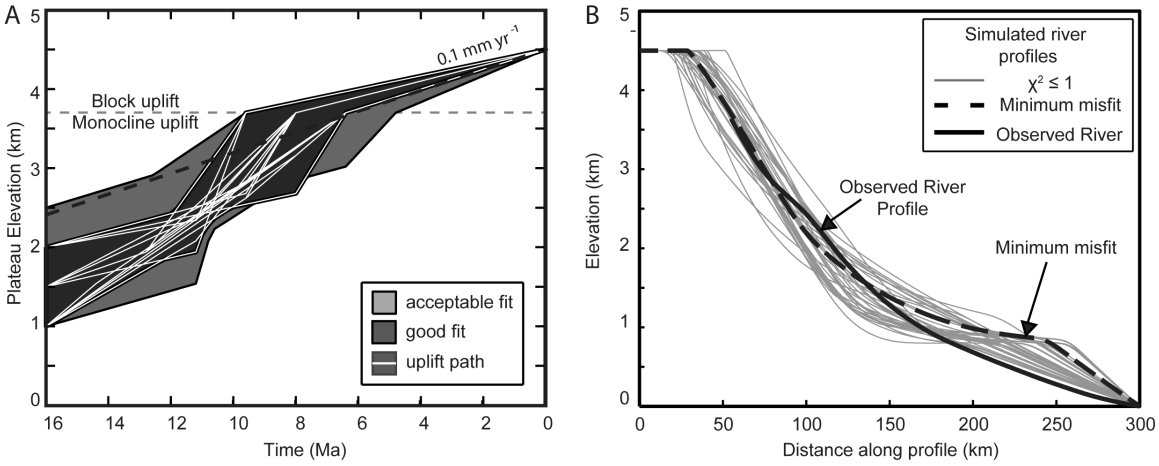

Figure 3.11. Block Uplift.

A) Range of uplift histories that fit the timing constraints with a $\chi^2 < 1$ (white lines on dark grey region), and with a $\chi^2 < 2$ (light grey region). The horizontal dashed line at 3.7 km indicates the elevation at which uplift transitions from monoclinal to block uplift. An uplift rate of 0.1 mm yr^{-1} is shown for reference. B) Range of simulated river profiles that match the modern river profile (black) with a χ^2 less than 1 in the block uplift simulations (Fig. 3.11A). The final river profile with the lowest χ^2 misfit found by the Monte Carlo search is shown in dashed black. Note that most profiles found in this search contain a knick point that is not present in the observed river profile.

3.5.4 Role of climate change in determining incision timing

A second aim of this study is to quantify the importance of paleoclimate and climate change to river incision processes. To the best of our knowledge, this study is unique in that it uses the results of a regional climate model as input to the river incision model and therefore accounts for both regional and orographic changes in climate. Here we describe the results of two additional Monte Carlo searches that were used to (1) demonstrate the importance of climate change though time, and (2) test the sensitivity of the model to the magnitude of precipitation. In the first of these additional Monte Carlo searches, precipitation was held constant at a rate corresponding to the modern Andean elevation (100%, Fig. 3.3C) throughout each individual simulation in the same way as the climate sensitivity experiment (Fig. 3.7). In the second search, precipitation rates are tied to elevation, as outlined in section 3.2, but the magnitude of discharge is reduced by 50% at all elevations.

Lower plateau elevations prior to ~10 Ma are favored when precipitation rates are held constant (Fig. 3.12A) than when precipitation rates increase with increasing elevation (Fig. 3.8). The range of initial plateau elevations is restricted to 1–2.5 km under constant precipitation rates. Between 16 and 12 Ma, the upper-bound of plateau elevations is ~500 m lower when precipitation is held constant (Fig. 3.8 and Fig. 3.12A). Furthermore, a large number of the good fit simulations are initiated at 2 km or less in the constant precipitation scenario whereas scenarios with elevation dependent precipitation rates were more commonly found to produce good fit scenarios when initiated at 2 km elevation or higher (Fig. 3.9D). The lower bound on plausible plateau elevations is also lower prior to ~6 Ma. After ~6 Ma, a wider range of elevations are permitted when climate is not dependent on surface elevation. Because precipitation rates do not vary through time, changes in erosion potential are driven solely by changes in slope, which in turn are governed by the uplift history. Elevations greater than 3 km prior to ~12 Ma are not compatible with a modern climate because the combination of high slopes and high discharge drive rapid incision that breaks the incision onset constraint.

Accounting for varying precipitation rates therefore alters the interpretation of surface uplift histories from records of river incision. Paleoelevation estimates

that account for increasing precipitation rates can be up to 500 m higher than estimates based on the modern precipitation distribution. Coupled climatic and tectonic changes both contribute significantly to the evolution of the river profile. Time variant precipitation rates modify erosion potential and, consequently, the response time of the system to perturbations [*Whipple*, 2001]. Note that it is possible to identify river profile evolution scenarios that are consistent with the 'slow and steady' end member model of Andean uplift even when a modern climate regime is assumed (Fig. 3.12A).

In the second climate sensitivity experiment, we test the sensitivity of the model to discharge magnitudes using a Monte Carlo search with 50% less discharge (Fig. 3.12B). This sensitivity experiment addresses two uncertainties in the original model formulation. First, infiltration and evaporation rates were not accounted for in the original Monte Carlo search (Fig. 3.8) and all precipitation is assumed to become surface runoff. Second, the experiment addresses uncertainties in the climate model inputs to the river simulations. River incision is sensitive to both the magnitude and spatial distribution of precipitation [*Roe et al.*, 2002]. In comparison with modern observations, RegCM over-estimates the magnitude of precipitation over South America for the modern climate, but simulates the spatial distribution of precipitation well [Fig. 3.2C, *Insel et al.*, 2010]. The simulated increase in precipitation with increasing plateau elevation is consistent with similar studies using climate models with different resolutions and precipitation parameterization [*Insel et al.*, 2012; *Jeffery et al.*, 2012]. Paleoclimate simulation results are supported by sedimentological evidence from northern Chile (19–21 °S) that indicates precipitation rates on the western edge of the Altiplano have increased since the middle Miocene whereas the coastal regions have experienced continued aridity [*Schlunegger et al.*, 2010]. The largest uncertainty in climate model inputs is therefore considered to be the magnitude of precipitation, which is addressed using the 50% discharge experiment.

Reducing the magnitude of discharge has a limited impact on the range of surface uplift histories (Fig. 3.8 and Fig. 3.12B). Between 16 and 11 Ma, the lower

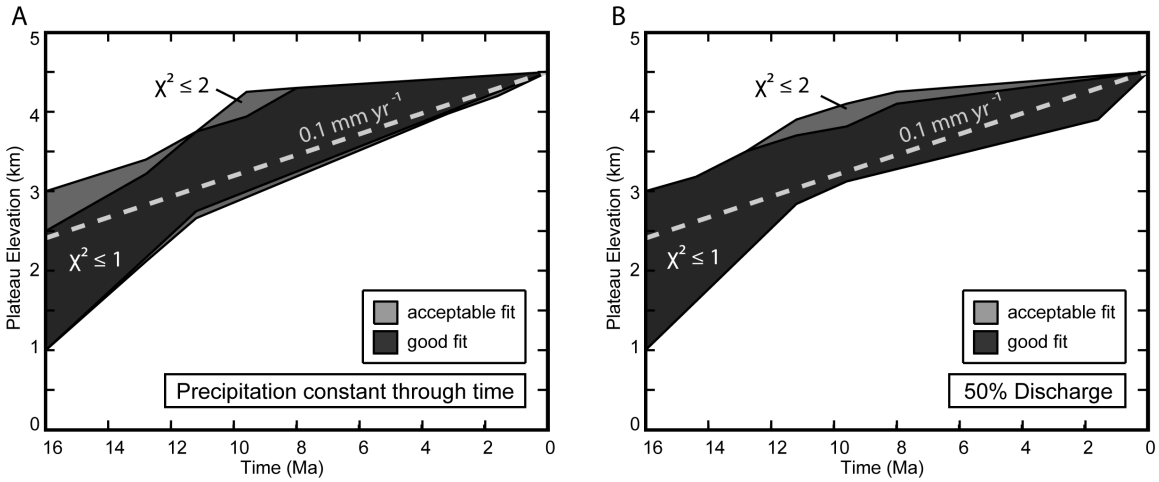

Figure 3.12 Climate influence on timing of incision

Past plateau elevations that fit both timing constraints with a $\chi^2 \leq 2$ (light gray) and a $\chi^2 \leq 1$ (dark gray) for simulations in which A) precipitation rate is held constant through time at a rate corresponding to 100% Andes elevation (Fig. 3.3C), and B) discharge is reduced to 50% compared with the original search (Fig. 3.8). The dashed gray line is a visual guide and indicates a steady uplift rate of 0.1 mm yr^{-1}.

limit of uplift ranges is up to 500 m lower in the 50% discharge case, with the maximum difference at the beginning of the simulation (16 Ma). However, only three uplift histories that were initiated with a plateau elevation <2.5 km gave a good fit to the model constraints. The upper limit on uplift ranges in the two scenarios is very similar throughout the simulation period (Fig. 3.8 and Fig. 3.12). We note that this minimal effect of changing precipitation magnitudes from the climate model on the river profiles is due to the fact that the erosion parameters, such as k_b (equation 6) and b_w (equation 4), offset the effect of discharge magnitude.

Extraction of uplift histories from river profiles is sensitive to both the temporal distribution and the magnitude of the assumed precipitation. In catchments where precipitation rates increase with increasing regional topography, such as the Ocoña, over-estimating the magnitude of precipitation can result in an under-estimation of the minimum elevation. Furthermore, ignoring the increase in precipitation rates with increasing topographic elevation can result in the underestimation of the maximum elevation. However, given the large uncertainties in river erosion parameterization, there is significant overlap in good-fit uplift histories under the three different climatic scenarios considered here (Figs 3.8 and

3.12). The range of uplift histories established in the original Monte Carlo search (Fig. 3.8) is therefore considered robust with respect to the uncertainties in climate model derived inputs to the model.

3.5.5 Model validation and sensitivity of results to model formulation

As with any modeling study, the simulations presented here include simplifications and assumptions. Geological factors that are not explicitly accounted for in the model include drainage re-organization, lithological variations, volcanic valley infill, mass wasting, and glaciation. The model also assumes that the river is governed by detachment-limited erosion and sediment flux is not explicitly accounted for. In order to validate our results, we examine and when possible quantify, the impact of these factors on the range of acceptable plateau histories identified by the model.

3.5.5.1 Drainage area

Conceivable changes to the catchment area include capture of the upper branches (Cotahuasi or Maran canyons, Fig. 3.1), and growth of the catchment by headward erosion. Capture of a drainage area similar in magnitude to the Cotahuasi branch would result in a step increase in discharge and trigger an increase in erosion rate that would propagate upstream. A drainage capture event could drive a rapid increase in incision rate and is an alternative to rapid surface uplift as a driver of incision. However, at present there is no direct evidence for a drainage capture event within this catchment. Similarly, drainage area increase by headward erosion would progressively increase the total discharge at a point on the profile. If the increase in erosional capacity causes the flow to exceed the erosion threshold, active incision would be initiated. Both of the catchment area scenarios are consistent with our key finding that the observed pulse of river incision does not necessitate low plateau elevations in the mid-Miocene.

3.5.5.2 Catchment properties

A wide range of values for the erosivity constant (k_b) was included in the Monte Carlo search (Table 3.1). However, for each simulation the selected value was

held constant in space and time. This model formulation assumes that the underlying lithology is uniform throughout the catchment, which in reality is not the case (see supplementary material). Elsewhere on the western Andean flank, Abbuehl et al. [2011] find evidence for incision through an erosion resistant caprock that delayed faster incision into the weaker, underlying rocks. However, the main lithological transition encountered by the river was from the conglomeratic Moquegua formation to the stronger, intrusive Paleozoic–Mesozoic basement. This transition may have slowed incision but did not stop it as >1 km of basement rock has been incised in the middle reaches.

3.5.5.3 Erosion law

This study uses a simple stream-power based erosion law with an effective linear exponent. However, plausible uplift histories are not sensitive to the choice of exponent (a) in the erosion law (Equation 3.1). A Monte Carlo search performed with $a = 5/2$ (not shown), consistent with erosion by suspended load abrasion, found good-fit uplift histories that are very similar to those found with $a = 3/2$. Good fit simulations found with $a = 5/2$ had a lower critical shear stress range than with $a = 3/2$.

The model used in this study assumes that erosion is detachment-limited. That is, incision is limited by the ability of the river to detach material from the bed. Influx of material to the valley by mass wasting or volcanic debris is not explicitly accounted for. The use of an erosion threshold term partly accounts for the need to transport a sediment load, but does not account for temporal variation in the amount of sediment cover or the function of sediment load as an erosion tool [*Sklar and Dietrich*, 1998]. However, Whipple and Tucker [2002] outline the behavior of transport- and detachment-limited systems and we apply their findings to the Ocoña catchment as follows.

1) Transition to a transport limited system is likely when uplift slows and the river approaches steady-state, and transient conditions can be difficult to detect based on river profiles. Low incision rates in the last ~2 Ma suggest that the lower reaches of the Ocoña catchment are approaching steady state. Combined with

observations of high sediment production through landsliding in the upper canyon reaches, it is likely that some of the river is now behaving as a transport-limited system, particularly downstream of the major Maran-Cotahuasi confluence.

2) Detachment limited systems adjust to changes in base level by upstream propagation of a knick-point whereas transport-limited systems tend to undergo more uniform lowering and knick-points, where present, are more diffuse. Our conclusions are dependent on the incision timing, which we have assumed to occur under detachment-limited conditions. This assumption is supported by two lines of evidence; (1) there is exposed bedrock in the Maran branch of the modern river, and (2) apatite $^{4}He/^{3}He$ thermochronometry data are consistent with the propagation of an incisional wave [*Schildgen et al.*, 2010], which is more consistent with a detachment-limited, rather than transport-limited system [*Whipple and Tucker*, 2002]. The importance of sediment flux to river incision is likely to have increased through time as uplift and incision rates have slowed. A change in uplift rate during the last ~5 Myr may not be evident in the modern topography if incision response times have increased since the late Miocene due to a transition from detachment to transport-limited conditions. Indeed, there is no evidence in the river profile of estimates of ~300 m of coastal uplift since ~800 ka inferred from coastal morphology [*Regard et al.*, 2010].

3.5.6 Monte Carlo Search as a tool for interrogating river profile evolution

In this study, we have demonstrated a Monte Carlo approach to extract uplift history from river profiles under a climate regime that is dependent on the orogen topography. Although the Monte Carlo search process did not identify a unique uplift history, it does succeed in (1) differentiating between uplift histories that were plausible under different climatic conditions and, (2) constraining the erosion parameters that could yield a good fit to observations. Furthermore, we show that the surface uplift history can be constrained in cases where river properties such as channel widths, erosivity and erosion mechanism are not well known. Because many of the parameters are not well known, most uplift histories could produce the modern river profile (Fig. 8). Additional constraints on the timing of incision were

necessary to reduce the range of plausible uplift histories sufficiently for the results to be useful. Application of this method is therefore restricted to regions where information is available on the initial conditions and timing of incision from, for example, thermochronometry data. Better constraints on the appropriate erosion rule could better constrain surface uplift histories in Ocoña catchment.

3.6 CONCLUSIONS

In order to determine surface uplift histories of orogens from observations of river incision, it is necessary to account for spatial and temporal gradients in precipitation. By using a regional climate model, it is possible to account for changes in regional climate associated with mountain belt development in addition to local orographic effects. This is particularly important on the leeward side of mountain ranges, such as the Ocoña canyon, because simple orographic models would predict a reduction in precipitation with increasing elevation.

River simulations with a Monte Carlo search successfully constrain a range of uplift histories and erosion parameters that are consistent with geological observations. In addition to the shape of the modern river profile, constraints on the timing and magnitude of incision were necessary to define a meaningful uplift history. Furthermore, the identification of the full range of good-fit uplift scenarios requires the inclusion of an erosion threshold in the model. Our results show that high magnitudes of incision do not necessitate contemporaneous, rapid, surface uplift but that a combination of climate change and surface uplift can drive rapid river incision when erosion thresholds are attained.

Uplift histories of the northern Andean plateau constrained by canyon incision are compatible with either a ‘slow and steady’ or ‘punctuated’ surface uplift model. Arguments that canyon incision indicates rapid surface uplift are therefore not unique to geologically constrained models of river dynamics. Future work that limits the erosion parameter space will improve this techniques ability to distinguish between different uplift scenarios.

3.7 ACKNOWLEDGEMENTS:

This work was funded by grants to T.A.E. and C.J.P. from the US National Science Foundation (EAR awards 0738822, 0907817). M.L.J. was also supported by a Fellowship from the German DAAD. N. Insel is thanked for providing access to the RegCM paleoprecipitation results. We are grateful for comments by K.W. Whipple, P. van der Beek and an anonymous reviewer on an earlier version of this manuscript. The ASTER GDEM data were obtained through the online Data Pool at the NASA Land Processes Distributed Active Archive Center (LP DAAC), USGS/Earth Resources Observation and Science (EROS) Center, Sioux Falls, South Dakota (http://lpdaac.usgs.gov/get_data). The Geological Map of Peru was obtained from the website of the Instituto Geológico Minero y Metalúrgico (INGEMMET) at http://www.ingemmet.gob.pe/form/plantilla01.aspx?Opcion=184.

3.8 REFERENCES

Abbuehl, L. M., K. P. Norton, J. D. Jansen, F. Schlunegger, A. Aldahan, and G. Possnert (2011), Erosion rates and mechanisms of knickzone retreat inferred from (10)Be measured across strong climate gradients on the northern and central Andes Western Escarpment, *Earth Surface Processes and Landforms*, *36*(11), 1464-1473. 10.1002/esp.2164

Attal, M., G. E. Tucker, A. C. Whittaker, P. A. Cowie, and G. P. Roberts (2008), Modeling fluvial incision and transient landscape evolution: Influence of dynamic channel adjustment, *Journal of Geophysical Research-Earth Surface*, *113*(F3). 10.1029/2007jf000893

Barke, R., and S. Lamb (2006), Late Cenozoic uplift of the Eastern Cordillera, Bolivian Andes, *Earth and Planetary Science Letters*, *249*(3-4), 350-367. 10.1016/j.epsl.2006.07.012

Barnes, J. B., and T. A. Ehlers (2009), End member models for Andean Plateau uplift, *Earth-Science Reviews*, *97*(1-4), 105-132. 10.1016/j.earscirev.2009.08.003

Barnes, J. B., T. A. Ehlers, N. McQuarrie, P. B. O'Sullivan, and J. D. Pelletier (2006), Eocene to recent variations in erosion across the central Andean fold-thrust belt, northern Bolivia: Implications for plateau evolution, *Earth and Planetary Science Letters*, *248*(1-2), 118-133. 10.1016/j.epsl.2006.05.018

Barnes, J. B., T. A. Ehlers, N. McQuarrie, P. B. O'Sullivan, and S. Tawackoli (2008), Thermochronometer record of central Andean plateau growth, Bolivia (19.5 degrees S), *Tectonics*, *27*(3). 10.1029/2007tc002174

Bookhagen, B., and M. R. Strecker (2008), Orographic barriers, high-resolution TRMM rainfall, and relief variations along the eastern Andes, *Geophysical Research Letters*, *35*(6), 6. 10.1029/2007gl032011

Bookhagen, B., and M. R. Strecker (2012), Spatiotemporal trends in erosion rates across a pronounced rainfall gradient: Examples from the southern Central Andes, *Earth and Planetary Science Letters*, *327*, 97 - 110.10.1016/j.epsl.2012.02.005

Campetella, C. M., and C. S. Vera (2002), The influence of the Andes mountains on the South American low-level, *Geophysical Research Letters*, *29*(17). 10.1029/2002gl015451

Clark, M. K., L. M. Schoenbohm, L. H. Royden, K. X. Whipple, B. C. Burchfiel, X. Zhang, W. Tang, E. Wang, and L. Chen (2004), Surface uplift, tectonics, and erosion of eastern Tibet from large-scale drainage patterns, *Tectonics*, *23*(1). 10.1029/2002tc001402

Crosby, B. T., and K. X. Whipple (2006), Knickpoint initiation and distribution within fluvial networks: 236 waterfalls in the Waipaoa River, North Island, New Zealand, *Geomorphology*, *82*(1-2), 16-38. 10.1016/j.geomorph.2005.08.023

DeCelles, P. G., and B. K. Horton (2003), Early to middle Tertiary foreland basin development and the history of Andean crustal shortening in Bolivia, *Geological Society of America Bulletin*, *115*(1), 58-77

Decou, A., H. von Eynatten, M. Mamani, T. Sempere, and G. Woerner (2011), Cenozoic forearc basin sediments in Southern Peru (15-18 degrees S): Stratigraphic and heavy mineral constraints for Eocene to Miocene evolution of the Central Andes, *Sedimentary Geology*, *237*(1-2), 55-72. 10.1016/j.sedgeo.2011.02.004

Duvall, A., E. Kirby, and D. Burbank (2004), Tectonic and lithologic controls on bedrock channel profiles and processes in coastal California, *Journal of Geophysical Research-Earth Surface*, *109*(F3), 18.10.1029/2003jf000086

Ehlers, T. A., and C. J. Poulsen (2009), Influence of Andean uplift on climate and paleoaltimetry estimates, *Earth and Planetary Science Letters*, *281*(3-4), 238-248. 10.1016/j.epsl.2009.02.026

Farias, M., R. Charrier, D. Comte, J. Martinod, and G. Herail (2005), Late Cenozoic deformation and uplift of the western flank of the Altiplano: Evidence from the depositional, tectonic, and geomorphologic evolution and shallow seismic activity (northern Chile at 19 degrees 30 ' S), *Tectonics*, *24*(4), 29. 10.1029/2004tc001667

Farias, M., R. Charrier, S. Carretier, J. Martinod, A. Fock, D. Campbell, J. Caceres, and D. Comte (2008), Late Miocene high and rapid surface uplift and its erosional response in the Andes of central Chile (33°S -35°S), *Tectonics*, *27*. 10.1029/2006tc002046

Foley, M. G. (1980), Bed-rock incision by streams, *Geological Society of America Bulletin, Part 2*, *91*, 2189-2213

Frailey, C. D., E. L. Lavina, A. Rancy, and J. P. de Souza Filho (1988), A proposed Pleistocene/Holocene lake in the Amazon basin and its significance to Amazonian geology and biogeography, *Acta Amazonica*, *18*, 119-143

Garcia, M., R. Riquelme, M. Farias, G. Herail, and R. Charrier (2011), Late Miocene-Holocene canyon incision in the western Altiplano, northern Chile: tectonic or climatic forcing?, *Journal of the Geological Society*, *168*(4), 1047-1060. 10.1144/0016-76492010-134

Garreaud, R. D. (1999), Multiscale analysis of the summertime precipitation over the central Andes, *Monthly Weather Review*, *127*(5), 901-921. 10.1175/1520-0493(1999)127<0901:maotsp>2.0.co;2

Garreaud, R. D., M. Vuille, and A. C. Clement (2003), The climate of the Altiplano: observed current conditions and mechanisms of past changes, *Palaeogeography Palaeoclimatology Palaeoecology*, *194*(1-3), 5-22. 10.1016/s0031-0182(03)00269-4

Garzione, C. N., and G. D. Hoke (2006), Paleoelevation and geomorphic constraints on the late miocene rise of the andes: Geodynamic implications for the

growth of orogenic plateaus, *Geochimica Et Cosmochimica Acta*, *70*(18), A195-A195. 10.1016/j.gca.2006.06.393

Garzione, C. N., P. Molnar, J. C. Libarkin, and B. J. MacFadden (2006), Rapid late Miocene rise of the Bolivian Altiplano: Evidence for removal of mantle lithosphere, *Earth and Planetary Science Letters*, *241*(3-4), 543-556. 10.1016/j.epsl.2005.11.026

Garzione, C. N., G. D. Hoke, J. C. Libarkin, S. Withers, B. MacFadden, J. Eiler, P. Ghosh, and A. Mulch (2008), Rise of the Andes, *Science*, *320*(5881), 1304-1307. 10.1126/science.1148615

Ghosh, P., C. N. Garzione, and J. M. Eiler (2006), Rapid uplift of the Altiplano revealed through C-13-O-18 bonds in paleosol carbonates, *Science*, *311*(5760), 511-515. 10.1126/science.1119365

Gotberg, N., N. McQuarrie, and V. C. Caillaux (2010), Comparison of crustal thickening budget and shortening estimates in southern Peru (12-14 degrees S): Implications for mass balance and rotations in the "Bolivian orocline", *Geological Society of America Bulletin*, *122*(5-6), 727-742. 10.1130/b26477.1

Gubbels, T. L., B. L. Isacks, and E. Farrar (1993), High-level surfaces, plateau uplift, and foreland development, Bolivian central Andes, *Geology*, *21*(8), 695 – 698, 10.1130/0091-7613(1993)021<0695:HLSPUA>2.3.CO;2

Gunnell, Y., J. C. Thouret, S. Brichau, A. Carter, and K. Gallagher (2010), Low-temperature thermochronology in the Peruvian Central Andes: implications for long-term continental denudation, timing of plateau uplift, canyon incision and lithosphere dynamics, *Journal of the Geological Society*, *167*(4), 803-815.10.1144/0016-76492009-166

Hack, J. T. (1957), Studies of longitudinal sream profiles in Virginia and Maryland, U.S. Geological Survey Professional Paper, p. 45-97.

Hall, S. R., D. L. Farber, L. Audin, and R. C. Finkel (2012), Recently active contractile deformation in the forearc of southern Peru, *Earth and Planetary Science Letters*, *337 - 338*, 85 - 92.10.1016/j.epsl.2012.04.007

Hancock, G. S., R. S. Anderson, and K. Whipple (1998), Beyond power: Bedrock river incision process and form, in *Rivers over Rock: Fluvial Processes in Bedrock Channels*, edited by K. Tinkler and E. E. Wohl, pp. 35-60, AGU, Washington, D.C.

Hartley, A. J., T. Sempere, and G. Worner (2007), A comment on "Rapid late Miocene rise of the Bolivian Altiplano: Evidence for removal of mantle lithosphere" by C.N. Garzione et al. Earth Planet. Sci. Lett. 241 (2006) 543-556, *Earth and Planetary Science Letters*, *259*(3-4), 625-629.10.1016/j.epsl.2007.04.012

Hoke, G. D., B. L. Isacks, T. E. Jordan, N. Blanco, A. J. Tomlinson, and J. Ramezani (2007), Geomorphic evidence for post-10 Ma uplift of the western flank of the central Andes 18 degrees 30'-22 degrees S, *Tectonics*, *26*(5).10.1029/2006tc002082

Houston, J., and A. J. Hartley (2003), The central andean west-slope rainshadow and its potential contribution to the origin of hyper-aridity in the Atacama desert, *International Journal of Climatology*, *23*(12), 1453-1464. 10.1002/joc.938

Howard, A. D., and G. Kerby (1983), Channel changes in badlands, *Geological Society of America Bulletin*, *94*(6), 739-782. 10.1130/0016-7606

Howard, A. D., W. E. Dietrich, and M. A. Seidl (1994), Modeling fluvial erosion on regional to continental scales, *Journal of Geophysical Research-Solid Earth*, *99*(B7), 13971-13986. 10.1029/94jb00744

Huffman, G. J., R. F. Adler, D. T. Bolvin, G. Gu, E. J. Nelkin, K. P. Bowman, Y. Hong, E. F. Stocker, and D. B. Wolff (2007), The TRMM Multisatellite Precipitation Analysis (TMPA): Quasi-Global, Multiyear, Combined-Sensor Precipitation Estimates at Fine Scales, *Journal of Hydrometeorology*, *8*, 38 - 55. 10.1175/JHM560.1

INGEMMET (2004), Carta Geológica Nacional del Perú, Instituto Geologico Minero y Metalurgico (INGEMMET).

Insel, N., C. J. Poulsen, and T. A. Ehlers (2010), Influence of the Andes Mountains on South American moisture transport, convection, and precipitation, *Climate Dynamics*, *35*(7-8), 1477-1492.10.1007/s00382-009-0637-1

Insel, N., C. J. Poulsen, T. A. Ehlers, and C. Sturm (2012), Response of meteoric $\delta^{18}O$ to surface uplift - Implications for Cenozoic Andean Plateau growth, *Earth and Planetary Science Letters*, *317 - 318*, 262-272.10.1016/j.epsl.2011.11.039

Isacks, B. L. (1988), Uplift of the central Andean plateau and bending of the the Bolivian orocline, *Journal of Geophysical Research-Solid Earth and Planets*, *93*(B4), 3211-3231

Jeffery, M. L., C. J. Poulsen, and T. A. Ehlers (2012), Impacts of Cenozoic global cooling, surface uplift, and an inland seaway on South American paleoclimate and precipitation $\delta^{18}O$, *Geological Society of America Bulletin*, *124*(3-4), 335-351. 10.1130/B30467.1

Kennan, L., S. H. Lamb, and L. Hoke (1997), High-altitude paleosurfaces in the Bolivian Andes: evidence for late Cenozoic uplift, in *Special Publication of the Geological Society of London*, edited by M. Widdowson, pp. 307-323.

Kirby, E., and K. Whipple (2001), Quantifying differential rock-uplift rates via stream profile analysis, *Geology*, *29*(5), 415-418.10.1130/0091-7613(2001)029<0415:QDRURV>2.0.CO;2

Kober, F., F. Schlunegger, G. Zeilinger, and H. Schneider (2006), Surface uplift and climate change: The geomorphic evolution of the Western Escarpment of the Andes of northern Chile between the Miocene and present, in *Tectonics, Climate, and Landscape Evolution*, edited by S. D. Willett, N. Hovius, M. T. Brandon and D. M. Fisher, pp. 75-86, Geological Soc Amer Inc, Boulder.

Kober, F., S. Ivy-Ochs, F. Schlunegger, H. Baur, P. W. Kubik, and R. Wieler (2007), Denudation rates and a topography-driven rainfall threshold in northern Chile: Multiple cosmogenic nuclide data and sediment yield budgets, *Geomorphology*, *83*(1-2), 97-120. 10.1016/j.geomorph.2006.06.029

Kutzbach, J. E., P. J. Guetter, W. F. Ruddiman, and W. L. Prell (1989), Sensitivity of Climate to Late Cenozoic Uplift in Southern Asia and the American West: Numerical Experiments, *Journal of Geophysical Research*, *94*(D15), 18393-18407. 10.1029/JD094iD15p18393

Lamb, S. (2011), Did shortening in thick crust cause rapid Late Cenozoic uplift in the northern Bolivian Andes?, *Journal of the Geological Society*, *168*(5), 1079-1092. 10.1144/0016-76492011-008

Lave, J., and J. P. Avouac (2001), Fluvial incision and tectonic uplift across the Himalayas of central Nepal, *Journal of Geophysical Research-Solid Earth*, *106*(B11), 26561-26591. 10.1029/2001jb000359

Lenters, J. D., and K. H. Cook (1995), Simulation and diagnosis of the regional summertime precipitation climatology of South America, *Journal of Climate*, *8*(12), 2988-3005

Leopold, L. B., and T. Maddock (1953), The hydraulic geometry of stream channels and some physiographic implications, *U.S. Geological Survey Professional Paper*, *252*, 56

McQuarrie, N. (2002), The kinematic history of the central Andean fold-thrust belt, Bolivia: Implications for building a high plateau, *Geological Society of America Bulletin*, *114*(8), 950-963, 10.1130/0016-7606(2002)114<0950:TKHOTC>2.0.CO;2

McQuarrie, N., J. B. Barnes, and T. A. Ehlers (2008a), Geometric, kinematic, and erosional history of the central Andean Plateau, Bolivia (15-17 degrees S), *Tectonics*, *27*(3).10.1029/2006tc002054

McQuarrie, N., T. A. Ehlers, J. B. Barnes, and B. Meade (2008b), Temporal variation in climate and tectonic coupling in the central Andes, *Geology*, *36*(12), 999-1002. 10.1130/g25124a.1

McQuarrie, N., B. K. Horton, G. Zandt, S. Beck, and P. G. DeCelles (2005), Lithospheric evolution of the Andean fold-thrust belt, Bolivia, and the origin of the central Andean plateau, *Tectonophysics*, *399*(1-4), 15-37.10.1016/j.tecto.2004.12.013

METI, and NASA (2001), ASTER GDEM edited, Ministry of Economy, Trade and Industry (METI) and NASA Land Processes Distributed Active Archive Center (LP DAAC), USGS/Earth Resources Observation and Science (EROS) Center, Sioux Falls, South Dakota.

Montgomery, D. R., and K. B. Gran (2001), Downstream variations in the width of bedrock channels, *Water Resources Research*, *37*(6), 1841-1846.10.1029/2000wr900393

Muñoz, N., and R. Charrier (1996), Uplift of the western border of the Altiplano on a west-vergent thrust system, northern Chile, *Journal of South American Earth Sciences*, *9*(3-4), 171 - 181. 10.1016/0895-9811(96)00004-1

Poulsen, C. J., T. A. Ehlers, and N. Insel (2010), Onset of Convective Rainfall During Gradual Late Miocene Rise of the Central Andes, *Science*, *328*(5977), 490-493. 10.1126/science.1185078

Quade, J., C. Garzione, and J. Eiler (2007), Paleoelevation reconstruction using pedogenic carbonates, in *Paleoaltimetry: Geochemical and Thermodynamic Approaches*, edited, pp. 53-87.

Rasanen, M. E., A. M. Linna, J. C. R. Santos, and F. R. Negri (1995), Late Miocene tidal deposits in the Amazonian foreland basin, *Science*, *269*(5222), 386-390

Regard, V., M. Saillard, J. Martinod, L. Audin, S. Carretier, K. Pedoja, R. Riquelme, P. Paredes, and G. Herail (2010), Renewed uplift of the Central Andean Forearc revealed by coastal evolution during the Quaternary, *Earth and Planetary Science Letters*, *297*(1 - 2), 199 - 210. 10.1016/j.epsl.2010.06.020

Rigon, R., I. Rodriguez-Iturbe, A. Maritan, A. Giacometti, D. G. Tarboton, and A. Rinaldo (1996), On Hack's Law, *Water Resources Research*, *32*(11), 3367-3374. 10.1029/96WR02397

Roe, G. H. (2005), Orographic precipitation, *Annual Review of Earth and Planetary Sciences*, *33*, 645-671. 10.1146/annurev.earth.33.092203.122541

Roe, G. H., D. R. Montgomery, and B. Hallet (2002), Effects of orographic precipitation variations on the concavity of steady-state river profiles, *Geology*, *30*(2), 143-146.10.1130/0091-13(2002)030<0143:eoopvo>2.0.co;2

Roe, G. H., D. R. Montgomery, and B. Hallet (2003), Orographic precipitation and the relief of mountain ranges, *Journal of Geophysical Research-Solid Earth*, *108*(B6). 10.1029/2001jb001521

Roperch, P., T. Sempere, O. Macedo, C. Arriagada, M. Fornari, C. Tapia, M. Garcia, and C. Laj (2006), Counterclockwise rotation of late Eocene-Oligocene fore-arc deposits in southern Peru and its significance for oroclinal bending in the central Andes, *Tectonics*, *25*(3), 29. 10.1029/2005tc001882

Schildgen, T. F., G. Balco, and D. L. Shuster (2010), Canyon incision and knickpoint propagation recorded by apatite He-4/He-3 thermochronometry, *Earth and Planetary Science Letters*, *293*(3-4), 377-387. 10.1016/j.epsl.2010.03.009

Schildgen, T. F., K. V. Hodges, K. X. Whipple, P. W. Reiners, and M. S. Pringle (2007), Uplift of the western margin of the Andean plateau revealed from canyon incision history, southern Peru, *Geology*, *35*(6), 523-526. 10.1130/g23532a.1

Schildgen, T. F., K. V. Hodges, K. X. Whipple, M. S. Pringle, M. van Soest, and K. Cornell (2009a), Late Cenozoic structural and tectonic development of the western margin of the central Andean Plateau in southwest Peru, *Tectonics*, *28*.10.1029/2008tc002403

Schildgen, T. F., K. V. Hodges, K. X. Whipple, M. S. Pringle, M. van Soest, and K. Cornell (2009a), Late Cenozoic structural and tectonic development of the western margin of the central Andean Plateau in southwest Peru, *Tectonics*, *28*.10.1029/2008tc002403

Schildgen, T. F., T. A. Ehlers, D. M. Whipp, M. C. van Soest, K. X. Whipple, and K. V. Hodges (2009b), Quantifying canyon incision and Andean Plateau surface uplift, southwest Peru: A thermochronometer and numerical modeling approach, *Journal of Geophysical Research-Earth Surface*, *114*.10.1029/2009jf001305

Schlunegger, F., K. P. Norton, and G. Zeilinger (2011), Climatic Forcing on Channel Profiles in the Eastern Cordillera of the Coroico Region, Bolivia, *Journal of Geology*, *119*(1), 97-107. 10.1086/657407

Schlunegger, F., F. Kober, G. Zeilinger, and R. von Rotz (2010), Sedimentology-based reconstructions of paleoclimate changes in the Central Andes in response to the uplift of the Andes, Arica region between 19 and 21 degrees S latitude, northern Chile, *Int. J. Earth Sci.*, *99*, S123-S137.10.1007/s00531-010-0572-8

Schlunegger, F., G. Zeilinger, A. Kounov, F. Kober, and B. Husser (2006), Scale of relief growth in the forearc of the Andes of Northern Chile (Arica latitude, 18 degrees S), *Terra Nova*, *18*(3), 217-223.10.1111/j.1365-3121.2006.00682.x

Seidl, M. A., and W. E. Dietrich (1992), The problem of channel erosion into bedrock, in *Catena Supplement* edited by K. H. Schmidt and J. de Ploey, pp. 101-124.

Simpson, G. (2004), Role of river incision in enhancing deformation, *Geology*, *32*(4), 341-344.10.1130/g20190.1

Sklar, L. S., and W. E. Dietrich (1998), River longitudinal profiles and bedrock incision models: stream power and the influence of sediment supply, in *Rivers over rock: fluvial processes in bedrock channels*, edited by K. J. Tinkler and W. E. E., pp. 237 - 260.

Sklar, L. S., and W. E. Dietrich (2004), A mechanistic model for river incision into bedrock by saltating bed load, *Water Resources Research*, *40*(6).10.1029/2003wr002496

Snyder, N. P., K. X. Whipple, G. E. Tucker, and D. J. Merritts (2000), Landscape response to tectonic forcing: Digital elevation model analysis of stream profiles in the Mendocino triple junction region, northern California, *Geological Society of America Bulletin*, *112*(8), 1250-1263.10.1130/0016-7606(2000)112<1250:LRTTFD>2.0.CO;2

Stock, J. D., and D. R. Montgomery (1999), Geologic constraints on bedrock river incision using the stream power law, *Journal of Geophysical Research-Solid Earth*, *104*(B3), 4983-4993.10.1029/98JB02139

Strecker, M. R., R. Alonso, B. Bookhagen, B. Carrapa, I. Coutand, M. P. Hain, G. E. Hilley, E. Mortimer, L. Schoenbohm, and E. R. Sobel (2009), Does the topographic distribution of the central Andean Puna Plateau result from

climatic or geodynamic processes?, *Geology*, *37*(7), 643-646. 10.1130/G25545A.1

Thouret, J. C., G. Woerner, Y. Gunnell, B. Singer, X. Zhang, and T. Souriot (2007), Geochronologic and stratigraphic constraints on canyon incision and Miocene uplift of the Central Andes in Peru, *Earth and Planetary Science Letters*, *263*(3-4), 151-166.10.1016/j.epsl.2007.07.023

Tucker, G. E. (2004), Drainage basin sensitivity to tectonic and climatic forcing: Implications of a stochastic model for the role of entrainment and erosion thresholds, *Earth Surface Processes and Landforms*, *29*(2), 185-205.10.1002/esp.1020

Victor, P. (2004), Uplift of the western Altiplano plateau: Evidence from the Precordillera between 20° and 21°S (northern Chile), *Tectonics*, *23*.10.1029/2003tc001519

Walcek, A. A., and G. D. Hoke (2012), Surface uplift and erosion of the southernmost Argentine Precordillera, *Geomorphology*, *153 - 154*, 156 - 168.10.1016/j.geomorph.2012.02.021

Whipple, K. X. (2001), Fluvial landscape response time: How plausible is steady-state denudation?, *American Journal of Science*, *301*(4-5), 313-325

Whipple, K. X. (2009), The influence of climate on the tectonic evolution of mountain belts, *Nature Geoscience*, *2*(2), 97-104.10.1038/ngeo413

Whipple, K. X., and G. E. Tucker (1999), Dynamics of the stream-power river incision model: Implications for height limits of mountain ranges, landscape response timescales, and research needs, *Journal of Geophysical Research-Solid Earth*, *104*(B8), 17661-17674.10.1029/1999JB900120

Whipple, K. X., and G. E. Tucker (2002), Implications of sediment-flux-dependent river incision models for landscape evolution, *Journal of Geophysical Research-Solid Earth*, *107*(B2).10.1029/2000jb000044

Whipple, K. X., G. S. Hancock, and R. S. Anderson (2000), River incision into bedrock: Mechanics and relative efficacy of plucking, abrasion, and cavitation, *Geological Society of America Bulletin*, *112*(3), 490-503

Whittaker, A. C., M. Attal, P. A. Cowie, G. E. Tucker, and G. Roberts (2008), Decoding temporal and spatial patterns of fault uplift using transient river long profiles, *Geomorphology*, *100*(3-4), 506-526, 10.1016/j.geomorph.2008.01.018

Willett, S. D. (1999), Orogeny and orography: The effects of erosion on the structure of mountain belts, *Journal of Geophysical Research-Solid Earth*, *104*(B12), 28957-28981.10.1029/1999jb900248

Wobus, C. W., G. E. Tucker, and R. S. Anderson (2010), Does climate change create distinctive patterns of landscape incision?, *Journal of Geophysical Research-Earth Surface*, *115*.10.1029/2009jf001562

Wolman, M. G., and J. P. Miller (1960), Magnitude and frequency of forces in geomorphic processes, *Journal of Geology*, *68*, 54-74

Wörner, G., D. Uhlig, I. Kohler, and H. Seyfried (2002), Evolution of the West Andean Escarpment at 18°S (N. Chile) during the last 25 Ma: uplift, erosion and collapse through time, *Tectonophysics*, *345*(1-4), 183 - 198. 10.1016/S0040-1951(01)00212-8

Wu, S. L., R. L. Bras, and A. P. Barros (2006), Sensitivity of channel profiles to precipitation properties in mountain ranges, *Journal of Geophysical Research-Earth Surface*, *111*(F1). 10.1029/2004jf000164

Yanites, B. J., and G. E. Tucker (2010), Controls and limits on bedrock channel geometry, *Journal of Geophysical Research-Earth Surface*, *115*.10.1029/2009jf001601

Yanites, B. J., G. E. Tucker, K. J. Mueller, and Y.-G. Chen (2010), How rivers react to large earthquakes: Evidence from central Taiwan, *Geology*, *38*(7), 639-642.10.1130/g30883.1

Zaprowski, B. J., F. J. Pazzaglia, and E. B. Evenson (2005), Climatic influences on profile concavity and river incision, *Journal of Geophysical Research-Earth Surface*, *110*(F3). 10.1029/2004jf000138

CHAPTER 4

PRECIPITATION AND VEGETATION CONTROLS ON TOPOGRAPHY OF THE CENTRAL ANDES

Abstract

Field observations and landscape evolution models indicate that landscape processes in active mountain belts are strongly dependent on vegetation and climate. In fluvial landscapes, erosional efficiency is commonly thought to depend on the intensity, frequency, and duration of precipitation events. We use Tropical Rainfall Measuring Mission (TRMM) observations to test the importance of precipitation intensity in determining geomorphology at the mountain belt scale. Precipitation metrics, including mean annual precipitation, and the mean intensity, duration, and frequency of precipitation events, are derived from the TRMM 3B42v7 product. Topographic characteristics are calculated from the SRTM 90 data set. The new precipitation datasets are then compared with mean hillslope gradients in the central Andes using correlation analyses and multiple linear regression. The importance of different precipitation metrics in controlling the regional topographic characteristics is quantified and spatial variations in bedrock lithology, and the amount and type of vegetation cover are considered in the analysis.

Results indicate that mean hillslope gradient correlates most strongly with percent vegetation cover ($r = 0.56$). Where vegetation cover is less than 95%, mean hillslope gradients increase with mean annual precipitation ($r=0.60$) and vegetation density ($r = 0.69$). Where vegetation cover is dense (>95%), mean hillslope gradients decrease with increasing precipitation intensity by ~0.5° /mm day^{-1} ($r = -0.56$). Climate influences on topography are therefore mediated by vegetation,

which itself is also dependent on mean annual precipitation (r = 0.77). Bedrock lithology and spatial variations in uplift rate also influence mean hillslope gradients. Observations from the central Andes are consistent with landscape evolution models in which hillslope gradients are determined as a balance between rock uplift, climatic erosional efficiency and erosional resistance of the landscape determined by bedrock lithology and vegetation.

4.1 INTRODUCTION

Through erosional processes, precipitation has the potential to determine topographic characteristics of active mountain belts from the catchment to orogen scales [*Koons*, 1990; *Willett*, 1999]. Detecting clear and consistent climatic signals in topography and the distribution of erosion has proved challenging [*Whipple*, 2009], in part because climate is also dependent on topography [*Galewsky*, 2009; *Kutzbach et al.*, 1989; *Roe et al.*, 2008]. Another factor is that climate–topography interactions are commonly explored using long-term mean observations, such as mean annual precipitation (MAP). However, the erosional efficiency of climate may be more usefully described in terms of the variability, or storminess, of precipitation [*Dadson et al.*, 2003; *Lague et al.*, 2005; *Molnar et al.*, 2006; *Tucker and Bras*, 2000]. Precipitation events can be described in terms of the intensity (P), duration (D) and frequency ($1/I$) [Fig. 1, *Eagleson*, 1978]. Landscape evolution models (LEMs) predict that at higher mean precipitation intensity, fluvial landscapes will have lower relief, higher drainage density and higher mean erosion rates [*Tucker*, 2004; *Tucker and Slingerland*, 1997; *Tucker and Bras*, 2000]. The role of precipitation variability is particularly important when the geomorphic process is dependent on discharge exceeding a critical erosion threshold [*Dietrich et al.*, 1992; *Lague et al.*, 2005; *D. R. Montgomery and Dietrich*, 1992; *Tucker*, 2004]. One factor affecting the critical erosion threshold is vegetation [*Collins and Bras*, 2010; *Collins et al.*, 2004; *Istanbulluoglu and Bras*, 2005], which modifies the effective erosion threshold through root cohesion and surface roughness [*Hales et al.*, 2009; *Schmidt et al.*, 2001; *Wainwright et al.*, 2000]. Furthermore, vegetation reduces surface runoff and

rain splash by canopy interception, leaf litter ground cover, and increasing soil infiltration capacity [*Wainwright et al.*, 2000].

Climate and vegetation have long been recognized as major inter-dependent controls on surface processes [e.g. *Abrahams and Ponczynski*, 1984; *Istanbulluoglu and Bras*, 2005; *Langbein and Schumm*, 1958; *Tucker and Slingerland*, 1997]. Sediment yield and topographic properties, such as drainage density and relief, have been explored in a range of climatic settings. For sites in the USA, Langbein and Schumm [1958] demonstrated that sediment yield increases with MAP until grassland vegetation is established. As MAP increases, sediment yield decreases and

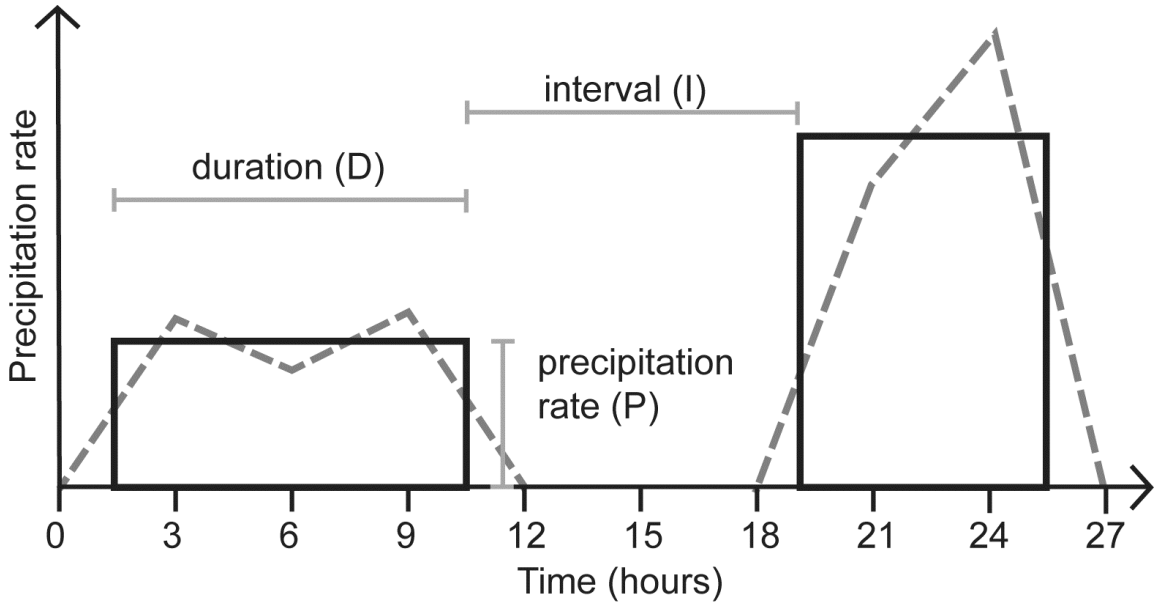

(modified after Eagleson, 1978)

Figure 4.1 Definition of precipitation metrics

Precipitation metrics are defined after Eagleson (1978) and Tucker and Bras (2000) as follows. Each precipitation event (dashed lines) is approximated as a rectangular pulse (solid lines) that is described by (1) precipitation rate ($\boldsymbol{P}$) that is the mean of all instantaneous observations during that event, (2) duration of the event ($\boldsymbol{D}$), and (3) the interval (I) before the next event begins. At each grid point in the TRMM dataset all precipitation events are extracted from the time series. The mean of these three metrics (P, D and I) is then calculated over all events, at each grid point, to give $\overline{\boldsymbol{P}}$, $\overline{\boldsymbol{D}}$, and $\overline{\boldsymbol{I}}$ (Fig. 3). Mean annual precipitation (MAP) is calculated independently as the total precipitation at each grid point divided by the number of years of observation.

then stabilizes under woodland forest. Observations from Australia [*Abrahams*, 1972], Guyana [*Daniel*, 1981], and additional USA sites [*Melton*, 1957] yield a similar trend. Drainage density is also shown to correlate with precipitation intensity in the USA, Australia, and the UK [*Abrahams*, 1972; *Abrahams and Ponczynski*, 1984; *Chorley and Morgan*, 1962; *Cotton*, 1964; *Musgrave*, 1947]. However, due to data availability at the time of publication of these studies, existing observational datasets explore these relationships at the catchment scale, and the spatial density of observations is low. Recent advances in satellite-based precipitation observations now enable observations of precipitation intensity in a broader range of climate and tectonic settings. Furthermore, remotely sensed vegetation and topography datasets are now also available in the same regions.

In this study, we complement previous efforts by using satellite-based observations of precipitation and vegetation to explore the relative importance of the mean climate state, precipitation variability, and vegetation in determining topographic characteristics in an active mountain belt. The mean intensity, duration and frequency of precipitation events are extracted from TRMM (Tropical Rainfall Measuring Mission) 3B42v7 observations and compared with vegetation, bedrock lithology, and topographic metrics. We use these datasets to explore which factors, if any, exert the strongest control on spatial patterns in modern topography of the central Andes. More specifically, we ask; 'Does modern topography more strongly reflect mean annual precipitation, precipitation intensity, or vegetation characteristics?' The analysis is performed in the central Andes, for three reasons: (1) the central Andes are characterized by large climatic gradients, (2) TRMM observations have a high quality at lower latitudes (<35°), and (3) relationships between erosion processes and climate over different time scales remains unresolved in this region [*Bookhagen and Strecker*, 2012b; *Insel et al.*, 2010b; *Jeffery et al.*, in press, see also Chapter 3 of this dissertation; *McQuarrie et al.*, 2008b].

4.2 HILLSLOPE GRADIENT RESPONSE TO VEGETATION AND CLIMATE

In an equilibrium landscape, catchment scale erosion rates are equal to rock uplift and mean hillslope gradients are a measure of the balance between erosional

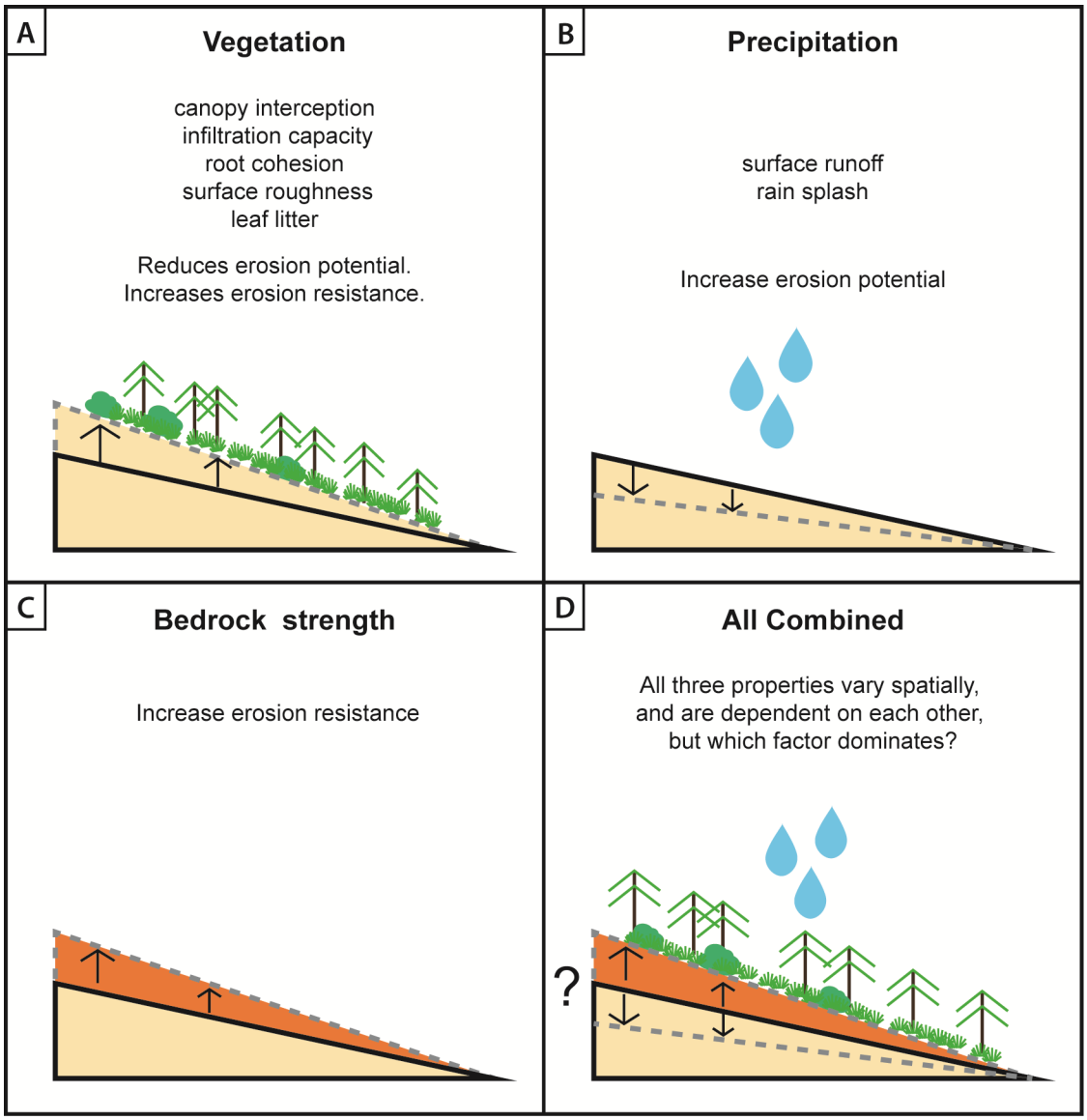

Figure 4.2 Predicted effects of vegetation and precipitation on hillslope gradients

Vegetation (A), precipitation (B) and bedrock lithology (C) are predicted to affect hillslope gradients by modifying the erosion resistance of the surface, or the erosion potential of the climate, or both [*Istanbulluoglu and Bras*, 2005; *Wainwright et al.*, 2000]. Hillslope responses to individual factors have been observed at the catchment scale and landscape evolution models, but the relative importance of different factors at the orogen scale is less well known (D).

efficiency and erosion resistance. Through changes in root cohesion and surface roughness, vegetation cover can increase erosion resistance, and by increasing canopy interception and infiltration capacities can also reduce erosion potential,

thus dense vegetation cover is expected to be associated with higher hillslope gradients [Fig. 4.2A, *Collins et al.*, 2004; *Istanbulluoglu and Bras*, 2005; *Wainwright et al.*, 2000]. Conversely, increasing precipitation amounts, and rates, are expected to increase erosional potential and decrease hillslope gradients [Fig. 4.2B, *Tucker and Bras*, 2000]. An additional factor controlling hillslope gradients is the strength, or erosional resistance, of the underlying material. To date, modeling studies have focused on one or two variables alone, and both modeling and observational studies have been executed at the catchment scale. It is not well known how inter-dependent variables, such as precipitation and vegetation, act in combination on large scales (Fig. 4.2D). In this study, we use satellite-based observations to test which precipitation characteristics and vegetation properties are most important in determining topography in the central Andes. In our initial analysis, we assume that the hillslopes are not at threshold gradients [*Schmidt and Montgomery*, 1995]; that is the hillslope gradient is sensitive to different climate or vegetation conditions and is not at an angle limited by the internal strength of the material.

4.3 DATA AND METHODS

4.3.1 Precipitation data

Spatial maps of mean precipitation intensity are derived from NASA's Tropical Rainfall Measuring Mission (TRMM) 3B42v7 product. TRMM 3B42v7 is a 3-hourly, 0.25° × 0.25° degree spatial resolution precipitation rate dataset that was derived by merging precipitation radar, infrared (IR), and microwave observations from multiple satellites, including the TRMM satellite [*Huffman et al.*, 2007]. Precipitation radar and microwave observations are used to calibrate IR observations with higher spatial and temporal coverage. The product is further calibrated using monthly GPCP rain gauge observations. TRMM 3B42v7 was chosen from the available precipitation datasets over South America because it has the highest spatial resolution with a temporal resolution that was sufficient to calculate precipitation intensity. Reanalysis datasets (e.g. NCEP-NCAR and CFSR) were also considered for their high temporal resolution, but precipitation rates were not well simulated over mountainous topography. Our analysis is based on observations from 2000 to 2011.

Years 1998 and 1999 of TRMM data were not included because additional satellites, and therefore increased spatial coverage, were introduced in 2000.

From this dataset, we calculate spatial variation in precipitation event metrics (P, D and I) by time series analysis. At each grid cell, consecutive time steps (3 hour) with non-zero precipitation rates are grouped into precipitation events. Each precipitation event is then characterized by the mean precipitation rate (intensity, P) of the event, the duration (D) of the event, and the time interval (I) before the next event (Fig. 4.1). The mean of each metric over all precipitation events is then calculated at each grid cell ($\overline{P}, \overline{D}$ *and* $\overline{I}$; Fig 4.3). These precipitation metrics are commonly used in landscape evolution models [e.g. CHILD, *Tucker et al.*, 2001] and the results of this study are therefore readily comparable with existing modeling studies. Finally, mean annual precipitation is also derived from the TRMM 3B42v7 dataset (Fig. 4.3). Because the data is discrete with three-hour time steps, each data point is assumed to be representative of that three-hour window.

MAP derived from the TRMM 3B42v7 dataset is consistent with the magnitudes and spatial distributions of MAP in other observational datasets [CRU, *Bookhagen and Strecker*, 2008; *Houston and Hartley*, 2003; *Hulme*, 1992]. Mean annual precipitation (MAP) rates are highest on the northeastern flanks (north of 18°S, Fig. 4.3A) where MAP rates decrease with increasing elevation from ~3-5 m yr^{-1} at ~600 m elevation to less than 2 m yr^{-1} near the drainage divide. Further south (>18°S) on the eastern flanks, MAP is less than 2 m yr^{-1} and the relationship with elevation is weaker. Mean annual precipitation on the eastern Andean flanks is high because (1) Andean topography deflects moisture transport southwards from the Amazon basin, driving the South American Low Level Jet and (2) orographic lifting induces convective precipitation [*Campetella and Vera*, 2002; *Insel et al.*, 2010a]. In contrast, MAP on the western flanks is extremely low (<1 m yr^{-1}) at all latitudes and much of the region receives less than 10 cm of rainfall a year. Hyper-arid conditions on the western flanks are attributed to (1) the subtropical location [*Rutllant et al.*, 2003]; (2) blocking of moisture by the Andes; and (3) the presence of the cold, Humboldt Current that generates a temperature inversion at the coast and traps moisture below ~800 m [*Houston and Hartley*, 2003].

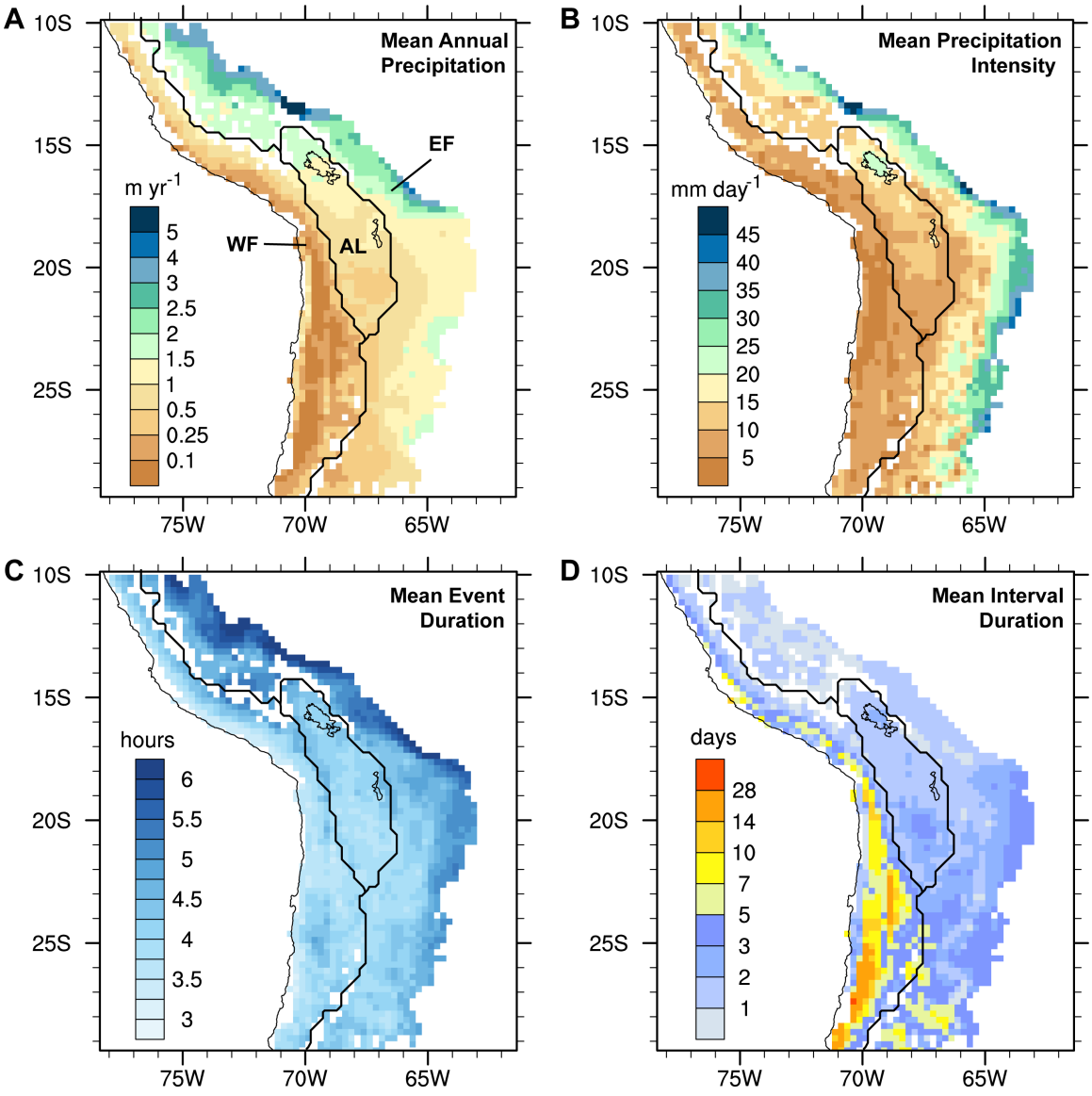

Figure 4.3 TRMM precipitation metrics

TRMM 3B42v7 precipitation observations processed to show A) mean annual precipitation (m yr^{-1}), B) mean precipitation intensity (mm day^{-1}), C) mean event duration (hours), and D) mean interval (days). Note the change in scale for mean annual precipitation (A) and mean interval (D). Each grid cell is 0.25° x 0.25° (~27 km). Only grid cells with an average elevation of >600 m and that were less than 40% glaciated at the LGM are shown. Altiplano lakes (Titicaca and Poopó) are outlined in black for spatial reference.

By decomposing MAP into intensity, duration, and interval components (Fig. 4.3), we can assess how the different aspects of rainfall contribute to the total MAP. MAP can be approximated from the mean of the individual metrics according to

$$MAP \approx \bar{P} * \frac{\bar{D}}{\bar{D}+\bar{I}} \qquad (4.1)$$

Over the study area, directly calculated MAP and MAP estimated from event metrics agree strongly (r^2 = 0.98). In many respects, mean precipitation intensity mirrors the mean annual precipitation pattern (Fig. 4.3B). Precipitation intensity increases from west to east, with peak intensities (> 45 mm day^{-1}) occurring on the eastern flank at 13°S. However, precipitation intensity does not have the same north-south variability as MAP on the eastern flanks. Instead, precipitation intensity decreases from >30 mm day^{-1} at the lowest elevations to <15 mm day^{-1} at the drainage divide along the length of the orogen. Precipitation events north of 18°S on the eastern flanks have a longer average duration and occur more frequently (Figs. 4.3C and 4.3D). A similar pattern is observed on the western flanks, but in a much more arid climate.

4.3.2 Topographic data

Precipitation patterns are compared with topographic metrics derived from the 90 m spatial resolution Shuttle Radar Topography Mission v3 digital elevation model [*Farr et al.*, 2007]. This study primarily focuses on the controls on mean hillslope gradient, which is calculated for each grid cell in ArcGIS as the rate of maximum change in elevation between neighboring cells in the local 3×3 grid. The results presented are also relevant to controls on landscape relief when averaged at the resolution of the precipitation dataset, as results of a subsequent analysis are similar. In order to make direct, quantitative comparisons, elevation and hillslope gradients are re-gridded to the same resolution as the precipitation data (0.25°, or ~27 km) by spatial averaging (Figures 4.4A and 4.4B). The re-gridding process determines the average value of all cells in the higher resolution dataset (~90,000 DEM grid points) contained within each grid cell of the lower resolution dataset.

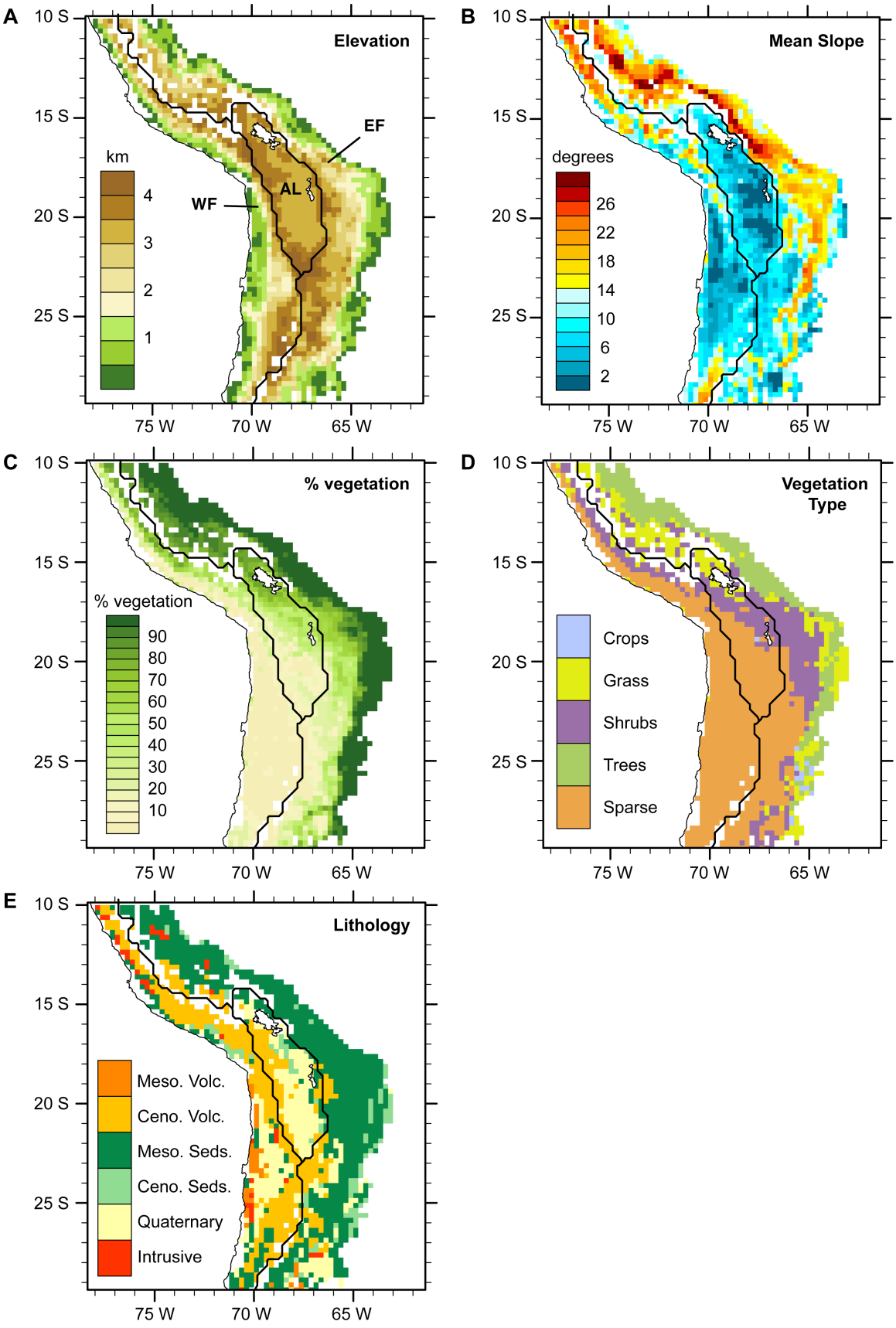
A
Elevation
km
4
3
2
1
EF
AL
WF
B
Mean Slope
degrees
26
22
18
14
10
6
2
C
% vegetation
% vegetation
90
80
70
60
50
40
30
20
10
D
Vegetation Type
Crops
Grass
Shrubs
Trees
Sparse
E
Lithology
Meso. Volc.
Ceno. Volc.
Meso. Seds.
Ceno. Seds.
Quaternary
Intrusive
10 S
15 S
20 S
25 S
75 W
70 W
65 W

Figure 4.4 Topography and surface properties

(previous page) Surface properties re-gridded to the TRMM precipitation grid (Fig. 2). A) Mean surface elevation (km), and B) mean surface slope (°) derived from 90 m SRTM data. C) Dominant bedrock lithology from USGS geologic maps. D) Percent vegetation cover, and E) modal vegetation type averaged from 0.05° resolution MODIS plant function type dataset (Lawrence and Chase, 2007). Only grid cells with an average elevation of >600 m and that were less than 40% glaciated at the LGM are shown. Altiplano lakes (Titicaca and Poopó) are outlined in black for spatial reference.

Based on the location of drainage divides, the central Andes are separated into three separate geographic regions: the western flank, the eastern flank, and the internally drained Altiplano (Fig. 4.4A). These three regions are separated because of the differences in climate, large scale topography, and broad lithological composition (see section 4.3.3 below). The western flank is a crustal scale monocline, with minor surface breaking faults and block uplift of the coastal region [*Farias et al.*, 2005; *Isacks*, 1988; *Schildgen et al.*, 2009a]. At the surface, this is expressed as a relatively smooth ramp from the western Cordillera to the Pacific Coast that is dissected by multiple deeply incised canyons. In contrast, the eastern flank is a fold and thrust belt [e.g. *Allmendinger et al.*, 1997], with a surface expression of ridges and valleys that are dissected along strike by large drainage networks. Deformation of the eastern Andean flank has migrated outward from the Eastern Cordillera (~40-22 Ma), to the Interandean zone by ~20–15 Ma, and the Subandes have been most active since ~15-10 Ma [*Barnes and Ehlers*, 2009]. Finally, the Altiplano is predominantly a depositional basin with localized inverted basins. The highest relief is at the basin margins in the western and eastern Cordilleras and in association with Quaternary volcanoes.

Highest mean hillslope gradients (>24°) are in the northern Central Andes, particularly the northeastern flanks (north of ~17°S). Peak mean hillslope gradients are associated with large, deeply incised drainage networks such as the upper catchment of the Río Beni on the northeastern flanks. Canyons are also the primary location of high hillslope gradients on the western flanks, e.g. the Cotahuasi-Ocoña canyon at ~16°S. Peak hillslope gradients in the southeastern flanks are also associated with river valleys (Río Pilcomayo and Río Grande) but maximum values

are lower (~20-24°). The Altiplano has consistently low mean hillslope gradients (<10°), as does the Atacama region of the western flanks (20-27°S).

4.3.3 Land Surface Data

To test the relative importance of climate and land surface properties in determining topographic morphology, we also include vegetation and geologic data in the analysis. The chosen vegetation dataset was developed by Lawrence and Chase [2007] from the Moderate Resolution Imaging Spectoradiometer (MODIS) instrument on NASA's Terra and Aqua satellites. In their derived dataset, vegetation is classified into 17 Plant Functional Types (PFT's) and each 0.05° grid cell is described in terms of the % of each PFT in that grid cell (including bare ground). We re-grid this dataset to the precipitation grid and re-classify the original PFTs to the following simpler subsets: 'not vegetated', 'shrubs', 'grass', and 'trees'. This grouping simplifies the analysis yet maintains distinctions between major vegetation types. In the analysis, we present the total percent vegetation cover (Fig 4.4C) and the modal vegetation type in each grid cell (Fig. 4.4D). If total vegetation cover is greater than 40%, the grid cell is classified as the most abundant vegetation type (excluding 'not-vegetated'). For grid cells that are <40% vegetated, 'not vegetated' is also included as an option for the most abundant vegetation type. This approach was taken because simply identifying the most abundant vegetation type, with 'not vegetated' as an equally weighted option, results in grid cells with >70% vegetation being classified as 'not vegetated'

Total vegetation cover increases strongly from the west to east (Fig. 4.4C) and also displays a weaker south to north gradient on the western flanks. The most densely vegetated regions (>90%) are dominated by trees (Figs. 4.4C and 4.4D). Grasses dominate the landscape south of 18°S, and at higher (>~2 km) elevations with 60-80% vegetation cover. The desert regions are bordered with shrubs, which also cover a large area of the northern Altiplano and high elevations on the eastern flanks between 17 and 22°S. Vegetation patterns strongly reflect the regional climate, with MAP corresponding to higher percent vegetation cover. A transition from not vegetated, through shrubs, to grass, and then trees, accompanies the

increase in percent vegetation cover (Fig. 4.5). These spatial patterns are revisited in more detail in the correlation and regression analyses presented later (section 4).

Lithological data from the USGS [*Schenk et al.*, 1999] is also re-classified and re-gridded (Fig. 4.4E). Lithology is divided into dominant rock types that are expected to have different strengths. First they are divided by general rock type (sedimentary, volcanic, intrusive, and metamorphic) and second by age (Quaternary, Cenozoic, and Mesozoic). We recognize that these divisions do not account for all lithological variations, for example differences between shales and sandstones, or for potentially important variations in the extent of rock fractures [Duhnforth et al., 2010; Larsen et al., 2010]. However, at the resolution of the precipitation data these categories serve as a useful starting point for differentiating between different rock strengths. The eastern flanks are dominantly underlain by Paleozoic to Mesozoic sediments, with the youngest sediments currently being uplifted at the eastern margin of the fold-and-thrust belt. Cenozoic volcanic deposits of the western Cordillera dominate the higher elevations in the western flanks. Large Quaternary sedimentary basins include the Altiplano and Atacama. Additional Quaternary sediments are found in fault-bounded basins on the eastern flanks (south of ~22°S). The 'Quaternary' group also encompasses Quaternary volcanoes and volcanic deposits, most of which are not large enough to dominate a grid cell. Minor intrusive and older volcanic rocks can be found on the Pacific Coast and scattered elsewhere.

Before statistical analyses are performed, some grid points are removed from the dataset to account for regions that have been affected by recent glaciations or have not experienced recent tectonic activity. Regions that were primarily shaped by glacial processes are removed from the analysis by removing grid cells in which >60% of the area was covered by glaciers at the Last Glacial Maximum [*J Ehlers et al.*, 2011]. Grid points with a mean elevation less than 600 m are removed to restrict the analysis to the active mountain belt. After removal of low elevation and previously glaciated grid points, 1739 grid points remain.

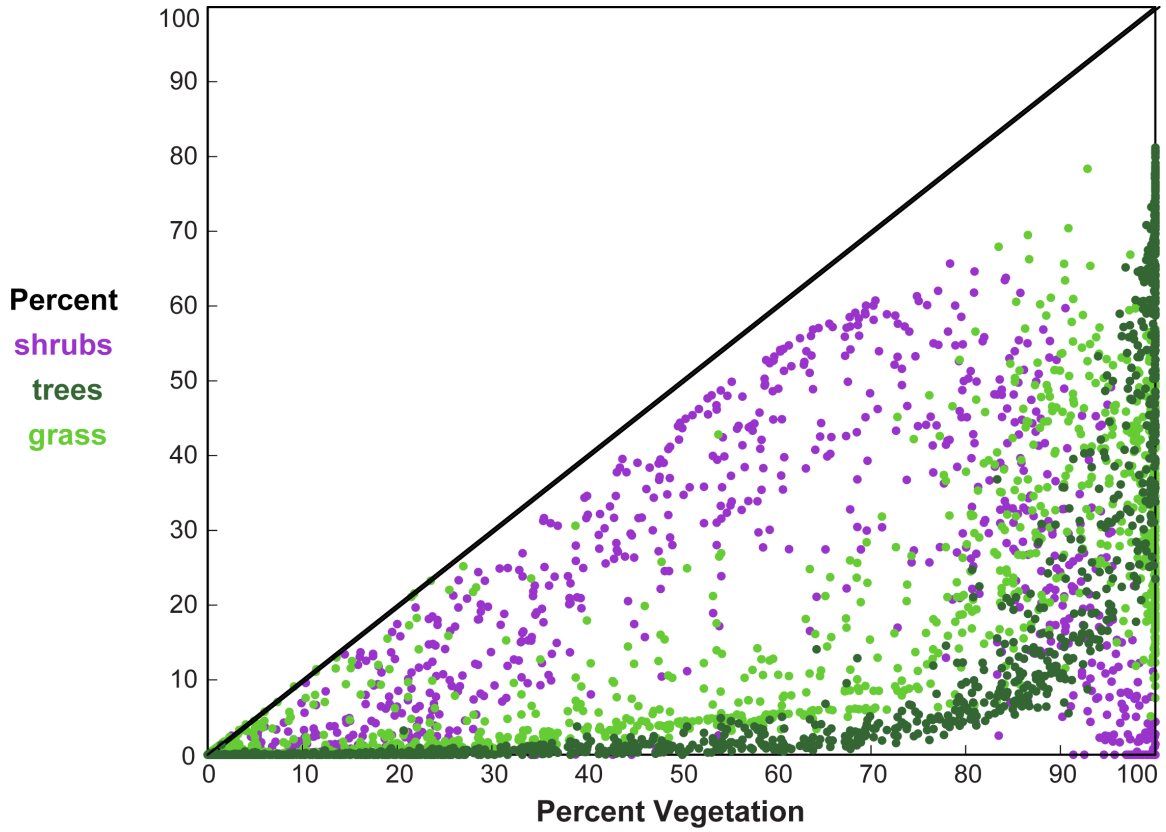

Figure 4.5 Vegetation type

The type of vegetation varies with increasing vegetation cover. Shrubs are the dominant vegetation type where total vegetation is less than ~80%, with some grass mixed in. The fraction of grass cover increases with increasing vegetation and is most abundant between ~80–95% vegetation cover. Finally, trees dominate only in the most densely vegetated regions.

4.3.4 Data Set Analysis Methods

The strength of correlations between all topography, vegetation, and climate variables is explored quantitatively using Pearson's correlation coefficient and a series of scatter plots. Correlation coefficients are used to identify the strongest linear correlations and compare the strengths of relationships between different variable pairs and subsets. Unless otherwise stated, all correlation coefficients reported are statistically significant at a $p<0.01$ level according to a two-tailed test. Scatter plots are generated for all parameter pairs, but only those selected to illustrate key findings are presented. Correlation coefficients alone are only able to

identify linear relationships, but the scatter plots enable the identification of non-linear trends and outliers. The analysis is presented in the following order: (1) direct correlation between hillslope gradients and precipitation metrics; (2) direct correlation between hillslope gradients and surface properties (vegetation and lithology); and (3) interdependent controls of climate and vegetation on hillslope gradients are explored with data subsets and multiple linear regression models.

4.4 RESULTS

4.4.1 Correlations between precipitation metrics and hillslope gradients

Of the precipitation metrics explored, mean hillslope gradients in the central Andes are most strongly correlated with mean event duration (r = 0.52, Table 1) and to a lesser degree with mean annual precipitation (r = 0.49). Correlations between mean hillslope gradient and mean event intensity and mean interval duration are lower (r = 0.26 and r = -0.32 respectively). However, it is evident from scatter plots of mean hillslope gradient against precipitation (Fig. 4.6) that relationships between mean hillslope gradient and precipitation are not linear. We begin a more rigorous interrogation of the dataset by sub-setting the observations according to geographic regions (western and eastern flanks, and the Altiplano; Section 3.2 and Fig. 4.4A) that are characterized by different climate regimes and dominant bedrock lithology.

Mean hillslope gradient generally increases with mean annual precipitation (Fig. 4.6A). As MAP increases, the maximum observed hillslope gradient increases from <20° at <0.1 m yr^{-1} MAP, to ~32° at 2 m yr^{-1} MAP. Over the same range in MAP, there is little change in the minimum observed hillslope gradient. However, where MAP exceeds 2 m yr^{-1}, mean hillslope gradients are greater than ~10°. High (>25°) hillslope gradients are found on both flanks (Fig. 4.6), but hillslopes on the Altiplano are low (<13°). This likely reflects the difference between erosional processes occurring on the flanks and predominantly depositional processes on the Altiplano. Correlation coefficients between hillslope gradient and MAP are stronger on the individual flanks (r > 0.44, Fig. 4.6A and Table 1) than on the Altiplano (r = 0.12). The best-fit linear relationship between mean hillslope gradient and MAP is steeper

Table 4.1 Correlation coefficients between mean hillslope gradient and precipitation metrics.

Pearson's correlation coefficients are given for all data and data separated according to percent vegetation, modal vegetation type and modal lithology. All correlations are statistically significant at the $p<0.01$ level; according to a two-tailed test, unless otherwise indicated. For correlations coefficients that are not significant at the $p<0.05$ level, no values are reported.

Classification	Pearson's Correlation Coefficient					Number of data points
	mean annual precipitation m yr^{-1}	mean event intensity mm day^{-1}	mean event duration hr	mean interval duration days	percent vegetation cover %	
All data	0.49	0.26	0.52	-0.32	0.56	1739
WF and EF	0.52	0.22	0.49	-0.44	0.58	1465
Region						
Eastern Flank	0.48	-	0.45	-0.59	0.50	934
Altiplano	-	*-0.14*[c]	0.44	-0.37	0.23	269
Western Flank	0.45	0.34	0.28	-0.35	0.60	531
Percent vegetation (WF and EF only)						
0 - 95 %	0.60	0.31	0.55	-0.42	0.69	1116
95 - 100 %	0.34	-0.56	0.32	-0.69	-0.31	349
Modal vegetation type (WF and EF only)						
not vegetated	0.19	-	0.16	-0.24	0.38	692
shrubs	0.32	-	0.25	-0.36	0.42	287
grass	0.46	-0.49	-	-0.67	-	204
trees	0.16	-0.54	-	-0.55	0.36	269
crops	-	-0.82	-0.88	-	-[a]	13
Lithology (WF and EF only)[b]						
Quaternary	0.35	-	0.23	-0.23	0.47	183
Cenozoic Sed.	*0.26*[c]	*-0.24*[c]	-	-0.46	-	93
Older Sed.	0.45	0.10	0.44	-0.40	0.51	738
Cenozoic Volc.	0.34	0.13	0.29	-0.29	0.57	372
Mesozoic Volc.	-	0.48	-	-	0.72	39
Intrusive	0.59	*0.37*[c]	0.51	-0.54	0.52	40

a. Cropland expected to change natural percent vegetation cover.
b. Abbreviations for lithologies are as follows: Sed. – Sedimentary rocks; Volc. – Volcanic Rocks; 'Older' – older than Cenozoic.
c. Correlation is significant at the $p<0.05$ level according to a two-tailed test, but not at $p<0.01$.

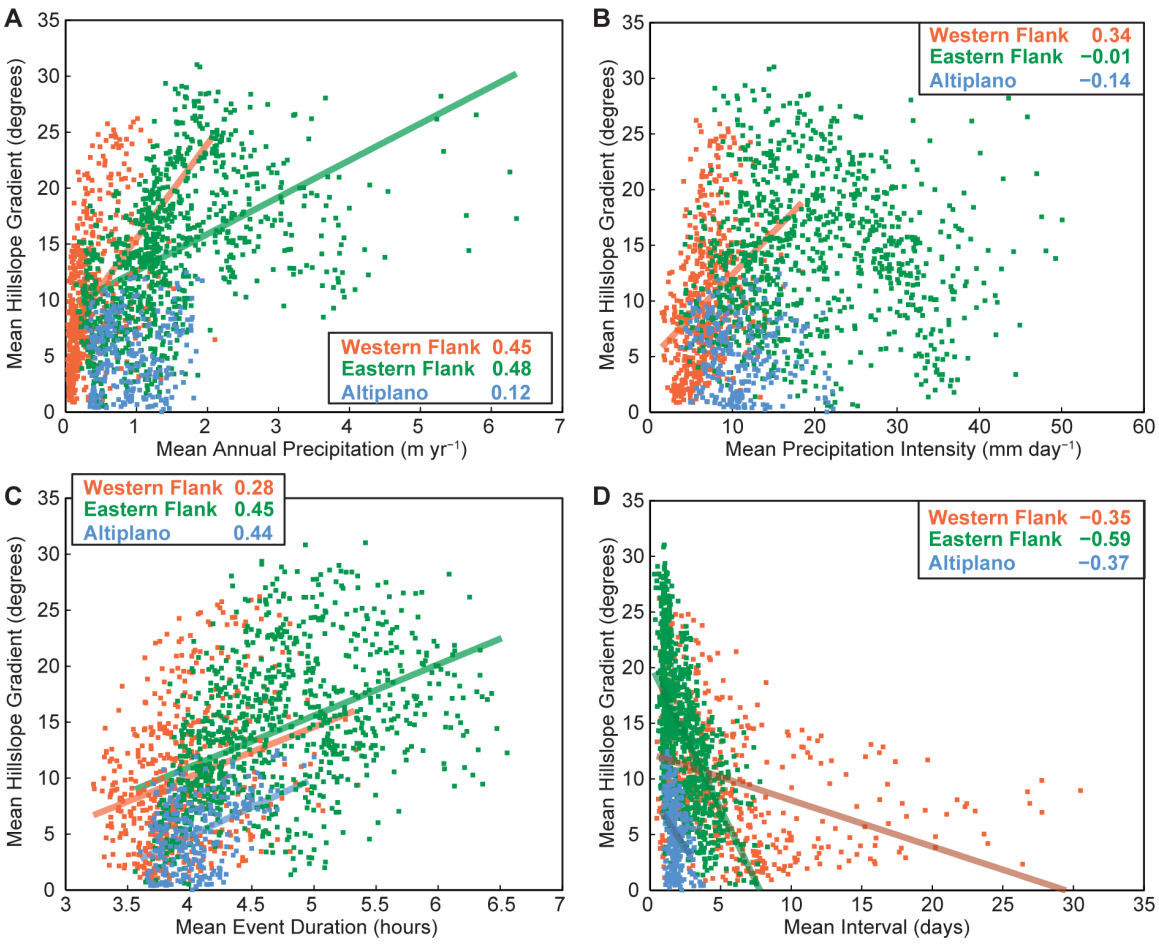

Figure 4.6 Mean hillslope dependence on precipitation metrics

Scatter plots of mean hillslope (Fig. 4.4B) against TRMM derived precipitation metrics. A) Mean annual precipitation (m yr^{-1}), B) mean precipitation intensity (mm day^{-1}), C) mean event duration (hours), and D) mean interval duration (days). Observations are subdivided according to geographic region (Fig. 4.4A); western flank (red), eastern flank (green), and Altiplano (blue). Correlation coefficient (r) between mean hillslope and precipitation metric is given for each region, and best-fit lines shown for subsets in which r exceeds 0.25.

on the western flank than the eastern flank (r^2_{west} = 0.2 and r^2_{east} = 0.23, respectively).

Precipitation intensity ($\bar{P}$) and mean hillslope gradient do not correlate strongly, either when the complete dataset is considered (r = 0.26, Table 1) or in the separate geographic regions (r < 0.35, Fig. 4.6B). Although there is a high degree of scatter in the plot of mean hillslope gradient against $\bar{P}$, figure 4.6B suggests a non-linear relationship between the two variables: mean hillslope gradient increases

with precipitation intensity when $\bar{P}$<~20 mm day^{-1}), and decreases when $\bar{P}$ exceeds 20-25 mm day^{-1}. Mean hillslope is most strongly correlated with mean event duration (r = 0.52, for all data), and mean hillslope gradients tend to increase with increasing event duration (Fig. 4.6B). Correlation coefficients are lower for individual geographic regions than for the whole dataset, but the best-fit linear relationship has a similar slope (4.7 °/hour) for all three regions (Fig. 4.6C). Finally, mean hillslope gradients generally decrease with increasing mean event interval ($\bar{I}$, Fig. 4.3D). Mean interval ($\bar{I}$) is not strongly correlated with hillslope gradients for the complete dataset (r = -0.32), or on the Altiplano or Western Flank (r = -0.37 and r = -0.35 respectively, Fig. 4.6D). However, the correlation coefficient between $\bar{I}$ and hillslope gradients on the Eastern Flank is -0.59, the highest correlation found in the regional breakdown analysis.

No single precipitation metric can explain the spatial variation in mean hillslope gradient for the entire dataset. In general, mean hillslope gradients increase with increasing MAP and event duration, and decrease with mean interval. Some precipitation metrics have a stronger correlation with hillslope gradient when individual regions are considered, e.g. mean interval on the eastern flanks. These initial findings appear to contradict modeling and observational studies that precipitation intensity is a strong control on erosion processes and landscape morphology. However, topography is also known to depend on surface properties such as vegetation and lithology. In the next section we explore the direct relationships between hillslope gradients and surface properties, before exploring how precipitation and surface properties act in combination to shape the landscape. Because hillslope gradients on the Altiplano are low, and because depositional processes are more important than uplift and erosion in this region, we focus on the western and eastern flanks for the remainder of the study.

4.4.2 Hillslope dependence on vegetation and bedrock lithology

Mean hillslope gradients are more strongly correlated with percent vegetation cover than any of the precipitation metrics (r = 0.56, Table 1 and Fig 4.7A). The range of mean hillslope gradients increases with increasing vegetation

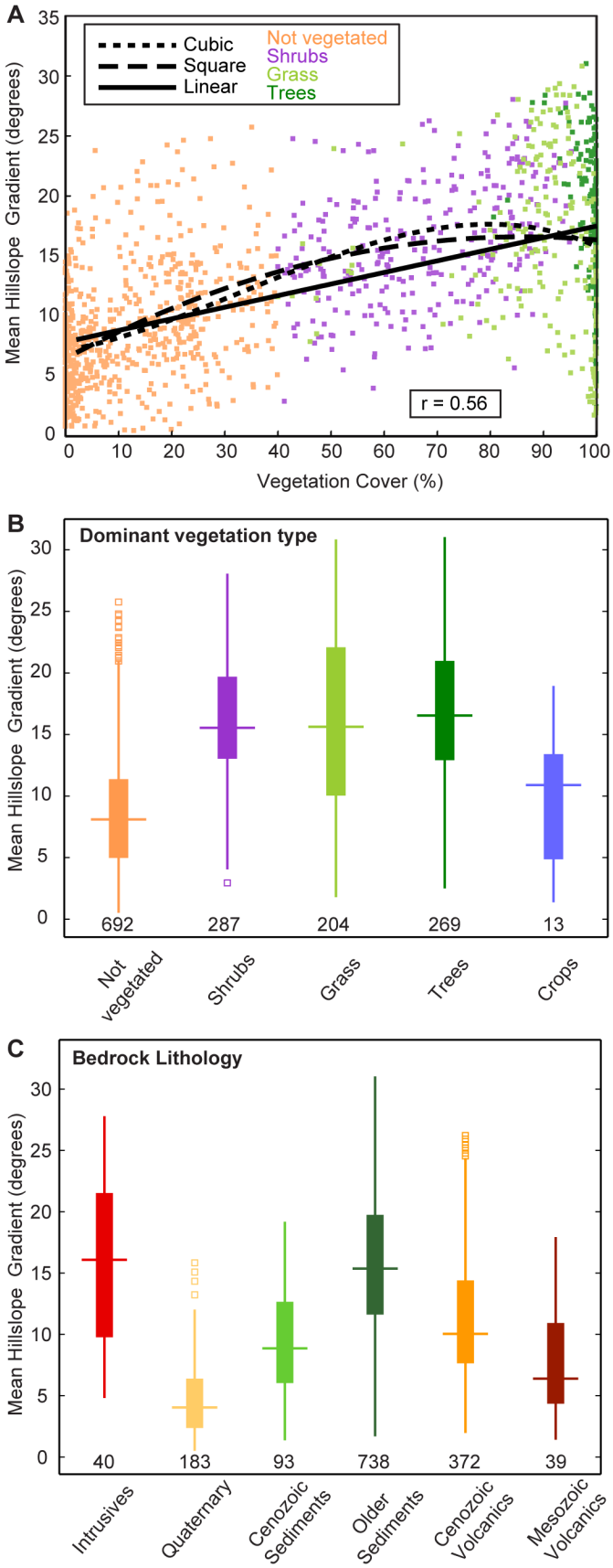
A
Cubic
Square
Linear
Not vegetated
Shrubs
Grass
Trees
r = 0.56
Mean Hillslope Gradient (degrees)
Vegetation Cover (%)
B
Dominant vegetation type
Mean Hillslope Gradient (degrees)
692
287
204
269
13
Not vegetated
Shrubs
Grass
Trees
Crops
C
Bedrock Lithology
Mean Hillslope Gradient (degrees)
40
183
93
738
372
39
Intrusives
Quaternary
Cenozoic Sediments
Older Sediments
Cenozoic Volcanics
Mesozoic Volcanics

Figure 4.7 Mean hillslope gradient dependence on surface properties.

A) Mean hillslope gradient (degrees) against percent vegetation cover (Fig. 4.4D) color-coded according to modal vegetation type. Best-fit linear, square and cubic lines are shown to indicate that the relationship is non-linear at high vegetation cover. B) Boxplots of mean slope, subdivided by modal vegetation type (Fig. 4.4E). Number of data points in each group is indicated at the base. C) Boxplots of mean slope, subdivided by modal bedrock lithology (Fig. 4.4C). Number of data points in each group is indicated at the base.

cover from 0-20° at no vegetation cover, to 0-32° at 100% vegetation cover. The relationship between hillslope gradient and percent vegetation cover is non-linear; mean hillslope gradients increase with increasing vegetation cover up to ~80% vegetation, but as vegetation cover increases further, the range of hillslope gradients widens and lower hillslopes (<10°) are again found. As vegetation cover increases, the modal vegetation type transitions from not vegetated, to shrubs, then grass and finally trees at >~95% vegetation cover (Fig. 4.7A). Below ~80% vegetation cover, an increase in vegetation cover is primarily an increase in shrubs, with some increase in grass cover (Fig. 4.5). The abundance of shrubs decreases steeply to <5% between 80 and 100% total vegetation cover. Trees are almost absent where total vegetation cover is less than 80% but tree cover increases rapidly above 80% to become the dominant functional type at 100% vegetation. However, classifying vegetation cover by plant functional type does not directly help to predict mean hillslope gradient (Fig. 4.7B). Where surface cover is classified as not vegetated, mean hillslope gradients are low (mean of ~13°), but the distribution of mean hillslope gradient is similar for shrubs, grass and trees (Fig. 4.7B). The lower hillslope gradients associated with agricultural land ('crops', Fig. 4.7B), are interpreted as a cause, not a consequence of the land cover type. Although different vegetation types are expected to affect the landscape via different mechanisms, there is not a clear relationship between dominant vegetation type and mean hillslope gradient in the central Andes.

In contrast, mean hillslope gradients show a strong association with the dominant bedrock lithology (Fig, 4.7C). Mean hillslope gradients are highest when underlain by intrusive rocks or 'older' (Mesozoic and Paleozoic) sedimentary rocks.

Lower hillslope gradients are generally found on younger sedimentary rocks and Quaternary sediments. Low hillslopes gradients in Quaternary sediments are likely due to the depositional nature of the systems. The opposite is true for volcanic rocks in that higher hillslope gradients are found in regions underlain by the younger (Cenozoic) rocks, although there is significant overlap in the range of hillslope gradients found in these two broad age categories. Higher hillslope gradients are generally found on harder, less easily eroded substrates. Percent vegetation cover and lithology exert the strongest influence on mean hillslope gradient in the central Andes. However, there remains a high degree of scatter in the data that cannot be explained by these two factors alone and we have not yet considered the interaction of different climate and vegetation properties. We address these details by considering smaller subsets of the data.

Table 4.2 Correlation coefficients between percent vegetation cover and precipitation metrics.

Pearson's correlation coefficients are given for all data and data separated according to percent vegetation and modal vegetation type. All correlations are statistically significant at the $p<0.01$ level; according to a two-tailed test, unless otherwise indicated. For correlations coefficients that are not significant at the $p<0.05$ level, no values are reported.

Classification	Pearson's Correlation Coefficient				Number of data points
	mean annual precipitation	mean event intensity	mean event duration	mean interval duration	
	m yr^{-1}	mm day^{-1}	hr	days	
All data	0.77	0.74	0.81	-0.43	1739
EF and WF	0.77	0.75	0.82	-0.47	1465
Percent vegetation (WF and EF only)					
0 - 95 %	0.79	0.56	0.75	-0.48	1116
95 - 100 %	*0.11*[a]	0.39	0.27	-	349
Modal vegetation type					
not vegetated	0.59	0.45	0.27	-0.33	692
shrubs	0.48	0.36	0.59	-0.18	287
grass	0.28	0.60	0.63	-	204
trees	-	0.35	0.29	*0.15*[a]	269

a. Correlation coefficient is significant at the $p<0.05$ level according to a two-tailed test, but not at $p<0.01$.

4.4.3 Inter-dependent controls on mean hillslope gradients

4.4.3.1 Vegetation categories

Although vegetation shows the strongest correlation with mean hillslope gradient, vegetation itself is also dependent on the climate (Table 4.2). The high correlation between mean annual precipitation and percent vegetation cover (r = 0.77, Table 4.2) is consistent with moisture availability being the limiting factor on net primary productivity in the Central Andes [Churkina and Running, 1998]. Factors that can explain the remaining spatial variability in vegetation cover include surface temperature, nutrient availability and solar radiation. Maximum correlation coefficients between vegetation and climate variables, and hillslope gradients are found when the observations are split into two groups with vegetation cover above and below 95–98%. Where vegetation cover is less than 95%, MAP has a high correlation with mean hillslope gradient (r = 0.60, Table 4.1 and Fig 4.8), but mean hillslope correlates more strongly with percent vegetation cover (r = 0.69, Table 4.1). For this same data subset, vegetation and MAP are also strongly correlated (r = 0.79, Table 4.2). The correlation coefficients suggest that, for this subset of the data, the influence of precipitation and vegetation on hillslopes is strongly coupled.

In contrast, both MAP and percent vegetation are poorly correlated with mean hillslope gradients in densely vegetated regions (r_{MAP} = 0.34 and r_{veg} = -0.31). Where vegetation cover is less than 95%, mean hillslope gradients generally increase with increasing vegetation cover. This trend breaks down at >95% vegetation cover where a wide range of hillslope gradients (2-32°) is found (Figs. 4.7A and 4.8), suggesting that other factors play a role in determining hillslope gradients in these regions. Correlation analyses show that mean hillslope gradient correlates most strongly with mean precipitation intensity ($\bar{P}$) and interval duration ($\bar{I}$) under dense vegetation cover (r_P = -0.56 and r_I = -0.69, Fig. 4.8B, Table 4.1). Where vegetation density can no longer increase, the effects of changing precipitation may be more direct. In the following sections we explore the physical mechanisms underlying the relationships between vegetation, climate and hillslope gradients in these two vegetation categories.

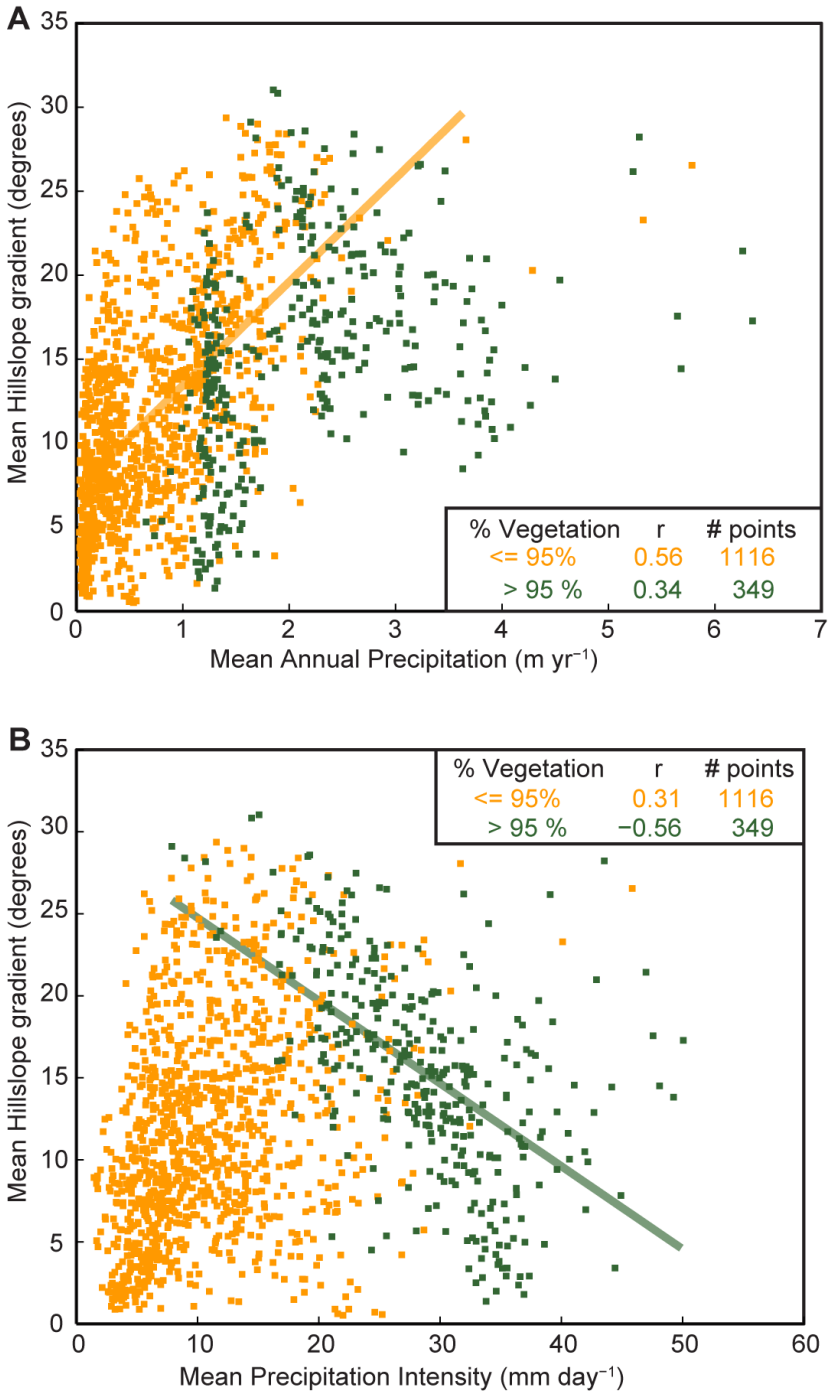

Figure 4.8 Combined vegetation and climate controls on mean hillslope

Scatter plots of hillslopes vs. precipitation metrics (first shown in figure 4) color coded according to amount of vegetation cover. A) Mean annual precipitation correlates more strongly with hillslope where vegetation cover is less than 95% (orange). B) Conversely, mean precipitation intensity correlates more strongly with hillslopes where vegetation cover exceeds 95 % (dark green). Observations in these plots are from the western and eastern flanks only.

4.4.3.2 Multiple linear regression

It is evident from the above correlation analyses that the explored variables are both interdependent, and have the potential to modify hillslopes in different ways. Stepwise multiple linear regression analyses were performed to determine whether a combination of variables could explain more of the variability in observed hillslope gradients than any one factor. Models were evaluated based on r^2 and F-statistic values, and acceptable models all have individual variable coefficients that are both significant at the 1% level and are reasonable with respect to the original correlation analyses. More complex models that fit these criteria are not presented because they did not explain more of the variability in the observations.

In the <95% vegetation category, the best-fit regression model incorporates percent vegetation cover and precipitation intensity, and has an r^2 of 0.49 (Fig. 4.9A);

$$Hillslope\ Gradient_{<95\%} = 7.96 - 0.12 * \bar{P} + 0.15 * \%\ vegetation \quad (4.2)$$

This model is only a marginal improvement on a regression with percent vegetation cover alone (r^2 = 0.48). It is useful to note that the precipitation intensity coefficient is negative, indicating that although vegetation cover effects dominate, hillslope gradients also decrease with increasing precipitation intensity in this category. Variability in bedrock lithology explains some of the additional variability in mean hillslope gradient. Hillslope gradients that are over-estimated by the regression model are more commonly on Quaternary or Cenozoic sediments, which are likely to be weaker and more easily eroded (Fig. 4.9A). In the >95% vegetation category, the best fit model includes mean precipitation intensity and mean interval and has an r^2 of 0.55 (Fig. 4.9B);

$$Hillslope\ Gradient_{>95\%} = 29.8 - 0.28 * \bar{P} - 2.89 * \bar{I} \quad (4.3)$$

As in the sparse vegetation category, hillslope gradients are overestimated on Quaternary and Cenozoic sediments.

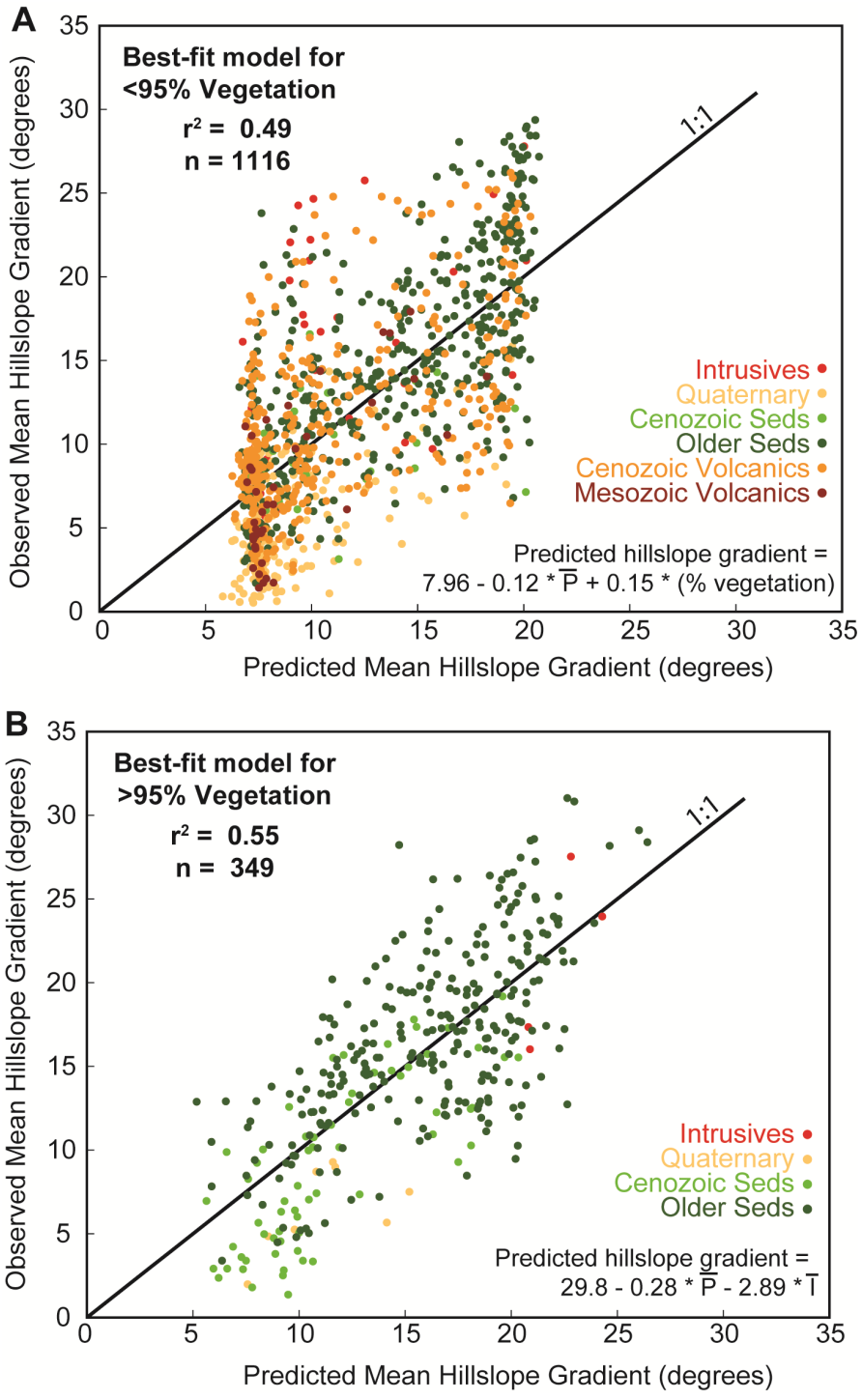

Figure 4.9 Multiple linear regression models

Comparison of observed and predicted hillslope gradients for the best multiple linear regression models found for A) <95% vegetation category, and B) >95% vegetation category. A 1:1 ratio (black line) is shown to aid comparison. Each data point is color coded according to bedrock lithology at that point.

4.5 DISCUSSION

In the central Andes, mean hillslope gradients correlate more strongly with vegetation cover (r = 0.56, Table 4.1) than any individual precipitation metric. However, vegetation cover also correlates strongly with precipitation (Table 4.2), highlighting the inter-dependence of these two controls on mean hillslope gradients. The strongest patterns emerge when the dataset is subset into two categories, vegetation cover greater than and less than 95% (Fig. 4.8). Within these categories, some additional variation in mean hillslope gradient can be explained by the underlying bedrock lithology (Fig. 4.7B). In the following sections we explore (1) possible physical mechanisms underlying the observations, (2) additional factors that affect hillslope gradients to explain scatter in the observed relationships, and (3) how these observations can inform future research avenues.

4.5.1 Erosional efficiency, erosion resistance, rock uplift, and equilibrium landscapes

In an equilibrium landscape, mean hillslope gradients adjust such that catchment wide erosion rates balance rock uplift. To understand how vegetation and climate controls influence mean hillslope gradient we discuss the effects of each factor on the erosional efficiency of the climate and the erosional resistance of the landscape. Any decrease in erosional efficiency, or increase in erosional resistance, is expected to require higher hillslope gradients to attain the same catchment scale erosion rates. High hillslope gradients can therefore be indicative of a low erosional efficiency or high erosional resistance, and vice versa, assuming uniform erosion rates. Two additional factors may confound this assumption. First, spatial variations in rock uplift may exert a stronger control than spatial variations in erosional efficiency. Initially we assume that uplift rates are uniform and then explore the implications of such an assumption and identify reasons to suggest that this factor is important. Second, modern topography is unlikely to have attained full equilibrium with the tectonic and climatic factors affecting it [*Whipple*, 2001]. Although, LEM's are commonly analyzed at equilibrium [e.g. *Collins and Bras*, 2010; *Tucker*, 2004], comparisons with observations are still useful as a means of testing the model

results in a real system. Collins and Bras [2010] argue that the natural landscape is likely to at least partly reflect an equilibrium landscape, because equilibrium states are often approached asymptotically. The ability of their model to explain much of the data presented in this study (Section 4.5.2, below) supports their conjecture regarding equilibrium landscapes.

4.5.2 Physical mechanisms of climate and vegetation control on mean hillslope gradients

In the two vegetation categories, different factors determine the balance between erosional efficiency, erosional resistance and uplift. Where vegetation is less than 95%, an increase in MAP is accompanied by an increase in vegetation cover (r = 0.79, Table 4.2). Increasing MAP has three competing effects. First, increasing MAP will increase moisture available for surface runoff. Second, an increase in vegetation will reduce surface runoff by increasing infiltration rates and by intercepting rainfall before it hits the ground. Third, roots can increase cohesion of the subsurface and increases surface roughness, thereby increasing erosional resistance. Only considering the first effect, increasing MAP would be expected to increase erosional efficiency and would result in lower hillslope gradients in an equilibrium landscape. However, in the second and third effects, vegetation decreases erosional efficiency requiring higher hillslope gradients in an equilibrium landscape. Our observations indicate that mean hillslope gradients generally increase with an increase in MAP that is accompanied by increasing vegetation cover. This suggests that the effects of vegetation cover outweigh those of increasing MAP, and that in the <95% vegetation category, the primary control of climate on erosion is through changing vegetation cover. Orogen scale observations in the central Andes are therefore consistent with catchment scale modeling studies in that hillslope gradient responses to climate are moderated by vegetation [*Collins and Bras*, 2010].

In the second category (vegetation >95%), an increase in MAP does not cause a significant increase in vegetation cover. Under dense vegetation cover, mean hillslope gradients decrease from ~25° at $\bar{P}$ = 10 mm day^{-1} to ~10° at $\bar{P}$ = 40 mm

day^{-1} with a correlation coefficient of r = -0.56 (Fig. 4.8B). As $\bar{P}$ increases, surface runoff and erosional efficiency increase, resulting in lower hillslope gradients. As vegetation cover is at a maximum, there is no additional indirect loss of moisture to infiltration or canopy interception, or increase in erosion resistance. The modal vegetation type can explain some additional variability in the relationship between $\bar{P}$ and mean hillslope gradient (Fig. 4.10A); trees are associated with slightly higher (4-5°) hillslope gradients than grass. A possible reason for this is that grass modifies the geomorphic effectiveness of precipitation primarily at the ground surface, whereas trees reduce the amount of precipitation reaching the ground surface by canopy interception. If MAP were solely dependent on $\bar{P}$, then increasing MAP would be expected to cause a decrease in hillslope gradient. However, our observations indicate that MAP is weakly positively correlated with mean hillslope gradient in this category. In the central Andes, spatial variability in MAP is strongly controlled by $\bar{D}$ and $\bar{I}$, in addition to $\bar{P}$ (Fig. 4.2). As a result, spatial variations in topography correlate more strongly with $\bar{P}$ than MAP on the heavily vegetated eastern flanks.

In the dense vegetation category, mean hillslope gradient also correlates with mean interval duration (r = -0.69). The negative correlation between mean hillslope gradient and $\bar{I}$ under dense vegetation is counter-intuitive; an increase in the frequency of events would be expected to increase the erosional efficiency, lower hillslope gradients and therefore produce a positive correlation with $\bar{I}$. Further insight may be gained by separating the data into regions north and south of 17.5°S (Fig. 4.10B). North of 17.5°S, the mean interval is less than 2 days, and hillslopes correlate poorly with $\bar{I}$ (r = -0.23) with a range in hillslope gradients of 8-32°. South of 17.5°S, hillslopes decrease from 15-25° at $\bar{I}$ = 2 days to 0-10° at $\bar{I}$ = 4.5 days (r = -0.62). One possible explanation is that mean hillslope gradient does not depend on mean interval, and that the observed relationship between mean interval and hillslope gradients is just an artifact of the relatively strong correlation between $\bar{P}$ and $\bar{I}$ south of 17.5°S (r = 0.49). A second possible explanation of the correlation

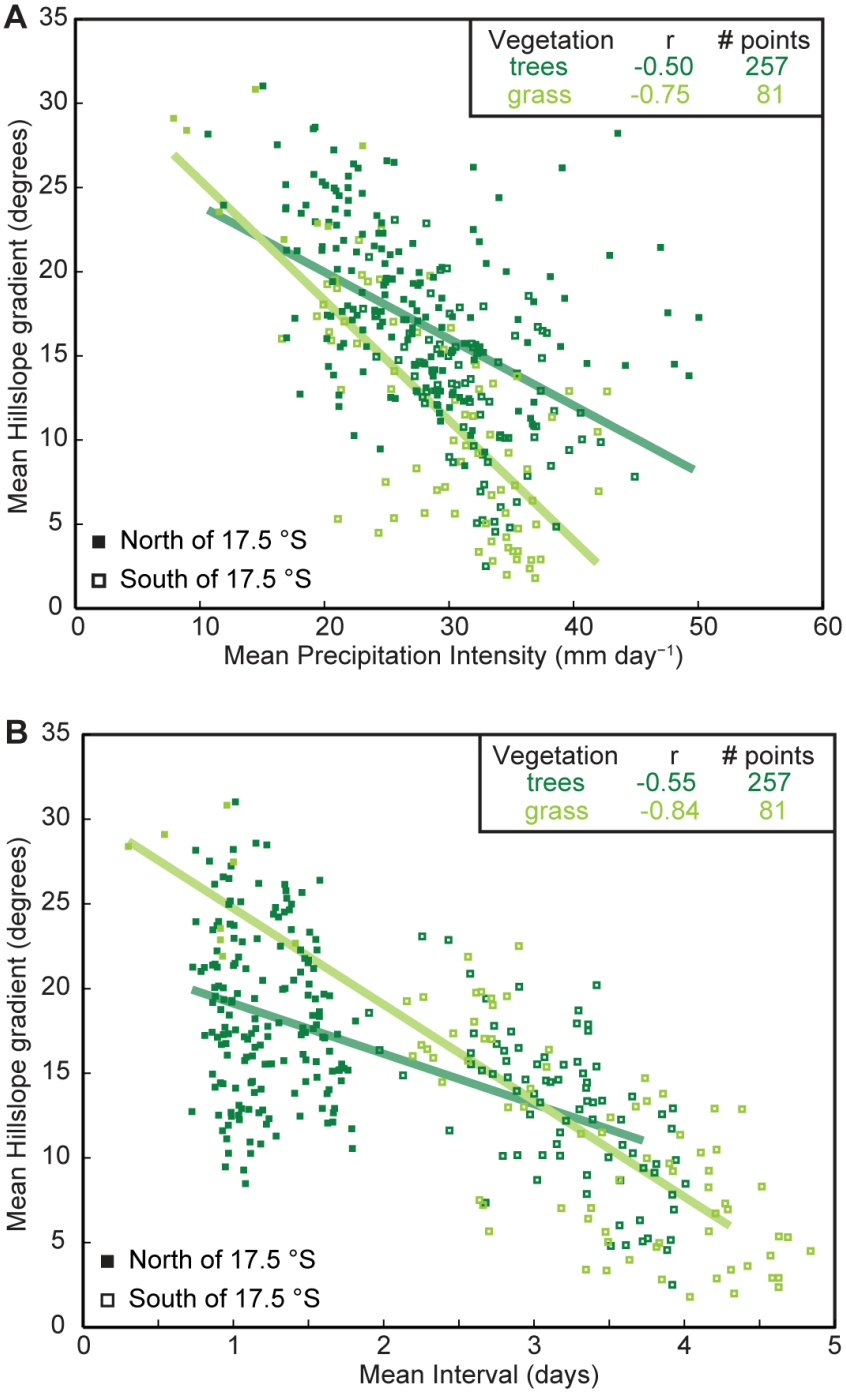

Figure 4.10 Precipitation controls on hillslope gradients in densely vegetated terrain

Scatter plots of hillslope gradients vs. precipitation metrics in densely vegetated (>95%) regions color-coded according to most abundant vegetation type: trees (dark green) and grass (light green). A) Mean hillslope gradient decreases with increasing precipitation intensity. B) Mean hillslope gradient generally decreases with mean interval, but hillslope gradeints spans a broad range (8-32°) where precipitation events occur almost daily (north of 17.5 °S, filled squares).

between hillslope gradient and $\bar{I}$ is that temporal clustering of precipitation events plays a role in determining erosional efficiency. The occurrence of landslides in particular is dependent on antecedent conditions, in addition to individual precipitation events [*Crozier*, 1999; *Gabet et al.*, 2004]. The data presented here are consistent with a fluctuation between dry and wet conditions being more erosive than a continuously wet environment.

As noted previously, precipitation intensity on the eastern flanks does not vary from north to south in the same manner as the other precipitation metrics. Consequently, the mean hillslope gradient against $\bar{P}$ plot is not separated into distinct groups when data points are classified by latitude (Fig. 4.10A). However, data points that do not fit the overall trend well (hillslopes >15° at precipitation intensity >~40 mm day^{-1}) are all situated north of 17.5°S. In these locations, high precipitation intensity does not drive sufficient erosional efficiency to maintain low hillslope gradients. There are two possible reasons for these high hillslope gradients: (1) locally high uplift rates may require steep hillslopes for erosion rates to keep pace with rock uplift, even under high erosional efficiency, or (2) the landscape may not be in equilibrium with the local climate and vegetation properties. Two lines of evidence support the former hypothesis. First, long term exhumation rates are higher north of 17.5°S [*Horton*, 1999; *Masek et al.*, 1994; *McQuarrie et al.*, 2008b] and may correspond to higher modern uplift rates [*Barnes and Pelletier*, 2006]. Second, the outlying data points are located at the eastern edge of the fold-and-thrust belt, which is the modern tectonically active region [*Barnes et al.*, 2008]. The complete dataset suggests that where erosional efficiency is low, steep hillslopes will develop regardless of the uplift rate. Spatial variability in uplift rates is hidden because maximum hillslope gradients are limited by the strength of the underlying material, rather than the erosional efficiency or uplift rate [*Larsen and Montgomery*, 2012; *Schmidt and Montgomery*, 1995]. As precipitation intensity increases, lower hillslope gradients only develop where uplift rates are sufficiently low that the increase in erosional efficiency is capable of balancing the mass flux from rock uplift without the need for steep hillslopes.

4.5.3 Comparison of results to simpler mean annual precipitation analyses

The observations presented in this study provide an extensive dataset that helps to elucidate the dominant controls on topography at the scale of a mountain belt. Observations from the Central Andes are consistent with the results of LEM studies in showing that (1) the amount and type of vegetation cover can play an important role in controlling mean hillslope gradients [*Collins et al.*, 2004; *Istanbulluoglu and Bras*, 2005], and (2) precipitation intensity can be strong control on erosional efficiency [*Tucker*, 2004; *Tucker and Bras*, 2000]. Observations from the central Andes also help to identify the dominant processes and forcing factors under different climate conditions, and provide quantitative constraints on the transitions between these domains. In the Andes, the transition from vegetation to precipitation intensity controlled hillslope gradients occurs over a broad range between 1 and 2 m yr^{-1} MAP (Fig. 4.8A). Maximum hillslopes, and inferred minimum erosional efficiency, occur at ~2 m yr^{-1} MAP. The role of vegetation amount in controlling the spatial variability of geomorphic processes is therefore not restricted to arid, or even sub-humid, conditions but is dictated by the amount of vegetation, which also depends on surface temperature, nutrients, and solar radiation.

Montgomery et al. [2001] demonstrated that hemisphere scale climate gradients exert a first order control on Andean topography. In their study, erosion potential was evaluated using an erosion intensity parametric based on the product of the local slope and the cumulative upslope discharge. At the scale of the Andes, this parametric is useful in explaining cross-range asymmetry and large-scale morphology. However, we have shown that hillslope gradients and precipitation rates are inter-dependent, through the effects of vegetation cover on the erosional efficiency of the climate. High hillslopes may indicate low erosion potential, but may also indicate high erosion thresholds set by the vegetation cover or bedrock lithology. If changes in precipitation act directly on hillslopes, then the product of precipitation and slope is a good indicator of erosion potential. However, because vegetation can also control hillslope gradients, care must be taken when defining an erosion potential parametric such as that used by Montgomery et al. [2001]. In

densely vegetated regions, high mean hillslopes associated with high precipitation intensities are a more robust indicator of high erosion potential (Fig. 4.10A).

Satellite-based observations such as TRMM datasets now enable the analysis performed in this study to be repeated in other active mountain belts. The quality of TRMM data is best at latitudes less than ~35°, but precipitation intensity is most important in humid, densely vegetated conditions, which are more commonly found in the low latitudes and encompasses mountain ranges in Taiwan, Papua New Guinea, northern South America, and parts of the Himalaya.

Finally, we consider the temporal implications of the observed spatial relationships. Because topography depends on vegetation cover and precipitation intensity, studies of climatic controls on temporal variation in erosion rates should consider these factors in addition to changes in mean annual precipitation alone. Perhaps most important is the consideration of how vegetation responds to climate change, because the amount and type of vegetation cover will respond to temperature changes, in addition to precipitation. Constraining past changes in vegetation, temperature and mean annual precipitation is possible through several proxies, including geologic records of pollen, oxygen isotope, and sedimentation rates and styles. Constraining precipitation intensity for past climates is more challenging. One possible approach is to use paleoclimate simulations, and we intend that the dataset presented here be a useful tool for model calibration.

4.5.4 Evaluation of precipitation and lithology datasets

The precipitation event metrics derived from TRMM 3B42v7 for this study show a spatial pattern that is consistent with modern understanding of central Andean climate. However, there are some limitations to the data. Precipitation rates in the TRMM 3B42v7 dataset are instantaneous measurements presented as a discrete 3-hourly timeseries. Peak precipitation intensities are therefore likely to be underestimated for each event, and therefore over all events. Additionally, all individual events therefore have a duration that is a multiple of 3 hours. Some events may be much shorter than 3 hours and the actual values of mean event duration derived by this method are therefore less meaningful than the spatial

distribution of event duration variability. Finally, we assume that precipitation events have a Poisson distribution that can be described entirely by the mean over all events [*Eagleson*, 1978; *Tucker and Bras*, 2000] and do not include a metric for seasonality or temporal clustering of events.

Due to the spatial resolution of the precipitation dataset, all of the variables were averaged over a 0.25° grid. Spatial averaging enables a statistical comparison between all variables, but properties such as vegetation are heterogeneous within a grid cell of this size. Relationships between topography, vegetation and climate that occur at smaller scale than the precipitation dataset, such as variation of vegetation cover with slope aspect [*Yetemen et al.*, 2010] and valley scale micro-climates, are therefore not accounted for in the analysis. The highest resolution dataset used in this analysis is the topography. Each 0.25° precipitation grid cell includes ~90,000 DEM grid cells and therefore also include multiple catchments with ridges, river valleys, trunk streams and hillslopes. Because hillslopes are spatially dominant in the landscape, compared to river beds for example, we assume that the mean hillslope gradient in a 0.25° grid cell is representative of the hillslope gradient in that region. Distributions of hillslope gradients from a few sample locations follow a normal distribution (not shown). Maximum hillslope gradients are a potentially useful metric because they may more closely represent the local threshold gradient, however the maximum hillslope over such a wide region would be more sensitive to outliers than the mean.

By necessity, the bedrock lithology was classified in fairly broad categories. A higher resolution, more detailed geological dataset may reveal further lithologic controls on mean hillslope gradients. Such an analysis would be particularly interesting on the eastern flanks where the bedrock is almost uniformly 'older sediments' and there is high variability in mean hillslope gradient. Other studies have shown that threshold hillslope gradients [*Larsen et al.*, 2010] and glacial erosion rates [*Duhnforth et al.*, 2010] depend on spatial variations in rock fracture density. Our observations suggest that, in the Andes, maximum hillslope gradients are also limited by the amount of vegetation cover (Fig. 4.6).

In addition to bedrock lithology, soil type can also be an important factor in hillslope processes and therefore may also affect hillslope gradients. For example, the cohesiveness of a soil affects how easily soil particles are moved by surface runoff and raindrop impact, and the porosity of surface layers determines the susceptibility of a hillslope to landslide failure, particularly during rain events. Distinguishing the effects of soil type on landscape morphology is challenging because soil type depends on many factors that can also directly affect surface processes, including bedrock lithology (parent material), climate, and vegetation. However, exploration of the variation in hillslope gradient with soil properties such as sand, silt and clay fractions may help to explain some of the scatter in the relationships presented above.

4.6 CONCLUSIONS

We present a new analysis of TRMM precipitation data that quantifies the variability in precipitation event intensity, duration and frequency. Topographic characteristics of the Central Andes correlate with these precipitation characteristics when considered in combination with vegetation. Where vegetation cover is less than 95%, both MAP and vegetation correlate strongly with mean hillslope gradients (r_{MAP} = 0.6 and $r_{\%\ veg}$ = 0.69). However, the response of hillslope gradients to vegetation and MAP changes is more consistent with vegetation being the mechanism controlling hillslope gradients. As vegetation cover increases, resistance to erosion increases (Fig 4.2A) and hillslope gradients increase. However, in the central Andes MAP can be considered as the underlying driving factor because vegetation is strongly dependent on MAP. In contrast, where vegetation cover is dense (>95%), precipitation intensity is a stronger predictor of mean hillslope gradient than MAP. An increase in mean precipitation intensity increases erosional efficiency, resulting in a return to lower mean hillslope gradients in the wettest regions with high intensity precipitation events (hillslope gradients decrease by ~0.5° / mm day^{-1}). Bedrock lithology and spatial variation in rock uplift rates also play a significant role in determining mean hillslope gradients.

When assessing climate-topography interactions, the relevant precipitation metric is therefore dependent on the vegetation cover. In the seasonal, wet climate of the central Andes, the transition between the two regimes occurs between 1 and 2 m yr^{-1} MAP, but may differ in other climates depending on the composition of the local plant community. Mean annual precipitation may be a sufficient means of characterizing climatic erosional efficiency, but only where it is the dominant control on vegetation cover.

4.7 ACKNOWLEDGEMENTS

This work was funded by grants to T.A.E. and C.J.P. from the US National Science Foundation (EAR awards 0738822, 0907817). M.L.J. was also supported by a Fellowship from the German DAAD.

4.8 REFERENCES

Abrahams, A. D. (1972), Drainage densities and sediment yields in eastern Australia, *Australian Geographical Studies*, *10*, 19 - 41

Abrahams, A. D., and J. J. Ponczynski (1984), Drainage density in relationship to to precipitation intensity in the USA, *Journal of Hydrology*, *75*(1-4), 383 - 388, 10.1016/0022-1694(84)90061-1

Allmendinger, R. W., T. E. Jordan, S. M. Kay, and I. B.L. (1997), The evolution of the Altiplano-Puna plateau of the Central Andes, *Annual Review of Earth and Planetary Sciences*, *25*, 139 - 174, 10.1146/annurev.earth.25.1.139

Barnes, J. B., and J. D. Pelletier (2006), Latitudinal variation of denudation in the evolution of the Bolivian Andes, *American Journal of Science*, *306*(1), 1-31, 10.2475/ajs.306.1.1

Barnes, J. B., and T. A. Ehlers (2009), End member models for Andean Plateau uplift, *Earth-Science Reviews*, *97*(1-4), 105-132, 10.1016/j.earscirev.2009.08.003

Barnes, J. B., T. A. Ehlers, N. McQuarrie, P. B. O'Sullivan, and S. Tawackoli (2008), Thermochronometer record of central Andean plateau growth, Bolivia (19.5 degrees S), *Tectonics*, *27*(3), 10.1029/2007tc002174

Bookhagen, B., and M. R. Strecker (2008), Orographic barriers, high-resolution TRMM rainfall, and relief variations along the eastern Andes, *Geophysical Research Letters*, *35*(6), 6, 10.1029/2007gl032011

Bookhagen, B., and M. R. Strecker (2012), Spatiotemporal trends in erosion rates across a pronunced rainfall gradient: Examples from the southern Central Andes, *Earth and Planetary Science Letters*(327-328), 97 - 110, 10.1016/j.epsl.2012.02.005

Campetella, C. M., and C. S. Vera (2002), The influence of the Andes mountains on the South American low-level, *Geophysical Research Letters*, *29*(17), 10.1029/2002gl015451

Chorley, R. J., and M. A. Morgan (1962), Comparison of morphometric features, Unaka mountains, Tennessee and North Carolina, and Dartmoor, England, *Geological Society of America Bulletin*, *73*(1), 17-34, 10.1130/0016-7606(1962)73[17:COMFUM]2.0.CO;2

Churkina, G., and S. W. Running (1998), Contrasting climatic controls on the estimated productivity of global terrestrial biomes, *Ecosystems*, *1*(2), 206-215, 10.1007/s100219900016

Collins, D. B., and R. L. Bras (2010), Climatic and ecological controls of equilibrium drainage density, relief, and channel concavity in dry lands, *Water Resources Research*, *46*, 10.1029/2009wr008615

Collins, D. B., R. L. Bras, and G. E. Tucker (2004), Modeling the effects of vegetation-erosion coupling on landscape evolution, *Journal of Geophysical Research*, *109*(F03004), 10.1029/2003JF000028

Cotton, C. A. (1964), The control of drainage density, *New Zealand Journal of Geology and Geophysics*, *7*(2), 348-352, 10.1080/00288306.1964.10420180

Crozier, M. J. (1999), Prediction of rainfall-triggered landslides: a test of the antecedent water status model, *Earth Surface Processes and Landforms*, *24*, 825 - 833, 10.1002/(SICI)1096-9837(199908)24:9<825::AID-ESP14>3.3.CO;2-D

Dadson, S., et al. (2003), Links between erosion, runoff variability and seismicity in the Taiwan orogen, *Nature*, *426*, 648-699, 10.1038/nature02150

Daniel, J. R. K. (1981), Drainage density as an index of climatic geomorphology, *Journal of Hydrology*, *50*(1-3), 147 - 154, 10.1016/0022-1694(81)90065-2

Dietrich, W. E., C. J. Wilson, D. R. Montgomery, J. McKean, and R. Bauer (1992), Erosion thresholds and land surface morphology, *Geology*, *20*, 675 - 679, 10.1130/0091-7613(1992)020<0675:ETALSM>2.3.CO;2

Duhnforth, M., R. S. Anderson, D. Ward, and G. M. Stock (2010), Bedrock fracture control of glacial erosion processes and rates, *Geology*, *38*(5), 423-426, 10.1130/G30576.1

Eagleson, P. S. (1978), Climate, Soil, and Vegetation 2. The distribution of annual precipitation derived from observed storm sequences, *Water Resources Research*, *14*(5), 713 - 721, 10.1029/WR014i005p00713

Ehlers, J., P. L. Gibbard, and P. D. Hughes (2011), Quaternary Glaciations - Extent and Chronolgy: A Closer Look, *Developments in Qauternary Science*, *15*

Farias, M., R. Charrier, D. Comte, J. Martinod, and G. Herail (2005), Late Cenozoic deformation and uplift of the western flank of the Altiplano: Evidence from the depositional, tectonic, and geomorphologic evolution and shallow seismic activity (northern Chile at 19 degrees 30 ' S), *Tectonics*, *24*(4), 29, 10.1029/2004tc001667

Farr, T. G., et al. (2007), The Shuttle Radar Topography Mission, *Rev. Geophys.*, *45*(2), RG2004, 10.1029/2005rg000183

Gabet, E. J., D. W. Burbank, J. K. Putkonen, B. A. Pratt-Sitaula, and T. Ojha (2004), Rainfall thresholds for landsliding in the Himalayas of Nepal, *Geomorphology*, *63*(3-4), 131-143, 10.1016/j.geomorph.2004.03.011

Galewsky, J. (2009), Rain shadow development during the growth of mountain ranges: An atmospheric dynamics perspective, *Journal of Geophysical Research*, *114*, 10.1029/2008jf001085

Hales, T. C., C. R. Ford, T. Hwang, J. M. Vose, and L. E. Band (2009), Topographic and ecologic controls on root reinforcement, *Journal of Geophysical Research - Earth Surface*, *114*(17), 10.1029/2008JF001168

Horton, B. K. (1999), Erosional control on the geometry and kinematics of thrust belt development in the central Andes, *Tectonics*, *18*(6), 1292-1304, 10.1029/1999TC900051

Houston, J., and A. J. Hartley (2003), The central andean west-slope rainshadow and its potential contribution to the origin of hyper-aridity in the Atacama desert, *International Journal of Climatology*, *23*(12), 1453-1464, 10.1002/joc.938

Huffman, G. J., R. F. Adler, D. T. Bolvin, G. Gu, E. J. Nelkin, K. P. Bowman, Y. Hong, E. F. Stocker, and D. B. Wolff (2007), The TRMM Multisatellite Precipitation Analysis (TMPA): Quasi-Global, Multiyear, Combined-Sensor Precipitation Estimates at Fine Scales, *Journal of Hydrometeorology*, *8*, 38 - 55, 10.1175/JHM560.1

Hulme, M. (1992), A 1951-80 global land precipitation climatology for the evaluation

of General Circulation Models, *Climate Dynamics*, *7*(2), 57-72, 10.1007/BF00209609

Insel, N., C. J. Poulsen, and T. A. Ehlers (2010a), Influence of the Andes Mountains on South American moisture transport, convection, and precipitation, *Climate Dynamics*, *35*(7-8), 1477-1492, 10.1007/s00382-009-0637-1

Insel, N., T. A. Ehlers, M. Schaller, J. B. Barnes, S. Tawackoli, and C. J. Poulsen (2010b), Spatial and temporal variability in denudation across the Bolivian Andes from multiple geochronometers, *Geomorphology*, *122*(1-2), 65-77, 10.1016/j.geomorph.2010.05.014

Isacks, B. L. (1988), Uplift of the central Andean plateau and bending of the Bolivian orocline, *Journal of Geophysical Research-Solid Earth and Planets*, *93*(B4), 3211-3231

Istanbulluoglu, E., and R. L. Bras (2005), Vegetation-modulated landscape evolution: Effects of vegetation on landscape processes, drainage density, and topography, *Journal of Geophysical Research*, *110*, 10.1029/2004jf000249

Jeffery, M. L., T. A. Ehlers, B. J. Yanites, and C. J. Poulsen (in press), Quantifying the role of paleoclimate and Andean plateau uplift on river incision, *Journal of Geophysical Research - Earth Surface*

Koons, P. O. (1990), The two‐sided orogen: Collision and erosion from the sand box to the Southern Alps, New Zealand. , *Geology*, *18*(8), 679‐682, 10.1130/0091-7613(1990)018<0679:TSOCAE>2.3.CO;2

Kutzbach, J. E., P. J. Guetter, W. F. Ruddiman, and W. L. Prell (1989), Sensitivity of Climate to Late Cenozoic Uplift in Southern Asia and the American West: Numerical Experiments, *Journal of Geophysical Research*, *94*(D15), 18393-18407, 10.1029/JD094iD15p18393

Lague, D., N. Hovius, and P. Davy (2005), Discharge, discharge variability, and the bedrock channel profile, *Journal of Geophysical Research*, *110*, 10.1029/2004JF000259

Langbein, W. B., and S. A. Schumm (1958), Yield of Sediment in Relation to Mean Annual Precipitation, *Transcations, American Geophsyical Union*, *39*(6), 1076 - 1084

Larsen, I. J., and D. R. Montgomery (2012), Landslide erosion coupled to tectonics and river incision, *Nature Geoscience*, *5*(7), 468-473, 10.1038/ngeo1479

Larsen, I. J., D. R. Montgomery, and O. Korup (2010), Landslide erosion controlled by hillslope material, *Nature Geoscience*, *3*, 10.1038/ngeo776

Lawrence, P. J., and T. N. Chase (2007), Representing a new MODIS consistent land surface in the Community Land Model (CLM 3.0), *Journal of Geophysical Research - Biogeosciences*, *112*(G01023), 10.1029/2006JG000168

Masek, J. G., B. L. Isacks, T. L. Gubbels, and E. J. Fielding (1994), Erosion and tectonics at the margins of continental plateaus, *Journal of Geophysical Research*, *99*(B7), 13941-13956, 10.1029/94JB00461

McQuarrie, N., T. A. Ehlers, J. B. Barnes, and B. Meade (2008), Temporal variation in climate and tectonic coupling in the central Andes, *Geology*, *36*(12), 999-1002, 10.1130/g25124a.1

Melton, M. A. (1957), *An analysis of the relations among elements of climate, surface properties and geomorphology*, Columbia University, Dept. of Geology, Technical Report, New York.

Molnar, P., R. S. Anderson, G. Kier, and J. Rose (2006), Relationships among probability distributions of stream discharges in floods, climate, bed load transport, and river incision, *Journal of Geophysical Research*, *111*, 10.1029/2005JF000310

Montgomery, D. R., and W. E. Dietrich (1992), Channel initiation and the problem of landscape scale, *Science*, *255*(5046), 926-830, 10.1126/science.255.5046.826

Montgomery, D. R., G. Balco, and S. D. Willett (2001), Climate, tectonics, and the morphology of the Andes, *Geology*, *29*(7), 579-582, 10.1130/0091-7613(2001)029<0579:CTATMO>2.0.CO;2

Musgrave, G. W. (1947), The quantitative evaluation of factors in soil water erosion - A first approximation, *Journal of soil and Water Conservation*, *2*, 133-138

Roe, G. H., K. X. Whipple, and J. K. Fletcher (2008), Feedbacks among climate, erosion, and tectonics in a critical wedge orogen, *American Journal of Science*, *308*(7), 815-842, 10.2475/07.2008.01

Rutllant, J. A., H. Fuenzalida, and A. P. (2003), Climate dynamics along the arid northern coast of Chile: The 1997-1998 Dinámica del Clima de la Región de Antofagasta (DICLIMA) experiment, *Journal of Geophysical Research - Atmospheres*, *108*(D17), 10.1029/2002JD003357

Schenk, C. J., R. J. Viger, and C. P. Anderson (1999), Maps Showing Geology, Oil and Gas Fields and Geologic Provinces of the South America Region, edited,

Schildgen, T. F., K. V. Hodges, K. X. Whipple, M. S. Pringle, M. van Soest, and K. Cornell (2009), Late Cenozoic structural and tectonic development of the western margin of the central Andean Plateau in southwest Peru, *Tectonics*, *28*, 10.1029/2008tc002403

Schmidt, K. H., and D. R. Montgomery (1995), Limits to relief, *Science*, *270*(5236), 617-620, 10.1126/science.270.5236.617

Schmidt, K. H., J. J. Roering, J. D. Stock, W. E. Dietrich, D. R. Montgomery, and T. Schaub (2001), The variability of root cohesion as an influence on shallow landslide susceptibility in the Oregon Coast Range *Canadian Geotechnical Journal*, *38*(5), 995-1024, 10.1139/t01-031

Tucker, G. E. (2004), Drainage basin sensitivity to tectonic and climatic forcing: Implications of a stochastic model for the role of entrainment and erosion thresholds, *Earth Surface Processes and Landforms*, *29*(2), 185-205, 10.1002/esp.1020

Tucker, G. E., and R. Slingerland (1997), Drainage basin responses to climate change, *Water Resources Research*, *33*(8), 2031-2047, 10.1029/97wr00409

Tucker, G. E., and R. L. Bras (2000), A stochastic approach to modeling the role of rainfall variability in drainage basin evolution, *Water Resources Research*, *36*(7), 1953-1964, 10.1029/2000wr900065

Tucker, G. E., S. T. Lancaster, N. M. Gasparini, and R. L. Bras (2001), The Channel-Hillslope Integrated Landscape Development (CHILD) Model, in *Landscape Erosion and Evolution Modeling*, edited by R. S. Harmon and W. W. D. III, pp. 349-388, Kluwer Academic/Plenum Publishers.

Wainwright, J., A. J. Parsons, and A. D. Abrahams (2000), Plot-scale studies of vegetation, overland flow and erosion interactions: case studies from Arizona and New Mexico, *hydrological Processes*, *14*(16-17), 2921-2943, 10.1002/1099-1085(200011/12)14:16/17<2921::AID-HYP127>3.0.CO;2-7

Whipple, K. X. (2001), Fluvial landscape response time; How plausible is steady-state denudation?, *American Journal of Science*, *301*(4-5), 313-325, 10.2475/ajs.301.4-5.313

Whipple, K. X. (2009), The influence of climate on the tectonic evolution of mountain belts, *Nature Geoscience*, *2*(2), 97-104, 10.1038/ngeo413

Willett, S. D. (1999), Orogeny and orography: The effects of erosion on the structure of mountain belts, *Journal of Geophysical Research-Solid Earth*, *104*(B12), 28957-28981, 10.1029/1999jb900248

Yetemen, O., E. Istanbulluoglu, and E. R. Vivoni (2010), The implications of geology, soils, and vegetation on landscape morphology: Inferences from semi-arid basins with complex vegetation patterns in Central New Mexico, USA, *Geomorphology*, *116*(3-4), 246-263, 10.1016/j.geomorph.2009.11.026

CHAPTER 5

CONCLUSIONS

To conclude, the key findings of each research chapter are summarized and implications for future research directions are considered. The two hypotheses that were introduced in Chapter one are evaluated, these hypotheses are: (1) proxy records that indicate a rapid surface uplift event in the late Miocene are compatible with a steady surface uplift rate when climate change is accounted for, and (2) precipitation intensity is a dominant control on landscape morphology and erosional efficiency in the Central Andes. Finally, the key results of this thesis are presented in a synthesis with other recent work that examines the topographic and climatic development of the Andes and outstanding research questions are identified.

5.1 SUMMARY OF RESULTS

5.1.1 Chapter 2

In this chapter, the relative importance of global and regional controls on Cenozoic climate and precipitation $\delta^{18}O$ in South America were explored using a global climate model with modified boundary conditions. The key results of this study are: (1) Precipitation rates in the Andes are sensitive to Andean surface elevation, the seaway and, to a lesser extent, CO_2 levels. Increasing Andean elevations and the presence of a seaway both cause large increases in precipitation, but in different parts of the Andes. (2) The stable isotopic composition of precipitation is sensitive to all of the parameters investigated. An increase in $\delta^{18}O_{prec}$

of up to 8 ‰ is found in simulations with higher atmospheric CO_2. In agreement with previous studies, $\delta^{18}O_{prec}$ decreases with increasing Andean elevation by an amount greater than that predicted by the modern adiabatic lapse rate. Furthermore, the presence of an inland seaway causes a decrease in $\delta^{18}O_{prec}$ of 1-8 ‰ in the northern and central Andes. Finally, we demonstrate that in addition to Andean uplift and associated climate change, CO_2 levels and an inland seaway are likely to have influenced $\delta^{18}O_{carb}$ records from South America.

The results of this study both facilitate and motivate further research. First, the conclusion that Andean topography is the strongest and longest lasting control on precipitation rates in the Central Andes enables further research to focus on surface uplift induced climate change as the primary control on central Andean precipitation rates in the late Cenozoic [e.g. *Barnes et al.*, 2012; *Jeffery et al.*, in press]. Second, Andean topography is also the strongest control on $\delta^{18}O_{prec}$. Together with other complimentary studies [*Insel et al.*, 2010a; *Insel et al.*, 2012; *Poulsen et al.*, 2010], we show that Andean stable isotope based paleoaltimetry estimates are consistent with a steady uplift of the Altiplano, which supports hypothesis 1 above. Third, the presence of an inland seaway is also capable of causing a strong (1-8 ‰) signal in South American $\delta^{18}O_{prec}$ proxy records. At present, the nature, timing and isotopic composition of the seaway is not sufficiently well constrained to confidently attribute $\delta^{18}O_{prec}$ proxy signals to the seaway with confidence. However, our study indicates the value of obtaining greater constraints on seaway characteristics.

Climate model simulations in which CO_2 levels were modified are also relevant to paleoaltimetry proxies from other mountain ranges, because the climate response to changing CO_2 levels is global in nature. Simulations presented in Chapter 2 were therefore also used to examine the impact of CO_2, and consequently global temperatures, on $\delta^{18}O_{prec}$ in other orogens. Poulsen and Jeffery [2011] showed that surface to troposphere gradients of both temperature and vapor $\delta^{18}O$ are lower at higher CO_2 levels. In major orogens, downwards mixing of vapor $\delta^{18}O$ decreases isotopic lapse rates further and so results in an amplified increase in $\delta^{18}O_{prec}$ at high elevations in comparison to low elevations. This phenomenon

further complicates the extraction of paleoelevations from $\delta^{18}O_{prec}$ proxy records, but quantitative constraints from climate model simulations may help to distinguish between paleoelevation and global paleoclimate signals. This concept is particularly important for paleoaltimetry analysis in the early Cenozoic when CO_2 concentrations were significantly higher [*Pagani et al.*, 2005].

5.1.2 Chapter 3

The climate and erosional history of the South Peruvian Cotahuasi-Ocoña River was explored using a numerical river profile evolution model. A Monte Carlo approach is used to explore the range of surface uplift and paleoclimate histories that are compatible with the modern river profile and geological constraints on the incision timing and magnitude. Simulation results indicate that the evolution of the Ocoña River is consistent with local plateau elevations of 1-3 km at 16 Ma, and either a steady or punctuated uplift of 1.5–3.5 km since then. The range of acceptable uplift histories is sensitive to the magnitude and temporal evolution of precipitation.

The results of this study have implications for both Andean paleoaltimetry and, more generally, the role of coupled climate and tectonic development. Geological constraints available for the Cotahuasi-Ocoña catchment are consistent with a wide range of paleoelevation histories, including both end-member models of surface uplift [*Barnes and Ehlers*, 2009]. The Cotahuasi-Ocoña catchment was chosen as a case study because good constraints on the timing and magnitude of incision are available. It would not have been possible to simulate river development without good constraints on the timing and amount of incision from local thermochronometry and sedimentology studies. In order to repeat this approach elsewhere, a river with suitable constraints, or a companion field study would be required. However, because estimates for late Miocene incision magnitude are larger for the Cotahuasi-Ocoña catchment than elsewhere on the Andean plateau margins, the same principle of climatic influence on the incision history is likely to

apply to other river in the region, particularly on the eastern flanks where the change in precipitation rates was greatest [*Insel et al.*, 2010a].

More generally, we show that river incision rates responded to a change in the distribution and magnitude of precipitation through time. The sensitivity of the river profile to precipitation change depends on the parameterization of erosion processes, and where these parameters are under-constrained a range of values must be considered. The use of climate model output as input to the river incision model is a continuation in a series of advances in simulating river incision under more realistic climate and tectonic conditions [*Roe et al.*, 2002; *Whipple and Tucker*, 1999; *Wobus et al.*, 2010].

A limitation of the river incision study (Chapter 3) is that only changes in mean annual precipitation rates are considered. As discussed in chapter 4, the variability of precipitation intensity may be a stronger control on erosion rates than mean annual precipitation. Modern observations suggest that vegetation and mean annual precipitation are more important controls on erosional efficiency in arid regions, such as the Ocoña catchment, which would support the approach used in chapter 3. However, the impact of precipitation and vegetation on topography was evaluated for hillslope gradients, and not channel gradients or channel incision rates. Further analysis is therefore required before mean annual precipitation can be considered the only relevant climate characteristic. The results of existing paleoclimate model simulations are not ideal for exploring past precipitation intensity characteristics because the resolution model resolution is coarse, and the precipitation intensity output from the models has not yet been tested against modern precipitation observations. Exploring and testing the possibilities for simulating precipitation intensity in the past is a future research goal.

5.1.3 Chapter 4

Finally, the precipitation characteristics that determine modern erosional efficiency in the Andes were evaluated using satellite-based precipitation observations. Correlation and multiple linear regression analyses indicate that: (1)

mean hillslope gradient correlates most strongly with percent vegetation cover (r = 0.56), (2) where vegetation cover is less than 95%, mean hillslope gradients increase with mean annual precipitation and vegetation density, (3) where vegetation cover is dense (>95%), mean hillslope gradients decrease with increasing precipitation density by ~0.5° /mm day^{-1} (r = -0.56), and (4) bedrock lithology and spatial variations in uplift rate also influence mean hillslope gradients. We therefore show the importance of vegetation in mediating the influence of climate on topography at the scale of an orogen.

An increase in vegetation cover both sets the critical erosion threshold and reduces surface runoff and rain splash impacts. In the central Andes, vegetation cover is primarily dependent on mean annual precipitation. Mean annual precipitation therefore acts as an indirect control on mean hillslope gradients through vegetation cover and may be the most important climatic variable in dictating long term topographic development. However, precipitation intensity is more important where vegetation cover is high. In the central Andes, the most densely vegetated region is the eastern flanks, which is also the location where climate-tectonic interactions are thought to be strongest [e.g *Barnes et al.*, 2012; *Horton*, 1999; *Masek et al.*, 1994]. Precipitation intensity cannot, therefore, be disregarded as an important variable in the long-term climate-tectonic development of the Andes.

The methods and datasets developed in this study have multiple further applications. First, the precipitation dataset spans 50°N to 50°S and encompasses several large, active mountain ranges, including the Himalaya, the Rockies and New Zealand. A similar analysis could therefore be repeated in other orogens, or at other latitudes in the Andes, to test whether similar patterns are observed in different climate and tectonic regimes. Second, the temporal variability of PDI characteristics on glacial–interglacial timescales may dictate the extent to which topography is in equilibrium with the modern day climate [*Tucker and Slingerland*, 1997]. If regional climate models are able to faithfully represent modern spatial variability in precipitation intensity, then a possible means of constraining temporal variability in precipitation intensity would be to simulate paleoclimate with a regional climate

model. Such constraints could be used in conjunction with erosion rates estimates from cosmogenic radionuclides to evaluate the role of climate in determining erosion rates and patterns on glacial-interglacial timescales. Based on the results presented in chapter 4, such a study would also need to include a consideration of changes in vegetation on the same timescales. Such a study would be particularly interesting if the limiting factor on vegetation growth transitions between precipitation and temperature on these timescales.

5.2 EVALUATION OF HYPOTHESES

Hypothesis 1 (proxy records that indicate a rapid surface uplift event in the late Miocene are compatible with a steady surface uplift rate when climate change is accounted for) is directly addressed in chapters 2 and 3. We show that qualitative suggestions that climate change significantly influenced paleoaltimetry records [*Barnes and Ehlers*, 2009; *T A Ehlers and Poulsen*, 2009] are also quantitatively robust. The evidence presented in this chapter, along with complimentary studies [*Insel et al.*, 2012; *Poulsen et al.*, 2010], shows that $\delta^{18}O_{prec}$ and fluvial incision based paleoaltimetry proxies do not require a late Miocene rapid uplift event of ~2.5 km. However, given the wide range in erosion parameters, including the influence of climate change on the incision history of the Ocoña catchment does not preclude a rapid surface uplift event.

The second hypothesis (precipitation intensity is a dominant control on landscape morphology and erosional efficiency in the Central Andes) was tested by the precipitation analysis performed and described in chapter 4. We find that precipitation intensity does influence landscape morphology in the central Andes, but that its influence is subsidiary to vegetation cover, which in turn depends on mean annual precipitation. Further examination of the spatial variability in erosion rates and an estimate of the state of precipitation variability for past climates are useful avenues for further evaluation of this hypothesis.

5.3 ANDEAN PALEOELEVATION

Paleoaltimetry is a major challenge in the study of orogenic development. Stable isotope based paleoaltimetry is appealing because, in principle, it has the capacity to provide quantitative estimates of past elevations at moderately high temporal resolution. However, recent work has highlighted multiple uncertainties associated with this approach, including: 1) constraining the temperature of formation with Δ_{47} clumped isotope thermometry, 2) potential seasonal bias in the formation of carbonates, 3) global controls on the isotopic composition of precipitation, and 4) changes in isotopic lapse rates with increasing orogeny elevation.

When this work began, the surface uplift history of the Andean Plateau was starting to be questioned. A commonly accepted uplift scenario was that around half of modern Andean elevation was attained during a late Miocene (10-6 Ma) rapid uplift event. Geological evidence for a rapid uplift event included (1) large shifts in the stable isotopic composition of carbonates from the plateau [*Garzione et al.*, 2006; *C N Garzione et al.*, 2008b; *Ghosh et al.*, 2006], and (2) evidence of a contemporaneous pulse of fluvial incision on the plateau margins [*Hoke et al.*, 2007; *Kennan et al.*, 1997; *Schildgen et al.*, 2007]. This evidence had been called into question based on developments in the understanding of how rising topography changed the regional climate [*Barnes and Ehlers*, 2009; *T A Ehlers and Poulsen*, 2009; *Insel et al.*, 2010a], and the consequent impacts on both the isotopic composition of carbonates and the rate and nature of surface processes. At this stage, arguments were primarily qualitative and therefore neither conclusive, nor able to better constrain surface uplift histories. There are three broad approaches that are able to advance the field of Andean paleoaltimetry: (1) quantification of climate change during mountain belt growth and the impact on paleoelevation records, (2) collection of additional field data, and (3) improved understanding of both soil carbonate formation and controls on precipitation $\delta^{18}O$. The work presented in this thesis primarily uses the first of these approaches. Here I synthesize this work with other recent complimentary studies.

Multiple paleoclimate modeling studies have been performed to assess different aspects of South American Cenozoic paleoclimate. Building on previous work by Lenters and Cook [1995] and Campetella and Vera [2002], Poulsen et al. [2010] focused on the impact of changing Andean topography on large scale climate patterns at both a coarse (T63) and finer (~50 km) resolution. A highlight of this work was the identification of threshold elevations (~70% modern elevation) above which precipitation rates on the eastern flanks increased significantly. Sepulchre [*Sepulchre et al.*, 2009] explored the influence of Andean topography on ocean circulation patterns in the eastern Pacific. Chapter 1 of this thesis [*Jeffery et al.*, 2012] explored global controls on South American paleoclimate at a fairly coarse resolution (T63). Finally, Insel et al. [2010a; 2012] explored the influence of Andean topography (1) on atmospheric circulation, specifically the South American low-level jet, and (2) the oxygen isotope composition of precipitation. Some of the key findings of these modeling studies are that: (1) the isotopic lapse rate on the eastern flanks increases with increasing Andean elevation, (2) precipitation $\delta^{18}O$ is highly variable both spatially and temporally (<10 years), (3) Andean elevation was the strongest control on precipitation and precipitation $\delta^{18}O$ in the central Andes during the late Cenozoic (Miocene to Present), and (4) decreasing global temperatures are accompanied by a decreased in precipitation $\delta^{18}O$ that is comparable in magnitude to changes caused by topography. In terms of paleoelevation, it is likely that initial interpretations of paleoelevation from the isotopic compositions of carbonates were under-estimations of the true elevations. Furthermore, dramatic shifts in oxygen isotopes, such as that observed in late Miocene carbonates [*Garzione et al.*, 2006; *Ghosh et al.*, 2006] are also consistent with changes in precipitation patterns when threshold elevations are attained [*Insel et al.*, 2012].

In order to provide good constraints on past surface elevations, an ideal stable isotope based paleoaltimetry estimate would: (1) be based on multiple locations across the plateau, and at both high and low modern elevations, (2) incorporate records that are continuous over several million years at the same location, (3) be interpreted in the context of paleoclimate model estimates of the co-evolution of orogen elevation and isotopic lapse rates, and (4) be accompanied by

sedimentary evidence of environmental conditions at the time of formation. These ideals may never be attained, simply due to limits of the geological record, but they do provide targets for future research. Furthermore, it is useful to know what is, and what is not, well-constrained by existing records.

Paleoclimate model results can also be used to understand changes in surface processes that accompany mountain belt growth (chapter 3 of this thesis), and to reassess paleoaltimetry estimates derived from geological constraints on river incision. By using paleoclimate model results and a Monte Carlo search of river profile evolution, we showed that a range of uplift histories are consistent with existing geological constraints and understanding of river incision processes. In terms of modeling, some additional advances may be possible by considering changes in the distribution of precipitation events through time, rather than mean annual precipitation alone. However, in terms of constraining past elevation, improving the geological constraints would be a more effective approach. Model results were constrained by the geological evidence, and accounting for additional variability in climate or incision mechanisms would more likely widen the acceptable parameter space than reduce it. In chapter 4, we demonstrate that vegetation plays a role in determining hillslope morphology, but do not address the role of vegetation in channel incision processes. Vegetation cover in the Ocoña catchment is sparse, but existent in the upper portion of the catchment. Vegetation cannot be ruled as an important factor in channel profile development, but modern processes are not yet sufficiently well understood to apply to the past in a quantitative manner.

Much of the work presented here highlights uncertainties in the interpretation of field data. However, it is important also to highlight the value of these datasets. Models alone cannot provide constraints on the timing and nature of geological events; they can help to understand some of the complex interactions between topography and climate and improve data interpretation. Furthermore, models themselves carry inherent uncertainties and cannot perfectly simulate past conditions, or incorporate all changes in boundary conditions. An example from this thesis is the spatial resolution of the climate model used to perform the

paleoclimate simulations presented in chapter 2. A higher resolution would have been computationally too expensive for the suite of model runs, but Andean topography had to be simplified in order to run simulations at the chosen resolution. Higher resolution models [e.g. *Insel et al.*, 2010a; *Insel et al.*, 2012] are able to resolve spatial patterns in topography, and precipitation better than the lower resolution model, but would not be able to address the same questions.

In combination, chapters 2 and 3 of this thesis demonstrate that the impact of long term climate change on paleoaltimetry proxies is sufficient to reconcile existing proxy records with a steadier surface uplift history than originally hypothesized. However, a steady uplift history is not required by proxy records considered in the context of uplift-induced climate change and therefore uplift histories that are either completely steady, or are somewhat temporally and spatially heterogeneous are consistent with existing paleoaltimetry records. Other lines of geological evidence, such as the volcanic and deformation history, do not require large scale heterogeneous patterns. At this time, therefore, it does not seem necessary to invoke large temporal and spatial differences in plateau surface uplift rate through the late Cenozoic.

5.4 IDENTIFICATION OF CLIMATE-TECTONIC FEEDBACKS IN THE CENTRAL ANDES: EXISTING EVIDENCE AND FUTURE CHALLENGES

A recent analysis of the topographic, climatic, and exhumational histories of the eastern flank of the central Andes [*Barnes et al.*, 2012], suggest that long-term exhumation rates are dependent on long-term precipitation patterns, that in turn are governed by the large-scale topography. This study demonstrates the value of an integrated approach that considers multiple aspects of Earth surface systems and processes to establish a coherent geologic history. The above study does have some limitations; the spatial scale is fairly coarse and climate was only considered in terms of mean annual precipitation. In chapter 4 of this thesis, I have demonstrated that present day erosional efficiency in the central Andes is also dependent on the intensity of precipitation, the amount of vegetation cover, and the bedrock lithology.

In contrast, the results presented in chapter 4 are limited in that they relate modern surface morphology with climate, rather than erosion rates as in the Barnes et al [2012] study. Measurements of erosion rates cover a wider timescale (thousands to millions of years), and are site specific. They are therefore not so amenable to the gridded, multivariate analysis approach presented in chapter 4. The role of precipitation variability and changing surface conditions in temporal changes in erosion rates has not been fully explored. For example, are erosion rates higher under glacial or inter-glacial conditions, and why? Or are changes in mean annual precipitation as a result of Andean uplift sufficiently large to dwarf any changes in precipitation variability?

Establishing unequivocal evidence for climatic feedbacks on orogen development remains challenging. Studies of the Andean orogen over the last decade have shown that topographic changes have significantly modified South American climate, and that precipitation responses to increasing plateau elevation were non-linear. The feedback aspect is less well-constrained. Spatial correlations between rainfall peaks and modern topography are consistent with a climatic influence on topographic development [*Bookhagen and Strecker*, 2008; *Horton*, 1999; *Schlunegger et al.*, 2011]. Barnes et al., [2012] also find evidence in support of spatial and temporal correlations between elevation controlled changes in mean annual precipitation and erosion rates and propagation of deformation in the eastern central Andes. These lines of evidence make a coherent story that is supported by theory. However, the timing of events still contains significant error, Altiplano paleoelevation remains under-constrained, and the magnitude of climatic vs. tectonic forcing on deformation rates and styles is not known. Recent work, including this thesis, has helped to identify and quantify some of the key uncertainties in reconstructing the geological history of the Andes. Knowledge of these uncertainties should help to guide further data collection and modeling studies.

5.5 REFERENCES

Barnes, J. B., and T. A. Ehlers (2009), End member models for Andean Plateau uplift, *Earth-Science Reviews*, *97*(1-4), 105-132, 10.1016/j.earscirev.2009.08.003

Barnes, J. B., T. A. Ehlers, N. Insel, N. McQuarrie, and C. J. Poulsen (2012), Linking orography, climate, and exhumation across the central Andes, *Geology*, 10.1130/G33229.1

Bookhagen, B., and M. R. Strecker (2008), Orographic barriers, high-resolution TRMM rainfall, and relief variations along the eastern Andes, *Geophysical Research Letters*, *35*(6), 6, 10.1029/2007gl032011

Campetella, C. M., and C. S. Vera (2002), The influence of the Andes mountains on the South American low-level, *Geophysical Research Letters*, *29*(17), 10.1029/2002gl015451

Ehlers, T. A., and C. J. Poulsen (2009), Influence of Andean uplift on climate and paleoaltimetry estimates, *Earth and Planetary Science Letters*, *281*(3-4), 238-248, 10.1016/j.epsl.2009.02.026

Garzione, C. N., P. Molnar, J. C. Libarkin, and B. J. MacFadden (2006), Rapid late Miocene rise of the Bolivian Altiplano: Evidence for removal of mantle lithosphere, *Earth and Planetary Science Letters*, *241*(3-4), 543-556, 10.1016/j.epsl.2005.11.026

Garzione, C. N., G. D. Hoke, J. C. Libarkin, S. Withers, B. J. MacFadden, J. Eiler, P. Ghosh, and A. Mulch (2008), Rise of the Andes, *Science*, *320*(5881), 1304-1307, 10.1126/science.1148615

Ghosh, P., C. N. Garzione, and J. M. Eiler (2006), Rapid uplift of the Altiplano revealed through C-13-O-18 bonds in paleosol carbonates, *Science*, *311*(5760), 511-515, 10.1126/science.1119365

Hoke, G. D., B. L. Isacks, T. E. Jordan, N. Blanco, A. J. Tomlinson, and J. Ramezani (2007), Geomorphic evidence for post-10 Ma uplift of the western flank of the central Andes 18 degrees 30'-22 degrees S, *Tectonics*, *26*(5), 10.1029/2006tc002082

Horton, B. K. (1999), Erosional control on the geometry and kinematics of thrust belt development in the central Andes, *Tectonics*, *18*(6), 1292-1304, 10.1029/1999TC900051

Insel, N., C. J. Poulsen, and T. A. Ehlers (2010), Influence of the Andes Mountains on South American moisture transport, convection, and precipitation, *Climate Dynamics*, *35*(7-8), 1477-1492, 10.1007/s00382-009-0637-1

Insel, N., C. J. Poulsen, T. A. Ehlers, and C. Sturm (2012), Response of meteoric $\delta^{18}O$ to surface uplift - Implications for Cenozoic Andean Plateau growth, *Earth and Planetary Science Letters*, *317 - 318*, 262-272, 10.1016/j.epsl.2011.11.039

Jeffery, M. L., C. J. Poulsen, and T. A. Ehlers (2012), Impacts of Cenozoic global cooling, surface uplift, and an inland seaway on South American paleoclimate and precipitation $\delta^{18}O$, *Geological Society of America Bulletin*, *124*(3-4), 335-351, 10.1130/B30467.1

Jeffery, M. L., T. A. Ehlers, B. J. Yanites, and C. J. Poulsen (in press), Quantifying the role of paleoclimate and Andean plateau uplift on river incision, *Journal of Geophysical Research - Earth Surface*

Kennan, L., S. H. Lamb, and L. Hoke (Eds.) (1997), *High-altitude paleosurfaces in the Bolivian Andes: evidence for late Cenozoic uplift*, 307-323 pp.

Lenters, J. D., and K. H. Cook (1995), Simulation and diagnosis of the regional summertime precipitation climatology of South America, *Journal of Climate*, *8*(12), 2988-3005

Masek, J. G., B. L. Isacks, T. L. Gubbels, and E. J. Fielding (1994), Erosion and tectonics at the margins of continental plateaus, *Journal of Geophysical Research*, *99*(B7), 13941-13956, 10.1029/94JB00461

Pagani, M., J. C. Zachos, K. H. Freeman, B. Tipple, and S. Bohaty (2005), Marked decline in atmospheric carbon dioxide concentrations during the Paleogene, *Science*, *309*(5734), 600-603, 10.1126/science.1110063

Poulsen, C. J., and M. L. Jeffery (2011), Climate change imprinting on stable isotopic compositions of high-elevation meteoric water cloaks past surface elevations of major orogens, *Geology*, *39*(6), 595-598, 10.1130/G32052.1

Poulsen, C. J., T. A. Ehlers, and N. Insel (2010), Onset of Convective Rainfall During Gradual Late Miocene Rise of the Central Andes, *Science*, *328*(5977), 490-493, 10.1126/science.1185078

Roe, G. H., D. R. Montgomery, and B. Hallet (2002), Effects of orographic precipitation variations on the concavity of steady-state river profiles, *Geology*, *30*(2), 143-146, 10.1130/0091-7613(2002)030<0143:eoopvo>2.0.co;2

Schildgen, T. F., K. V. Hodges, K. X. Whipple, P. W. Reiners, and M. S. Pringle (2007), Uplift of the western margin of the Andean plateau revealed from canyon incision history, southern Peru, *Geology*, *35*(6), 523-526, 10.1130/g23532a.1

Schlunegger, F., K. P. Norton, and G. Zeilinger (2011), Climatic Forcing on Channel Profiles in the Eastern Cordillera of the Coroico Region, Bolivia, *Journal of Geology*, *119*(1), 97-107, 10.1086/657407

Sepulchre, P., L. C. Sloan, M. Snyder, and J. Fiechter (2009), Impacts of Andean uplift on the Humboldt Current system: A climate model sensitivity study, *Paleoceanography*, *24*, PA4215, 10.1029/2008PA001668

Tucker, G. E., and R. Slingerland (1997), Drainage basin responses to climate change, *Water Resources Research*, *33*(8), 2031-2047, 10.1029/97wr00409

Whipple, K. X., and G. E. Tucker (1999), Dynamics of the stream-power river incision model: Implications for height limits of mountain ranges, landscape response timescales, and research needs, *Journal of Geophysical Research-Solid Earth*, *104*(B8), 17661-17674, 10.1029/1999JB900120

Wobus, C. W., G. E. Tucker, and R. S. Anderson (2010), Does climate change create distinctive patterns of landscape incision?, *Journal of Geophysical Research-Earth Surface*, *115*, 10.1029/2009jf001562

APPENDIX A

ADDITIONAL MATERIAL IN SUPPORT OF CHAPTER 2 - IMPACTS OF CENOZOIC GLOBAL COOLING, SURFACE UPLIFT AND AN INLAND SEAWAY ON SOUTH AMERICAN PALEOCLIMATE AND PRECIPITATION $\delta^{18}O$

A.1 MATERIAL DESCRIPTION

These supplementary figures provide additional information in support of the key findings of the main paper. Figure A1 presents the results of additional, similar simulations with different boundary conditions. Figures A2 to A5 present the austral summer, austral winter, and mean annual climatology and $\delta^{18}O_{prec}$ results from the main experiments discussed in the paper. These additional results are intended to supplement the key results in the main text and are relevant for regions in which DJF is not the dominant rainfall season. The results in shown in figures A2 to A5 are from the same simulations as those presented in figures 2.4 and 2.5 in the main text and are averaged over 20 years.

Figure A.1 Austral summer $\delta^{18}O_{prec}$ for additional experiments

A-E) 20 year average simulated amount-weighted summer $\delta^{18}O_{prec}$ (‰) predicted by GENESIS with A) Half Andes, B) $2xCO_2$, C) Half Andes, $2xCO_2$ D) Half Andes, SW_{marine}, E) No Ice, no Antarctic Ice Sheet and modern $\delta^{18}O_{ocean}$. F-J) Summer $\delta^{18}O_{prec}$ difference (simulation minus control) between the sensitivity simulation and the control run (Fig. 2.1D) for the simulations in (A-E). Note that the contour interval changes at 4‰.

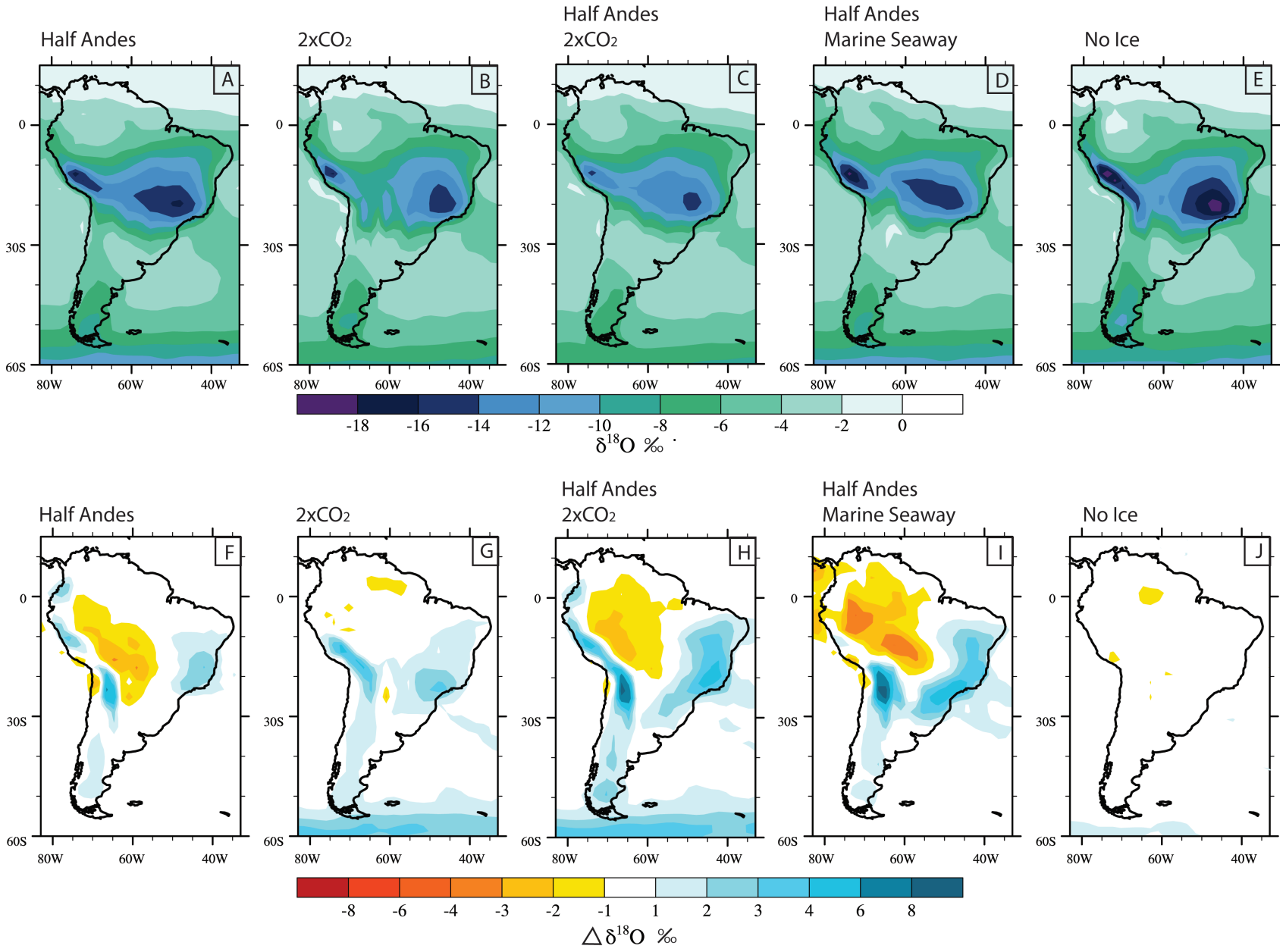
Half Andes
2xCO2
Half Andes
2xCO2
Half Andes
Marine Seaway
No Ice
A
B
C
D
E
0
30S
60S
80W
60W
40W
-18
-16
-14
-12
-10
-8
-6
-4
-2
0
δ18O ‰
Half Andes
2xCO2
Half Andes
2xCO2
Half Andes
Marine Seaway
No Ice
F
G
H
I
J
-8
-6
-4
-3
-2
-1
1
2
3
4
6
8
△δ18O ‰

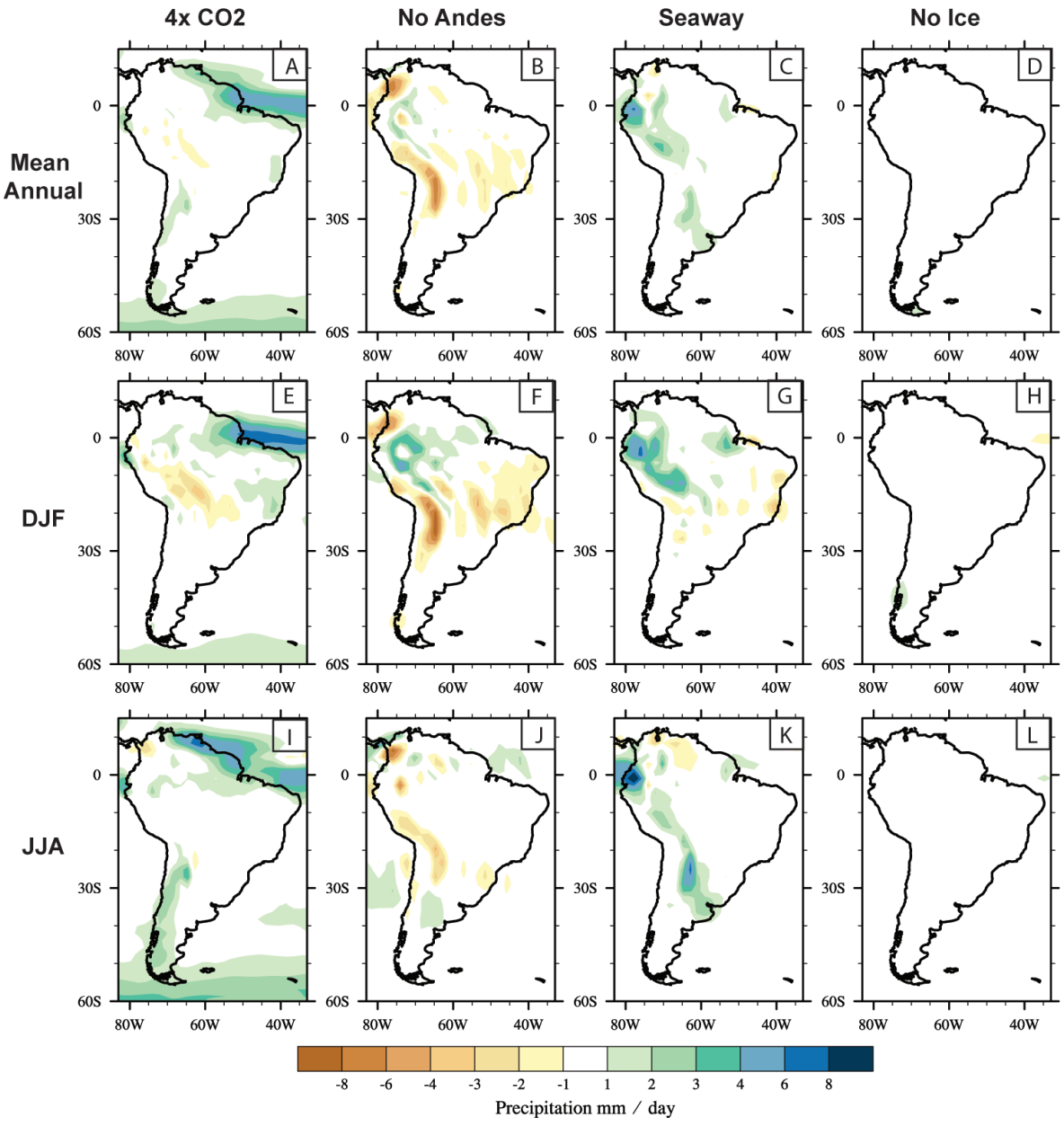

Figure A.2 Mean annual and seasonal difference in precipitation (mm/day)

Simulated differences in precipitation for mean annual (a-d), austral summer (e-h) and austral winter (i-l) between simulation and control (simulation minus control) for a, e and i) 4xCO2, b, f and j) No Andes, c, g and k) Seaway, and d, h and l) No Ice. Note that the contour intervals change at 6 mm/day.

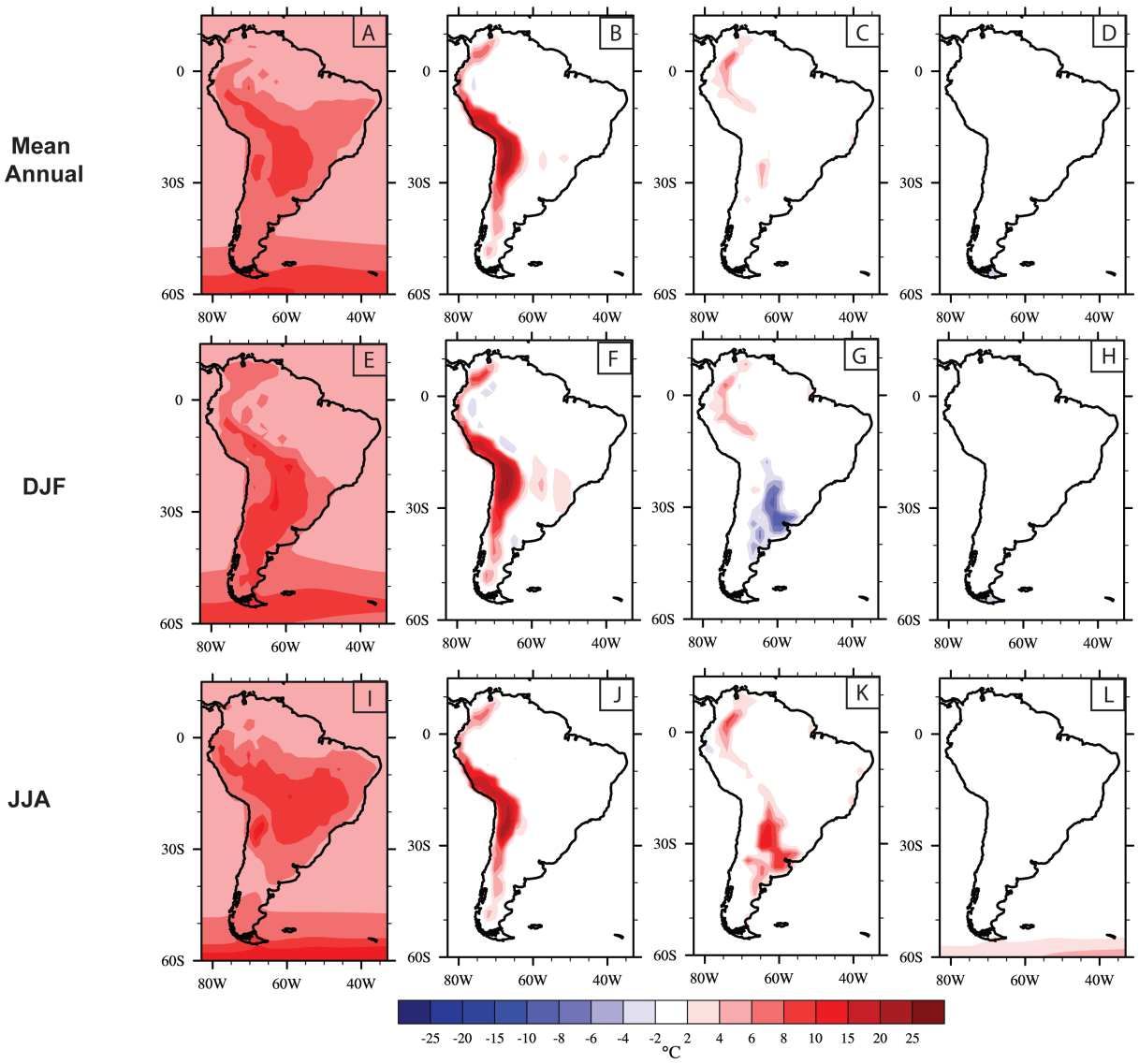

Figure A.3 Mean annual and seasonal difference in temperature (°C)

(previous page) Simulated differences in temperature for mean annual (a-d), austral summer (e-h) and austral winter (i-l) between simulation and control (simulation minus control) for a, e and i) 4xCO2, b, f and j) No Andes, c, g and k) Seaway, and d, h and l) No Ice. Note that the contour intervals change at 10°C.

Figure A.4 Mean annual and seasonal $\delta^{18}O_{prec}$

(following page) Simulated $\delta^{18}O_{prec}$for mean annual (a-f), austral summer (g-l) and austral winter (m-r). a, g and m) control simulation, b, h and n) 4xCO2, c, i and o) No Andes, d, j and p) Seaway with a marine isotopic composition, e, k and q) Seaway with a freshwater isotopic composition and f, l and r) No Ice.

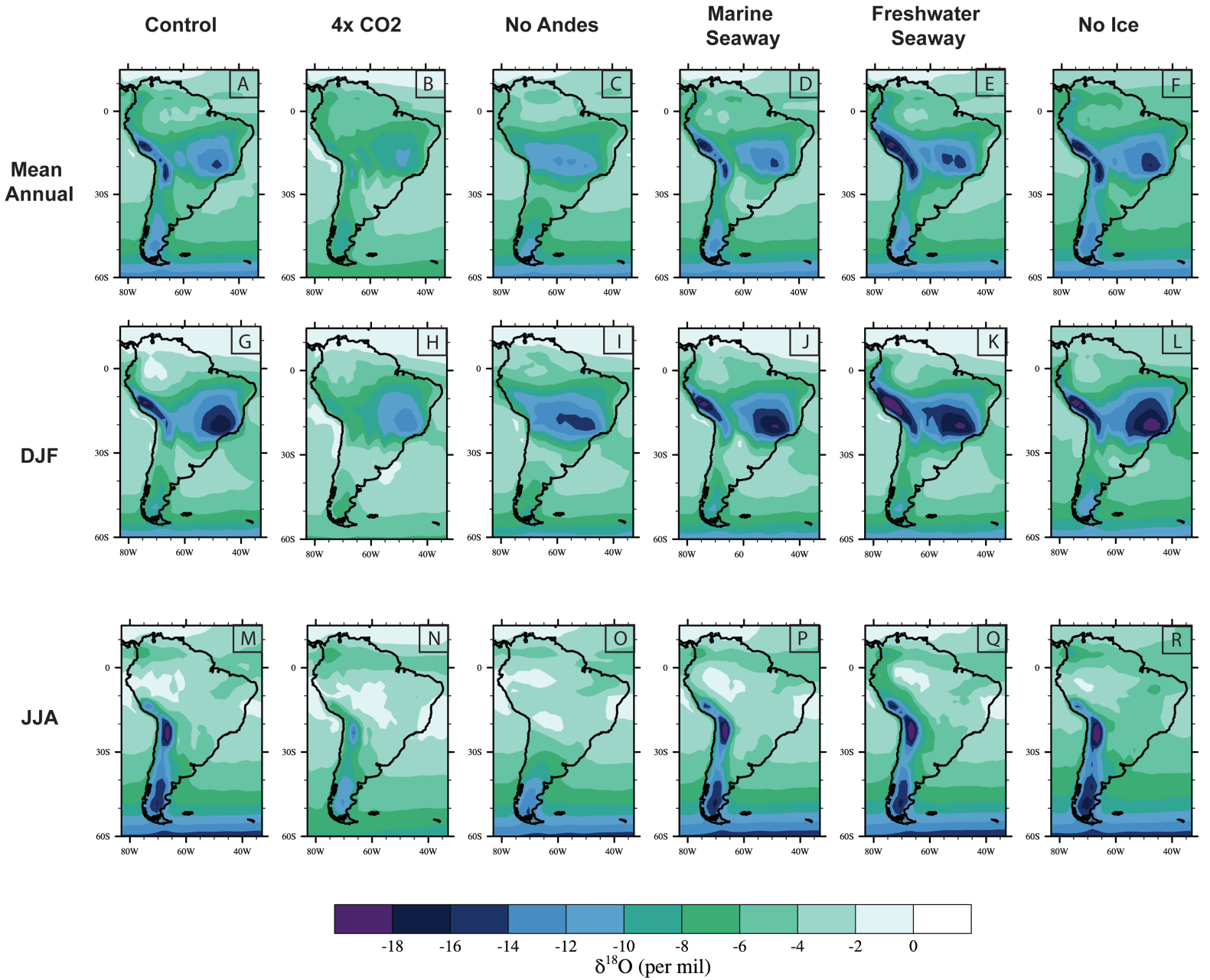
Control
4x CO2
No Andes
Marine Seaway
Freshwater Seaway
No Ice
Mean Annual
DJF
JJA
A
B
C
D
E
F
G
H
I
J
K
L
M
N
O
P
Q
R
0
30S
60S
80W
60W
40W
60
-18
-16
-14
-12
-10
-8
-6
-4
-2
0
δ18O (per mil)

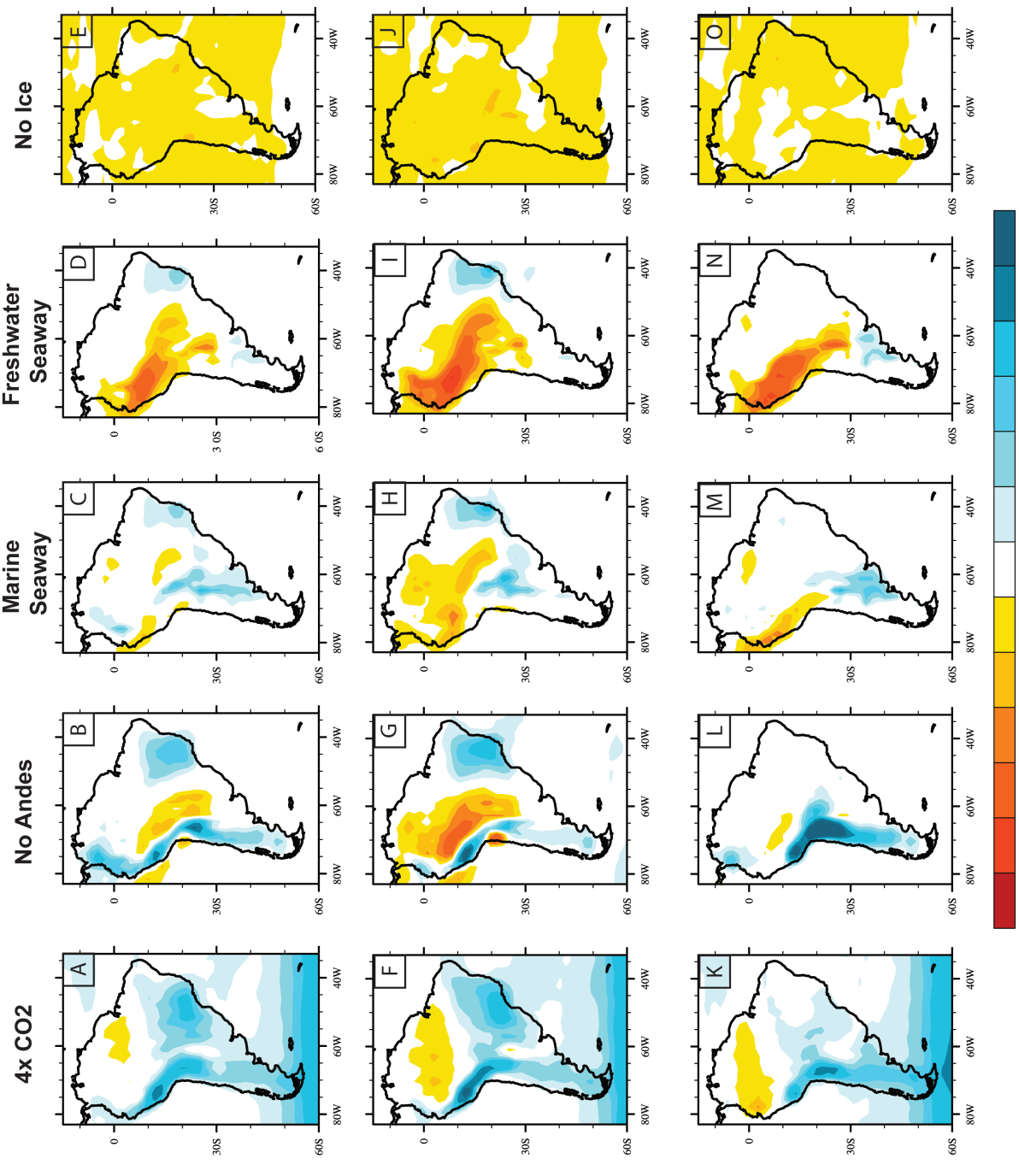
4x CO2
No Andes
Marine Seaway
Freshwater Seaway
No Ice
Mean Annual
DJF
JJA
A
B
C
D
E
F
G
H
I
J
K
L
M
N
O
0
30S
60S
80W
60W
40W
-8
-6
-4
-3
-2
-1
1
2
3
4
6
8
Δδ18O ‰

Figure A.5 Mean annual and seasonal difference in $\delta^{18}O_{prec}$

(previous page) Simulated difference in $\delta^{18}O_{prec}$ for mean annual (a-f), austral summer (g-l) and austral winter (m-r). Differences in $\delta^{18}O_{prec}$ between simulation and control (simulation minus control) for a, f and k) 4xCO2, b, g and l) No Andes, c, h and m) Seaway with a marine isotopic composition, d, i and n) Seaway with a freshwater isotopic composition, and e, j and o) No Ice.

APPENDIX B

ADDITIONAL MATERIAL IN SUPPORT OF CHAPTER 3 - QUANTIFYING THE ROLE OF PALEOCLIMATE AND ANDEAN PLATEAU UPLIFT ON RIVER INCISION

B.1 MATERIAL DESCRIPTION

The modern elevation of a regionally extensive paleosurface is an important constraint on the amount of incision occurring in the Ocoña catchment since the mid-Miocene. Here we describe how this elevation is extracted from regional 1:100,000 geological maps [INGEMMET] and the 30m ASTER GDEM [METI and NASA, 2001] in ArcMAP v9.3. First, geo-referenced geologic maps were simplified to identify the key stratigraphic units, specifically the Miocene Moquegua formation and the 16 – 14 Ma Huaylillas ignimbrite (Figure B.1). Following Schildgen et al. [2007], the paleosurface is defined as the base of the 16 – 14 Ma Huaylillas ignimbrite. Control points, where the Huaylillas ignimbrite overlies Miocene sediments at the surface, were identified and the modern elevation of these points extracted from an ASTER 30 DEM (Figure B.1). Second, the elevation of these control points is interpolated using a tension spline fit to generate a surface (Figure B.2). Due to a lack of available data on the plateau (north of ~15.5 °S), the elevation of the paleosurface north of 15.4 °S was defined as 4500 m. This elevation is based on mapped contacts between Paleozoic to early Cenozoic sediments, and overlying late Cenozoic volcanic deposits. Finally, for use in the river incision model, the elevation of the paleosurface is extracted at 25 km intervals along the profile of the modern river (Fig. 3.1, main text).

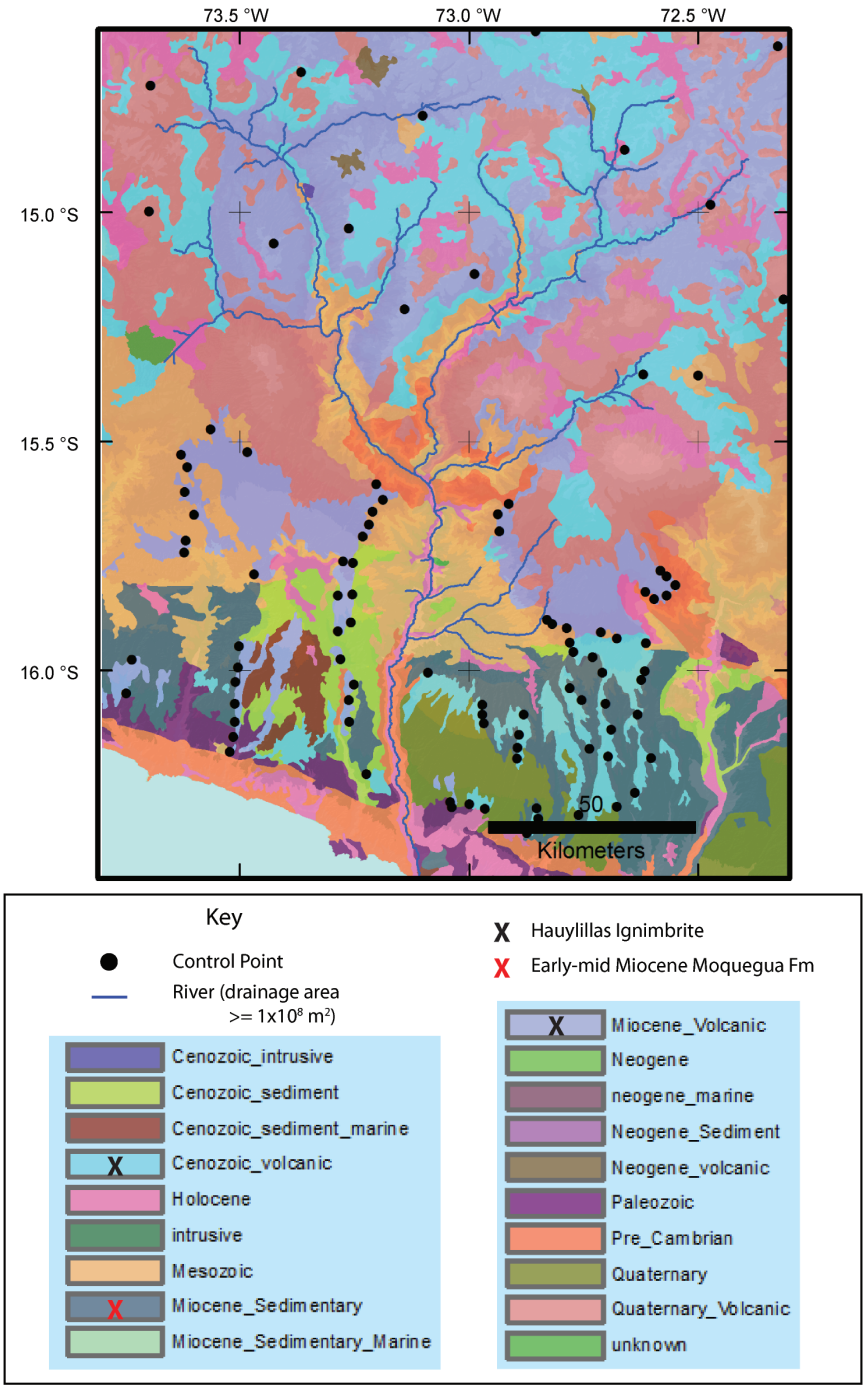

Figure B.1 Control points on regional geological map

Black circles indicate control points that were selected on the boundary of outcrops of mid-to-late Miocene volcanics that overly early-Miocene and older sediments. Key geological units are indicated with an 'X' in the key. The location of the modern river (blue) is indicated for comparison with Figure 1 in the main text. North of ~15.4?S, the Huaylillas ignimbrite is not well defined. The paleosurface was therefore fixed at 4500 m, based on the lowest elevation of more recent volcanic deposits.

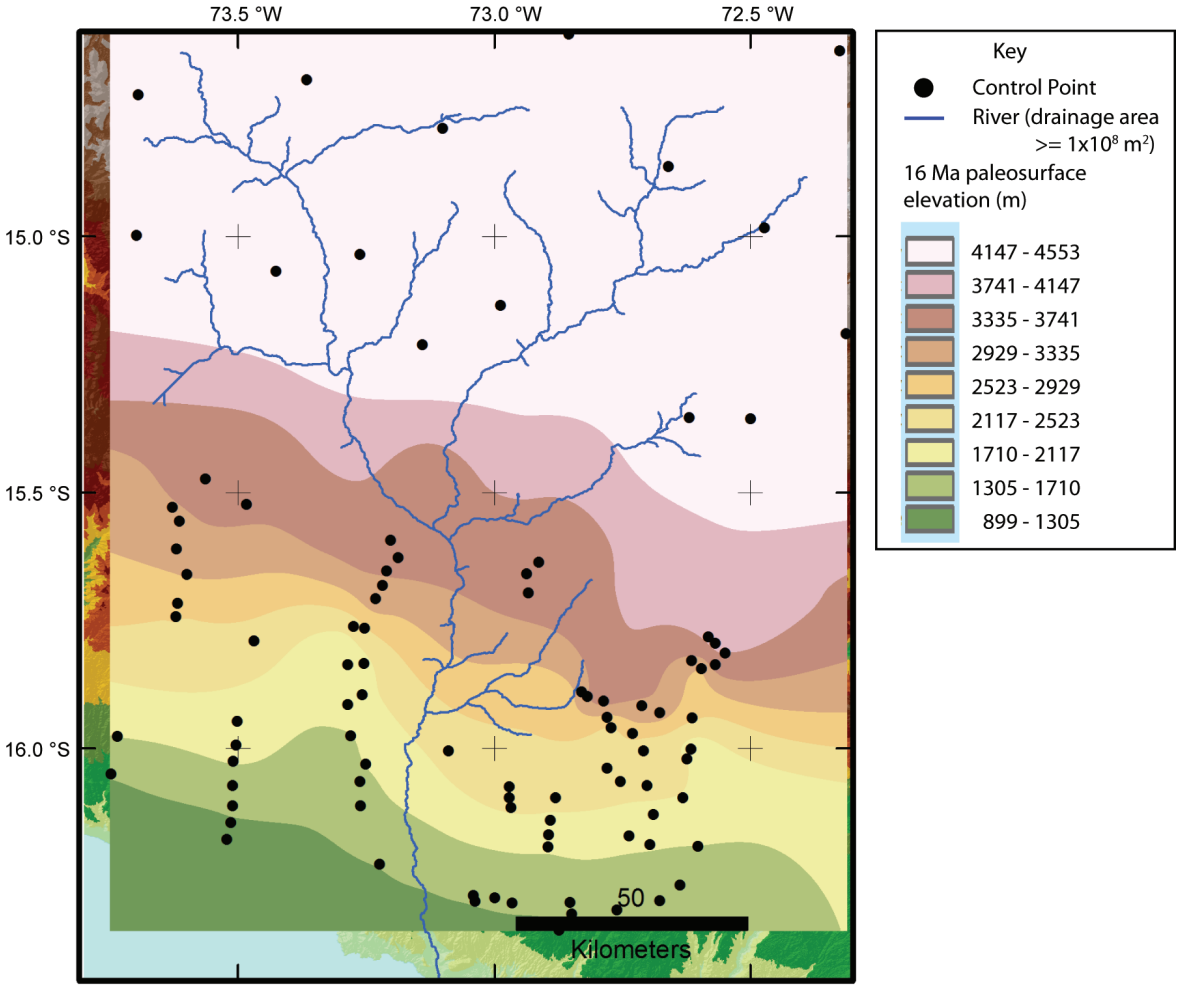

Figure B.2 Elevation of the 16 Ma Paleosurface

Elevation of the surface generated by spline fitting to the elevation of the control points identified in Supplementary Figure 1.

B.2 REFERENCES

INGEMMET - Instituto Geológico Minero y Metalúrgico (2004) Carta Geológica Nacional del Perú. Data accessed in November 2010 from http://www.ingemmet.gob.pe/form/plantilla01.aspx?Opcion=184.

METI, and NASA (2001), ASTER GDEM edited, Ministry of Economy, Trade and Industry (METI) and NASA Land Processes Distributed Active Archive Center (LP DAAC), USGS/Earth Resources Observation and Science (EROS) Center, Sioux Falls, South Dakota.

Schildgen, T. F., K. V. Hodges, K. X. Whipple, P. W. Reiners, and M. S. Pringle (2007), Uplift of the western margin of the Andean plateau revealed from canyon incision history, southern Peru, *Geology*, *35*(6), 523-526.